Iowa State University
Digital Repository

2015

Advanced mission planning and impact risk assessment of near-Earth asteroids in application to planetary defense

George Vardaxis
Iowa State University

Follow this and additional works at: https://lib.dr.iastate.edu/etd

Part of the Aerospace Engineering Commons

Advanced mission planning and impact risk assessment of near-Earth asteroids in application to planetary defense

by

George Vardaxis

A dissertation submitted to the graduate faculty

in partial fulfillment of the requirements for the degree of

DOCTOR OF PHILOSOPHY

Major: Aerospace Engineering

Program of Study Committee:

Bong Wie, Major Professor

John Basart

Ran Dai

Ping Lu

Peter Sherman

Iowa State University

Ames, Iowa

2015

DEDICATION

I would like to thank my parents, brothers, and all my family and friends who have helped me throughout my life. Without your help and support this would not have been possible.

TABLE OF CONTENTS

LIST OF TABLES

LIST OF FIGURES

ACKNOWLEDGEMENTS

I would like to take this opportunity to express my thanks to those who helped me with various aspects of conducting research and the writing of this thesis. First and foremost, Dr. Bong Wie for his guidance and support throughout this research and the writing of this thesis. I would also like to thank my committee members for their efforts and contributions to this work: Dr. John Basart, Dr. Ran Dai, Dr. Ping Lu, and Dr. Peter Sherman. I would additionally like to thank Dr. Dale Chimenti for his guidance through the later stages of my undergraduate degree and throughout my graduate career.

CHAPTER 1.   INTRODUCTION

The problem of orbital prediction is not new to the field of orbital mechanics, however the results of the orbital prediction problem could be more important now than ever before. The threat from asteroids, and other interplanetary bodies, that Earth faces everyday is very real and ever-present. In most cases, the objects are too small to do any damage on the surface because they burn up in the atmosphere, but there are the rare instances where an object does make landfall. Despite the lack of a known immediate impact threat from an asteroid or comet, historical, scientific evidence suggests that the potential for a major catastrophe created by an asteroid or comet impacting Earth is very real. Fortunately, the human race is in a unique position to do something about those threats to mitigate and/or eliminate them and therefore must be prepared to deal with such an event that could otherwise cause a regional or global catastrophe. Spurred by the Chelyabinsk meteorite airburst event that occurred in Russia on February 15, 2013 and the near miss by asteroid 367943 Duende (2012 DA14), approximately 40 m in size, on the same day, there is now growing national and international interest in developing a global plan to protect the Earth from a catastrophic impact by a hazardous near-Earth object (NEO).

NASA, as well as other organizations, have put a lot of effort into the detection/tracking of all near-Earth objects - threatening and non-threatening. Given all that effort and knowledge, a variety of NEO deflection/disruption technologies, such as nuclear explosions, kinetic impactors, and slow-pull gravity tractors (GTs), have been investigated by planetary defense researchers during the past two decades [8, 9, 10, 11, 12, 13, 14, 15, 16, 17]. Through all the study and investigation however, there is no concensus on how to reliably deflect or disrupt hazardous NEOs in a timely or efficient manner. All the non-nuclear techniques studied found that they will require mission lead times much longer than 10 years, even for a relatively small

NEO. When the time-to-impact with the Earth exceeds a decade, the velocity perturbation needed to alter the target's orbit sufficiently is relatively small (approximately 1 to 2 cm/s). Thus, most non-nuclear options as well as a nuclear standoff explosions can be implemented for deflection missions when sufficiently long warning times exist. It is important to note and emphasize that any NEO deflection effort must produce an actual orbital change much larger than predicted orbital perturbation uncertainties from all sources in order to ensure mission success. Likewise, any NEO deflection/disruption approach must be robust against the unknown material properties of a given target NEO. At the Asteroid Deflection Research Center (ADRC), there has been a lot of research work done on the mitigation of near-Earth asteroids with short warning times (< 10 years) by studying potential mission designs to disrupt hazardous asteroids.

Kinetic impactors and nuclear explosions may be considered as the most mature technologies for asteroid deflection or disruption, as concluded in the 2010 NRC report [17]. As impulsive and energy-rich approaches, the final momentum change can be considerably more than that present in the original impactor, or in the expanded vaporization layer (from a nuclear standoff explosion). Both impulsive methodologies are expected to eject some debris which depends on surface material properties, where high porosity affects the ability to convert the excess energy into additional momentum. Some asteroids like Itokawa have been determined to have densities (and thus porosities) comparable to terrestrial material with well-characterized shock propagation properties, while others appear to have very low porosity that may absorb excess energy without the hydrodynamic rebound that can amplify the original impulse.

Since nuclear energy densities are nearly a million times higher than those possible with chemical bonds, a nuclear explosive device (NED) is the most mass-efficient means for storing energy with today's technology. The mass and energy efficiency of an NED enables a wider range of mission designs to be possible and could prove the difference between an asteroid being reachable and unattainable. However, deflection methods with sufficiently high energy density are often preferred over a nuclear disruption approach due to the implied risk of putting a nuclear explosive on a launch vehicle and sending it through Earth's atmosphere on route to its interplanetary target. Nuclear standoff explosions however, are assessed to be much more

effective than any other non-nuclear alternatives, especially for larger asteroids. This deflection method utilizes a nuclear explosion at a specified standoff distance from the target NEO, to effect a large velocity change by ablating and blowing off a thin layer of the NEO's surface. The precise outcome of a NEO deflection attempt using a nuclear standoff explosion is dependent on a myriad variables, with critical factors including the shape and composition of the target NEO. Ideally, a separate mission would be launched prior to a successful nuclear deflection attempt, in order to characterize these critical target properties. Other techniques involving the use of surface or subsurface nuclear explosives are assessed to be more efficient than the nuclear standoff explosion, although they may cause an increased risk of fracturing the target asteroid [17].

Given the various uncertainties and constraints in asteroid detection and tracking, the warning time or mission lead time prior to a potential impact can be very short. With no warning at all, an 18-m diameter meteor exploded with the energy of 30 Hiroshima nuclear bombs, 30 km above the city of Chelyabinsk, Russia on February 15, 2013. Asteroid 367943 Duende (2012 DA14) had a near miss of the Earth on the same day as the Chelyabinsk event, and it was initially discovered on February 23, 2012. That is, we would have had only one year of warning time to deal with the threat, if the 40 m 2012 DA14 was going to collide with Earth. Another recent example of a near miss by an asteroid on the Earth is asteroid 2014 RC, which had a close encounter with Earth on September 7, 2014. This 20-m asteroid was initially discovered on August 31, 2014 by the Catalina Sky Survey near Tucson, Arizona, and was independently detected the next night by the Pan-STARRS 1 telescope, located on the summit of Haleakala on Maui, Hawaii. If 2014 RC was going to collide with Earth, there would only be one week of warning time for a mitigation strategy to be constructed and enacted.

If a NEO on an Earth-impacting trajectory is detected with a short warning time (e.g., much less than 5 years), the challenge becomes how to mitigate its threat with the amount of time given prior to the potential impact. For a small asteroid impacting in a sufficiently unpopulated region, mitigation may simply involve evacuation [17]. However, for larger asteroids, or asteroids impacting sufficiently developed regions, the threat may be mitigated by either disrupting the asteroid (i.e. destroying or fragmenting the target with substantial orbital dispersion), or by

altering its trajectory such that it will either avoid impacting the predicted impact location, or ideally miss the Earth entirely. It's not difficult to understand that when the time to impact with Earth is short, the velocity change required to deflect an NEO becomes extremely large. Thus, for the most probable mission scenarios, in which the warning time is shorter than 5 years, the use of high-energy nuclear explosives in space will become inevitable [17]. Figure 1.1 shows the results of a Near-Earth asteroid survey conducted by NASA in 2010. It can be
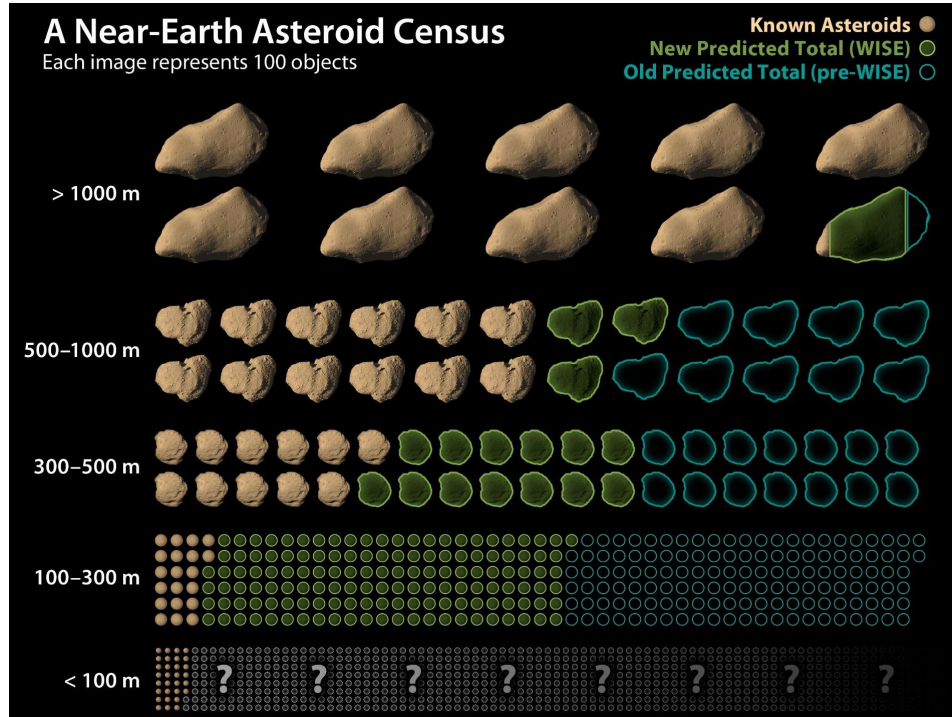
Figure 1.1   A graphic representation of the known and predicted Near-Earth asteroid population, according to size.

seen that a large majority of the asteroid bodies, 500 meters or more in diameter are known, while less than 40% of the asteroids between 300 and 500 meters in diameter and far fewer asteroids with diameters less than 300 meters are known. A scenario in which a small (e.g., 50 to 150 m) Earth-impacting NEO is discovered with short warning time is considered the most probable scenario because smaller NEOs greatly outnumber larger NEOs, and smaller NEOs are more difficult to detect. Most direct intercept missions with a short warning time will result in arrival closing velocities of 10 to 30 km/s with respect to the target asteroid. A rendezvous mission to a target asteroid that requires such an extremely large arrival ΔV is not feasible.

The problem looking to be solved through the work done in this dissertation is the construction of a tool that can analyze the future propagation of a target asteroid's orbit, assess the future risk the asteroid possesses with respect to the Earth, design a mission to the target that could help further evaluate the orbit or deflect/disrupt the body in its orbit, and finally evaluate the deflection/disruption attempt in terms of the risk posed by the asteroid, or asteroid fragments, on the current encounter and future encounters with the Earth. Techniques such as a high-precision gravitational simulator, encounter geometry, B-plane mapping, and gravitational keyholes are used to quantitatively evaluate the orbital characteristics of an asteroid and its associated impact risk. Using state information about the asteroid, a high-fidelity gravitational model can be used to propagate the body into the future to see if and when it would come in close proximity to a planet, particularly Earth. These planetary encounters would change the asteroid's orbit, in shape and/or orientation. From the encounter geometry, the post-encounter heliocentric orbit of the asteroid could be in a resonance with that planet resulting in another encounter, or potentially an impact. Taking advantage of keyhole theory and the encounter's B-plane, an estimate of the current and future impact probability of the asteroid can be made.

CHAPTER 2.   ORBIT PROPAGATION

2.1   Introduction

One of the main challenges in Orbital Mechanics, that needs to be dealt with before work can truly begin on any problem, is the propagation of a body through space. Orbit propagation has two distinct components, the propagation model and the propagation method. The model used dictates the fidelity and accuracy of the expected solution. Low-fidelity models such as kepler's equation and the two-body equations of motion are very simple models that can be incorporated easily and produce results in a very efficient amount of time. More moderate-fidelity models like the universal variable formulation can produce results that are a bit more accurate, but will require more time to produce those results. High-fidelity models like the so-called Standard Dynamical Model (SDM) incorporate third-body perturbations and non-conservatives effects into the model to enable a high accuracy result. The only drawback to the SDM is that with so many extra terms to be added, the propagation method would require more time to build the orbit solution.

When dealing with the ordinary differential equations (ODEs) that describe the equations of motion (EOMs) of the body of interest, there are several propagation methods that exist to find their solutions at any point in time. The complexity of the propagation method determines the accuracy of the solution that can be found. Simpler methods like the use of a state transition matrix (STM) linearize the equations of motion and allow a solution to be found quickly, while sacrificing some of the accuracy from the nonlinearity of the EOMs. More commonly used methods for solving the EOMs are numerical integration schemes that vary from low-order schemes like Runge-Kutta second (RK2) and fourth (RK4) order schemes to higher-order ones like Runge-Kutta-Fehlberg seventh eighth order (RKF78) schemes, and even predictor-

corrector, double integration, and Adams-Bashforth methods. Most of these methods involve several EOM function calls and include variable time-step numerical integration techniques that minimize the local error for each time-step in an attempt to minimize the absolute error over the period of propagation.

The simulations conducted over the course of the studies discussed throughout this work include two-body, three-body, and n-body equations of motion presented within the Standard Dynamical Model. The schemes used to find solutions to the EOMs were state transition matrix state progation and numerical integration using a Runge-Kutta-Fehlberg 7(8) method. The details of these models and schemes are presented below.

2.2   Orbit Propagation Models

2.2.1   Two-Body Equations of Motion

Consider a system of two bodies of mass M and m. Let an inertial set of cartesian coordinates (X', Y', Z') exist, and a set of non-rotating coordinates (X, Y, Z) that are parallel to the inertial axes and have an origin that is coincident with the body of mass M, as seen in Figure 2.1. Also, let the position vectors of bodies M and m with respect to the inertial
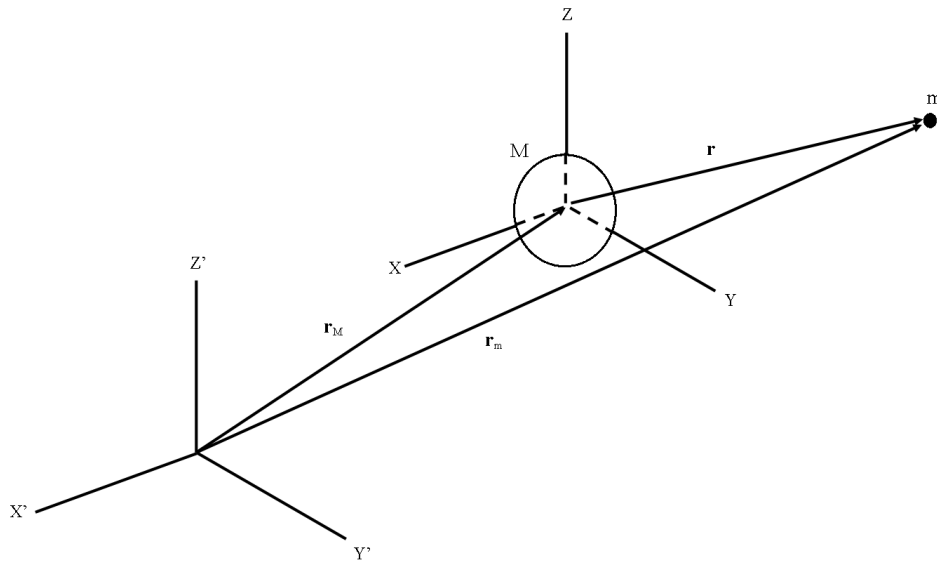
Figure 2.1   Illustration of the reference frame and associated vectors for a system with two bodies.

coordinate system are $\vec{r}_M$ and $\vec{r}_m$, respectively. The position vector of the body of mass m with respect to mass M is defined as

$$\vec{r} = \vec{r}_m - \vec{r}_M \tag{2.1}$$

Applying Newton's laws in the inertial frame, we obtain

$$m\ddot{\vec{r}}_m = -\frac{GMm}{r^2}\frac{\vec{r}}{r} \tag{2.2}$$

and

$$M\ddot{\vec{r}}_M = \frac{GMm}{r^2}\frac{\vec{r}}{r} \tag{2.3}$$

Rewriting Eq. 2.2 and Eq. 2.3 and subtracting Eq. 2.3 from Eq. 2.2, the resulting equation takes the following form

$$\ddot{\vec{r}} = -\frac{G(M+m)}{r^3}\vec{r} \tag{2.4}$$

Eq. 2.4 is the vector differential equation of the relative motion for the two-body problem. Given that the (X, Y, Z) coordinate system is non-rotating in relation to the (X', Y', Z') coordinate system, the magnitudes and directions of $\vec{r}$ and $\ddot{\vec{r}}$ will be equal with respect to either coordinate system. So, despite having assumed the existence of an inertial coordinate system, it can be discarded and just measure relative position, velocity, and acceleration in the non-rotating, non-inertial coordinate system with its origin at the central body [18]. Since the body of interest is a near-Earth asteroid, and the central body that the asteroid will be measured with respect to will either be the Sun or a planet, then it can be approximated that $G(M + m) \approx GM$. And, for convenience, μ is defined as $\mu = GM$, so that Eq. 2.4 becomes

$$\ddot{\vec{r}} = -\frac{\mu}{r^3}\vec{r} \tag{2.5}$$

Eq. 2.5 is the more iconic form of the two-body equations of motion displayed in most Orbital Mechanics texts.

2.2.2 N-Body Equations of Motion

The standard two-body equations form the relations that underlie much of the general work done in Orbital Mechanics, but sometimes there is the need for a more realistic model that

includes other bodies. First, let's consider a three-body system that includes the Sun, Earth, and satellite orbiting the Earth, as illustrated in Figure 2.2. For this three-body system in
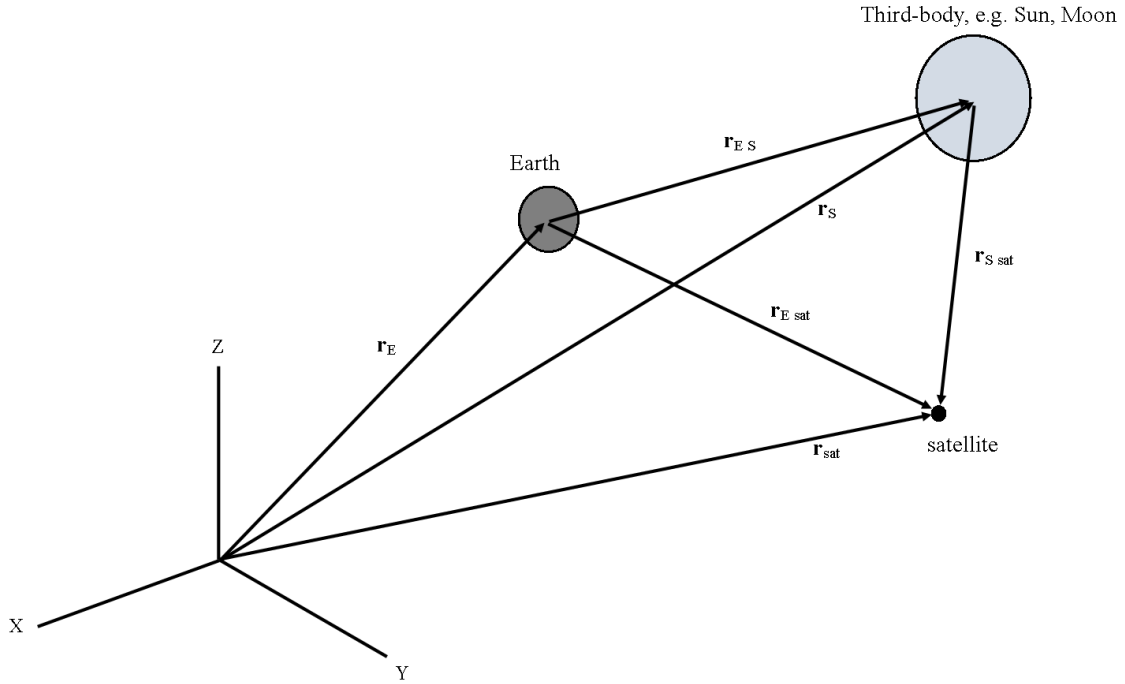
Figure 2.2 Illustration of the reference frame and associated vectors for a system with three bodies.

an inertial (XYZ) reference frame, we examine the individual forces between the Earth and the satellite.

$$\vec{r}_{Esat} = \vec{r}_{sat} - \vec{r}_E \quad \rightarrow \quad \ddot{\vec{r}}_{Esat} = \ddot{\vec{r}}_{sat} - \ddot{\vec{r}}_E \tag{2.6}$$

Based on Newton's Second Law and the Law of Gravitation, the sum of the forces acting on the Earth is

$$\sum \vec{F}_{gE} = m_E \ddot{\vec{r}}_E = \frac{G m_E m_{sat} \vec{r}_{Esat}}{r_{Esat}^3} + \frac{G m_E m_S \vec{r}_{ES}}{r_{ES}^3} \tag{2.7}$$

where $\ddot{\vec{r}}_E$ is the acceleration an observer would see from the origin of the inertial XYZ system, m_E is the mass of the Earth, m_{sat} is the mass of the satellite, m_S is the mass of the Sun, G is the universal gravitational constant, $\vec{r}_{Esat}$ and r_{Esat} are the vector and magnitude of the distance between Earth and the satellite, and $\vec{r}_{ES}$ and r_{ES} are the vector and magnitude of the distance between Earth and the Sun. The first term in Eq. 2.7 is the gravitational pull of the satellite on the Earth, and the second term is the gravitational pull of the Sun on the Earth.

The sum of the gravitational forces acting on the satellite, shown in Eq. 2.8, can be expressed in the form

$$\sum \vec{F}_{gsat} = m_{sat}\ddot{\vec{r}}_{sat} = -\frac{Gm_E m_{sat}\vec{r}_{Esat}}{r_{Esat}^3} - \frac{Gm_S m_{sat}\vec{r}_{Ssat}}{r_{Ssat}^3} \tag{2.8}$$

where the terms represent the pull of the Earth and Sun, respectively, on the satellite. Both forces are negative because they are in a direction opposite that of the vectors to the satellite. Plugging Eq. 2.7 and Eq. 2.8 into Eq. 2.6, the resulting equation takes the form

$$\ddot{\vec{r}}_{Esat} = -\frac{Gm_E \vec{r}_{Esat}}{r_{Esat}^3} - \frac{Gm_S \vec{r}_{Ssat}}{r_{Ssat}^3} - \frac{Gm_{sat}\vec{r}_{Esat}}{r_{Esat}^3} + \frac{Gm_S \vec{r}_{ES}}{r_{ES}^3}. \tag{2.9}$$

Using the fact that $\vec{r}_{satS} = -\vec{r}_{Ssat}$, Eq. 2.9 simplifies to

$$\ddot{\vec{r}}_{Esat} = -\frac{G\left(m_E + m_{sat}\right)\vec{r}_{Esat}}{r_{Esat}^3} + Gm_S \left(\frac{\vec{r}_{satS}}{r_{satS}^3} - \frac{\vec{r}_{ES}}{r_{ES}^3}\right). \tag{2.10}$$

This form of Eq. 2.10 is sometimes referred to as the "relative" form of the equations of motion. This is however a bit misleading as the only thing that has been done is transform the acceleration to a different origin. The first term is the two-body acceleration of the Earth acting on the satellite. The second term has two parts and it represents the perturbation, or the additional forces beyond simple two-body motion, acting on the satellite. The left-hand term is called the direct effect because it's the acceleration of the Sun (or third body) directly on the satellite. The right-hand term is called the indirect effect because it's the acceleration of the Sun (third body) on the Earth. The finite sum for the total acceleration of the ith body due to the gravitational attraction from n bodies takes the form

$$\ddot{\vec{r}}_i = -G \sum_{j=1, j\neq i}^{n} \frac{m_j}{r_{ji}^3}\vec{r}_{ji}, \quad \vec{r}_{ji} = \vec{r}_i - \vec{r}_j, \quad i = 1, ..., n. \tag{2.11}$$

The three-body problem is a special case where $n = 3$. The general series representation of the relative acceleration equation shown in Eq. 2.10, where 1 is the primary body and 2 is replaced with the satellite, is

$$\ddot{\vec{r}}_{Esat} = -\frac{G\left(m_1 + m_{sat}\right)\vec{r}_{1sat}}{r_{1sat}^3} + G\sum_{j=3}^{n} m_j \left(\frac{\vec{r}_{satj}}{r_{satj}^3} - \frac{\vec{r}_{1j}}{r_{1j}^3}\right). \tag{2.12}$$

This general series representation is useful in real world applications because it is more convenient to reference the primary body's center [19].

In order for an orbit to be defined, it must be parameterized. The National Aeronautics and Space Administration (NASA) and the NASA Jet Propulsion Laboratory (JPL) choose to parameterize orbits in terms of six classical Keplerian orbital elements: eccentricity (e), perihelion distance (q), time of perihelion passage (T_p), right ascension of the ascending node (Ω), argument of perihelion (ω), and inclination to the ecliptic (i). There are many choices of how to parameterize the orbit of a body and throughout this work most of the same orbital elements will be used, with two exceptions: the perihelion distance will be replaced with the semi-major axis length (a) and the time of perihelion passage will be replaced by the true anomaly angle (ν). There can be an issue using a instead of q due to the singularity that can arise with parabolic orbits (which long period comets very closely follow), but since the focus of this work is on near-Earth asteroids, the substitution is made with no trepidation. The equations of motion, in the form of the Standard Dynamical Model, are most easily computed in terms of heliocentric postion and velocity vectors ($\vec{r}$ and $\vec{v}$ respectively) within the inertial-frame. The Newtonian n-body EOMs used for the free-space propagation of the asteroid bodies, takes the form [20]

$$\frac{d^2\vec{r}}{dt^2} = -\frac{\mu}{r^3}\vec{r} + \sum_{k=1}^{n} \mu_k \left(\frac{\vec{r}_k - \vec{r}}{|\vec{r}_k - \vec{r}|^3} - \frac{\vec{r}_k}{r_k^3} \right) + \vec{f} \tag{2.13}$$

where $\mu = GM$ is the gravitational parameter of the Sun, n is the number of perturbing bodies, μ_k and $\vec{r}_k$ are the gravitational parameter and heliocentric position vector of perturbing body k, respectively, and $\vec{f}$ represents other non-conservative orbital perturbation acceleration. The three most well-known are solar radiation pressure (SRP), relativistic effects, and the Yarkovsky effect, the former two being the most prevalent effects. Solar radiation pressure provides a radial outward force on the asteroid body from the interaction of the Sun's photons impacting the asteroid surface. The SRP model is given by

$$\vec{a}_{SRP} = (K)(C_R) \left(\frac{A_R}{M} \right) \left(\frac{L_S}{4\pi c r^3} \right) \vec{r} \tag{2.14}$$

where $\vec{a}_{SRP}$ is the solar radiation pressure acceleration vector, C_R is the coefficient for solar radiation, A_R is the cross-sectional area presented to the Sun, M is the mass of the asteroid, K is the fraction of the solar disk visible at the asteroid's location, L_S is the luminosity of the Sun, c is the speed of light, and $\vec{r}$ and r is the distance vector and magnitude of the asteroid from the

Sun, respectively. The relativistic effects of the body are included because for many objects, especially those with small semi-major axes and large eccentricities, those effects introduce a non-negligible radial acceleration toward the Sun. One form of the relativistic effects is represented by

$$\vec{a}_R = \frac{k^2}{c^2 r^3} \left[\frac{4k^2 \vec{r}}{r} - \left(\dot{\vec{r}} \cdot \dot{\vec{r}} \right) \vec{r} + 4 \left(\vec{r} \cdot \dot{\vec{r}} \right) \dot{\vec{r}} \right] \tag{2.15}$$

where $\vec{a}_R$ is the acceleration vector due to relativistic effects, k is the Gaussian constant, c is the speed of light, $\vec{r}$ is the position vector of the asteroid, and $\dot{\vec{r}}$ is the velocity vector of the asteroid [21]. In the case of near-Earth asteroids, the acceleration term due to relativistic effects is not necessary, but is included in this discuss for completeness.

In the case when the Earth is considered the central body, as is done when dealing with the flyby of the asteroid, another perturbation must be added to the model in order to maintain accuracy. The extra perturbation would be due to the Earth's oblateness, known as the J2 gravity perturbation. This perturbation has to be taken into account for orbits about Earth because of the non-uniformity of Earth's surface, which is assumed when dealing with the equations of motion. For most circumstances, the equations of motion are fine as given above because the distances between the simulated body and any other body is large enough that they can be assumed to be a point mass. During planetary flybys, particularly flybys with the Earth, the simulated body can pass close enough to the planet that it can't be assumed to be a uniform sphere that can mathematically be represented as a point mass. When considering orbits about Earth, an additional potential energy term must be added to the overall potential energy of the planet, as shown in Eq. 2.16,

$$V(x, y, z) = \frac{\mu}{r} + \frac{c}{r^3} \left[3 \left(\frac{z}{r} \right)^2 - 1 \right] \tag{2.16}$$

where

$$c = \frac{J_2 \mu R_{\oplus}^2}{2} \tag{2.17}$$

$r = \sqrt{x^2 + y^2 + z^2}$, with μ being the Earth's gravitational constant, $J_2 = 1.082617 \times 10^{-3}$ is the second zonal harmonic, and $R_{\oplus}$ is the mean equatorial radius of the Earth. So, to describe the motion of a body with respect to the Earth, incorporating the J_2 gravitational perturbation

- represented by the additional term on the right-hand side of the equations, the equations of motion from Eq. 2.5 become

$$\ddot{x} = \frac{\partial V}{\partial x} \quad = \quad -\frac{\mu x}{r^3} + 3c \left(\frac{x}{r^5} \right) \left(1 - \frac{5z^2}{r^2} \right), \tag{2.18}$$

$$\ddot{y} = \frac{\partial V}{\partial y} \quad = \quad -\frac{\mu y}{r^3} + 3c \left(\frac{y}{r^5} \right) \left(1 - \frac{5z^2}{r^2} \right), \tag{2.19}$$

$$\ddot{z} = \frac{\partial V}{\partial z} \quad = \quad -\frac{\mu z}{r^3} + 3c \left(\frac{z}{r^5} \right) \left(3 - \frac{5z^2}{r^2} \right). \tag{2.20}$$

The coordinate system is fixed to the xy plane that is defined by the Earth's equatorial plane [22].

2.3   Orbit Propagation Schemes

2.3.1   State Transition Matrix

The state transition matrix is a linearization of the dynamics of a system, such that it is assumed that a solution is known for one trajectory and we are interested in finding the solution to a neighboring trajectory. The linearization allows for the development of a simplified approximation to compute the differences between the trajectories over a limited time interval. The only major constraint to this type of formulation is that the differences between the two trajectories need to remain small so that the higher order terms in Eq. 2.21

$$\dot{\mathbf{Y}} = \vec{f}(\mathbf{X}) + \frac{\partial \vec{f}(\mathbf{X})}{\partial \mathbf{X}} \delta \mathbf{x} + \frac{\partial \vec{f}^2(\mathbf{X})}{2! \partial \mathbf{X}^2} \delta \mathbf{x}^2 + ... \tag{2.21}$$

can be neglected. The two trajectories are $\mathbf{X}$ and $\mathbf{Y}$, where the expressions of the initial conditions and derivatives of the states are

$$\mathbf{X}(t_0) = \mathbf{X}_0 \qquad \dot{\mathbf{X}} = \vec{f}(\mathbf{X}) \tag{2.22}$$

$$\mathbf{Y}(t_0) = \mathbf{Y}_0 \qquad \dot{\mathbf{Y}} = \vec{f}(\mathbf{Y}) \tag{2.23}$$

where f denotes a function of the state and $\delta \mathbf{x}$ is the difference between the two trajectories given by

$$\mathbf{Y} = \mathbf{X} + \delta \mathbf{x} \tag{2.24}$$

The resulting expression, stemming from the simplification of Eq. 2.21, results in an expression of the form

$$\delta \dot{\mathbf{x}} = \frac{\partial \vec{f}(\mathbf{X})}{\partial \mathbf{X}} \delta \mathbf{x} + \mathbf{u} = \mathbf{F}(t) \partial \mathbf{x} + \mathbf{u} \tag{2.25}$$

where $\mathbf{u}$ represents the neglected terms of second order and higher, and $\mathbf{F}(t)$ is the matrix of partial derivatives (also known as the Jacobian matrix) of the state rates. Eq. 2.25 represents the linearized dynamics of the equations of motion and its solution is the time-varying difference between the original trajectory and the nearby trajectory [19].

The more detailed the force model, the more complex $\mathbf{F}$ becomes. Its primary use is to find the error state transition matrix and that can be done using various different techniques like analytical, numerical, or finite difference. The state used for orbit propagation is comprised of position and velocity vectors. The state vectors are taken from an inertial reference frame, and the accelerations are applied in that frame. The states and derivative of the states are

$$\mathbf{X}_{2-body} = \begin{bmatrix} \vec{r} \\ \vec{v} \end{bmatrix} \quad and \quad \dot{\mathbf{X}}_{2-body} = \begin{bmatrix} \vec{v} \\ -\frac{\mu \vec{r}}{r^3} \end{bmatrix} \tag{2.26}$$

The two-body contribution is obtained from the partial derivatives of the two-body accelerations

$$\frac{\partial \dot{\mathbf{X}}_{2-body}}{\partial \mathbf{X}} = \mathbf{F} = \begin{bmatrix} 0 & 0 & 0 & 1 & 0 & 0 \\ 0 & 0 & 0 & 0 & 1 & 0 \\ 0 & 0 & 0 & 0 & 0 & 1 \\ -\frac{\mu}{r^3} + \frac{3\mu r_I^2}{r^5} & \frac{3\mu r_I r_J}{r^5} & \frac{3\mu r_I r_K}{r^5} & 0 & 0 & 0 \\ \frac{3\mu r_I r_J}{r^5} & -\frac{\mu}{r^3} + \frac{3\mu r_J^2}{r^5} & \frac{3\mu r_J r_K}{r^5} & 0 & 0 & 0 \\ \frac{3\mu r_I r_K}{r^5} & \frac{3\mu r_J r_K}{r^5} & -\frac{\mu}{r^3} + \frac{3\mu r_K^2}{r^5} & 0 & 0 & 0 \end{bmatrix} \tag{2.27}$$

The equations for the $\mathbf{F}$ matrix are exact for the given two-body acceleration. Analytic methods for calculating either the error state transition matrix ($\mathbf{\Phi}$) or the state transition matrix ($\mathbf{\Phi}_S$) assume analytic expressions for the state as functions of the time and epoch elements, as shown below for the position and velocity vector states

$$\vec{r}(t) = \vec{r}_0 + \vec{v}_0\Delta t + \frac{1}{2}\frac{d\vec{v}}{dt}|_{t=t_0}\Delta t^2 + ... \tag{2.28}$$

$$\approx \vec{r}_0 + \vec{v}_0\Delta t - \frac{\mu\vec{r}_0}{2r_0^3}\Delta t^2 \tag{2.29}$$

$$\vec{v}(t) = \vec{v}_0 + \frac{d\vec{v}}{dt}|_{t=t_0}\Delta t + ... \tag{2.30}$$

$$\approx \vec{v}_0 - \frac{\mu\vec{r}_0}{r_0^3}\Delta t + \left(\frac{\mu\vec{v}_0}{r_0^3} + \frac{\mu\vec{r}_0 v_0}{r_0^4}\right)\frac{\Delta t^2}{2} \tag{2.31}$$

$$= \vec{v}_0 - \frac{\mu\vec{r}_0}{r_0^3}\Delta t \tag{2.32}$$

$$\tag{2.33}$$

Ignoring the higher-order terms, the error state transition matrix comes to be

$$\left.\begin{array}{c}\frac{\partial \mathbf{X}}{\partial \mathbf{X}_0} \\ \Phi \end{array}\right\}_{2-body} \cong \begin{bmatrix} 1 + \frac{3\mu\Delta t^2 r_I^2}{2r_0^5} - \frac{\mu\Delta t^2}{2r_0^3} & \frac{3\mu\Delta t^2 r_I r_J}{2r_0^5} & \frac{3\mu\Delta t^2 r_I r_K}{2r_0^5} & \Delta t & 0 & 0 \\ \frac{3\mu\Delta t^2 r_I r_J}{2r_0^5} & 1 + \frac{3\mu\Delta t^2 r_J^2}{2r_0^5} - \frac{\mu\Delta t^2}{2r_0^3} & \frac{3\mu\Delta t^2 r_J r_K}{2r_0^5} & 0 & \Delta t & 0 \\ \frac{3\mu\Delta t^2 r_I r_K}{2r_0^5} & \frac{3\mu\Delta t^2 r_J r_K}{2r_0^5} & 1 + \frac{3\mu\Delta t^2 r_K^2}{2r_0^5} - \frac{\mu\Delta t^2}{2r_0^3} & 0 & 0 & \Delta t \\ \frac{3\mu\Delta t r_I^2}{2r_0^5} - \frac{\mu\Delta t}{2r_0^3} & \frac{3\mu\Delta t r_I r_J}{2r_0^5} & \frac{3\mu\Delta t r_I r_K}{2r_0^5} & 1 & 0 & 0 \\ \frac{3\mu\Delta t r_I r_J}{2r_0^5} & \frac{3\mu\Delta t r_J^2}{2r_0^5} - \frac{\mu\Delta t}{2r_0^3} & \frac{3\mu\Delta t r_J r_K}{2r_0^5} & 0 & 1 & 0 \\ \frac{3\mu\Delta t r_I r_K}{2r_0^5} & \frac{3\mu\Delta t r_J r_K}{2r_0^5} & 1 + \frac{3\mu\Delta t r_K^2}{2r_0^5} - \frac{\mu\Delta t}{2r_0^3} & 0 & 0 & 1 \end{bmatrix} \tag{2.34}$$

To find the state transition matrix, it is approached as with the derivation of the error state transition matrix. The position and velocity vector Taylor series expansion are taken and put in matrix form (no partials derivatives need be taken). This finds the state transition matrix for state propagation directly.

$$\mathbf{\Phi}_S \cong \begin{bmatrix} \left[1 - \frac{\mu\Delta t^2}{2r_0^3}\right] & [\Delta t] \\ \left[-\frac{\mu\Delta t}{2r_0^3}\right] & [1] \end{bmatrix} \tag{2.35}$$

In Eq. 2.35, the common diagonal elements of each 3x3 diagonal submatrix are shown [19], and it is expected that the results of the entire matrix can be obtained independently using the outlined information shown.

2.3.2 Numerical Integration

The problem of orbit propagation requires the solution to a system of differential equations that change over time. Specifically, the problem requires the solution to an initial-value problem, and the solution to the differential equations must satisfy a given set of initial conditions. The differential equations that are used within the Standard Dynamical Model are too complicated to solve exactly, so an approach is taken to approximate the solution. Numerical integration is a method for approximating the solution to original differential equations, and these methods give more accurate results and realistic error information [23]. The numerical integration method that is used to find the solution to the SDM equations of motion is the Runge-Kutta-Fehlberg 7(8) (RKF78) scheme.

The RKF78 method is an adaptive variable time-stepping routine that approximates the solution of the differential equation $\dot{y} = f(x, y)$ with the initial condition $y(x_0) = c$. When applied to the equations of motion for the SDM, the differential equations look closer to $\dot{\mathbf{x}} = f(t, \mathbf{x})$ where $\mathbf{x}(t_0) = \mathbf{x}_0$ are the initial conditions to the differential equations. The implementation of this scheme requires the evaluation of $f(t, \mathbf{x})$ thirteen times per time step using an embedded seventh and eighth order Runge-Kutta estimates that not only estimate the solution but also the error at time t. The next step size is calculated using a preassigned tolerance value and error estimate [24].

For the problem of orbit propagation, we let $\mathbf{x} = [x, y, z, \dot{x}, \dot{y}, \dot{z}]^T$, $\mathbf{x}_0 = [x_0, y_0, z_0, \dot{x}_0, \dot{y}_0, \dot{z}_0]^T$, and $h = t_{i+1} - t_i$. At step $i + 1$,

$$\mathbf{x}(t_{i+1}) = \mathbf{x}(t_i) + h \left[\frac{41}{840} k1 + \frac{34}{105} k6 + \frac{9}{35} k7 + \frac{9}{35} k8 + \frac{9}{280} k10 + \frac{41}{840} k11 \right] \tag{2.36}$$

where the equations for the $k(n)$ equations can be found to be in terms of the previous $k(n)$ equations

$$k1 = f(t, \mathbf{x}), \tag{2.37}$$

$$k2 = f(t + \frac{2h}{27}, \mathbf{x} + \frac{2hk1}{27}), \tag{2.38}$$

$$k3 = f(t + \frac{h}{29}, \mathbf{x} + \frac{h}{36}(k1 + 3k2)), \tag{2.39}$$

$$k4 = f(t + \frac{h}{6}, \mathbf{x} + \frac{h}{24}(k1 + 3k3)), \tag{2.40}$$

$$k5 = f(t + \frac{5h}{12}, \mathbf{x} + \frac{h}{48}(20k1 - 75k3 + 75k4)), \tag{2.41}$$

$$k6 = f(t + \frac{h}{2}, \mathbf{x} + \frac{h}{20}(k1 + 5k4 + 4k5)), \tag{2.42}$$

$$k7 = f(t + \frac{5h}{6}, \mathbf{x} + \frac{h}{108}(-25k1 + 125k4 - 260k5 + 250k6)), \tag{2.43}$$

$$k8 = f(t + \frac{h}{6}, \mathbf{x} + h(\frac{31}{100}k1 + \frac{61}{225}k5 - \frac{2}{9}k6 + \frac{13}{900}k7)), \tag{2.44}$$

$$k9 = f(t + \frac{2h}{3}, \mathbf{x} + h(2k1 - \frac{53}{6}k4 + \frac{704}{45}k5 - \frac{107}{9}k6 + \frac{67}{90}k7 + 3k8)), \tag{2.45}$$

$$k10 = f(t + \frac{h}{3}, \mathbf{x} + h(-\frac{91}{108}k1 + \frac{23}{108}k4 - \frac{976}{135}k5 + \frac{311}{54}k6 - \frac{19}{60}k7 + \frac{17}{6}k8 \tag{2.46}$$
$$-\frac{1}{12}k9)),$$

$$k11 = f(t + h, \mathbf{x} + h(\frac{2383}{4100}k1 - \frac{341}{164}k4 + \frac{4496}{1025}k5 - \frac{301}{82}k6 + \frac{2133}{4100}k7 + \frac{45}{82}k8 \tag{2.47}$$
$$+\frac{45}{164}k9 + \frac{18}{41}k10)),$$

$$k12 = f(t + h, \mathbf{x} + h(\frac{3}{205}k1 - \frac{6}{41}k6 - \frac{3}{205}k7 - \frac{3}{41} + \frac{3}{41}k9 + \frac{6}{41}k10 \tag{2.48}$$

$$k13 = f(t + h, \mathbf{x} + h(-\frac{1777}{4100}k1 - \frac{341}{164}k4 + \frac{4496}{1025}k5 - \frac{289}{82}k6 + \frac{2193}{4100}k7 \tag{2.49}$$
$$\frac{51}{82}k8 + \frac{33}{164}k9 + \frac{12}{41}k10 + k12)).$$

The error at every step of the integration process is estimated to be

$$err = -\frac{41}{840}h(k1 + k11 - k12 - k13) \tag{2.50}$$

Within the RKF78 numerical integration scheme, a fixed or variable step size can be used to forward propagate the target body's state. A fixed step size allows for a more standard forward propagation that can be used without the need for checking the local error after every step. If the step size is allowed to vary, in order to reduce the local error at every time step, then a more accurate solution can be obtained. As long as the local error that is estimated for the given, current step size is below a certain threshold, the integration process is allowed to continue

as normal. If the error estimate is larger than the defined threshold value, then a smaller step size has to be calculated such that the error is reduced to an appropriate level. Efficient implementation of such a numerical integration scheme, along with a high-fidelity model, allows for an accurate estimation of a body's state over long time intervals.

2.3.3   Scheme Validation

Establishing a high-fidelity model to describe the motion of a body in space, along with a good numerical integration scheme, is good in principle but has to be validated against an accepted true compilation of body states in order to ensure its accuracy over time. Given that the topic of this dissertation relates to near-Earth asteroids, it fits that the validation of the SDM including the added perturbations of all eight planets, Pluto, Earth's Moon, and the three largest asteroids in the Main Belt (Ceres, Pallas, and Vesta) using the Runge-Kutta-Fehlberg 7(8) numerical integration scheme is done using a well-known near-Earth asteroid such as 99942 Apophis.

Near-Earth objects (NEOs) are asteroids and comets with perihelion distance (q) less than 1.3 astronomical units (AU). The vast majority of NEOs are asteroids, which are referred to as Near-Earth Asteroids (NEAs). NEAs are divided into three groups (Aten, Apollo, Amor) based on their perihelion distance, aphelion distance (Q), and semi-major axes (a). Atens are Earth-crossing NEAs with semi-major axes smaller than Earth's (a < 1.0 AU, Q > 0.983 AU). Apollos are Earth-crossing NEAs with semi-major axes larger than Earth's (a > 1.0 AU, q < 1.017 AU). Amors are Earth-approaching NEAs with orbits exterior to Earth's but interior to Mars' (a > 1.0 AU, 1.017 < q < 1.3 AU) [1].   Figure 2.3 shows representative orbits for the three class of asteroids in reference to Earth's orbit. Apophis is an Aten class asteroid which up until recently posed a real threat to Earth.

Upon discovery in 2004, Apophis was briefly predicted to have a 2.7% impact probability with the Earth in April 2029. With the addition of more observations and measurements, it was determined that the approximately 325 meter diameter object posed no impact risk to Earth at that time, but would have a close encounter with the Earth. At that time, there was an estimated risk of about 4-in-one million chance that after the 2029 close encounter
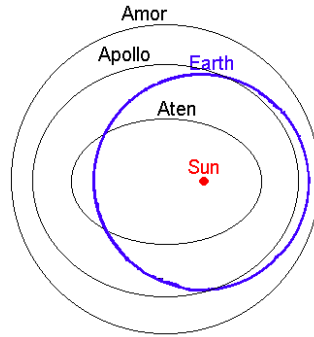
Figure 2.3   Typical Orbits of Apollo, Aten, and Apollo Asteroids.

Apophis would impact Earth in 2036. Taking into account more observations including those as late as 2013, as well as extensions to the Standard Dynamical Model, particularly in the time frame around the April 2029 close encounter, the potential impact in 2036 was also ruled out [1]. Given that the time near planetary flybys are highly dynamical periods for asteroids, where non-conservative effects such as a planet's oblateness and errors in the estimation of the asteroid's spin and surface temperature can cause large deviations in the simulated state of the asteroid body [1], the near 7 year period between May 2029 (a month after the close approach) to March 2036 (a month prior to the non-existent flyby) seems to be a good time period to use for a validation simulation case.

All test cases conducted are compared against the orbital data obtained from NASA JPL's Horizons system. The first test case conducted was to simply look at the radial error between the results obtained between the in-house propagator as compared to Horizons, which can be seen in Figure 2.4. While the numerical integration scheme is a variable step size integrator, there is the ability to control when data is presented back to the user by telling the integrator that every 6 hours, for example, of simulated time report the asteroid state and continue using the reported data as the initial conditions for the next integration step. The more often that data would be reported back, the longer the propagation process would take. However, it is necessary to see if there would need to be a trade-off between the amount of time that it would take to complete the full asteroid propagation versus the accuracy of the solution.

Table 2.1 shows the amount of time required to complete the propagation of the asteroid state as compared to the frequency with which results were asked to be reported. Looking at

Table 2.1   Results of time study comparing the difference in time to complete state propagation of the asteroid compared to the frequency with which the results were to be reported.

Frequency	Time (sec)
1 minute	888.392
5 minutes	173.155
10 minutes	86.605
1 hour	14.775
6 hours	2.771

the results from Table 2.1 and Figure 2.4, it can be seen that while there were differences in the amount of time required to complete the numerical integration of the states from the start date to the end date, there is no significant difference in the radial error between the results and Horizons. This implies that given any reasonable reporting frequency, free-space propagation (propagation of the asteroid body far from the direct influence of any other major body besides the Sun) is independent of the reporting frequency as far as the numerical results are concerned, the only thing to be concerned about is the amount of time required to complete the propagation.

Looking a little closer at the results from Figure 2.4, it can be seen that the error of the estimated states of Apophis between the in-house propagator and Horizons grows as time progresses. At first the error is fairly small, but as time continues to move towards the beginning of 2036, the error has grown to $[-127.63 \quad 102.395]$ km relative to the Horizons estimates. It is important to keep in mind here that the results were obtained using the Standard Dynamical Model with the additional perturbations of the eight planets, Pluto, Earth's Moon, Ceres, Pallas, and Vesta, propagated forward in time using a Kunge-Kutta-Fehlberg 7(8) numerical integrator. As a point of comparison, a study conducted within the ADRC [25] also propagated the state of Apophis over the same time period, using the same exact initial conditions, to find the impact probability between Earth and Apophis in 2036. The two main tools used in the study were AGI's Satellite Toolkit (STK) version 9.2 and NASA General Mission Analysis Tool (GMAT) R2011a. The STK program was run using the same RKF78 numeri-
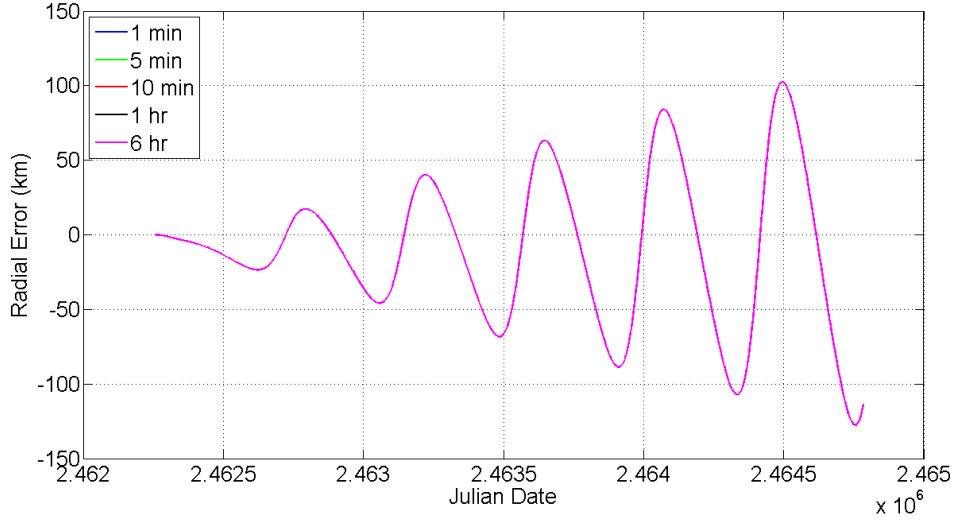
Figure 2.4   Radial error between data from the ADRC's in-house propagator and JPL's Horizons system for asteroid Apophis. All traces indicated in the legend are very close to each other and therefore lie on top of one another, implying that during free-space propagation the solutions to the EOMs are the various timesteps are consistent.

cal integrator incorporating third-body gravitational effects from DE-421 (planetary and lunar ephemeris data), and also included a solar radiation pressure model. The GMAT program was run using a Runge-Kutta 8(9) numerical integrator incorporating third-body gravitational effects from DE-405, and included a solar radiation pressure model. Both commercial programs, while making use of similar order numerical integrators, had higher-fidelity planetary and lunar ephemeris data when dealing with third-body gravitational effects and also took into account the additional perturbation from solar radiation. Even with these similarities and advantages however, they did not out-perform the in-house propagator. The error towards the beginning of 2036 had become $[-538.15 \quad 611.004]$ km for GMAT and over $[-4000 \quad 5000]$ km for STK, far exceeding the numbers given by the in-house propagator. The results of the study had shown that GMAT was able to be used to find a good estimate for the impact probability of Apophis with the Earth in 2036 of 4.2E-06, and STK was not able to obtain an impact probability given the large radial error in the results. After a later discussion with other experts who have done similar studies in the past, it was concluded that there must have been an error on the part of the team from the ADRC in terms of what was being done with STK because those kinds of

erroneous results are not common for the commercial program, even though no evidence of an error could be found. Regardless, the results from the in-house propagator in comparison to Horizons were very encouraging and when compared to the commercial programs of STK and GMAT only more confidence could be placed in the capabilities of the in-house propagator to be able to accurately estimate the state of a body over a given time interval.

Simply looking at the radial error does not give enough information about where the radial error is actually coming from. Figure 2.5 shows the positional error (in all three coordinate directions) for the in-house propagator. For comparison, the radial position error is shown on the plot, as well as the position magnitude error. It can be seen that the propagator remained
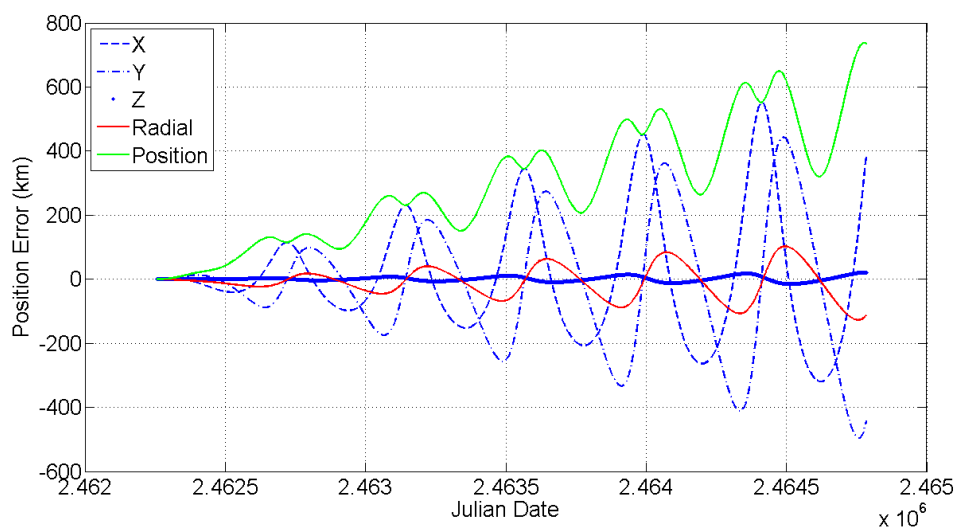
Figure 2.5   Comparison of positional error, in all three directions, between in-house propagator and JPL's Horizons data for asteroid Apophis.

pretty accurate when it came to the out-of-plane position of the asteroid, while the in-plane components error grew at a faster rate, implying that the position magnitude error can be mostly attributed to the error in the in-plane components of Apophis' trajectory. The reasons for difference between the estimated trajectory obtained from the in-house propagator and the Horizons trajectory could be due to a difference in model or the effects of additional perturbations that are not present in the in-house propagator. Nevertheless, the results of the validation study have shown that the in-house propagator can provide a relatively accurate solution, in a fair small amount of time, thus allowing for its use in more complicated simulations.

CHAPTER 3.   ASTEROID MISSION DESIGN SOFTWARE TOOL

3.1   Introduction

As the number of identified potentially hazardous near-Earth asteroids increases, the ability to design and plan for deflection/disruption missions to these target bodies ceases to be a simple exercise but a necessity. Previous research activities at the ADRC have included target selection and spacecraft system design, as well as preliminary mission designs that have looked at launch vehicle selection and initial mission orbit determination. Asteroid target selection and mission designs, along with general mission analysis, are components of an overall, complete mission design concept, previously let separate to focus on the individual components themselves. In this chapter, they are shown to be components of an overall NEO mission design tool developed at the ADRC, known as the Asteroid Mission Design Software Tool (AMiDST).

3.2   Overview of Existing Mission Design Tools

This section contains a brief discussion of the existing mission design tools used by NASA, developed by The Aerospace Corporation, and the AMiDST program developed at the ADRC, as well as a comparison of the capabilities of these tools.

3.2.1   An On-line Tool by The Aerospace Corporation

The Aerospace Corporation has been developing an on-line tool to aid in the design and understanding of deflection impulses necessary for guarding against objects that are on an Earth-impacting trajectory. Using several variables to characterize the target NEO (warning time, size/density, orbit parameters, etc.) and mitigation mission design parameters (ΔV impulse vector, number of days before impact to launch, number of days before impact to

deflect, etc.), users can simulate the designed mission transfer from Earth to the target NEO and deflected NEO orbit. After the applied deflection and propagation time, the Earth miss distance would be determined on the Earth B-plane in Earth radii. As of 2012, this on-line tool was still under development, with the hopes of incorporating several more design variables and limitations to only allow feasible mission designs based on current launch and mission capabilities [26].

3.2.2 NASA's Mission Design Software Tools

Through the In-Space Propulsion Technologies Program, in the Space Science Projects Office at NASA Glenn Research Center, several optimization tools have been developed for trajectory and mission optimization, such as MALTO, COPERNICUS, OTIS, Mystic, and SNAP. [27]

3.2.2.1 COPERNICUS

Originally developed by the University of Texas at Austin, under the technical direction of Johnson Space Center, Copernicus is a generalized trajectory design and optimization program that allows the user to model simple to complex missions using constraints, optimization variables, and cost functions. Copernicus can be used to model simple impulsive maneuvers about a point mass to multiple spacecraft with multiple finite and impulse maneuvers in complex gravity fields. The models of Copernicus contain an n-body tool and as a whole is considered high fidelity.

3.2.2.2 OTIS

The Optimal Trajectories by Implicit Simulation (OTIS) program was developed by the NASA Glenn Research Center and Boeing. OTIS is named for its original implicit integration method, but includes capabilities for explicit integration and analytic propagation. Earlier versions of OTIS have been primarily been launch vehicle trajectory and analysis programs. Since then, the program has been updated for robust and accurate interplanetary mission analyses, including low-thrust trajectories. OTIS is a high fidelity optimization and simulation

program that uses SLSQP and SNOPT to solve the nonlinear programming problem associated with the solution of the implicit integration method.

3.2.2.3 Mystic

Mystic, developed at the Jet Propulsion Laboratory (JPL), uses a Static/Dynamic optimal control (SDC) method to perform nonlinear optimization. The tool is an n-body tool and can analyze interplanetary missions as well as planet-centered missions in complex gravity fields. One of the strengths of Mystic is its ability to automatically find and use gravity assists, and also allows the user to plan for spacecraft operation and navigation activities. The mission input and post processing can be performed using a MATLAB based GUI.

3.2.3 NASA's General Mission Analysis Tool

Developed by NASA Goddard Space Flight Center, the General Mission Analysis Tool (GMAT) is a space trajectory optimization and mission analysis system. Analysts use GMAT to design spacecraft trajectories, optimize maneuvers, visualize and communicate mission parameters, and understand mission trade space. GMAT has several features beyond those that are common to many mission analysis systems, features that are less common or unique to GMAT. Its main strength over other software choices is GMAT's versatility. Its scripting ability is easy to use and edit without knowledge of computer languages. And, the MATLAB plug-in allows an expansion of the user's ability to personalize each mission. [28]

3.2.4 AMiDST Overview

An in-house design tool name The Asteroid Mission Design Software Tool (AMiDST) is used to conduct the mission and trajectory design for near-Earth asteroid missions. While it does not have the high-fidelity as some of the existing trajectory and mission optimization tools (such as Mystic, MALTO, Copernicus, SNAP, OTIS, and GMAT), it focuses instead on the launch and terminal phases of a NEO mission. AMiDST looks into several launch vehicle and spacecraft configurations based upon several evaluation criteria such as launch vehicle mass capacity and mission ΔV requirements, as well as relative approach velocity and approach

angle. In addition to these features, it also provides an estimated total mission cost, used as a final determination factor between mission configurations.
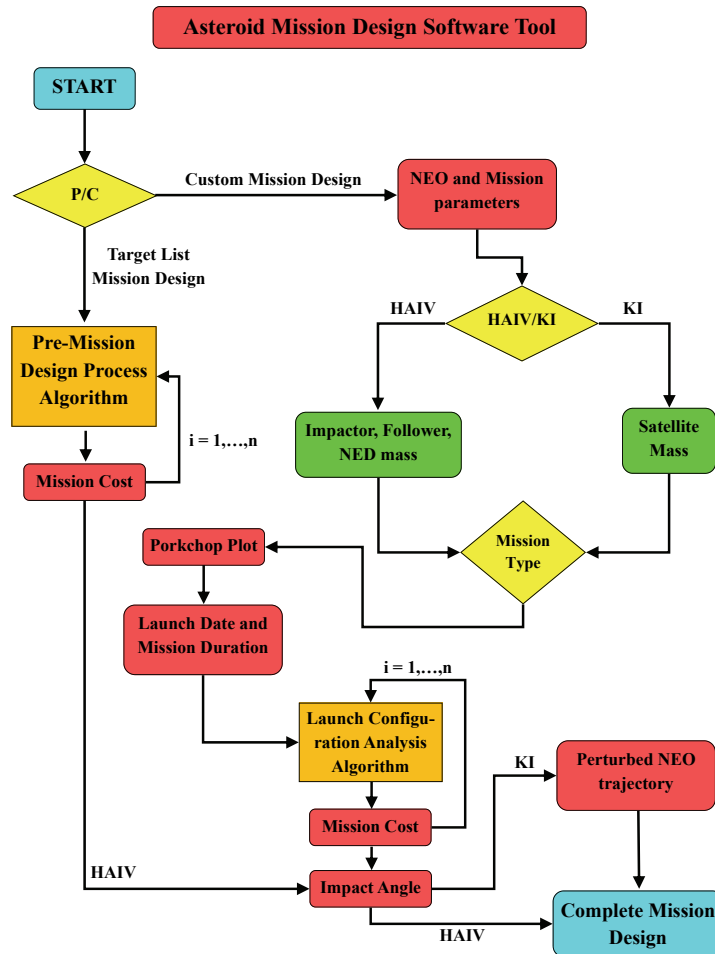
Figure 3.1   Flowchart Illustration of the AMiDST.

Figure 3.1 shows a flow-chart illustration of the AMiDST. The design tool begins with a choice between analyzing a pre-determined list of target NEOs to design a mission for or build a custom mission design for a personally selected target NEO. With the pre-determined NEO target list, the software follows the Pre-Mission Design Algorithm to analyze all launch configurations for a pre-determined target list, shown in Table 3.1 [29].   These asteroids are Amor class asteroids, their orbits do not cross the Earth's path, and therefore pose no threat to the planet. Due to the non-existant threat that these asteroids possess towards Earth, the pre-determined target list option is meant more as an introduction to some of AMiDST's

Table 3.1   A list of target NEOs selected for planetary defense technology demonstration missions. [1]

Target NEO	Estimated Diameter (m)	a (AU)	e	i (deg)	ω (deg)	Ω (deg)
2003 GA	300	1.28153	0.19124	3.84189	66.76837	192.93186
2006 SJ198	1200	2.08969	0.45631	2.43325	212.25852	266.89138
2009 TB3	300	1.31863	0.21926	12.22404	249.57728	22.17938
2007 FS35	620	1.92244	0.38986	0.31887	107.40624	183.00756
2003 QC	400	2.57094	0.53140	7.85444	37.43616	321.68183
2004 GY	480	1.44817	0.21804	23.43610	182.87114	50.88706
2001 SX269	280	1.88042	0.34613	4.02404	29.53738	320.17092
1998 SB15	330	1.22609	0.16126	15.62791	67.63148	67.93695
2004 KE1	240	1.29867	0.18079	2.88387	283.67731	42.77468
2011 BX10	1000	2.82541	0.64134	9.73567	348.36692	79.118387

capabilities. A launch date is given for each individual asteroid, leaving no need for too much user input. With the launch date determined and the target defined then the spacecraft's orbital trajectory is well-defined and no longer a concern. The AMiDST analyzes all the possible launch configurations available to complete the mission, the arrival at the target NEO, and the estimated mission costs. The outputs are then made available for the user to examine and understand the results of the NEO mission design analyses [30].

For custom mission designs, the user begins by entering information about the target NEO of interest and various mission criteria, including launch date, mission duration, spacecraft mass, and desired arrival speed and angle range. For further design customization, the user is able to select the important mission variables to judge the potential mission design options against through an intrinsically defined cost function. More detailed information regarding the trajectory and mission design optimization will be provided later in this chapter. After all the potential mission design options are evaluated, the top 10 missions are presented to the user in full detail for final selection of the desired mission.

3.2.5   Mission Design Program Comparisons

The trajectory and mission optimization tools developed through the In-Space Propulsion Technologies Program are all rather high fidelity programs. One of the common denominators of all these tools is that they primarily look at the intermediate stage of a mission, the spacecraft trajectory from one target to another. The other two mission stages are more or less overlooked in comparison to the spacecraft's mission trajectory. The AMiDST does not possess the high-fidelity trajectory optimization of Copernicus, Otis, or Mystic, but instead focuses on the launch

and terminal phase of an NEO mission. Looking into several launch vehicle and spacecraft configurations to complete a given mission design to a designated target NEO, the mission design software evaluates the possible combinations based upon several evaluation criteria such as space in the launch vehicle fairing, mission ΔV requirements, and excess launch vehicle ΔV. A staple of this mission design tool is the evaluation of estimated total mission cost, the determining factor between mission configurations in the cases where more than one launch configuration can result in a successful mission. Using the impact angle and arrival velocities of both the spacecraft and target NEO, along with both masses, the trajectory of the perturbed asteroid can be tracked in order to find how much the trajectory is altered from the previous unperturbed orbit [30, 31].

3.3 AMiDST Components

In this section a discussion will be provided regarding the major portions of the AMiDST program: launch vehicle selection, mission cost estimation, and trajectory optimization.

3.3.1 Launch Vehicles

The mission design studies conducted using this tool considered three classes of launch vehicle: i) Delta II, ii) Delta IV, and iii) Atlas V. Originally, the payload capacity of the individual launch vehicles and the cost associated with launching a given rocket only certain launch vehicle classes where considered for different size NEDs and target asteroids - Delta II class launch vehicles for 300-kg NED missions, Delta IV and Atlas V class launch vehicles for 1000-kg NED missions, and the Delta IV Heavy launch vehicle for 1500-kg NED missions. The launch vehicles would be carrying specially designed HAIV spacecrafts, comprised of an impactor and follower spacecraft, with the NED payload contained within the follower spacecraft.

3.3.1.1 Delta II Launch Vehicles

The Delta II launch vehicles have a 98% reliability record, with capabilities to launch from either the East or West coast. The vehicles can be configured with two or three stages with up to nine strap-on graphite-epoxy motors, and two sizes of payload fairings [2]. The versatility
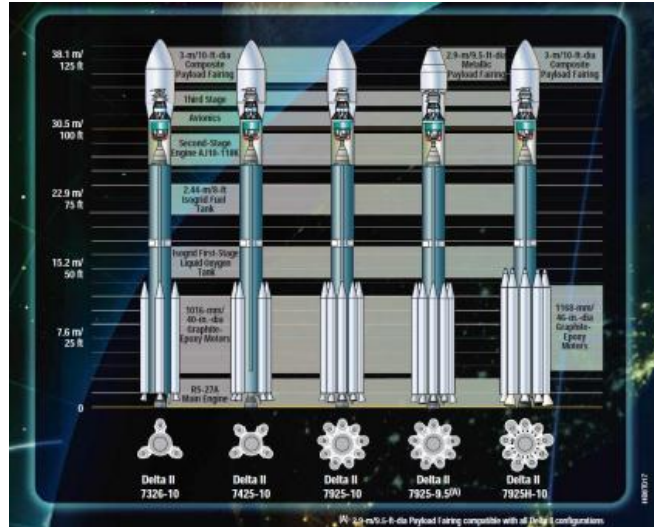
Figure 3.2   Delta II launch vehicle configurations [2].

and the low cost of the Delta II launch vehicles makes it ideal for target bodies that are easer to reach.   The types of Delta II launch vehicles considered are the Delta II 732X, Delta II 742X, Delta II 792X, and Delta II 792XH, where X can be 0 (no third stage), 5 (STAR-48B third stage), or 6 (STAR-37FM third stage). The major differences between the two and three stage configurations of the Delta II are the payload and orbit injection capabilities. Two-stage Delta II rockets can really only take payloads into low Earth orbits (LEOs), while the three-stage configurations have the ability to inject payloads into hyperbolic C3 orbits.

As mentioned, the three-stage configuration of the Delta II launch vehicle is capable of placing its payload into a C3 orbit - an Earth escape trajectory. The C3 value is defined by the energy of the orbit that the payload is placed in, expressed as

$$\text{C3} = v_\infty^2 \tag{3.1}$$

where v_∞ is the hyperbolic excess speed of the spacecraft.

3.3.1.2   Delta IV and Atlas V Launch Vehicles

The Delta IV class of launch vehicles are much larger launch vehicles, capable of not only taking large payloads to LEO but directly injecting them into higher C3 orbits.   The Atlas V launch vehicles are also rather powerful rockets, with comparable if not better payload
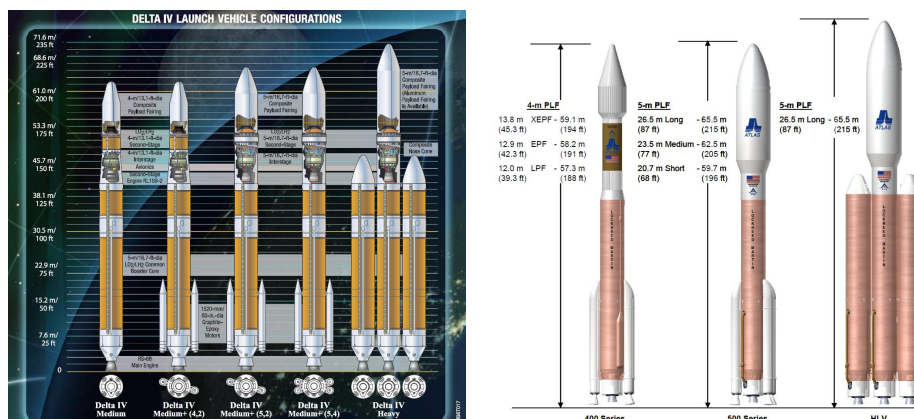
Figure 3.3   Delta IV (left) and Atlas V (right) launch vehicles [3, 4].

capabilities to that of their equivalent Delta IV rocket counterparts, with the exception of the Delta IV Heavy launch vehicle. The currently available rockets for use from either of these two launch vehicle classes are: Delta IV Medium, Delta IV M+(4,2), Delta IV M+(5,4), Delta IV Heavy, Atlas V 401, Atlas V 431, and Atlas V 551.

3.3.2   Spacecraft Selection

In order to run the AMiDST program, the user must input the type of spacecraft that will be used to conduct the mission. While technically the spacecraft type does not really have much bearing on the way the program runs, the only difference to the program is the type of information that is expected to be entered. The user has two possible spacecraft configurations, a single-body kinetic impactor and a two-body Hypervelocity Asteroid Intercept Vehicle (HAIV) spacecraft. The kinetic impactor option, which is designed simply as another spacecraft with the full-suite of instruments, requires only the total mass of the spacecraft that will be impacting the asteroid body. The HAIV option requires a couple additional inputs. Since the spacecraft is broken down into two separable portions, the program asks for the mass of the fore and aft body, as well as the mass of the nuclear explosive device (NED) housed in the aft-body.

The desire to use a spacecraft concept like the HAIV comes from the fact that most direct intercept mission with a short warning time (7-10 years) will result in relative arrival velocities

of 10 to 30 km/s. If there is a desire to conduct a rendezvous mission to the target asteroid, at any time during that timespan, is not practically feasible because of those relative arrival speeds. However, a nuclear subsurface explosion can deliver enough energy into the target body so that there is a likelihood of totally disrupting the asteroid. However, the current nuclear subsurface penetrator technology limits the impact velocity to less than about 300 m/s, due to the fact that higher impact speeds prematurely destroy the fusing mechanisms of the NEDs [17, 6]. The HAIV concept was developed in order to overcome these technological limitations. As previously mentioned, the HAIV is a two-body spacecraft that consists of a fore-body (leader) and an aft-body (follower), as illustrated in Figures 3.4 and 3.5.
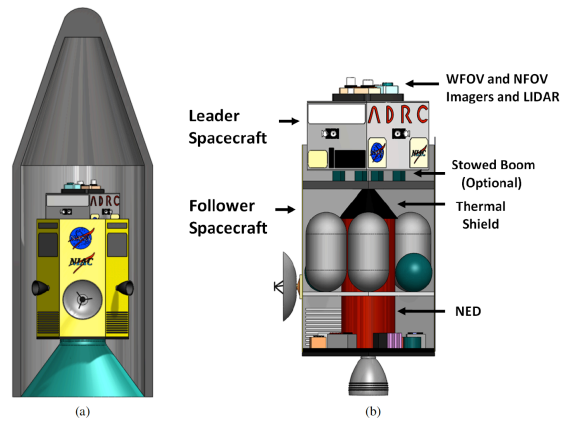
Figure 3.4   (a) View of the HAIV spacecraft in the payload fairing of a launch vehicle. (b) View of the interior of the HAIV, showing the location of the NED as well as the various spacecraft instruments [5].

After detachment, or separation, of the leader and follower spacecrafts, the leader spacecraft creates a kinetic-impact crater that the follower spacecraft carries the NED into and makes a robust and effective subsurface explosion of the target asteroid body [6], as seen in Figure 3.6. The HAIV configuration depicted in Figure 3.5 utilizes a deployable Astro-Mast boom that will provide the necessary separation between the impactor and follower during the terminal arrival phase. This optional configuration ensures that the two parts of the spacecraft remain collinear prior to impact, customized to the desired length for the particular mission scenario such that there is an appropriate delay between when the leader creates a crater on the NEO and when the follower arrives in the crater and detonates. More details regarding the trade-off
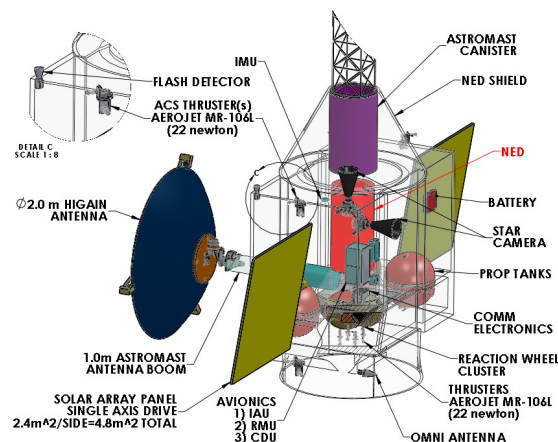
Figure 3.5   Potential configuration of the HAIV developed by the Mission Design Lab at NASA Goddard Space Flight Center [6].

studies that went into the design of the HAIV spacecraft and the terminal phase approach of the mission can be found in the ADRC's NASA NAIC Phase II Report [6].

3.3.3   Mission Cost Estimation

Mission cost estimation to design and fabricate the missions is an important task necessary for an early assessment of the mission viability and feasibility. The final total cost of each mission is given as a combination of the cost for the launch vehicle, the HAIV spacecraft, and mission operations. A cost estimation algorithm was developed to determine the costs associated with constructing the HAIV, based on a number of previous spacecraft missions with similar goals and parameters. Spacecraft such as Deep Impact, Stardust, and Dawn were researched to find the cost of developing their spacecraft and a linear polynomial fit was applied to the data to come up with an analytic formula relating spacecraft mass and cost. Before the results of the cost estimation algorithm are discussed, it is important to note that the mass/cost of the NED was not included when the estimations were made. In addition, the total mass margin of the spacecraft was left intact when estimating the cost of the HAIV development, in order for the estimate to be thought of as a relative maximum. As a comparison, the initial mission cost estimates were run through NASA's Advanced Mission Cost Model (AMCM) [32], to get a rough order of magnitude approximation. The estimates form the AMCM came out to
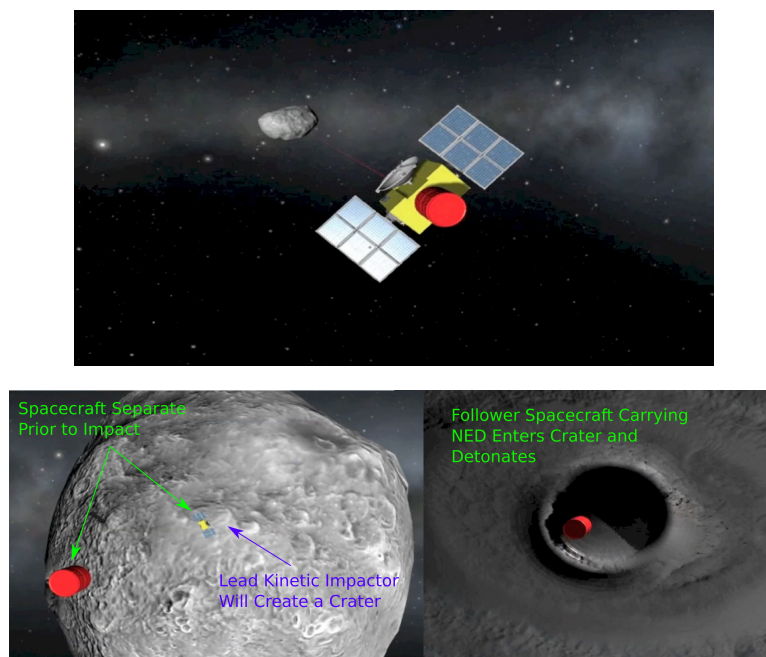
Figure 3.6   Depiction of HAIV on final approach to target asteroid, shown in the detached
configuration.

be rather rough, mostly due to the fact that the HAIV spacecraft designs don't exactly fit into
a single mission category from the available choices. However, the spacecraft cost estimates
from the NASA AMCM did verify that the spacecraft cost estimates from AMiDST are in the
appropriate cost range. And finally, AMiDST incorporates the mission operations costs by
adding 30% of the estimated total cost of the launch vehicle and spacecraft design.

3.3.4   Trajectory Optimization

For custom mission designs, the user begins by entering information about the target NEO of
interest and the low-Earth orbit (LEO) departure radius. Then the choice is given between two
types of spacecraft to be used for the mission, the ADRC's Hypervelocity Asteroid Intercept
Vehicle (HAIV) concept or a Kinetic Impactor (KI). For the HAIV spacecraft, information
about the mass of the impactor, follower, and NED are obtained from the user, while in the KI
spacecraft case the total mass of the satellite is needed. In either case, the user is prompted
with a decision between three mission types: a direct intercept, a direct intercept at a relative
speed of 10 km/s, or rendezvous. For direct intercept missions, the arrival speed is taken as

the relative speed difference between the asteroid body and the spacecraft when the two are considered to be at the same location. For direct intercept missions at a relative speed of 10 km/s the program is instructed to add an impulsive arrival burn to the mission requirements such that the relative speed between the asteroid body and the spacecraft at arrival is equal to 10 km/s. And for rendezvous missions, the impulsive arrival burn being added to the mission requirements is such that at arrival the spacecraft has the same velocity magnitude and direction as the asteroid. Regardless of the decision, the user then enters mission parameter data related to the dates in which they would like the mission to be conducted between, as well as the upper and lower bound mission duration - being the amount of time the spacecraft can take traveling from Earth to the target. Given only this information, the AMiDST constructs a porkchop plot (graph of launch date and mission duration evaluated in terms of total mission ΔV) over the defined time period. The porkchop plot is filled by taking every possible pair of mission duration and launch duration and finding the corresponding mission ΔV by solving Lambert's Problem. After all solutions have been found and the porkchop plot is constructed the entire grid space is analyzed using a customizable cost function, to find the optimal mission trajectory defined by the appropriate state variables which encompass parameters at the beginning and end of the mission trajectory. With all missions evaluated, the mission design options are sorted based on the cost function scores, where the best missions have the lowest cost function values due to the lack of penalty accumulation because they are closer to the desired mission parameter values set by the user. Finally, the top 10 missions are presented to the user for the final decision of the desired mission design, where the AMiDST will accept the selection and create an executable m-file for the user to run and be given all the desired data for the chosen mission design.

3.3.5 Lambert's Problem

Lambert's Problem is characterized by two position vectors and a time of flight between them, so in this context is an initial orbit-determination technique. While the two position vectors and the time of flight between them is known, the orbit between the two endpoint vectors is not yet fully known. There exist several formulations of this problem such as the minimum

energy method, Gauss's solution, the universal variable approach, and Battin's method. The technique used to obtain the results shown throughout this work is the Lambert-Battin method which uses continued fractions to guarantee convergence and does not suffer from the 180deg-transfer difficulty of most Lambert routines [19, 31]. The solution to Lambert's Problem allows for the examination of several useful situations. For initial orbit determination, the Lambert techniques result in velocity vectors from sets of observed position vectors. The problem could also be two positions in one orbit, known as a transfer orbit, used to plan maneuvers of a body between two separate positions. Another application of Lambert's Problem is the case where the two position vectors lie in two separate orbits [19]. The latter case is the application to which Lambert's Problem is being used to solve, where the spacecraft begins in an orbit about the Earth (more generally, in Earth's solar orbit) and ends in the target asteroid's orbit. The solutions from Lambert's Problem, in the case of finding a transfer orbit between two different orbits given the starting and ending position vectors and the transfer time, are the two velocity vectors within the transfer orbit. Removing the speed that the spacecraft would be traveling at insertion into the transfer orbit and only taking into account the speed change necessary for arrival at the asteroid's orbit, the total change in velocity (ΔV) to connect the two orbits is left. Mapping a set of those ΔVs against the corresponding spacecraft departure dates and mission durations creates a porkchop plot [31].

3.3.5.1   Initial Problem Formulation

The solution to Lambert's Problem is based on the given information of an initial and final radius vector and the time-of-flight given as $\vec{r}_1, \vec{r}_2, \Delta t$, respectively. Two additional values are needed for the solution to be found, the chord (c) and the semiperimeter (s). The chord is simply defined as the distance between the initial and final radius vectors and the semiperimeter is half the sum of the sides of the triangle that is formed from the radius vectors and the chord, represented as

$$c = \sqrt{r_1^2 + r_2^2 - 2r_1 r_2 \cos \Delta \nu} \tag{3.2}$$

$$s = \frac{r_1 + r_2 + c}{2} \tag{3.3}$$

The transfer angle within the orbit connecting the initial and final radius vectors ($\Delta\nu$) can be determined fairly simply

$$\cos\Delta\nu = \frac{\vec{r}_1 \cdot \vec{r}_2}{r_1 r_2} \tag{3.4}$$

However, taking the inverse cosine of the resulting value from the right-hand side of the equation can result in a quadrant ambiguity that can lead to incorrect solutions. A solution to the quadrant ambiguity issue when solving for $\Delta\nu$ is presented below [33]. Normally, the solution to Lambert's Problem requires the indication of the direction that the solution to take, being either a short-way or long-way trajectory, instead the decision to be made is between a prograde or retrograde orbit. For a prograde orbit, the transfer angle $\Delta\nu$ is determined as follows

$$\Delta\nu = \begin{cases} \cos^{-1}\left(\frac{\vec{r}_1 \cdot \vec{r}_2}{r_1 r_2}\right) & : \ (\vec{r}_1 \times \vec{r}_2)_k \geq 0 \\ 2\pi - \cos^{-1}\left(\frac{\vec{r}_1 \cdot \vec{r}_2}{r_1 r_2}\right) & : \ (\vec{r}_1 \times \vec{r}_2)_k < 0 \end{cases} \tag{3.5}$$

where the subscript k indicates the out-of-plane component of the vector cross product. In the case of a retrograde orbit, the transfer angle can similarly be determined as follows

$$\Delta\nu = \begin{cases} \cos^{-1}\left(\frac{\vec{r}_1 \cdot \vec{r}_2}{r_1 r_2}\right) & : \ (\vec{r}_1 \times \vec{r}_2)_k < 0 \\ 2\pi - \cos^{-1}\left(\frac{\vec{r}_1 \cdot \vec{r}_2}{r_1 r_2}\right) & : \ (\vec{r}_1 \times \vec{r}_2)_k \geq 0 \end{cases} \tag{3.6}$$

The time to traverse the arc between the two vectors is related to the transfer orbit by Kepler's time-of-flight equation. From Kepler's equation, Lagrange developed a proof of Lambert' theorem. Lagrange's equation removes the orbit eccentricity from Kepler's time-of-flight equation and is only a function of $r_1 + r_2$, c, and the semi-major axis (a)

$$\sqrt{\frac{\mu}{a^3}}\Delta t = (\alpha - \beta) - (\sin\alpha - \sin\beta) \tag{3.7}$$

The two angular parameters (α and β), are defined in terms of the physical parameters c, s, and a, as follows:

$$\sin\frac{\alpha}{2} = \pm\sqrt{\frac{s}{2a}} \tag{3.8}$$

$$\sin\frac{\beta}{2} = \pm\sqrt{\frac{s-c}{2a}} \tag{3.9}$$

The quadrant abiguities for the α and β parameters can be resolved by making the following restrictions

$$0 \leq \alpha \leq 2\pi, \ \ 0 \leq \beta \leq \pi \ \ : \ \ \Delta\nu \leq \pi$$

$$0 \leq \alpha \leq 2\pi, \ \ -\pi \leq \beta \leq 0 \ \ : \ \ \Delta\nu \geq \pi$$

3.3.5.2   Battin's Method

Lambert's Problem is described as two-point boundary value problem that states that the time-of-flight is a function of a, $r_1 + r_2$, and c. Therefore, if these three physical parameters are held constant, the resulting orbit can be transformed into any conic section (circle, ellipse, parabola, or hyperbola). The solution can be transformed such that the semi-major axis of the resulting orbit is perpendicular to the chord (c), which by definition connects the initial and final radius vectors [34]. The transformed ellipse is shown in Figure 3.7,   and further
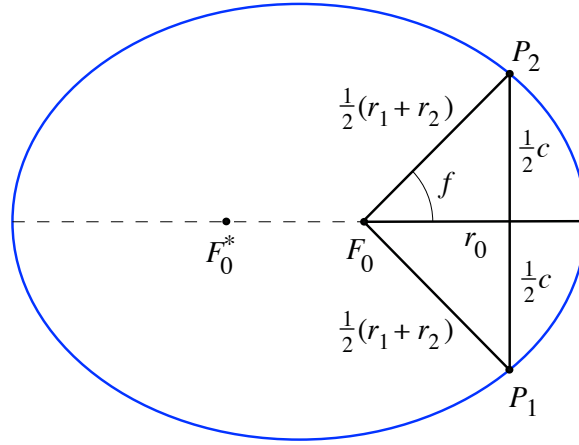
Figure 3.7   Transformed ellipse used in Lambert-Battin solution of Lambert's Problem [7].

explanation of the transformed orbit can be found in [34]. What follows is a discussion of the Lambert-Battin method of solving Lambert's Problem, more detail regarding other methods of solving Lambert's Problem (including Battin's method) can be found in [7], and for full details of the Battin solution methodology can be seen in [19, 34].

Battin formulates the problem in such a way by defining two non-dimensional parameters (l and m), which are functions only of the problem geometry. First, a non-dimensional Lambert parameter (λ)

$$\lambda = \frac{\sqrt{r_1 r_2}}{s} \cos \frac{\Delta \nu}{2} = \pm \sqrt{\frac{s - c}{s}} \tag{3.10}$$

is introduced in order to describe the geometry of the problem, where $\lambda \in (-1, 1)$. The potential sign ambiguity in the square root can be resolved as follows: $\lambda > 0$ for $0 < \Delta \nu < \pi$ and $\lambda < 0$ for $\pi < \Delta \nu < 2\pi$. The dimensionless time-of-flight parameter used in the algorithm is

$$T = \sqrt{\frac{8\mu}{s^3}} \Delta t \tag{3.11}$$

Using this transformation, the equation for the pericenter radius (r_0) is described as

$$r_0 = a\left(1 - e_0\right) = r_{0p} \sec^2 \frac{1}{4}\left(E_2 - E_1\right) \tag{3.12}$$

where e_0 is the eccentricity of the transformed orbit and r_{0p} is the mean point of the parabolic orbit from P_1 to P_2. The mean point of the parabolic radius (r_{0p}) is expressed as

$$r_{0p} = \frac{1}{4}\left(r_1 + r_2 + 2\sqrt{r_1 r_2}\cos\frac{\theta}{2}\right) = \frac{1}{4}s\left(1 + \lambda\right)^2 \tag{3.13}$$

Battin then defines the dimensionless parameters l and m, which are always positive and solely dependent on the problem geometry

$$l = \left(\frac{1 - \lambda}{1 + \lambda}\right)^2 \tag{3.14}$$

$$m \equiv \frac{\mu \Delta t^2}{8 r_{0p}^3} = \frac{T^2}{(1 + \lambda)^6} \tag{3.15}$$

Utilizing the dimensionless parameters to transform Kepler's time-of-flight equation, the final result takes the following form

$$y^3 - \left(1 + h_1\right)y^2 - h_2 = 0 \tag{3.16}$$

where y is a function of the problem parameters l, x, and m, defined as

$$y^2 \equiv \frac{m}{(l + x)(1 + x)} \tag{3.17}$$

The independent variable (x) is then determined from y for all orbit types

$$x = \sqrt{\left(\frac{1 - l}{2}\right)^2 + \frac{m}{y^2}} - \frac{1 + l}{2} \tag{3.18}$$

The flattening parameters $(h_1$ and $h_2)$ are functions of l, m, x, and the continued fraction $\xi(x)$, defined as

$$h_1 = \frac{(l + x)^2 (1 + 3x + \xi(x))}{(1 + 2x + l)\left[4x + \xi(x)(3 + x)\right]} \tag{3.19}$$

$$h_2 = \frac{m(x - l + \xi(x))}{(1 + 2x + l)\left[4x + \xi(x)(3 + x)\right]} \tag{3.20}$$

The function $\xi(x)$, which is needed for the computation of the flattening parameters, is defined by a continuous fraction

$$\xi(x) = \cfrac{8\left(\sqrt{1+x}+1\right)}{3+\cfrac{1}{5+\eta+\cfrac{\frac{9}{7}\eta}{1+\cfrac{c_\eta\eta}{1+\cfrac{c_\eta\eta}{1+...}}}}} \tag{3.21}$$

where η and c_η are represented by the following expressions

$$\eta = \frac{x}{\left(\sqrt{1+x}+1\right)^2}, \quad \eta \in (-1,1) \tag{3.22}$$

$$c_\eta = \frac{\eta^2}{(2n)^2-1}, \quad \eta = 4,5,... \tag{3.23}$$

respectively.

The non-dimensional Kepler time-of-flight equation shown in Eq. 3.16 is a third order polynomial in y, and its largest root must be found in order to proceed. Several methods exist to solve a third order polynomial, including analytic and numerical approaches, the method suggested by Battin utilizes a successive substitution algorithm that solves for the largest root of y and determines the new value of x through its definition in Eq. 3.18. The first step in the successive substitution algorithm is to calculate B and u using the following equations

$$B = \frac{27h_2}{4\left(1+h_1\right)^3} \tag{3.24}$$

$$u = \frac{B}{2\left(\sqrt{1+B}+1\right)} \tag{3.25}$$

To determine the final solution of y, Battin defines a second continued fraction expansion $K(u)$

$$K(u) = \cfrac{\frac{1}{3}}{1+\cfrac{\frac{4}{27}u}{1+\cfrac{\frac{8}{27}u}{1+\cfrac{\frac{2}{9}u}{1+\cfrac{\frac{22}{81}u}{1+\ddots}}}}} \tag{3.26}$$

The odd and even coefficients of the $K(u)$ continued fraction expansion are determined according to the following two respective expressions

$$\gamma_{2n+1} = \frac{2\,(3n+2)\,(6n+1)}{9\,(4n+1)\,(4n+3)} \tag{3.27}$$

$$\gamma_{2n} = \frac{2\,(3n+1)\,(6n-1)}{9\,(4n-1)\,(4n+1)} \tag{3.28}$$

Then, the largest positive real root of the cubic equation is found using

$$y = \frac{1+h_1}{3}\left(2 + \frac{\sqrt{1+B}}{1+2u\,(K(u))^2}\right) \tag{3.29}$$

Once the solution to Eq. 3.16 is found and the value of x has converged, the semi-major axis of the transfer orbit can be found. With a value for the semi-major axis of the transfer orbit calculated

$$a = \frac{\mu\,(\Delta t)^2}{16 r_{0p}^2 x y^2} \tag{3.30}$$

the initial and final velocities can be easily calculated using the standard Lagrange coefficients f, g, $\dot{f}$, and $\dot{g}$ using the following equations

$$\vec{v}_1 = \frac{1}{g}\left(\vec{r}_2 - f\vec{r}_1\right) \tag{3.31}$$

$$\vec{v}_2 = \frac{1}{g}\left(\dot{g}\vec{r}_2 - \vec{r}_1\right) \tag{3.32}$$

The initial conditions for x that guarantee convergence are

$$x_0 = \begin{cases} 0, & parabola, hyperbola \\ l, & ellipse \end{cases} \tag{3.33}$$

The dimensionless parabolic time-of-flight, which is a function of the Lambert parameter, needed to assign the initial condition x_0 is defined as

$$T_p = \frac{4}{3}\left(1 - \lambda^3\right) \tag{3.34}$$

Basically, Battin's method to determine the transfer orbit that fits two given radius vectors and a time-of-flight is outlined simply below. All continued fractions are always calculated to at least 20 total fraction levels, because this provides sufficient numerical accuracy, typically

within a small margin of error (less than 10^{-8}) when compared to their Lambert solution algorithms.

Using the solution formulation of Lambert's Problem described above, the steps to find the initial and final velocity vectors for the transfer orbit are as follows:

1. Compute the dimensionless parameters l, m, and r_{0p}.

2. From the parabolic time-of-flight, T_p, determine x_0.

3. Calculate: η, ξ, h_1, h_2, B, u, $K(u)$, in that order.

4. Compute the solution for y from Eq. 3.29 and the updated value of x from Eq. 3.18.

5. Go to step 3 and repeat the calculations until the value of x converges to the desired tolerance, or the maximum number of iterations is exceeded.

6. Output the converged semi-major axis (a), the Lagrange coefficients, and the initial and final velocity vectors.

3.3.6   Cost Function Formulation

As previously mentioned, the entire design space of mission durations and launch dates is analyzed using a customizable cost function according to user defined mission parameters. The potential design variables are

$$\mathbf{X} = [JD, \Delta V, C3, disp, dur, v_{arr}, \alpha_{arr}, \alpha_{LOS}, \alpha_{Sun}] \tag{3.35}$$

where JD represents the Julian date at mission departure, ΔV is the total mission change in velocity required, $C3$ is the associated mission hyperbolic excess energy at departure from Earth's sphere of influence, $disp$ is the dispersion time after disruption, dur is the mission duration, v_{arr} is the relative arrival velocity between the asteroid and the spacecraft, α_{arr} is the relative arrival angle between the asteroid and spacecraft at intercept, α_{LOS} is the line-of-sight angle between Earth and the asteroid at the time of intercept, and α_{Sun} is the approach angle of the spacecraft to the asteroid with respect to the Sun. The overall cost function used

to quantitatively compare the various potential NEO mission designs is constructed in the following manner

$$C(\mathbf{X}) = f(\mathbf{X}) + g(\mathbf{X}) \tag{3.36}$$

where $f(\mathbf{X})$ is a constant cost attributed to every mission trajectory and $g(\mathbf{X})$ is a variable cost that is dependent on the state variables used within the trajectory optimization [35]. The components of the overall cost function $f(\mathbf{X})$ and $g(\mathbf{X})$ take the form

$$f(\mathbf{X}) = \Delta v + \sqrt{C3} \tag{3.37}$$

and

$$g(\mathbf{X}) = g(JD) + g(disp) + g(dur) + g(v_{arr}) + g(\alpha_{arr}) + g(\alpha_{LOS}) + g(\alpha_{Sun}) \tag{3.38}$$

The exact penalty functions used to construct the various components of $g(\mathbf{X})$ are described below. The component cost functions are defined based on the user defined upper and lower bounds for the state variables used in the cost function evaluation of the mission design space. If the user would like to define a desired launch window within the potential launch timespan, then the algorithm will penalize launch dates that are either below the launch date lower bound or above the launch date upper bound

$$g(JD) = \begin{cases} 0, & JD_{lower} < JD < JD_{upper} \\ 100, & JD < JD_{lower}, JD > JD_{upper} \end{cases} \tag{3.39}$$

Similarly, if the user chooses to include the dispersion time after impact or the mission duration in the cost function, the penalty functions take the same form as that of the launch date

$$g(disp) = \begin{cases} 0, & disp_{lower} < disp < disp_{upper} \\ 100, & disp < disp_{lower}, disp > disp_{upper} \end{cases} \tag{3.40}$$

$$g(dur) = \begin{cases} 0, & dur_{lower} < dur < dur_{upper} \\ 100, & dur < dur_{lower}, dur > dur_{upper} \end{cases} \tag{3.41}$$

Given that the launch date, dispersion time, and mission duration are a bit more subjective user-defined parameters, the penalty functions are simple conditional arguments that if true don't penalize the mission but heavily penalize the mission if any of the three conditions are

violated, virtually ensuring that the given mission could not be best mission design given the established cost function. Constructing a mission to a hazardous, near-Earth asteroid utilizing the HAIV concept spacecraft that the ADRC has created requires the knowledge of the expected relative arrival velocity. The two-body configuration of the spacecraft requires knowing the speed that the spacecraft would be approaching the target so that the distance and timing between the two parts of the vehicle can be considered a given, making the arrival velocity to target an extremely important state variable with regards to the overall mission. So, the penalty function for the relative arrival velocity is as follows

$$g(v_{arr}) = \begin{cases} 0, & v_{arr,lower} < v_{arr} < v_{arr,upper} \\ |v_{arr} - v_{arr,b}|, & v_{arr} < v_{arr,lower}, v_{arr} > v_{arr,upper} \end{cases} \tag{3.42}$$

where $v_{arr,b}$ is short-hand notation signifying the arrival velocity bound (either the upper or lower bound). Another important parameter to consider when making the final approach to a target is the relative arrival angle between the spacecraft and the target. With kinetic impactor missions, the angle that the spacecraft and the target would collide is important as far as determining the how much the target is perturbed due to the impact, so if the user would want define a range of arrival angles for the spacecraft to impact the target, the associated penalty function for missions that don't have arrival angles within the range is defined as

$$g(\alpha_{arr}) = \begin{cases} 0, & \alpha_{arr,lower} < \alpha_{arr} < \alpha_{arr,upper} \\ exp\left(-\frac{1}{1-\alpha_{arr}^2}\right), & else \end{cases} \tag{3.43}$$

During critical portions of the mission, communication with Earth is a must, so a line-of-sight angle during the final terminal impact phase can be included to help ensure mission feasibility. Communication between Earth and the spacecraft during that terminal phase is the only way to determine mission success. The line-of-sight angle is found as

$$\alpha_{LOS} = \arccos\left(\frac{\vec{R}_{\oplus} \cdot \vec{R}_{ast}}{R_{\oplus} R_{ast}}\right) \tag{3.44}$$

where $\vec{R}_{\oplus}$ and $\vec{R}_{ast}$ are the Earth and asteroid radius vectors at the time of impact, respectively [35]. To ensure that the line-of-sight angle is in the correct quadrant, the z component of the cross product between the two radius vectors is used

$$\vec{c} = \vec{R}_{\oplus} \times \vec{R}_{ast} \tag{3.45}$$

$$\alpha_{LOS} = 2\pi - \alpha_{LOS}, \quad c(3) \leq 0 \tag{3.46}$$

The user may define an angle range for the line-of-sight angle if they desire a particular view of the impact, otherwise the penalty function penalizes missions that have a value for α_{LOS} near π, as follows

$$g(\alpha_{LOS}) = \begin{cases} 0, & \alpha_{LOS,lower} < \alpha_{LOS} < \alpha_{LOS,upper} \\ exp\left(-\frac{1}{1-(\alpha_{LOS}-\pi)^2}\right), & else \end{cases} \tag{3.47}$$

The final potentially added penalty function is again more used to ensure mission feasibility and penalizes missions according to the relative asteroid velocity vector with respect to the asteroid's position vector relative to the Sun. The reason for this is so that the spacecraft arrives on the sunlight side of the asteroid, resulting in conditions that are favorable for the terminal guidance of the spacecraft. To avoid numerical scaling issues due to the difference in magnitude of the vectors, unit vectors are used in the calculation of the Sun angle.

$$\alpha_{SA} = \arccos\left(\vec{e}_r \cdot \vec{e}_v\right) \tag{3.48}$$

Different than the line-of-sight angle penalty, here all angles greater than 0 (indicating that the approach is directly along the asteroid-Sun line from the sunward side) are penalized using a linear function [35].

$$g(\alpha_{SA}) = \left(\frac{1}{\pi}\right)\alpha_{SA} \tag{3.49}$$

The penalty functions can be altered, or others can be added, to shape the solution as the user desires. Given a defined cost function for the desired mission type, the optimal mission trajectories will be found by the algorithm and the top 10 mission design results will be reported, along with their state variable values, for the user to select the desired mission design.

3.4 Sample Mission Designs using AMiDST

Before the implementation of the trajectory optimization, the customizable cost function, the AMiDST program was a little more user-dependent. Once the user defines the target asteroid, the program would construct the porkchop plot and present it to the user in order for the user to select any number of points from the contour plot as design points (pairs of

launch dates and mission durations) for the program to analyze and report the results back to the user. This lower fidelity mission design gave the user more control of the initial conditions for the potential mission designs, without knowing anything about the mission parameters at the back-end of the mission trajectory. In order to show the capabilities and output from the AMiDST program, results of three asteroid case studies (1999 RQ36, 2011 AG5, 2012 DA14) will be shown from lower-fidelity versions of the AMiDST program [31] and results from the higher-fidelity version will be provided on different target asteroids later in this work.

3.4.1 Asteroid 1999 RQ36

The selected design point for this HAIV disruption mission is chosen to occur at a late launch date within the given launch window. The cross-hairs and black box on Figure 3.8 show the region from which the design point was chosen from. The selected launch date comes
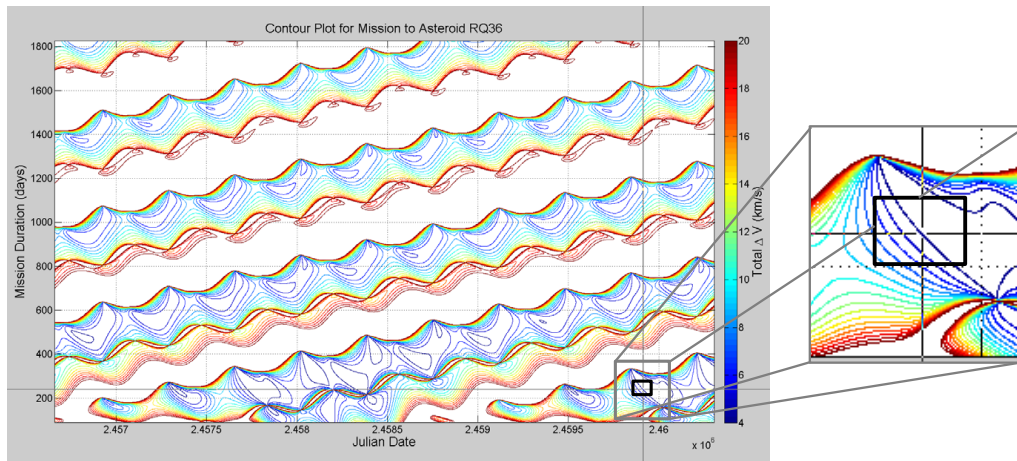
Figure 3.8 Selection of launch date and mission duration for 1999 RQ36 disruption mission.

out to be December 6, 2022 with a mission duration of 233 days. Given the launch date and mission duration pair, the resulting departure ΔV from the 185-km circular low-Earth orbit is just over 4 km/s. From these mission parameters, the spacecraft's trajectory is plotted in red along with the Earth's path (green line) and 1999 RQ36's trajectory (blue line) over the mission timespan in Figure 3.9 on the left. The HAIV would depart from Earth (red triangle) on December 6, 2022 and travel for 233 days until it would encounter the target NEO on July 27, 2023 (red circle).
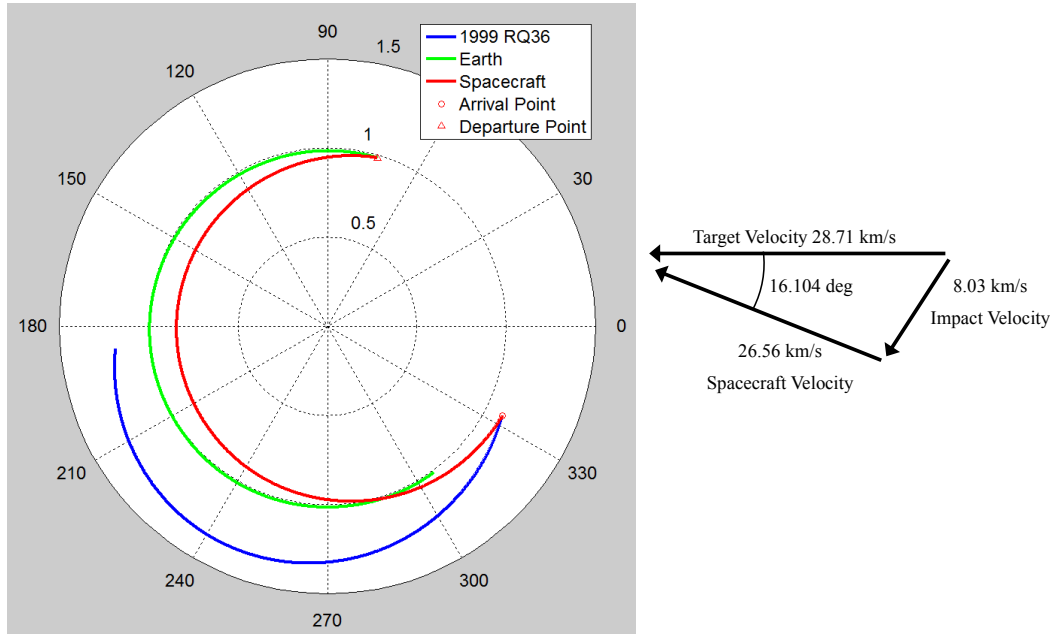
Figure 3.9   Left: Orbit diagram of transfer trajectory from Earth to 1999 RQ36. Right: Speeds and angle between spacecraft and 1999 RQ36 at impact.

On the right side of Figure 3.9, there is a depiction of the arrival conditions for the HAIV with respect to 1999 RQ36. Arriving at 1999 RQ36 on July 27, 2023 the HAIV would be travelling at about 26.5 km/s at a 16.1 degree angle to the target NEO's 28.7 km/s velocity, resulting in about an 8-km/s velocity difference.   Thanks to the large spacecraft mass and required departure ΔV, the only launch vehicle capable of completing the given mission, from the Delta II, Atlas V, and Delta IV class vehicles analyzed, is the Delta IV Heavy. With such a powerful launch vehicle and massive spacecraft comes a large price tag as well, the estimated mission cost for this nuclear disruption mission is nearly \$1.8B. Since only the Atlas V class of launch vehicles are currently able to be launched, due to the decommissioning of the Delta II and Delta IV launch vehicles, a new launch date and/or mission duration would have to be found for a feasible mission design. Based upon the given mission parameters, Table 3.2 gives all the pertinent HAIV mission results. [30, 31]

Table 3.2   Mission design parameters for intercept with Asteroid 1999 RQ36.

Mission Parameter	Value
Asteroid	1999 RQ36
Asteroid Mass (kg)	1.4E+11
LEO altitude (km)	185
Spacecraft Designation	HAIV
NED Mass (kg)	1500
Impactor Mass (kg)	670
Follower Mass (kg)	3550
Total HAIV Mass (kg)	5720
Departure ΔV (km/s)	4.002
C3 (km^2/s^2)	17.669
Launch Vehicle	Delta IV Heavy
Departure Date	December 6, 2022
Mission Duration (days)	233
Arrival Angle (deg)	16.104
Impact Velocity (km/s)	8.03
Arrival Date	July 27, 2023
Estimated Mission Cost ($)	1797.66M

3.4.2   Asteroid 2011 AG5

If asteroid 2011 AG5 were deemed a realistic threat to the survival of the planet, a deflection/disruption mission would need to be launched. The case study for this direct intercept mission has a departure date April 15, 2027 and a mission duration of 350 days. Figure 3.10 shows the contour plot for a direct intercept mission with 2011 AG5. The cross-hairs and black box in the diagram show the selected launch date and mission duration, which are used to design the disruption mission.   With nearly a full year of transit time, the HAIV would not arrive to the target NEO until March 30, 2028, about 12 years before the estimated impact date. The orbit plot on the left of Figure 3.11 shows the impact between the HAIV and the target to occur inside the Earth's orbital radius. The spacecraft will depart from Earth on April 15, 2027, represented by the red triangle, and travel for 350 days until its encounter with asteroid 2011 AG5 on March 30, 2028, shown as the red circle. The spacecraft, asteroid, and Earth's orbits are depicted by the red, blue, and green lines, respectively.

The right side of Figure 3.11 shows the anticipated encounter between the HAIV and target
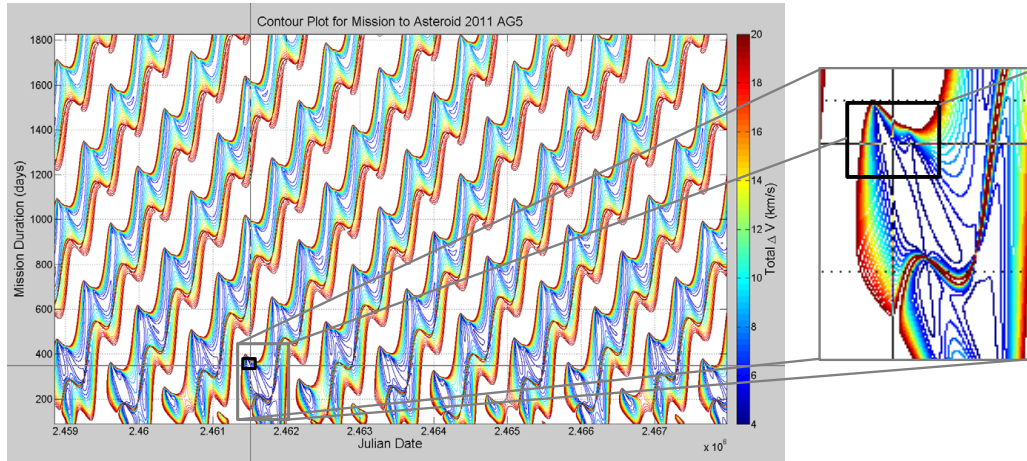
Figure 3.10   Selection of launch date and mission duration for 2011 AG5 disruption mission.

NEO. Arrival at 2011 AG5 from the given trajectory will result in an impact angle of about 14.3 degrees, the angle between the asteroid and spacecraft's velocity vectors at the time of impact. Such an arrival angle results in a relative velocity between the asteroid and the HAIV of over 9 km/s. High relative impact velocities, similar to the one present in this mission, are the reasons why the ADRC has been developing the HAIV concept.   The pertinent mission parameters for this direct intercept disruption mission are given in Table 3.3. The departure ΔV for this case study is rather high, at just under 6 km/s. Given such a large ΔV, an Atlas V 551 launch vehicle is smallest launch vehicle from the Delta II, Atlas V, and Delta IV classes capable of imparting the required change in velocity from low-Earth orbit. And, since the decommissioning of the Delta II and Delta IV launch vehicles, the Atlas V 551 is the only launch vehicle available, and capable, of completing the aforementioned mission. The estimated mission cost for this particular mission design is nearly $1B. It is interesting to note that while there are several regions where a feasible mission can be designed, there are many more design points where there is no feasible launch configuration that will apply enough ΔV to inject the spacecraft into the required direct transfer orbit. [30, 31]

3.4.3   Asteroid 2012 DA14

Asteroid 2012 DA14 is an Aten class near-Earth asteroid with an estimated mass of about 30 meters. The NEO was discovered on February 23, 2012 in Spain. Upon initial observation,
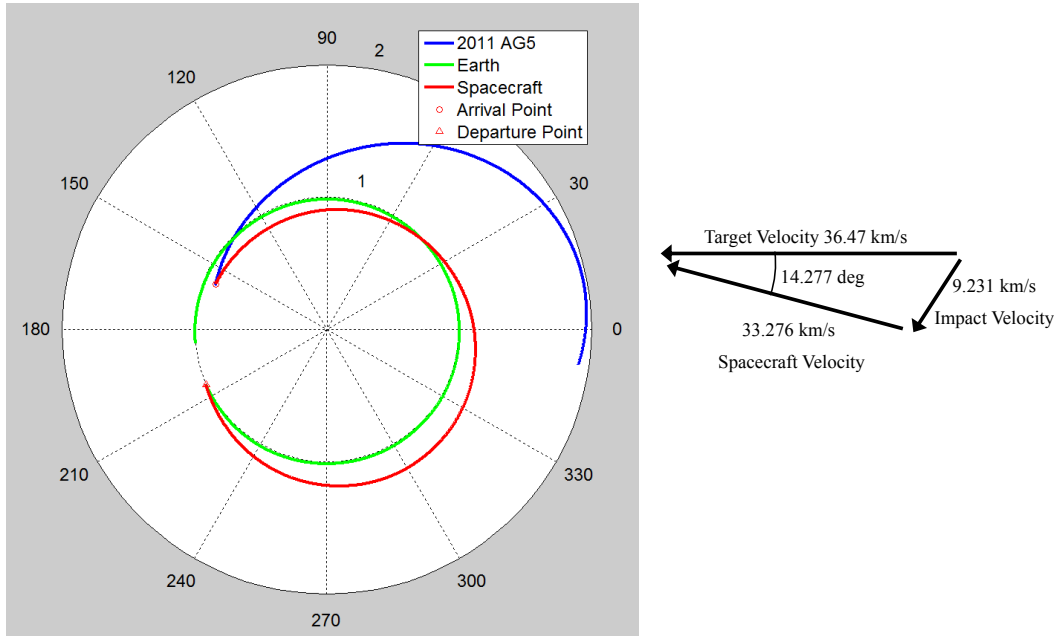
Figure 3.11   Left: Orbit diagram of transfer trajectory from Earth to 2011 AG5. Right: Speeds and angle between spacecraft and 2011 AG5 at impact.

the odds of 2012 DA14 impacting Earth between 2026 and 2069 were about 1-in-3000, with no possibility of the asteroid hitting Earth during its close-encounter in 2013. Table 3.4 shows the orbital elements of the asteroid.   Let's assume that the current date is around the end of February 2012, and asteroid 2012 DA14 was just discovered, it has a high likelihood of impacting Earth on February 15, 2013, and that we are launch ready at this point in time. These pieces of information are/were not true, but we assume them to be true for the sake of the problem that they establish.

With the impact date set with respect to the discovery date, a mission window is established where the spacecraft has to be launched after discovery, travel to meet the asteroid, and allow time for the disrupted pieces of the asteroid to disperse before the anticipated impact date. This mission timeline is much more stringent than the one for 2013 A1 since everything has to occur within one year. Given that the asteroid is a near Earth object, there should be more options for missions to it, either long-term or short-term. Figure 3.12 depicts a contour plot of total mission ΔV in terms of launch date and mission flight time. The porkchop plot agrees with the earlier assessment that upon initial views there are plenty of feasible mission options.

Table 3.3 Mission design parameters for intercept with Asteroid 2011 AG5.

Mission Parameter	Value
Asteroid	2011 AG5
Asteroid Mass (kg)	4.1E+9
LEO altitude (km)	185
Spacecraft Designation	HAIV
NED Mass (kg)	300
Impactor Mass (kg)	360
Follower Mass (kg)	1183
Total HAIV Mass (kg)	1843
Departure ΔV (km/s)	5.961
C3 (km^2/s^2)	67.709
Launch Vehicle	Atlas V 551
Departure Date	April 15, 2027
Mission Duration (days)	350
Arrival Angle (deg)	14.277
Impact Velocity (km/s)	9.231
Arrival Date	March 30, 2028
Estimated Mission Cost ($)	860.340M

Due to the wide range of mission possibilities within the one year time line that has been established for 2012 DA14, three mission case studies were analyzed. The three mission case studies included: (1) an early launch, short-term mission, (2) an early launch, long-term mission, and (3) a late launch, short-term mission. Each case study was analyzed from the stand point of the mission parameters that make the mission feasible and the resulting orbital parameters [30, 31].

3.4.3.1 Early launch, short-term mission

One of the big assumptions made for this exercise is that we are launch ready at the time of discovery of asteroid 2012 DA14. If the main point of the mission design process is to maximize the dispersion time, with the lowest mission ΔV, by keeping the mission flight time to 60 days or less, then this course of action would indicate an early mission launch with a short flight time. Because a longer mission duration would result in lower $\Delta V's$, the mission duration

Table 3.4   The orbital elements of asteroid 2012 DA14 at an epoch of April 18, 2013. [1]

Orbital Element	Value	Units
a	0.91032	AU
e	0.0894	
i	11.6081	deg
ω	195.5346	deg
Ω	146.996	deg
M	231.097	deg

tends towards its upper bound. The resulting early launch date and short mission flight time parameters are shown in Table 3.5.

Table 3.5   Optimal constrained mission parameters for early launch, short-term impact mission to asteroid 2012 DA14.

Parameter	Value
Departure Date	February 24, 2012
Flight Time (days)	60
Departure ΔV (km/s)	5.036
Dispersion time (days)	297

Given the long dispersion time associated with this mission architecture, a smaller spacecraft can be used to impact the asteroid body. Using the associated mission parameters, the overall mission construction can be summarized in Table 3.6.   With the small size of asteroid 2012 DA14, the spacecraft type that would be used in these situations would be a kinetic impactor. But, with the small relative impact velocity a kinetic impactor may not be able to disrupt the asteroid enough, if at all, to be effective. So, a smaller scaled version of the ADRC's HAIV would be the spacecraft of choice for this mission. Due to the higher departure ΔV for this mission, a midsize Delta IV launch vehicle is chosen for this mission. With the spacecraft intercepting the asteroid on April 24, 2012, there would be almost 300 days for the fragments of the disrupted body to disperse before February 15, 2013.
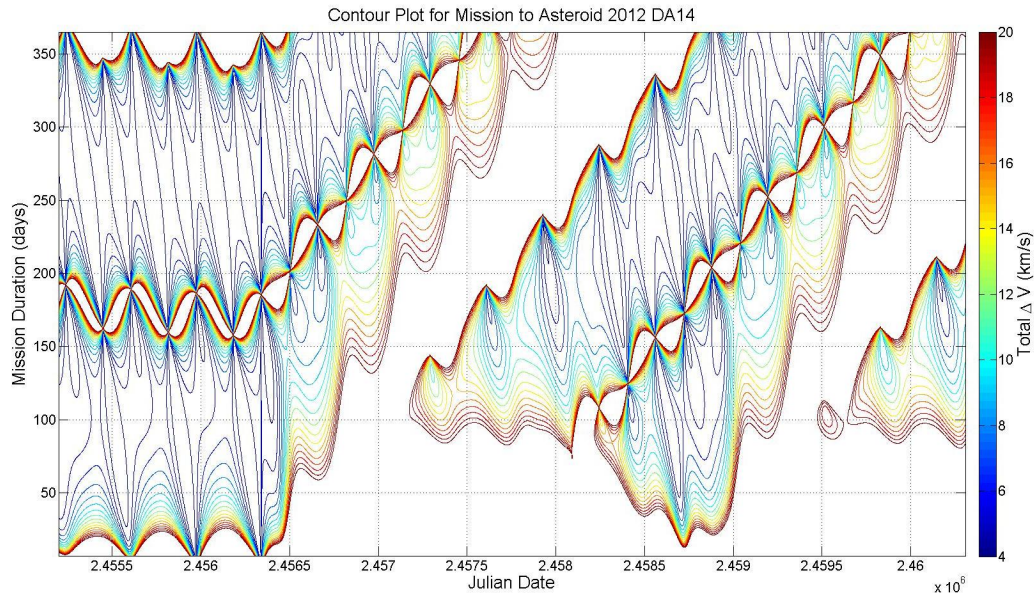
Figure 3.12   Mission contour plot of total ΔV in terms of launch date and mission flight time for asteroid 2012 DA14.

3.4.3.2   Early launch, long-term mission

Again, assuming that we are launch ready from the time of discovery for an early launch date, but lower mission ΔV is valued over dispersion time, then the mission construction would lean toward a longer mission duration. So, the constraint on dispersion time is relaxed with respect to the constraints put in place for the first case study. The transfer trajectory parameters for this early launch, long-term mission design are shown in Table 3.7.

By allowing a longer mission flight time, the departure ΔV drops to about 3.6 km/s to inject into an orbit to intercept asteroid 2012 DA14. With such a low departure velocity a smaller launch vehicle can be used to conduct the mission. Launching on April 27, 2012 with a 263 day flight time results in asteroid intercept on January 15, 2013 - allowing for 31 days of dispersion time for the disrupted asteroid.

3.4.3.3   Late launch, short-term mission

In the case where there is no possibility for an early launch, there are still feasible missions to disrupt the threatening body and allow for at least a little time for the fragments to disperse.

Table 3.6 Mission design parameters for a early launch, short-term intercept mission to asteroid 2012 DA14.

Mission Parameter	Value
Asteroid	2012 DA14
LEO altitude (km)	185
Spacecraft Designation	HAIV
Total HAIV Mass (kg)	1000
Departure ΔV (km/s)	5.036
C3 (km^2/s^2)	43.121
Launch Vehicle	Delta IV M+(4,2)
Departure Date	February 24, 2012
Mission Duration (days)	60
Arrival Angle (deg)	2.001
Impact Velocity (km/s)	0.9571
Arrival Date	April 24, 2012
Estimated Mission Cost ($)	601.376M

Table 3.7 Optimal constrained mission parameters for early launch, long-term impact mission to asteroid 2012 DA14.

Parameter	Value
Departure Date	April 27, 2012
Flight Time (days)	263
Departure ΔV (km/s)	3.602
Dispersion time (days)	31

If the mission flight time is limited to 30 days or less and dispersion time of 15 days or more, the situation that arises is the worst case scenario for Earth in which something can still be done to the threatening body. Given these constraints to the mission design, the following mission parameters are obtained: While there is a limited amount of time for the disrupted pieces of the body to scatter before the expected impact date, that time would allow for some fragments to miss the planet and only a subset of the entire body to impact the Earth, hopefully resulting in most of the smaller pieces burning up in Earth's atmosphere. The complete mission architecture for such a scenario is summarized in Table 3.10. This mission scenario results in the largest relative impact velocity of the case studies discussed, despite the small departure

Table 3.8 Mission design parameters for a early launch, long-term intercept mission to asteroid 2012 DA14.

Mission Parameter	Value
Asteroid	2012 DA14
LEO altitude (km)	185
Spacecraft Designation	Kinetic Impactor
Total Spacecraft Mass (kg)	1400
Departure ΔV (km/s)	3.602
C3 (km^2/s^2)	8.383
Launch Vehicle	Delta IV Medium
Departure Date	April 27, 2012
Mission Duration (days)	263
Arrival Angle (deg)	10.901
Impact Velocity (km/s)	6.049
Arrival Date	January 15, 2013
Estimated Mission Cost ($)	717.658M

Table 3.9 Optimal constrained mission parameters for late launch, short-term impact mission to asteroid 2012 DA14.

Parameter	Value
Departure Date	December 31, 2012
Flight Time (days)	30
Departure ΔV (km/s)	3.789
Dispersion time (days)	16

ΔV. The reason for this is because of where the asteroid is being intercepted. The asteroid is approaching its perihelion, meaning that its speed is increasing as it crosses Earth-orbit, and since there is not a long flight time for the spacecraft, it would not have lost a lot of its launch energy, making for a more energetic collision.

3.4.3.4   Asteroid 2014 DA14 Case Study Conclusions

While all three missions are completely feasible and would probably result in the salvation of the planet, each mission has its own time and place. The early launch, short term mission scenario should always be the first option. Making an attempt on the threatening body as

Table 3.10   Mission design parameters for a late launch, short term intercept mission to asteroid 2012 DA14.

Mission Parameter	Value
Asteroid	2012 DA14
LEO altitude (km)	185
Spacecraft Designation	Kinetic Impactor
Total Spacecraft Mass (kg)	1800
Departure ΔV (km/s)	3.789
C3 (km^2/s^2)	12.6798
Launch Vehicle	Delta IV Medium
Departure Date	December 31, 2012
Mission Duration (days)	30
Arrival Angle (deg)	17.481
Impact Velocity (km/s)	9.371
Arrival Date	January 30, 2013
Estimated Mission Cost ($)	842.26M

early as possible would give some time afterwards in case something were to go wrong and the mission were to fail. But, this mission construction makes the assumption that we are ready to launch a spacecraft upon discovering a threat, if not, then this scenario is worthless. It would be this author's opinion that the second option mission scenario would be an early launch, with a longer mission flight time. In the event that the body threatening Earth were similar to Comet 2013 A1 with a highly energetic and inclined orbit, launching early and intercepting the body as far from Earth as possible would be the best option, and that would likely require a longer mission duration. If neither of the first two options are available, or fail, the last option should be a late launch with a short flight time mission scenario. This mission construction would be a last resort option, and should not be thought of as the first choice in hopes that new data would prove the NEO is no longer a threat. Regardless of the option chosen given the situation, any action would be better than inaction [30, 31].

CHAPTER 4.   PLANETARY ENCOUNTERS

4.1   Introduction

When a body undergoes an encounter with a planet, there are a number of ways that its orbit will be affected. The environment around a planet is very dynamic in nature, and small inaccuracies in modeling can result in drastic differences between the simulated trajectories and the actual trajectory. Getting a good understanding behind the geometry of planetary close-approaches and the effect that they have on the orbital elements of the bodies that undergo them should assist with the task of predicting the resulting orbital trajectory after a close flyby of a planet [36]. In this chapter, there will be a discussion of various orbital theories associated with planetary flyby encounters: encounter geometry, planetary flybys, target B-planes, and keyhole theory.

4.2   Encounter Geometry

The dynamical system under consideration in the following analysis consists of the Sun, a planet orbiting the Sun on a circular orbit, and an asteroid, viewed as a particle, that is on an eccentric and inclined orbit around the Sun that crosses the orbit of the planet. Assume the planet has an orbital radius $R = 1$, the product $k\sqrt{M} = 1$, where k is the Gaussian constant and M is the mass of the Sun, and the asteroid has orbital parameters $(a, e, i, \omega, \Omega)$. In order to have the asteroid cross the orbital path of the planet, the asteroid must meet the following criteria: $a(1-e) < 1 < a(1+e)$. The frame of reference established for this analysis is centered on the planet, the x-axis points radially opposite to the Sun, the y-axis is the direction of motion of the planet itself, and the z-axis completes the right-handed system by pointing in the direction of the planet's angular momentum vector - illustrated in Figure 4.1.   The three
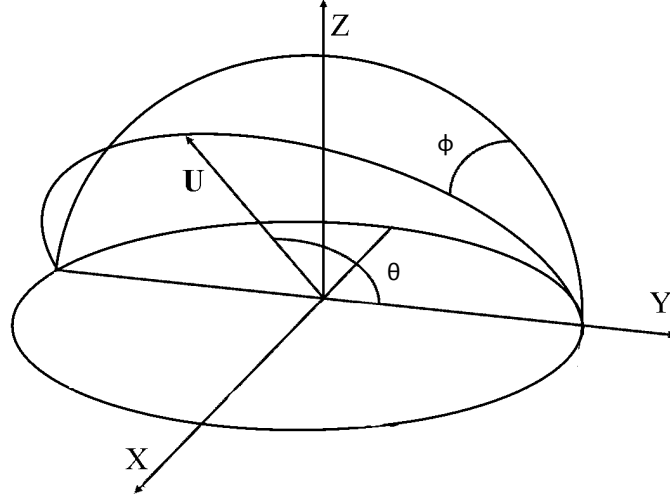
Figure 4.1   Reference frame of $\vec{U}$. The origin is placed at the planet's center, the positive x-axis is opposite the direction of the Sun, the y-axis is in the direction of the planet's motion, and the z-axis is parallel to the planet's angular momentum vector. The angles ϕ and θ define the direction of $\vec{U}$.

most important orbital elements used in the analysis are the semi-major axis a, the eccentricity e, and the inclination i.

4.2.1   Relationship Between Orbital Parameters a, e, i and U, ϕ, θ

Let $\vec{U} = (U_x, U_y, U_z)$ and U be the relative velocity vector and magnitude between the planet and the asteroid [37], defined as

$$U = \sqrt{3 - \left[\frac{1}{a} + 2\sqrt{a(1 - e^2)}\cos i\right]} \tag{4.1}$$

$$U_x = U\sin\theta\sin\phi \tag{4.2}$$

$$U_y = U\cos\theta \tag{4.3}$$

$$U_z = U\sin\theta\cos\phi \tag{4.4}$$

where θ and ϕ are the angles that define the direction of U by

$$\phi = \tan^{-1}\left[\pm\sqrt{\frac{2a - 1}{a^2(1 - e^2)} - 1}\frac{1}{\sin i}\right] \tag{4.5}$$

$$\theta = \cos^{-1}\left[\frac{1 - U^2 - 1/a}{2U}\right] \tag{4.6}$$

where θ may vary between 0 and π, and ϕ between $-\pi/2$ and $\pi/2$.

In terms of a, e, and i, the components of $\vec{U}$ are given by

$$U_x = \left[2 - \frac{1}{a} - a(1 - e^2)\right]^{1/2} \tag{4.7}$$

$$U_y = \sqrt{a(1 - e^2)}\cos i - 1 \tag{4.8}$$

$$U_z = \sqrt{a(1 - e^2)}\sin i \tag{4.9}$$

and, inversely, we have

$$a = \frac{1}{1 - U^2 - 2U_y} \tag{4.10}$$

$$e = \left[U^4 + 4U_y^2 + U_x^2(1 - U^2 - 2U_y) + 4U^2 U_y\right]^{1/2} \tag{4.11}$$

$$i = \sin^{-1}\sqrt{U_z^2/[U_z^2 + (1 + U_y)^2]} \tag{4.12}$$

Within the scope of potential impacting bodies, one of the most important regions of the planetocentric system defined by the body's orbital elements is the B-plane (discussed in detail in Appendix A). Looking back at Figure 4.1, it can be seen that the angles ϕ and θ are defined within the planetocentric reference frame (X, Y, Z) with respect to the relative velocity vector U. So, if a reference frame (ξ, η, ζ) is defined on the B-plane of the encounter, then the angles θ and ϕ can be used to transform between the two reference frames. This coordinate transformation is accomplished by first rotating through an angle $-\phi$ about Y and then rotating through an angle $-\theta$ about ξ (perpendicular to the old Y-axis and to $\vec{U}$). In matrix notation, the coordinate transformation can be written as

$$\begin{bmatrix} \xi \\ \eta \\ \zeta \end{bmatrix} = \mathbf{R}_\xi(-\theta)\mathbf{R}_Y(-\phi) \begin{bmatrix} X \\ Y \\ Z \end{bmatrix} \tag{4.13}$$

and the inverse transformation can be accomplished by rotating through the positive angles in reverse order [37].

4.2.2 Post-Keyhole Geometry

After the asteroid has an encounter with the target planet, the $\vec{U}$ vector is rotated by an angle γ in the direction ψ, where ψ is the angle measured counter-clockwise from the meridian containing the $\vec{U}$ vector, as seen in Figure 4.2. The deflection angle γ is related to the
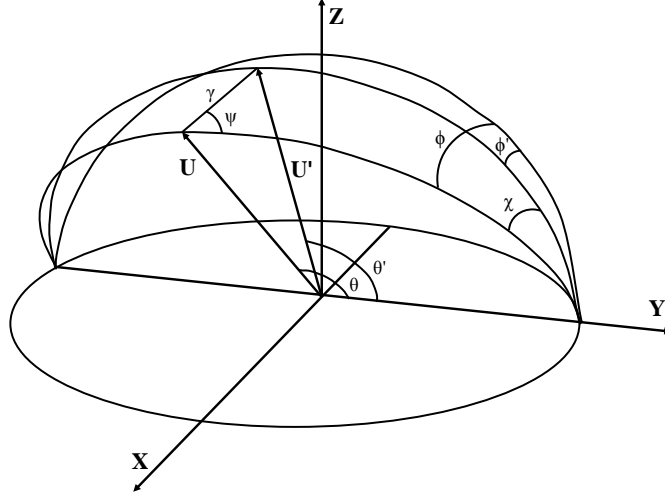
Figure 4.2   Reference frame of $\vec{U}$ and $\vec{U}'$. After the body's encounter with the planet, the vector $\vec{U}$ is rotated by an angle γ in the direction of ψ.

encounter parameter b by

$$\tan \frac{1}{2}\gamma = \frac{m}{bU^2} \tag{4.14}$$

where m is the mass of the planet, in units of the Sun's mass. The angle θ after the encounter, denoted by θ', is calculated from

$$\cos \theta' = \cos \theta \cos \gamma + \sin \theta \sin \gamma \cos \psi \tag{4.15}$$

and, defining $\chi = \phi - \phi'$, we have

$$\sin \chi \quad = \quad \sin \psi \sin \gamma / \sin \theta' \tag{4.16}$$

$$\cos \chi \quad = \quad (\cos \gamma \sin \theta - \sin \gamma \cos \theta \cos \psi) / \sin \theta' \tag{4.17}$$

$$\tan \chi \quad = \quad \sin \psi \sin \gamma / (\cos \gamma \sin \theta - \sin \gamma \cos \theta \cos \psi) \tag{4.18}$$

$$\tan \phi' \quad = \quad (\tan \phi - \tan \chi) / (1 + \tan \phi \tan \chi) \tag{4.19}$$

Evaluating for the post-encounter variables θ' and ϕ', the values of a', e', and i' can be obtained accordingly [37].

4.2.3 Post-Keyhole Orbital Elements

In order to get a better understanding of what kind of insight can be gained by the encounter geometry, applying the established theory to an asteroid like 2011 AG5 can prove to be a learning exercise to show how the approach and post-encounter geometries relate to each other in the context of an Earth-threatening asteroid. The important orbital parameters to the analysis are given in Table 4.1.

Table 4.1 Orbital elements of asteroid 2011 AG5 prior to an Earth encounter.

Orbital Element	Value
a	1.43065
e	0.390126
i	1.39408°

4.2.3.1 Post-Keyhole Semi-major Axis

Given that $|\vec{U}|$ is constant, the variation in the semi-major axis Δa depends only on the parameters θ and θ' as

$$\Delta a = \frac{a' - a}{a} = \frac{1 - U^2 - 2U\cos\theta}{1 - U^2 - 2U\cos\theta'} - 1 \tag{4.20}$$

Figure 4.3 shows the variation in the semi-major axis a. The colors on the mesh depict the value of the variation, and the black dotted line depicts the resulting semi-major axis variation of 2013 PDC-E from its Earth encounter. From the figure, it can be seen that the asteroid is susceptible to having its semi-major axis increased or decreased, depending on the values of γ and ψ. Preliminary observations show that values of ψ between about $\pi/2$ and $3\pi/2$ will cause 2013 PDC-E to have a smaller post-encounter semi-major axis than its pre-encounter value, and a larger post-encounter semi-major axis for values of ψ less than $\pi/2$ and greater than $3\pi/2$. As far as the turn value γ, the closer the value is to $\pi/2$ means the more drastic an effect the encounter will have on the orbit, either by enlarging it or shrinking it.
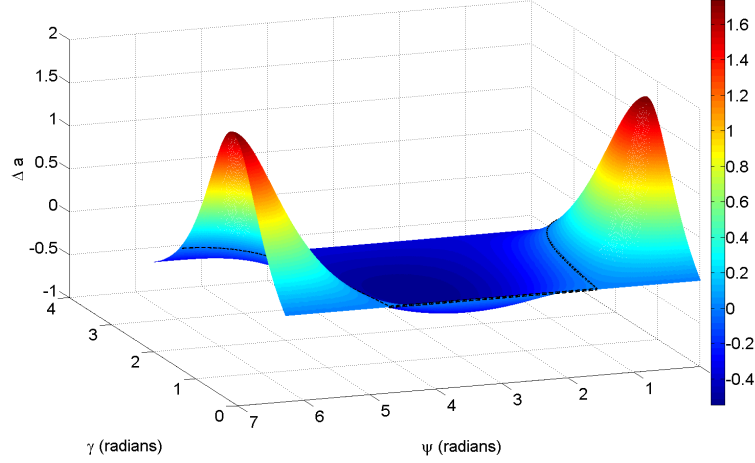
Figure 4.3   Surface plot of variation of semi-major axis for asteroid 2011 AG5.

4.2.3.2   Post-Keyhole Inclination

The tangent of inclination is defined as

$$\tan i = \frac{\cos\phi\sin\theta}{1/U + \cos\theta} = \frac{U_z}{1 + U_y} \tag{4.21}$$

and after the rotation of the relative velocity vector by the deflection angle γ in the direction of ψ, it becomes

$$\tan i' = \frac{\cos\phi\sin\theta\cos\gamma - \cos\phi\cos\theta\sin\gamma\cos\psi + \sin\phi\sin\gamma\sin\psi}{1/U + \cos\theta\cos\gamma + \sin\theta\sin\gamma\cos\psi} \tag{4.22}$$

The variation in inclination can be described by $\Delta i = \tan i' - \tan i$ [37].   Figure 4.4 depicts the variation of the inclination of the orbits of asteroid 2013 PDC-E. The black dotted line on the meshed grid shows the resulting variation of the inclination after the encounter with the Earth. The plot of post-encounter inclination variation has two distinct sections to it. When ψ is less than π the post-encounter inclination would be greater than the pre-encounter inclination, and when ψ is greater than π the inclination would decrease. The largest change in inclination seems to occur at ψ values of $\pi/2$ and $3\pi/2$.

4.2.3.3   Post-Keyhole Eccentricity

Recalling that

$$e^2 = U^4 + 4U_y^2 + U_x^2(1 - U^2 - 2U_y) + 4U^2U_y \tag{4.23}$$
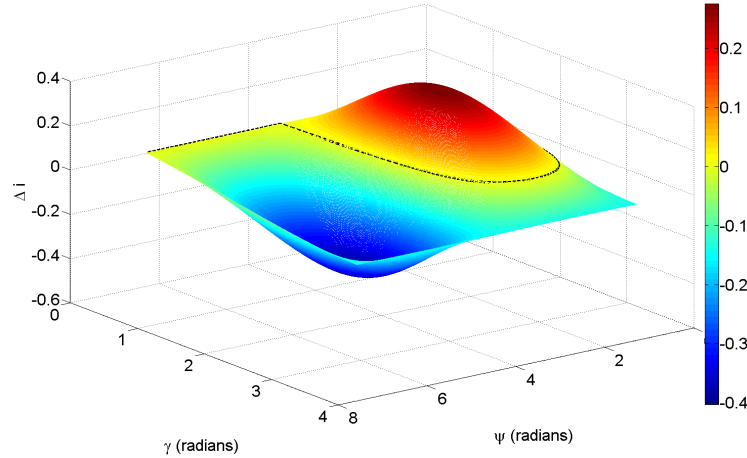
Figure 4.4   Surface plot of variation of inclination for asteroid 2011 AG5.

the expression for the pre-encounter eccentricity of the asteroid orbit can be expressed in terms of the relative velocity magnitude and its components. Making a substitution for the corresponding post-encounter terms, the value of the eccentricity after the encounter with the target planet can be calculated as

$$e' = \sqrt{U'^4 + 4U_y'^2 + U_x'^2(1 - U'^2 - 2U_y') + 4U'^2 U_y'} \qquad (4.24)$$

Taking the difference between the post- and pre-encounter eccentricities shows the variation in the orbital eccentricity ($\Delta e = e' - e$) based on the planetary encounter.   Figure 4.5
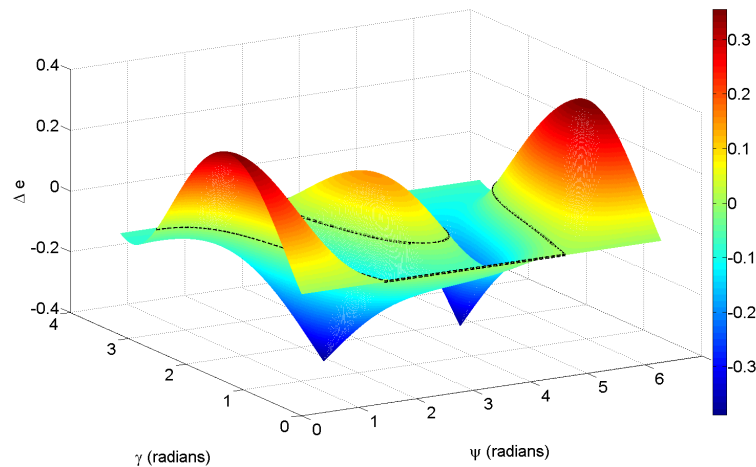
Figure 4.5   Surface plot of variation of eccentricity for asteroid 2011 AG5.

depicts the variation of the eccentricity of asteroid 2011 AG5. The black dotted lines shown

in the figure indicate the level of variation between the pre- and post-encounter eccentricities of the asteroid. The plot of eccentricity variation has a bit more complicated structure for this asteroid than the semi-major axis or inclination. Asteroid 2011 AG5 would have more eccentric post-encounter orbits for values of ψ that approach the ends of the feasible domain $[0, 2\pi]$ and values near π. The magnitude of the change in eccentricity however, is not as great for values of ψ near π as they are towards 0 and 2π. Values of ψ near $\pi/2$ and $3\pi/2$ seem to have a negative effect on the orbital eccentricities of the body.

A closer look at the variation equations of $(\Delta a, \Delta i, \Delta e)$ reveals cases where these equations can be further simplified, or interesting results become more apparent. Such an analysis is omitted in this discussion, as the simplifications do not have a direct effect to the calculations of the orbital variations or how they are used later on in the encounter analysis. As is, this analysis only enables us to understand the potential variations in the orbital elements of a body having an encounter with the planet, to get a firm grasp of the exact variation in the orbital elements would require either an analytic or numerical analysis of the encounter to find the ψ and γ values.

4.3   Planetary Flybys

Based on the encounter geometry analysis, the orbital variations for a body are shown via surface plots like the ones in the previous section. The amount of the orbit change depends on the speed the body has relative to the planet and how close it gets, but it is possible to find the varied orbital trajectory of the body after encounter. Short of using a high-fidelity gravitational model to track the progress of the body through numerical integration, the encounter phase can be modeled as two-body motion governed by the planet as the central body.

During a flyby of a planet, the incoming and outgoing v-infinity vectors and the pre- and post-encounter heliocentric velocities connect at the flyby planet through the following relationships

$$\vec{v}_\infty^- = \vec{v}_{fb,pre} - \vec{v}_{pre} \tag{4.25}$$

$$\vec{v}_\infty^+ = \vec{v}_{post} - \vec{v}_{fb,post} \tag{4.26}$$

where $\vec{v}_\infty^-$ and $\vec{v}_\infty^+$ are the incoming and outgoing v-infinity vectors, respectively, $\vec{v}_{fb,pre}$ and $\vec{v}_{fb,post}$ are the velocities of the flyby planet upon entry and exit of the planetary sphere of influence, and $\vec{v}_{pre}$ and $\vec{v}_{post}$ are the heliocentric velocity vectors entering and leaving the sphere of influence of the planet, respectively. During the encounter, the planet will turn body through an angle ϕ, determined by

$$\phi = 2 \arcsin \frac{1}{1 + r_p v_\infty^2 / \mu} \tag{4.27}$$

where r_p is the periapse radius of the flyby hyperbola, v_∞ is the magnitude of the incoming v-infinity vector, and μ is the gravitational parameter of the flyby planet [38].

The heliocentric speed gained by the body through the planetary encounter and the heliocentric delta-v vector caused by the flyby can be determined through the following two equations

$$\delta v = 2 v_\infty / e \tag{4.28}$$

$$\delta \vec{v} = \vec{v}_{pre} - \vec{v}_{post} \tag{4.29}$$

where e is the eccentricity of the flyby hyperbola [38]. Numerically, the following nonlinear equality path constraint must be true to ensure that no laws of physics are violated.

$$|\vec{v}_\infty^-| - |\vec{v}_\infty^+| = 0 \tag{4.30}$$

The resulting difference from the constraint may not necessarily be zero, however, a small tolerance of error can be allowed.

Regardless of the analysis conducted here being done analytically or numerically, the results should be rather similar. Thus, given the pre- and post-encounter heliocentric velocity vectors of the body, along with their respective heliocentric position vectors, the orbital elements of the heliocentric orbits can be found and compared to see just how much the orbit of the body has changed. Beyond seeing just how much the heliocentric trajectory would be changed due to the planetary close encounter, the data on orbital variations can be used to find resonance orbits.

The key parameter for resonant return orbits is the post-encounter semi-major axis. Scaling everything so that the Earth-Sun distance and the Sun's gravitational constant are equal to 1

$$T^2/a^3 \approx 4\pi^2 \tag{4.31}$$

where T and a are the period and semi-major axis of the body, respectively, in nondimensional units. Given that Earth's orbital period is 2π, the encountering body's post-encounter orbital period is $2\pi(a')^{3/2}$, where a' is the post-encounter semi-major axis. If the Earth and post-encounter body's periods are commensurable, then after h periods of the asteroid and k periods of the Earth have passed, where k and h are integers, a new encounter will take place as

$$(a')^{3/2} = k/h \tag{4.32}$$

Picking a number of Earth orbits to elapse, and an acceptable tolerance for the orbital ratio (k/h), the number of asteroid orbits can be found that would correspond to a resonance orbit existing between the asteroid and Earth from a given post-encounter semi-major axis.

4.4   Target B-planes

A target plane is defined as a geocentric plane oriented to be normal to the asteroid's geocentric velocity vector. By observing the point of intersection of an asteroid trajectory with the target plane can lend significant insight into the nature of a future encounter. In general, there are two distinct planes and several coordinate systems that can be used in such a framework. The classical target plane is referred to as the B-plane, which has been used in astrodynamics since the 1960s. The B-plane is oriented normal to the incoming asymptote of the geocentric hyperbola, or normal to the unperturbed relative velocity $\vec{v}_\infty$. The plane's name is a reference to the so-called impact parameter b, the distance from the geocenter to the intercept of the asymptote on this plane, known as the minimum encounter distance along the unperturbed trajectory [39]. Figure 4.6 depicts the relationship between the target B-plane and the trajectory plane of the asteroid.

The B-plane parameters (such as the impact parameter b or the vectors that define the B-plane) can be computed by making the following assumptions: (1) the spacecraft has arrived
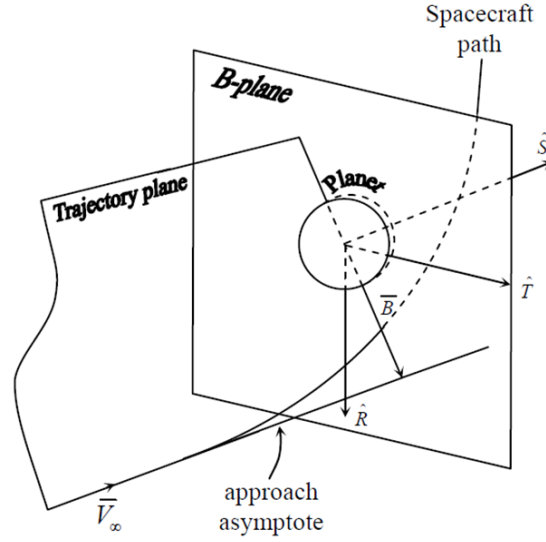
Figure 4.6   Representation of the target B-plane of a planet with respect to the incoming approach of a body on the trajectory plane.

at the target planet sphere of influence (SOI), (2) two-body theory can be used to determine the resulting $\vec{b}$, and (3) if perturbations to the spacecraft or target planet are included, the B-plane targeting can be accomplished by numerical integration of the equations of motion. In order to derive the B-plane and the B-vector, the incoming asymptote $\hat{S}$ needs to be calculated. First, the spacecraft's orbit normal unit vector $(\hat{n})$ from the position $(\vec{r})$ and velocity $(\vec{v})$ at periapse

$$\hat{n} = \frac{\vec{r} \times \vec{v}}{|\vec{r} \times \vec{v}|} \tag{4.33}$$

The calculation of $\hat{n}$ fixes the body's orbit plane orientation in space. Next, the eccentricity vector is calculated

$$\hat{e} = \left(\frac{v^2}{\mu} - \frac{1}{r} \right) \vec{r} - \frac{(\vec{r} \cdot \vec{v})}{\mu} \vec{v} \tag{4.34}$$

and thus fixes the direction of periapse. Next, the semi-major (a) and semi-minor (b) axes values are calculated

$$a = \left(\frac{2}{r} - \frac{v^2}{\mu} \right)^{-1} \tag{4.35}$$

$$b = -a\sqrt{e^2 - 1} \tag{4.36}$$

The semi-major axis is obtained from the energy expression, keeping in mind that the orbit of the body with respect to the planet is hyperbolic meaning that the value of a is negative and the energy of the orbit is positive. The semi-minor axis is computed from the equations $b^2 = a^2 + c^2$ and $e = c/a$. Now that the body's orbit has been characterized, the direction of $\hat{S}$ can be determined. Since the incoming asymptote lies in the orbit plane itself, only two orthonormal vectors within the orbit plane are needed to uniquely determine the position of $\hat{S}$. The eccentricity vector ($\hat{e}$) forms a natural X-axis, and the cross product of $\hat{e}$ and $\hat{n}$ forms the Y-axis. The incoming asymptote unit vector ($\vec{S}$) can then be calculated as

$$\hat{S} = \cos\alpha\,\hat{e} + \sin\alpha\,(\hat{n} \times \hat{e}) \tag{4.37}$$

where α is the hyperbolic asymptote angle, or the half bend angle, and is calculated from

$$\alpha = \cos^{-1}\left(\frac{1}{e}\right) \tag{4.38}$$

In order to calculate the unit vectors that define the B-plane, another vector ($\hat{N}$) is constructed that is centered on the planet and generally not perpendicular to $\hat{S}$. Normally, one of two vectors is chosen, either the body's polar vector or its orbit normal. For the analyses discussed and conducted in this work, the orbit normal is the vector used for $\hat{N}$. Crossing $\hat{N}$ with $\hat{S}$, a perpendicular vector ($\hat{T}$) is formed

$$\hat{T} = \frac{\hat{S} \times \hat{N}}{|\hat{S} \times \hat{N}|} \tag{4.39}$$

The final vector needed to define the B-plane is the $\hat{R}$ vector, and it is obtained from $\hat{S}$ and $\hat{T}$

$$\hat{R} = \hat{S} \times \hat{T} \tag{4.40}$$

Finally, based on this formulation the B-vector is given by

$$\vec{b} = b\left(\hat{S} \times \hat{n}\right) \tag{4.41}$$

where $\vec{b}$ exist on the B-plane. If desired, $\vec{b}$ can be expressed in terms of the B-plane coordinate system as well, where b_T and b_R are the components of $\vec{b}$ [40, 41].

$$b_T = \vec{b} \cdot \hat{T} \tag{4.42}$$

$$b_R = \vec{b} \cdot \hat{R} \tag{4.43}$$

4.4.1   Target Plane Coordinates

Generally it is conventional to place the origin of the B-plane's coordinate system at the geocenter, but the orientation of the coordinate axes on the plane is arbitrary. The system has been fixed at times by aligning the axes in a way so that one of the nominal target plane coordinates is zero, or by aligning one of the coordinate axes with either the projection of the Earth's polar axis or the projection of the Earth's heliocentric velocity.

One of the most important functions of the target plane is to determine whether a collision is possible, and if not, how deep the encounter will be. With the B-plane, we obtain the minimum distance of the unperturbed asteroid orbit at its closest approach point with the Earth - the impact parameter b. That single variable however does not tell whether the asteroid's perturbed trajectory will intersect the image of the Earth on the following encounter, but the information can be extracted by scaling the Earth radius $R_\oplus$ according to the following relationship

$$b_\oplus = R_\oplus \sqrt{1 + \frac{v_e^2}{v_\infty^2}} \tag{4.44}$$

where v_e is the Earth escape velocity

$$v_e = \sqrt{\frac{2GM_\oplus}{R_\oplus}} \tag{4.45}$$

With this formulation a given trajectory impacts the Earth if $b < b_\oplus$, and would not otherwise. Alternatively, the impact parameter could be scaled while leaving the image of the Earth on the B-plane unchanged. The two scalings are equivalent for a single orbit, but when computing the coordinates for different asteroids with different $\vec{v}_\infty$, the scaling is not uniform [42].

A convenient and common target plane coordinate system (ξ, η, ζ) is obtained by aligning the negative ζ-axis with the projection of the Earth's heliocentric velocity $\vec{V}_\oplus$, the positive η-axis with the geocentric velocity (normal to the B-plane), and the positive ξ-axis in such a way that the reference frame is positively oriented, expressed by the following

$$\vec{\eta} = \frac{\vec{U}}{U} \tag{4.46}$$

$$\vec{\xi} = \frac{\vec{\eta} \times \vec{V}_\oplus}{|\vec{\eta} \times \vec{V}_\oplus|} \tag{4.47}$$

$$\vec{\zeta} = \vec{\xi} \times \vec{\eta} \tag{4.48}$$

where $\vec{U}$ and U are the geocentric velocity vector and magnitude of the asteroid, respectively. With this reference frame, it can be seen that $\vec{\xi}$ and $\vec{\zeta}$ are on the B-plane itself, where (ξ, ζ) are the target plane coordinates that indicate the cross track and along track miss distances, respectively. That way, ζ is the distance in which the asteroid is early or late for the minimum possible encounter distance. The early or late timing of the asteroid crossing the target plane $(\eta = 0)$ is given by

$$\Delta t = \frac{\zeta}{V_{\oplus} \sin \theta} \tag{4.49}$$

where θ is the angle between $\vec{v}_{\infty}$ and $\vec{V}_{\oplus}$. The ξ coordinate, on the B-plane, refers to the minimum distance achieved by altering the timing of the encounter between the asteroid and the Earth, known as the Minimum Orbital Intersection Distance (MOID). It is important to note that this particular interpretation of the coordinates of the B-plane is only valid as a linear approximation, and is considered unusable for planetary encounters beyond several lunar distances.

Such a formulation of the problem gives rise to the thought that an asteroid can avoid impact if either the timing of the encounter is off or by being in an orbit that does not even intersect the Earth's orbit. Therefore, to have an impact occur the asteroid must have a small enough MOID and be on time for the encounter. So, an encounter can be well-defined given only the MOID and the Δt. The manner in which the encounters are characterized in this paper are according to the analytic theory developed by Valsecchi et al. [42].

4.5   Keyhole Theory

Bodies that can potentially impact the planet, known as virtual impactors (VI), are normally found through numerical simulations, due to the fact that a physically realistic model of their motion is rather complex and difficult to duplicate. Exploring the problem of virtual impactors through analytic methodologies can lend knowledge to the approximate location and states of those that could exist [42]. To begin the discussion, the simple case of a VI whose impact takes place on a resonant return orbit is considered.

A resonant return orbit is a consequence of an encounter with Earth, such that the asteroid

is perturbed into an orbit of period $P' \approx k/h$ years, with h and k integers. After h revolutions of the asteroid and k revolutions of the Earth, both bodies are in the same region of the first encounter, causing a second encounter between the asteroid and the Earth.

The analytic theory of resonant returns that has been developed by Valsecchi et al.[42] treats close encounters with an extension of Opik's theory, adding a Keplerian heliocentric propagation between the encounters. The heliocentric propagation establishes a link between the outcome of the first encounter and the initial conditions of the next one. During the Earth encounter, the motion of the asteroid is assumed to take place on one of the asymptotes of the encounter hyperbola. The asymptote is directed along the unperturbed geocentric encounter velocity $\vec{v}_\infty$, crosses the B-plane at a right angle, and the vector from the Earth to the intersection point is denoted by $\vec{b}$ [39].

According to Opik's theory, the encounter of the asteroid with the Earth consists of the instantaneous transition, when the body reaches the B-plane, from the pre-encounter velocity vector $\vec{v}_\infty$ to the post-encounter velocity vector $\vec{v}'_\infty$, such that $v'_\infty = v_\infty$. And, the angles θ' and ϕ' are simple functions of v_∞, θ, ϕ, ξ, and ζ, where θ is the angle between $\vec{v}_\infty$ and the Earth's heliocentric velocity $\vec{V}_\oplus$ and ϕ is the angle between the plane containing $\vec{v}_\infty$ and $\vec{V}_\oplus$ and the plane containing $\vec{V}_\oplus$ and the ecliptic pole. The deflection angle γ is the angle between $\vec{v}_\infty$ and $\vec{v}'_\infty$, described by

$$\tan \frac{\gamma}{2} = \frac{c}{b} \tag{4.50}$$

where $c = GM_\oplus / v_\infty^2$. In addition, simple expressions relate (a, e, i) to (v_∞, θ, ϕ), and (ω, Ω, ν) to (ξ, ζ, t_0), where t_0 is the time at which the asteroid passes the node closer to the encounter [42, 39].

A resonance orbit corresponds to certain values of a' and θ', that can be denoted by a'_0 and θ'_0. If the post-encounter is constrained in such a way that the ratio of periods between the Earth and the asteroid is k/h, then we have

$$a'_0 = \left(\frac{k}{h}\right)^{2/3} \tag{4.51}$$

$$\cos \theta'_0 = \frac{1 - U^2 - 1/a'_0}{2U} \tag{4.52}$$

$$= \cos \theta \frac{b^2 - c^2}{b^2 + c^2} + \sin \theta \frac{2c\zeta}{b^2 + c^2} \tag{4.53}$$

Thus, for a given U, θ, and θ_0' in the pre-keyhole B-plane, the locus of points leading to a given resonant return can be found, using the following expression

$$\cos\theta_0' = \cos\theta\cos\gamma + \sin\theta\sin\gamma\cos\psi \tag{4.54}$$

If we solve for $\cos\psi$ and use $\zeta = b\cos\psi$ we get

$$\zeta = \frac{(b^2 + c^2)\cos\theta_0' - (b^2 - c^2)\cos\theta}{2c\sin\theta} \tag{4.55}$$

Replacing b^2 with $\xi^2 + \zeta^2$ and rearranging we obtain

$$\xi^2 + \zeta^2 - \frac{2c\sin\theta}{\cos\theta_0' - \cos\theta}\zeta + \frac{c^2(\cos\theta_0' + \cos\theta)}{\cos\theta_0' - \cos\theta} = 0 \tag{4.56}$$

Equation (4.56) is that of a circle centered on the ξ-axis. If we say that R is the radius of the circle and D is the value of the ξ-coordinate of its center, then Eq. (4.56) becomes

$$\xi^2 + \zeta^2 - 2D\zeta + D^2 = R^2 \tag{4.57}$$

Thus, the circle is centered at $(0, D)$ with

$$D = \frac{c\sin\theta}{\cos\theta_0' - \cos\theta} \tag{4.58}$$

and has a radius

$$R = \left|\frac{c\sin\theta_0'}{\cos\theta_0' - \cos\theta}\right|. \tag{4.59}$$

The circle intersects the ζ-axis at the values

$$\zeta = D \pm R = \frac{c(\sin\theta \pm \sin\theta_0')}{\cos\theta_0' - \cos\theta} \tag{4.60}$$

which represents the extreme values that b can take for a given a'. The circle intersects the ξ-axis at

$$\xi = \pm c\sqrt{\frac{\cos\theta + \cos\theta_0'}{\cos\theta - \cos\theta_0'}}, \tag{4.61}$$

and the maximum value of $|\xi|$ for which a given θ_0' is accessible is R. The maximum value of a' accessible for a given U is for $\theta_0' = 0$, and is obtained for a value of ζ expressed as

$$\zeta = \frac{c\sin\theta}{1 - \cos\theta} \tag{4.62}$$

and the minimum value of a' is for $\theta'_0 = \pi$, and is obtained for a value of ζ expressed as the negative of Eq. 4.62

$$\zeta = -\frac{c\sin\theta}{1 + \cos\theta} \tag{4.63}$$

In both cases we must have $\xi = 0$, meaning that this occurs for zero local MOID.

Asteroids that are viewed as potentially Earth hazardous bodies tend to have more than one encounter with the planet and can be used for resonance analyses. An asteroid that has an encounter with the planet has the possibility to be sent into a resonance orbit that would result in the body coming back to have another encounter with the planet in the future. Taking asteroid 1999 AN10 as an example, a resonance analysis can be conducted to see the location and size of the resonance circles, described above, for the body on the initial encounter's B-plane.

Table 4.2   Resonance circles size and location using analytic theory for asteroid 1999 AN10.

Asteroid Orbits	Earth Orbits	Circle Radius (Earth Radii)	Circle Center (Earth Radii)
7	4	43.3796	-43.4043
9	5	16.5996	16.5752
11	6	8.8116	8.7875
12	7	11.7312	-11.7562
16	9	42.1116	42.0871
17	10	9.0265	-9.0517
19	11	16.0366	-16.0616
20	11	11.1728	11.1485

Table 4.2 shows a variety of resonance orbits between the 1999 AN10 and Earth, along with the location and size of the resonance circles. Just looking at these numbers doesn't really give a good idea as to what they represent. Looking at the resonance circles on the B-plane of asteroid 1999 AN10 with Earth will give a better depiction of their meaning and reveal a few subtle details about potential keyhole locations.

Figure 4.7 gives a few of the resonance circle sizes and locations of asteroid 1999 AN10 on the B-plane of its August 2027 encounter with Earth.   The small green circle at the origin of the figure is the depiction of the Earth on the target plane. The purple, red, and
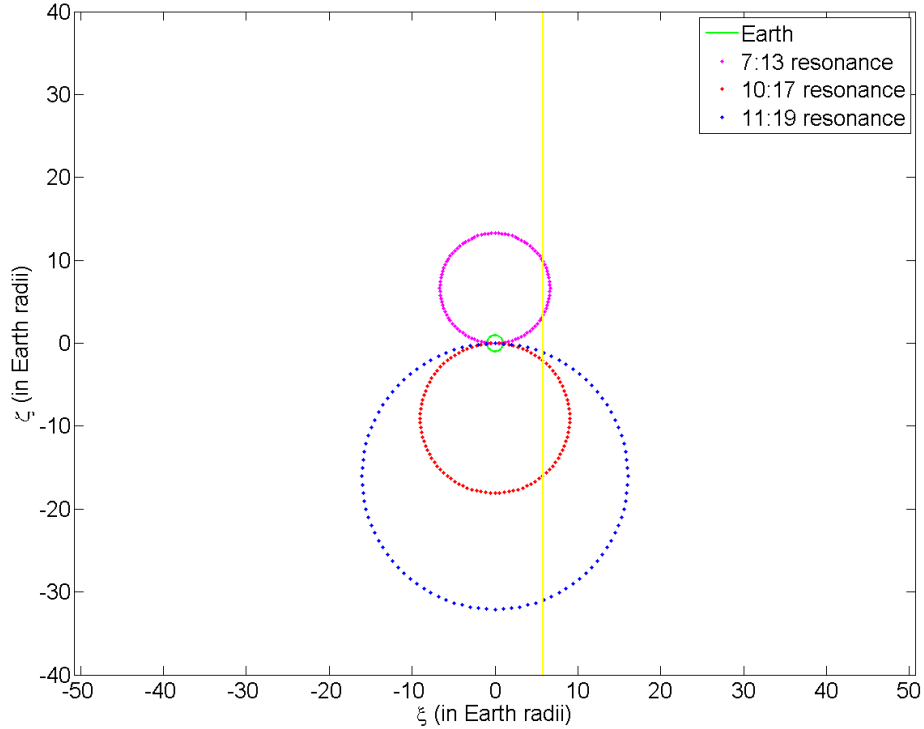
Figure 4.7 Depiction of the size and location of the potential resonance circles of 1999 AN10.

blue circles are the 7:13, 10:17, and 11:19 resonance circles for asteroid 1999 AN10. Finally, the yellow vertical line represents the local minimum orbital intersection distance (MOID) for the asteroid, about 5.8 Earth radii for this particular encounter. The intersection between the MOID and the resonance circles is a location for potential keyholes that could result future Earth impacts. Depending on the asteroid's arrival conditions, the asteroid could be put into one of those resonance orbits. It is important to note that if the resonance circle does not extend out far enough to intersect the MOID, then the potential of the asteroid entering into such a resonance orbit upon encounter can be neglected.

The term 'keyhole' is used to indicate small regions of the B-plane of a specific close encounter so that if the asteroid passes through one of those regions, it will hit the Earth on the next return. An impact keyhole is one of the possible pre-images of the Earth's cross section on the B-plane tied to the specific value for the post-encounter semi-major axis that allows the subsequent encounter at the given date [39].

To obtain the size and shape of an impact keyhole we can model the secular variation of the MOID as a linear term affecting ξ'' (the value of ξ at the next encounter)

$$\xi'' = \xi' + \frac{d\xi}{dt}(t_0'' - t_0'), \tag{4.64}$$

where t_0' and t_0'' are the times of passage at the node, on the post-first-encounter orbit that are closest to the first and second encounter, respectively. The time derivative of ξ can be calculated either by a secular theory for crossing orbits or by deduction from a numerical integration scheme. To compute the size and shape of the size and shape of the impact keyhole we start from the image of the Earth on the B-plane of the second encounter, and we denote the coordinates axes in this plane as ξ'', ζ''. The circle is centered on the origin and has a radius $b_\oplus$. The points on the target plane of the first encounter that are mapped to the points of the Earth image circle on the second encounter B-plane constitute the Earth pre-image that we are looking for [42].

To answer the question of the size and shape of the impact keyhole, we must examine the submatrix of partial derivatives $\partial(\xi'', \zeta'')/\partial(\xi, \zeta)$. Finding the structure of this submatrix requires the understanding of the evolution from before the first encounter to before the second encounter, depicted by

$$\frac{\partial(U'', \theta'', \phi'', \xi'', \zeta'', t_0'')}{\partial(U, \theta, \phi, \xi, \zeta, t_0)} = \frac{\partial(U'', \theta'', \phi'', \xi'', \zeta'', t_0'')}{\partial(U', \theta', \phi', \xi', \zeta', t_0')} \cdot \frac{\partial(U', \theta', \phi', \xi', \zeta', t_0')}{\partial(U, \theta, \phi, \xi, \zeta, t_0)} \tag{4.65}$$

where the second encounter derivatives matrix is regarded as a function of the pre-first-encounter variables $(U, \theta, \phi, \xi, \zeta, t_0)$. The first derivatives matrix, with the post-first-encounter variables related to the pre-first-encounter variables, shows the relationship obtained from the asteroid's first encounter with the Earth, depicted by

$$\frac{\partial(U', \theta', \phi', \xi', \zeta', t_0')}{\partial(U, \theta, \phi, \xi, \zeta, t_0)} = \begin{bmatrix} 1 & 0 & 0 & 0 & 0 & 0 \\ \frac{\partial\theta'}{\partial U} & \frac{\partial\theta'}{\partial\theta} & 0 & \frac{\partial\theta'}{\partial\xi} & \frac{\partial\theta'}{\partial\zeta} & 0 \\ \frac{\partial\phi'}{\partial U} & \frac{\partial\phi'}{\partial\theta} & \frac{\partial\phi'}{\partial\phi} & \frac{\partial\phi'}{\partial\xi} & \frac{\partial\phi'}{\partial\zeta} & 0 \\ \frac{\partial\xi'}{\partial U} & \frac{\partial\xi'}{\partial\theta} & \frac{\partial\xi'}{\partial\phi} & \frac{\partial\xi'}{\partial\xi} & \frac{\partial\xi'}{\partial\zeta} & 0 \\ \frac{\partial\zeta'}{\partial U} & \frac{\partial\zeta'}{\partial\theta} & \frac{\partial\zeta'}{\partial\phi} & \frac{\partial\zeta'}{\partial\xi} & \frac{\partial\zeta'}{\partial\zeta} & 0 \\ \frac{\partial t_0'}{\partial U} & \frac{\partial t_0'}{\partial\theta} & \frac{\partial t_0'}{\partial\phi} & \frac{\partial t_0'}{\partial\xi} & \frac{\partial t_0'}{\partial\zeta} & 1 \end{bmatrix} \tag{4.66}$$

and, for the second derivatives matrix, with the pre-second-encounter variables related to the post-first-encounter variables, calculated from a purely Keplerian heliocentric propagation between encounters,

$$\frac{\partial(U'', \theta'', \phi'', \xi'', \zeta'', t_0'')}{\partial(U', \theta', \phi', \xi', \zeta', t_0')} = \begin{bmatrix} 1 & 0 & 0 & 0 & 0 & 0 \\ 0 & 1 & 0 & 0 & 0 & 0 \\ 0 & 0 & 1 & 0 & 0 & 0 \\ 0 & 0 & 0 & 1 & 0 & 0 \\ \frac{\partial \zeta''}{\partial U'} & \frac{\partial \zeta''}{\partial \theta'} & \frac{\partial \zeta''}{\partial \phi'} & \frac{\partial \zeta''}{\partial \xi'} & \frac{\partial \zeta''}{\partial \zeta'} & 0 \\ \frac{\partial t_0''}{\partial U'} & \frac{\partial t_0''}{\partial \theta'} & \frac{\partial t_0''}{\partial \phi'} & \frac{\partial t_0''}{\partial \xi'} & \frac{\partial t_0''}{\partial \zeta'} & 1 \end{bmatrix} \tag{4.67}$$

so the composite matrix relating the pre-second-encounter variables to the pre-first-encounter variables has the following structure

$$\frac{\partial(U'', \theta'', \phi'', \xi'', \zeta'', t_0'')}{\partial(U, \theta, \phi, \xi, \zeta, t_0)} = \begin{bmatrix} 1 & 0 & 0 & 0 & 0 & 0 \\ \frac{\partial \theta'}{\partial U} & \frac{\partial \theta'}{\partial \theta} & 0 & \frac{\partial \theta'}{\partial \xi} & \frac{\partial \theta'}{\partial \zeta} & 0 \\ \frac{\partial \phi'}{\partial U} & \frac{\partial \phi'}{\partial \theta} & \frac{\partial \phi'}{\partial \phi} & \frac{\partial \phi'}{\partial \xi} & \frac{\partial \phi'}{\partial \zeta} & 0 \\ \frac{\partial \xi'}{\partial U} & \frac{\partial \xi'}{\partial \theta} & \frac{\partial \xi'}{\partial \phi} & \frac{\partial \xi'}{\partial \xi} & \frac{\partial \xi'}{\partial \zeta} & 0 \\ \frac{\partial \zeta''}{\partial U} & \frac{\partial \zeta''}{\partial \theta} & \frac{\partial \zeta''}{\partial \phi} & \frac{\partial \zeta''}{\partial \xi} & \frac{\partial \zeta''}{\partial \zeta} & 0 \\ \frac{\partial t_0''}{\partial U} & \frac{\partial t_0''}{\partial \theta} & \frac{\partial t_0''}{\partial \phi} & \frac{\partial t_0''}{\partial \xi} & \frac{\partial t_0''}{\partial \zeta} & 1 \end{bmatrix}. \tag{4.68}$$

As previously mentioned, the submatrix of particular interest is that of $\partial(\xi'', \zeta'')/\partial(\xi, \zeta)$, which gives the derivatives of the second encounter B-plane coordinates with respect to the first encounter B-plane coordinates. It is important to note that the Keplerian propagation between encounters does not effect the MOID ($\xi'' = \xi'$), so the first row of the matrix is

$$\frac{\partial \xi''}{\partial \xi} = \frac{\partial \xi'}{\partial \xi} \tag{4.69}$$

$$\frac{\partial \xi''}{\partial \zeta} = \frac{\partial \xi'}{\partial \zeta} \tag{4.70}$$

showing that the ξ dimension of the Earth's pre-image is essentially unchanged. The Keplerian propagation affects ζ only through a', given that U is invariant in this type of motion. Therefore, the second row of the submatrix has the following structure

$$\frac{\partial \zeta''}{\partial \xi} = \frac{\partial \zeta''}{\partial \theta'}\frac{\partial \theta'}{\partial \xi} + \frac{\partial \zeta'}{\partial \xi} \tag{4.71}$$

$$\frac{\partial \zeta''}{\partial \zeta} = \frac{\partial \zeta''}{\partial \theta'}\frac{\partial \theta'}{\partial \zeta} + \frac{\partial \zeta'}{\partial \zeta} \tag{4.72}$$

Now, what we want is the pre-image of the point $(\xi'', \zeta'' = 0)$ on the second-encounter B-plane that takes place h revolutions after the first-encounter. To begin, we find the images of two points, with coordinates (ξ_1, ζ_1) and (ξ_2, ζ_2) on the first-encounter B-plane, on the second-encounter B-plane (ξ_1'', ζ_1'') and (ξ_2'', ζ_2''). We choose ξ_1 and ξ_2 such that $\xi_1 = \xi_2$ - note that generally ξ_1'' will be slightly different than ξ_2'', by a very small amount, since ξ'' is a slowly varying function of ζ. Next, we check if $\zeta_1''\zeta_2'' < 0$. If the product of the two second-encounter terms is not negative, we choose another pair of values for ζ_1 and ζ_2 until the condition is satisfied. Now, we find the pre-image of a point ζ such that $\zeta'' = 0$ by using regula falsi iterations, or a similar method, we can call the coordinates of that point (ξ_0, ζ_0) and the coordinates of that point's image $(\xi_0'', 0)$. The basis for this procedure is that while the distance along the ξ-axis on the B-plane remains essentially the same between the encounters, the distance along the ζ-axis is stretched by a large factor that is mostly a consequence of the Keplerian propagation between encounters. The pre-image of the Earth on the first-encounter B-plane, preceeding the collision, will look like a thickened arclet. The small size of the impact keyholes is attributed to the non-area-preservation nature of the Keplerian propagation [42].

Look to Appendix A for a more detailed, analytic discussion of the computational details regarding how the pre-encounter orbit is mapped to the current target B-plane and then mapped to the next encounter B-plane [42].

4.6 Application to 2012 DA14

In order to test this analysis, an asteroid is selected to be analyzed - 2012 DA14. Asteroid 2012 DA14 is a well-known asteroid because of its surprisingly close encounter with Earth occurred on February 15, 2013 [31].

The orbital elements before the encounter in February of 2013 are given in Table 4.3. From the pre-encounter orbital elements, the post-encounter orbital element distributions can be

Table 4.3   Orbital elements of asteroid 2012 DA14 for its pre-encounter trajectory.

	Pre-Encounter
a	1.00502 AU
e	0.10867
i	$10.338°$
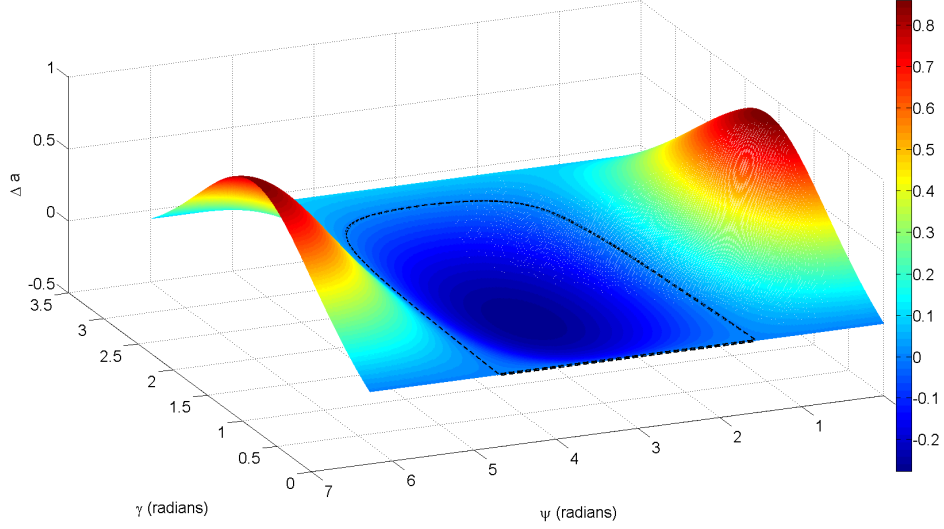
Figure 4.8   Surface plot of variation of semi-major axis for asteroid 2012 DA14.

found and shows how the approach and post-encounter geometries relate to each other in the context of an Earth-threatening asteroid.

Given that $|\mathbf{U}|$ is constant, the variation in the semi-major axis Δa depends only on the parameters θ and θ' as

$$\Delta a = \frac{a' - a}{a} = \frac{1 - U^2 - 2U\cos\theta}{1 - U^2 - 2U\cos\theta'} - 1 \tag{4.73}$$

Figure 4.8 shows the variation in the semi-major axis a. The colors on the mesh depict the value of the variation, and the black dotted line depicts the line of zero variation in semi-major axis for 2012 DA14 from its Earth encounter. From the figure, it can be seen that the asteroid is susceptible to having its semi-major axis increased or decreased, depending on the values of γ and ψ. Preliminary observations show that values of ψ between about $\pi/2$ and $3\pi/2$ will cause 2012 DA14 to have a smaller post-encounter semi-major axis than its pre-encounter
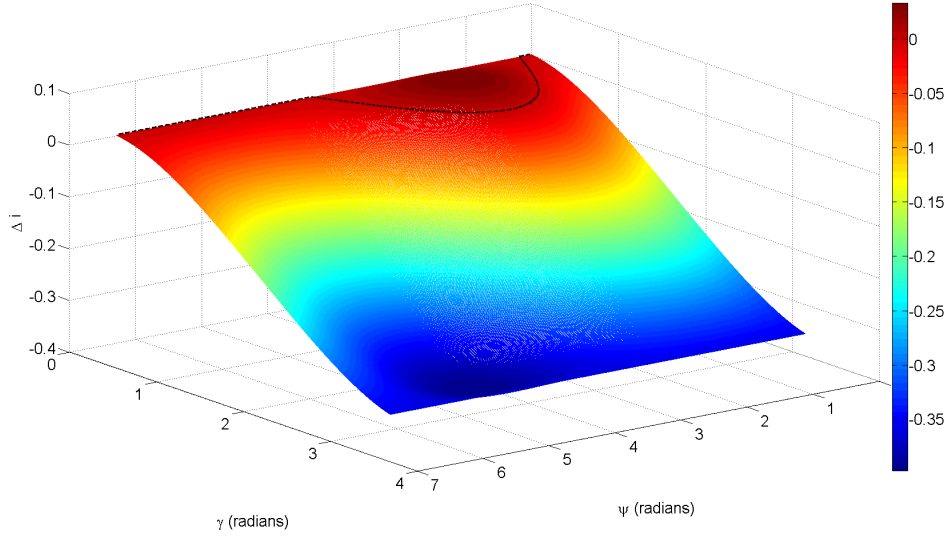
Figure 4.9   Surface plot of variation of inclination for asteroid 2012 DA14.

value, while a value of ψ outside that region will result in a larger semi-major axis after the Earth encounter.

The tangent of inclination is defined as

$$\tan i = \frac{\cos\phi\sin\theta}{1/U + \cos\theta} = \frac{U_z}{1 + U_y} \tag{4.74}$$

and after the rotation of the relative velocity vector by the deflection angle γ in the direction of ψ, it becomes

$$\tan i' = \frac{\cos\phi\sin\theta\cos\gamma - \cos\phi\cos\theta\sin\gamma\cos\psi + \sin\phi\sin\gamma\sin\psi}{1/U + \cos\theta\cos\gamma + \sin\theta\sin\gamma\cos\psi} \tag{4.75}$$

The variation in inclination can be described by $\Delta i = \tan i' - \tan i$ [37].   Figure 4.9 depicts the variation of the inclination of the orbits of asteroid 2012 DA14. The black dotted line on the meshed grid shows the line of zero variation of the inclination after the encounter with the Earth. The plot of the post-encounter inclination variation shows that the assumed inclination of the asteroid after the encounter will mostlikely decrease - the question being by how much. There is a small region of the surface that would result in a small increase in inclination, very small deflection angles and values of ψ around $\pi/2$.

Recalling that

$$e^2 = U^4 + 4U_y^2 + U_x^2(1 - U^2 - 2U_y) + 4U^2U_y \tag{4.76}$$
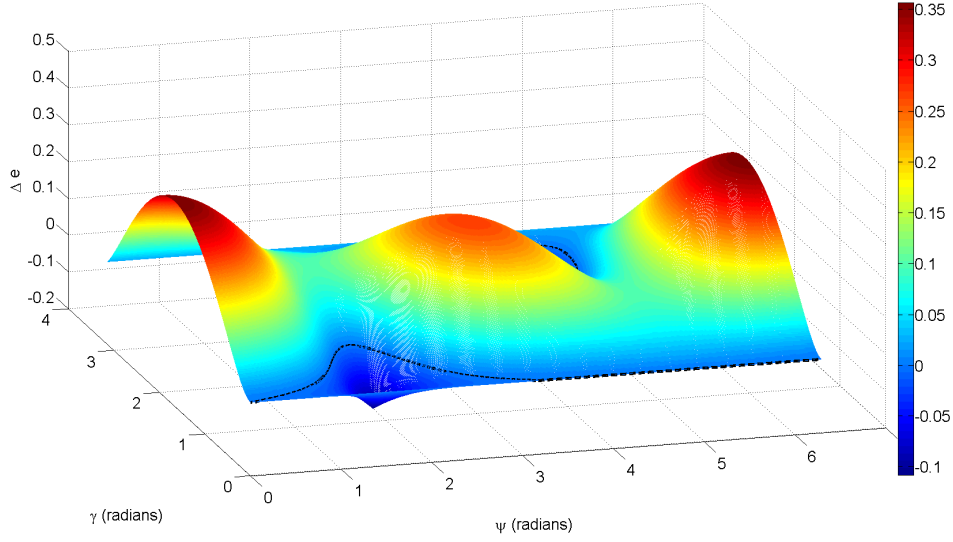
Figure 4.10   Surface plot of variation of eccentricity for asteroid 2012 DA14.

the expression for the pre-encounter eccentricity of the asteroid orbit can be expressed in terms of the relative velocity magnitude and its components. Making a substitution for the corresponding post-encounter terms, the value of the eccentricity after the encounter with the target planet can be calculated as

$$e = \sqrt{U'^4 + 4U_y'^2 + U_x'^2(1 - U'^2 - 2U_y') + 4U'^2U_y'} \tag{4.77}$$

Taking the difference between the post- and pre-encounter eccentricities shows the variation in the orbital eccentricity ($\Delta e = e' - e$) based on the planetary encounter.   Figure 4.10 depicts the variation of the eccentricity of asteroid 2012 DA14. The black dotted lines shown in the figure indicate the level of zero variation between the pre- and post-encounter eccentricities of the asteroid. The plot of eccentricity variation has a bit more complicated structure for this asteroid than semi-major axis or inclination, and shows the opposite outcome than the inclination variation - showing a post-encounter eccentricity greater than the pre-encounter value. Asteroid 2012 DA14 would have more eccentric post-encounter orbits for values of ψ that approach the ends of the feasible domain $[0, 2\pi]$ and values near π. Values of ψ near $\pi/2$ and $3\pi/2$ seem to have a negative effect on the orbital eccentricities of the body, especially with small or large turning angles.

Before finding the potential orbital resonances that exist for 2012 DA14 after its encounter with Earth, it would be helpful to first see what the resulting post-encounter orbital parameters are for the asteroid. Using the encounter analysis described in the Post-Encounter Orbital

Table 4.4 Orbital elements of asteroid 2012 DA14 for its post-encounter trajectory.

Orbital Element	Value
a	0.9108 AU
e	0.0888
i	11.75°

Trajectory section, the orbital elements of the post-encounter heliocentric orbit are calculated, as shown in Table 4.4. It can be seen based on the resulting orbital elements that the inclination of the asteroid is predicted to increase and both the eccentricity and semi-major axis would decrease. These results seem to agree with the variations shown in Figures 4.8, 4.9, and 4.10.

Now that we know the expected post-encounter semi-major axis of 2012 DA14, the potential orbital resonances can be searched through to find any that the asteroid could fall into. Using a small two percent error tolerance for the orbital ratio (k/h), 2012 DA14 doesn't fall into an orbital resonance that would come back to impact the Earth in the next 10 years. There are orbital resonances that have similar semi-major axes however, as shown in Table 4.5. Despite

Table 4.5 Potential orbital resonances for asteroid 2012 DA14.

Earth orbits	Asteroid orbits	a' lower bound (AU)	a' upperbound (AU)
6	7	0.9013	0.9035
7	8	0.9138	0.9161
8	9	0.9241	0.9252

the fact that the estimated post-encounter semi-major axis is close to these orbital resonance regions, it will be shown later on why there are no keyholes on the February 2013 B-plane of 2012 DA14.

Using the conditions, with respect to the Earth, at sphere of influence entrance as the initial conditions for the orbital simulations, a field of virtual asteroids is created by putting

some small error ($\sigma = 1000$ km, 0.1 km/s in each direction) onto those intial conditions. The distribution of the virtual asteroids orbital elements are shown in Figure 4.11. Propagating
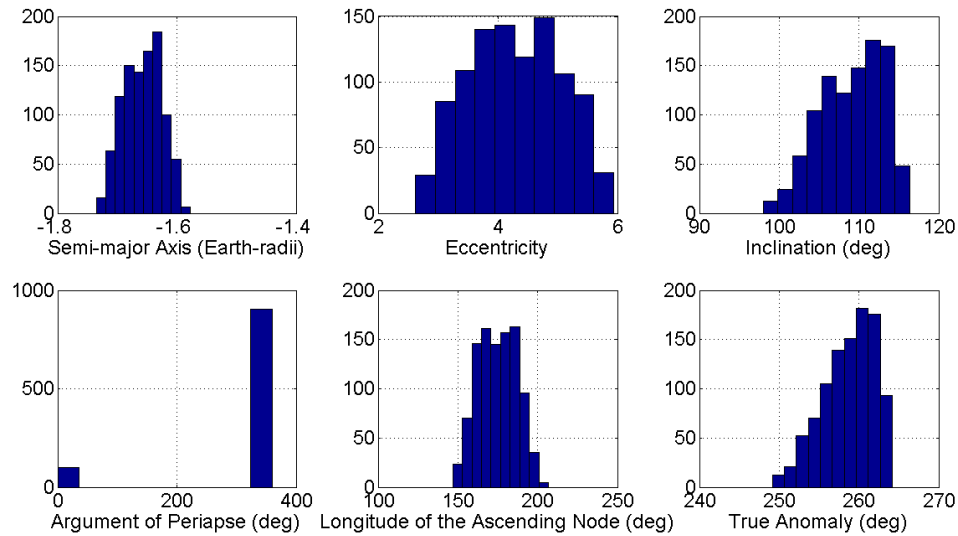
Figure 4.11   Orbital element initial condition distribution.

that set of initial conditions through the original asteroid's B-plane gives a region where 2012 DA14 can be expected to cross.

The distribution of the crossing locations of the virtual asteroids, on the original asteroid's B-plane, can tell a lot about the possibility of the asteroid impacting the planet on that pass or in the future by passing through a keyhole on that B-plane. If the resonances given in Table 4.5 are mapped against the crossing points of the virtual asteroids on the target B-plane, such as in Figure 4.12, an understanding can be gained about the likelihood of an Earth impact and potential keyhole crossings on this encounter.   The green circle centered on the origin of the plot represents the projection of the Earth on the asteroid's B-plane. The purple, red, and blue circles represent 7:6, 8:7, 9:8 orbital resonances, respectively, for 2012 DA14 with Earth. The vertical yellow line on the B-plane represents the anticipated ξ location of the Earth in the next encounter on the current encounter B-plane, based on analytic keyhole theory. The distribution of cyan and black stars on the figure show the crossing points of the simulated virtual asteroids on the B-plane obtained via numerical integration and state transition matrix propagation, giving a sense of consistency for the gathered results. As mentioned previously,
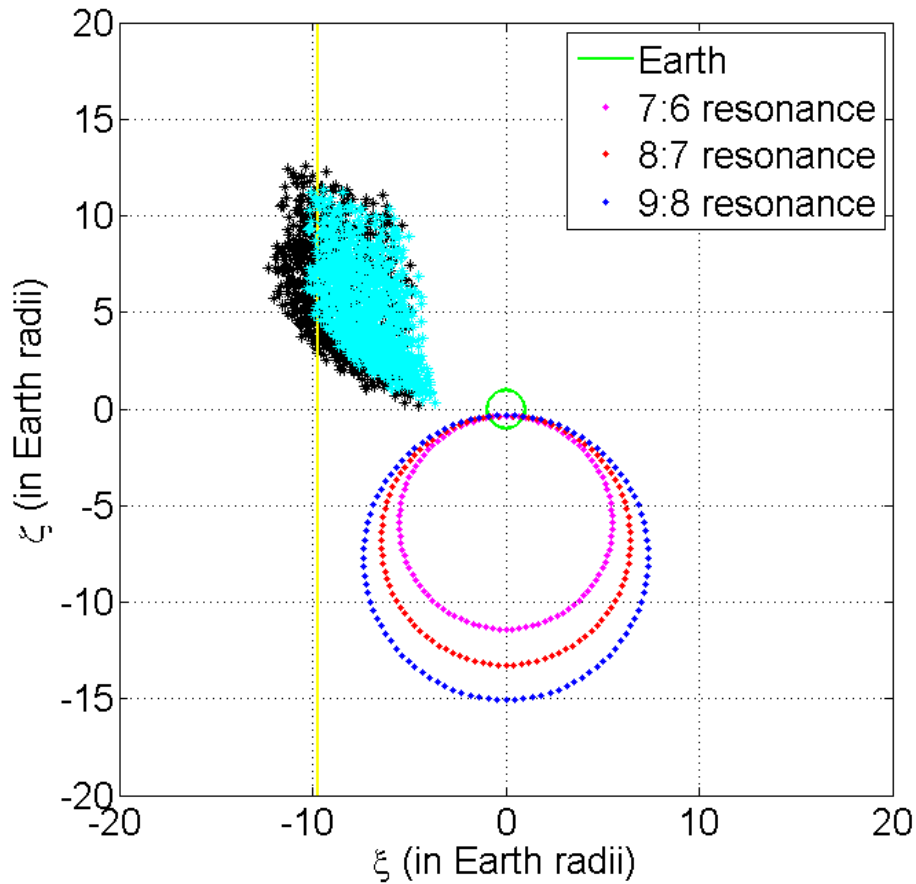
Figure 4.12   Encounter B-plane for February 2013 encounter of 2012 DA14 with Earth.

the shown resonance circles do not intersect the yellow line at any point, implying that no keyhole exists on this plane for those particular orbital resonances. Given no resonance circle intersections, focus can be drawn to the potential of an Earth impact on this encounter, rather than the possibility of a keyhole passage. In either case, a potential Earth impact or keyhole passage, an assessment of those events occurring must be developed in order to quantize the current and future threats.

CHAPTER 5. RISK ASSESSMENT

5.1 Introduction

As a follow-up to the question of how to predict the future trajectory of a body in space over a long period of time, it is logical to ask what the likelihood of bodies in space impacting each other. In the previous chapter, a discussion of analytic keyhole theory was presented as a means of identifying the possibility of a NEO impact with Earth within a given time-period. The probability of objects colliding in space, or conjunction probability, can be simplified when considered over short-term encounters. Most conjunction probability theory is concerned with the likelihood of spacecraft, satellite, or asteroid collisions with each other. Within the context of this work, the events of interest are the potential collision between an asteroid or asteroid fragments with a planet (in particular, Earth), and the likelihood of an asteroid/fragment passing through a gravitational keyhole.

5.2 Orbital Conjunction Analyses

Early formulations of spacecraft collision were based on the Poisson distribution and used concepts from kinetic theory of gases where the molecules move linearly and their numerical density is statistically uniform. More current formulations, being more realistic, are based on positional Gaussian distributions, and uses the concept of covariance matrices which can be obtained from orbit determination of the encountering bodies. In general terms, there are four main models used for conjunction probability analysis, developed by Foster [43], Chan [44], Patera [45], and Alfano [46]. In this section, a brief discussion of previous methodologies used for calculating conjunction probabilities.

5.2.1 Early Orbital Collision Model

5.2.1.1 Kessler's Collision Probability Between Orbiting Bodies

The equations derived by Kessler [47, 48] relate orbital parameters to the probability of collision between orbiting objects. The situation that is created is analogous to the kinetic models of a gas

$$F = SV \tag{5.1}$$

where F is the number of impacts per unit cross-sectional area per unit time, S is the spatial density, or the number of objects found within a unit volume, and V is the velocity of the objects relative to the detection area. The average number of collisions (N) on an object of cross-sectional area σ in time t would be given by

$$N = F\sigma t \tag{5.2}$$

The cross-sectional area between two randomly oriented objects of average radii r_1 and r_2 and masses m_1 and m_2 respectively, is represented by

$$\sigma = \pi \left(r_1 + r_2\right)^2 \left(1 + V_e^2/V^2\right) \tag{5.3}$$

where the escape velocity given by

$$V_e = \left[2\left(m_1 + m_2\right)G/\left(r_1 + r_2\right)\right]^{1/2} \tag{5.4}$$

and G is the universal gravitational constant. In general, the value of S for a single object is found from

$$S = \Delta t/T\Delta U \tag{5.5}$$

where Δt is the time spent in the volume element ΔU over time T.

The distribution of Ω and ω for sporadic meteors, asteroids, comets, or artificial satellites around the Earth are nearly random, and the base assumption made is that all values of the two parameters are equally probable. With this assumption, the spatial density around a central body will not vary with longitude, and will only be a function of the distance from the body and the latitude. It is assumed that the latitude dependence is a function of the inclination of

the encountering body's orbit, and the distance dependence is assumed to be a function of the periapse and apoapse distances. So, it can be written that

$$S(R, \beta) = f(\beta) \cdot s(R) \tag{5.6}$$

where $s(R)$ is the spatial density at a distance R from the central body averaged over all latitudes, and $f(\beta)$ is the ratio of the spatial density at latitude β to the spatial density average over all latitudes.

For the radial dependence, it is assumed that there exists a spherical shell of radius R and thickness ΔR, between the periapse q and the apoapse q' distances of an orbit. So, the volume of the shell is

$$\Delta U = 4\pi R^2 \Delta R \tag{5.7}$$

For each revolution of an object in the orbit, the object passes through the shell twice. The time in the shell for one orbital period is

$$\Delta t = 2\Delta R / V_r \tag{5.8}$$

where V_r is the radial velocity component of the object velocity vector relative to the central body. The orbital period is given by $T = 2\pi \left(a^3 / \mu \right)^{1/2}$. The velocity of an orbiting object relative to its central body is

$$V_c = \mu^{1/2} \left(2/R - 1/a \right)^{1/2} \tag{5.9}$$

where μ is the gravitational parameter of the central body and a is the semi-major axis length of the orbiting body. The radial velocity can be found from

$$V_r = V_c \sin \gamma \tag{5.10}$$

where γ is the angle between the object velocity vector and the tangent of the spherical shell. Conservation of angular momentum requires that

$$\cos^2 \gamma = \frac{qq'}{R(2a - R)} \tag{5.11}$$

Thus, the radial velocity is

$$V_r = \left[\mu \left(\frac{2}{R} - \frac{1}{a} \right) \left(1 - \frac{qq'}{R(2a - R)} \right) \right]^{1/2} \tag{5.12}$$

The spatial density averaged over all latitudes at a distance R from the central body can now be expressed as

$$s(R) = \frac{1}{4\pi^2 Ra\left[(R-q)\left(q'-R\right)\right]^{1/2}} \tag{5.13}$$

where $q < R < q'$, and when $R < q$ or $R > q'$ then $s(R) = 0$.

The latitude dependence of the spatial density is assumed to be due entirely to the inclination (i) of the orbit and the secular change in the argument of periapse. The spatial density averaged over all the latitudes is simply one divided by the volume of the spherical shell

$$s'(R_1) = \frac{1}{4\pi R_1^2 \Delta R} \tag{5.14}$$

The spatial density between latitudes β and $\beta + \Delta\beta$ is given by Equation 5.5, where the value of Δt is now the time the object spends between those two latitudes during one revolution of the argument of periapse, T is the time for the argument of periapse to make one revolution, and ΔU is the volume between the given latitudes. If the argument of periapse is moving at an angular velocity $\dot\theta$, then

$$\Delta t_1 = 2\Delta\beta/\dot\theta \sin\alpha \tag{5.15}$$

where α is the angle between the path of the encountering body and the line of constant latitude. From geometry, $T_1 = 2\pi/\dot\theta$ and

$$\Delta U_1 = 2\pi R_1^2 \cos\beta \Delta\beta \Delta R \tag{5.16}$$

so

$$S'(R_1, \beta) = \frac{\Delta t_1}{T_1 \Delta U_1} = \frac{1}{2\pi^2 R_1^2 \sin\alpha \cos\beta \Delta R} \tag{5.17}$$

where $0 < \beta < i$. $S'(R_1, \beta)$ is the spatial density at R_1 and β, given a unit probability that the object is between R_1 and $R_1 + \Delta R$. By definition,

$$f(\beta) = 2/\pi \sin\alpha \cos\beta \tag{5.18}$$

where the value of α is found from spherical geometry

$$\cos\alpha = \cos i/\cos\beta \tag{5.19}$$

The spatial density at any particular distance and latitude is dependent on the size and orientation of the orbit, expressed as

$$S(R, \beta) = \frac{1}{2\pi^2 Ra \left[\left(\sin^2 i - \sin^2 \beta\right)(R - q)(q' - R)\right]^{1/2}} \qquad (5.20)$$

where $q < R < q'$ and $0 < \beta < i$.

So, assume a spacecraft is located for a time t at a distance R from the central body at a latitude β, and assume that an orbiting object has orbital parameters q, q', i, an equally probable longitude of the node and argument of periapse, and velocity V relative to the spacecraft. Then, the probability of a collision between the spacecraft and the orbiting object is

$$N = \frac{V\sigma t}{2\pi^3 Ra \left[\left(\sin^2 i - \sin^2 \beta\right)(R - q)(q' - R)\right]^{1/2}} \qquad (5.21)$$

5.2.2 Modern Orbital Collision Models

5.2.2.1 General Probability Computation

Space object collision probability analysis (COLA) is typically conducted by modeling the objects as spherical bodies, therefore eliminating the need to keep track of the attitude of the encountering bodies. The relative motion between the bodies is considered to be linear by assuming the effect of the relative acceleration is small compared to that of the velocity. The positional errors of the encountering bodies are assumed to be zero-mean, Gaussian, uncorrelated, and constant during the encounter. The assumption that the object covariance matrices are uncorrelated, allows for them to simply be summed to form one large, combined covariance ellipsoid centered on the primary object. It is also assumed that the relative velocity at the point of closest approach is sufficiently large to ensure a brief encounter time and static covariance. The region in which the encounter between the two objects will take place is defined when one object is within n standard deviations of the combined covariance ellipsoid. The value of n is user-defined, three-dimensional, and centered on the primary object of interest. If the secondary body passes through the ellipsoid, it creates a tube-shaped path that is referred to as a collision tube. The probability of collision is obtained by evaluating the integral of the three-dimensional probability density function (pdf) within the long circular collision

tube, and it can be shown that it is equivalent to evaluating the integral of a two-dimensional pdf within a circle on a plane perpendicular to the relative velocity at closest approach. The two-dimensional probability equation on that encounter plane in Cartesian space is

$$P = \frac{1}{2\pi\sigma_x\sigma_y} \int_{-OBJ}^{OBJ} \int_{-\sqrt{OBJ^2-x^2}}^{\sqrt{OBJ^2-x^2}} exp\left[-\frac{1}{2}\left[\left(\frac{x-x_m}{\sigma_x}\right)^2 + \left(\frac{y-y_m}{\sigma_y}\right)^2\right]\right] dydx \qquad (5.22)$$

where OBJ is the combined object radius, x lies along the minor axis, y lies along the major axis, x_m and y_m are the respective components of the projected miss distance, and σ_x and σ_y are the corresponding standard deviations. The four methods express Equation 5.22 numerically (Foster, Patera, Alfano) or by analytic approximation (Chan) [49].

5.2.2.2   Foster's Method

The Foster formulation of a collision probability model uses polar coordinates in the encounter (U-W) plane where R_0 and ϕ define the combined object center's location, OBJ is the combined object radius, σ_u and σ_w are standard deviations along the principal axes, and r and θ define the relative position of the segmented object.

$$P = \frac{1}{2\pi\sigma_u\sigma_w} \int_0^{OBJ} \left[\int_0^{2\pi} exp\left[-\frac{1}{2}\left[\left(\frac{R_0\sin\phi - r\sin\theta}{\sigma_u}\right)^2 + \left(\frac{R_0\cos\phi - r\cos\theta}{\sigma_w}\right)^2\right]\right] rd\theta\right] dr \qquad (5.23)$$

When numerically implemented, Foster measured angle ϕ from the W-axis, the angle θ step size is $0.5°$, and the radius r step size is $OBJ/12$. This model is used by NASA to assess on-orbit risk for the International Space Station and shuttle missions, and can also be found in The Aerospace Corporation's Collision Vision Tool [49].

5.2.2.3   Chan's Method

Chan developed an approximation to Equation 5.22 as an analytic series expression. The transformation takes the two-dimensional Gaussian pdf to a one-dimensional Rician pdf and uses the concept of equivalent areas. In the encounter plane, OBJ is the combined object radius centered at (x_m, y_m), with associated standard deviations of (σ_x, σ_y). The series expression is represented as

$$P = exp\left(-\frac{v}{2}\right) \sum_{m=0}^{\infty} \left[\frac{v^m}{2^m \cdot m!}\left(1 - exp\left(-\frac{u}{2}\right)\sum_{k=0}^{m} \frac{u^k}{2^k \cdot k!}\right)\right] \qquad (5.24)$$

$$u = \frac{OBJ^2}{\sigma_x \sigma_y} \tag{5.25}$$

$$v = \frac{x_m^2}{\sigma_x^2} + \frac{y_m^2}{\sigma_y^2} \tag{5.26}$$

This series formulation of the collision probability formula has the added benefit of being easily differentiated for other types of probability analysis, and is implemented in Analytical Graphics, Inc., Satellite Tool Kit [49].

5.2.2.4 Patera's Method

The equivalent model to Equation 5.22, developed by Patera, is set as a one-dimensional line integral where r is the distance to the hardbody perimeter and θ is the covariance-centric angular position measured from the x-axis. The probability density symmetrically enables the two-dimensional integral to be reduced to a one-dimensional path integral

$$P = -\frac{1}{2\pi} \oint_{ellipse} exp\left(-\alpha r^2\right) d\theta \tag{5.27}$$

if the miss distance exceeds the combined object radius, and

$$P = 1 - \frac{1}{2\pi} \oint_{ellipse} exp\left(-\alpha r^2\right) d\theta \tag{5.28}$$

if the combined object radius exceeds the miss distance. The computation of the α term and the numerical implementation of Patera's equation involves coordinate rotation, scaling, and trigonometric functions as explained in Patera's paper. This method is employed in The Aerospace Corporation's Collision Vision Tool and Satellite Orbit Analysis Program (SOAP), and is also used by various government and civil organizations [49].

5.2.2.5 Alfano's Method

Alfano developed a series expression to represent Equation 5.22 as a combination of error functions and exponential terms. In the encounter plane, the object's center is located (x_m, y_m) with associated standard deviations σ_x and σ_y and combined object radius OBJ, expressed as

$$P = \frac{2 \cdot OBJ}{\sqrt{8\pi}\sigma_x n} \sum_{i=0}^{n} \left[erf\left[\frac{y_m + \frac{2 \cdot OBJ}{n}\sqrt{(n-i) \cdot i}}{\sigma_y \sqrt{2}} \right] + erf\left[\frac{-y_m + \frac{2 \cdot OBJ}{n}\sqrt{(n-i) \cdot i}}{\sigma_y \sqrt{2}} \right] \right] \cdot exp\left[\frac{-\left[\frac{OBJ \cdot (2i-n)}{n} + x_m \right]^2}{2\sigma_x^2} \right] \tag{5.29}$$

The method breaks the series into m-even and m-odd components and makes use of Simpson's one-third rule. An expression that can be used to determine a sufficiently small number of terms is given by

$$m = int \left(\frac{5 \cdot OBJ}{min \left(\sigma_x, \sigma_y, \sqrt{x_m^2 + y_m^2} \right)} \right) \qquad (5.30)$$

with a lower bound of 10 and an upper bound of 50. The method is implemented in Analytical Graphics, Inc., Satellite Tool Kit [49].

5.2.3 Analytic Collision Probability

The method by Bombardelli [50] et al. is a fully analytic formulation that computes the miss distance between the encountering bodies and their collision probability. The formulation establishes two objects S_1 and S_2 with an expected closest approach relative position r_e. It is assumed that a collision will occur when

$$|\vec{r}| = |\vec{r}_1 - \vec{r}_2| < S_A \qquad (5.31)$$

where $\vec{r}_1$ and $\vec{r}_2$ are the randomly distributed positions of their respective objects, and S_A can be taken as the sum of the radii of the spherical envelopes centered at S_1 and S_2. It is also assumed that the two objects follow Keplerian orbits.

In general terms, the probability of a collision between objects S_1 and S_2 as the the triple integral of the probability distribution function $f_r(\vec{r})$ of the relative position of S_1 with respect to S_2 over the volume swept over the volume V, depicted by the sphere of radius S_A centered at S_2.

$$P = \int_V f_r(\vec{r}) d\vec{r} \qquad (5.32)$$

When the $f_r(\vec{r})$ is Gaussian, then it can be written as

$$f_r(\vec{r}) = \frac{exp \left(-\frac{1}{2} \left(\vec{r} - \vec{r}_e \right)^T \mathbf{C}_r^{-1} \left(\vec{r} - \vec{r}_e \right) \right)}{(2\pi)^{3/2} \sqrt{det \left(\mathbf{C}_r \right)}} \qquad (5.33)$$

where $\mathbf{C}_r$ is the covariance matrix of $\vec{r}$, which corresponds to the sum of the individual covariance matrices of $\vec{r}_1$ and $\vec{r}_2$ (expressed in the same orthonormal base) when the two quantities are statistically independent.

The S_2-centered B-plane reference system, expressed in the B-plane coordinates (ξ, η, ζ), is defined with

$$\vec{u}_\xi = \frac{\vec{v}_2 \times \vec{v}_1}{|\vec{v}_2 \times \vec{v}_1|} \tag{5.34}$$

$$\vec{u}_\eta = \frac{\vec{v}_1 - \vec{v}_2}{|\vec{v}_1 - \vec{v}_2|} \tag{5.35}$$

$$\vec{u}_\zeta = \vec{u}_\xi \times \vec{u}_\eta \tag{5.36}$$

Under a rectilinear approximation, V becomes a cylinder along the η-direction, and the collision probability can now be written in the (ξ, η, ζ) system and integrated for $-\infty < \eta < \infty$, resulting in the following expression

$$P = \int_A \frac{1}{2\pi\sigma_\xi\sigma_\zeta\sqrt{1-\rho_{\xi\zeta}}} exp\left[-\left[\frac{\left(\frac{\xi-\xi_e}{\sigma_\xi}\right)^2 + \left(\frac{\zeta-\zeta_e}{\sigma_\zeta}\right)^2 - 2\rho_{\xi\zeta}\left(\frac{\zeta-\zeta_e}{\sigma_\zeta}\right)\left(\frac{\xi-\xi_e}{\sigma_\xi}\right)}{2\left(1-\rho_{\xi\zeta}^2\right)}\right]\right] d\xi d\zeta \tag{5.37}$$

where $\vec{r}_e = (\xi_e, 0, \zeta_e)^T$ is the expected closest approach relative position in B-plane axes, A is the circular domain of radius S_A, and σ_ξ, σ_ζ, and $\rho_{\xi\zeta}$ can be extracted from the relative position covariance matrix in B-plane axes

$$\mathbf{C}_{\xi\zeta} = \begin{bmatrix} \sigma_\xi^2 & \rho_{\xi\zeta}\sigma_\xi\sigma_\zeta \\ \rho_{\xi\zeta}\sigma_\xi\sigma_\zeta & \sigma_\zeta^2 \end{bmatrix} \tag{5.38}$$

Computation of the collision probability can be made equivalent to integrating a properly-scaled isotropic Gaussian distribution function over an elliptical cross-section. If the elliptical cross-section is approximated as a circular cross-section of equal area, then the collision probability computation reduces to a Rician integral that can be computed with the convergent series

$$P(u,v) = e^{-v/2} \sum_{m=0}^\infty \frac{v^m}{2^m m!} \left(1 - e^{-u/2}\sum_{k=0}^m \frac{u^k}{2^k k!}\right) \tag{5.39}$$

where

$$u = \frac{S_A^2}{\sigma_\xi\sigma_\zeta\sqrt{1-\rho_{\xi\rho}^2}} \tag{5.40}$$

$$v = \left(\frac{\xi_e}{\sigma_\xi}\right)^2 + \left(\frac{\zeta_e}{\sigma_\zeta}\right)^2 - 2\rho_{\xi\zeta}\frac{\xi_e}{\sigma_\xi}\frac{\zeta_e}{\sigma_\zeta} \tag{5.41}$$

The collision probability decreases exponentially for increasing V (as the size of the ellipse increases) [50].

5.3 Asteroid Risk Assessment

One of the simplest ways, in theory not necessarily computationally, of calculating an impact probability of an asteroid and a planet is to simply construct a fiels of virtual asteroids about the reference trajectory of the asteroid, propagate them all through the anticipated encounter date, and calculate the impact probability by dividing the number of virtual asteroids that hit the planet, known as virtual impactors, by the total number of virtual asteroids used in the computation. A drawback of this method is that it can be computationally expensive, and the number of virtual asteroids that would need to be used needs to be at least equal to the inverse of the impact probability [39]. Alternative methods of impact probability computation have been developed in the literature by using an impact probability model of the form

$$IP = \int \int \int_{V_\oplus} PDF(x,y,z) dx dy dz \tag{5.42}$$

To simplify the calculation, the three-dimensional PDF can simplified to one-dimensional by converting the (x,y,z) position data to spherical coordinates (r, θ, ϕ), and the triple integral would turn into a single integral over the radius of Earth,

$$IP = \int_0^{r_\oplus} PDF(r) \; dr = CDF(r_\oplus) - CDF(0) \tag{5.43}$$

where CDF denotes the cumulative density function resulting from the radial PDF. It has been shown previously [51, 52]

$$IP = \frac{1}{2}\left[erf\left(\frac{r_\oplus - \mu}{\sigma\sqrt{2}}\right) - erf\left(\frac{0 - \mu}{\sigma\sqrt{2}}\right)\right] \tag{5.44}$$

that the difference between the CFD value at zero and at Earth's radius results in a difference in the error function, in terms of the mean (μ) and standard deviation (σ) of the virtual asteroid close-approach radii.

This formulation is incorrect in that analysis however, particularly Equation 5.44. If the initial variations in (x,y,z) position are normally distributed about their own means and associated standard deviations, then the the resulting error function stemming from the radial PDF would be incorrect. The probability density function of the error function is a normal distribution, meaning that the radius values of the close-approach values would have to be normally distributed, which is not true given that (x,y,z) are normal and $r = \sqrt{x^2 + y^2 + z^2}$. The

radial distribution would be Rayleigh or shifted Rayleigh, using two normally distributed, independent variables (x, y), or even two planar orthogonal coordinates (e.g. (ξ, ζ)). The vector magnitude of the crossing points would be a Rayleigh distribution, assuming the components are uncorrelated with equal variance and zero mean. The crossing data will not necessarily have equal variance or zero mean, so a distribution can be fit to the data using the true component means and covariance matrix in order to find a better estimate of the impact probability. The formulation results in a number between 0 and 1, corresponding to the probability of impact. Having a larger pool of virtual asteroids used in the computation increases the computation time, but should yield a more accurate impact prediction.

5.3.1 Asteroid 2012 DA14

Recalling Figure 4.12, through the use of close encounter geometry, the variation in orbital elements between pre-encounter and post-encounter heliocentric orbits were calculated. Using those orbital variations, potential orbital resonances between the asteroid and Earth were found. The concept of B-plane mapping enabled the construction of the asteroid's encounter B-plane, which was used to ascertain the crossing points of virtual asteroids propagated through the B-plane. Applying analytic keyhole theory to the potential orbital resonances found, the location of keyholes on the encounter B-plane could be found.

Let's assume that a mission was carried out to disrupt the asteroid in its orbit on October 1, 2012, about four and a half months before its anticipated encounter with Earth in the middle of February of 2013. The result of the disruption mission is 2012 DA14 becoming 21 pieces, 20 fragmented pieces of the asteroid and a piece that represents the original asteroid, still on a potential collision course with Earth. Even with the disruption of the asteroid body, the center of mass of the fragmented asteroids will still be on the same original orbit as the original asteroid. The fragments however, will have small deviations in their position and velocity from the original asteroid. With each fragment having a different state vector, every set of initial conditions is propagated from the initial epoch to encounter with the Earth's sphere of influence, or through a few days after the expected encounter date if the fragment doesn't cross the Earth's path. Each fragment has a 6-dimensional hypersphere margin of error as to

its orbital position and velocity as it approaches Earth, so each fragment represents an orbital region where the fragment could actually reside in. To account for this orbital uncertainty, each fragment will be simulated by 1001 virtual asteroids about the fragment's orbital path.

To simulate the fragmentation of the asteroid body, a fragmentation model was created to add a certain amount of radial velocity to the asteroid fragments, as follows

$$\Delta v_i = \frac{\Delta v_{nominal} * r_i}{1 + (r_{max} - r_i)} \tag{5.45}$$

where Δv_i is the velocity added to the ith fragment, $\Delta v_{nominal}$ is the desired amound of velocity to be added, r_i is the relative radius of the ith fragment from the original asteroid's position, and r_{max} is the maximum radial distance of a fragment from the original asteroid's position after the fragmentation. The equation is an exponential decay function set up in such a way that the further the fragment is from the original asteroid position, the less radial velocity has been added to the fragment. Figure 5.1 shows the distribution of the asteroid fragment velocity additions using the above fragmentation model. After each fragment has had its
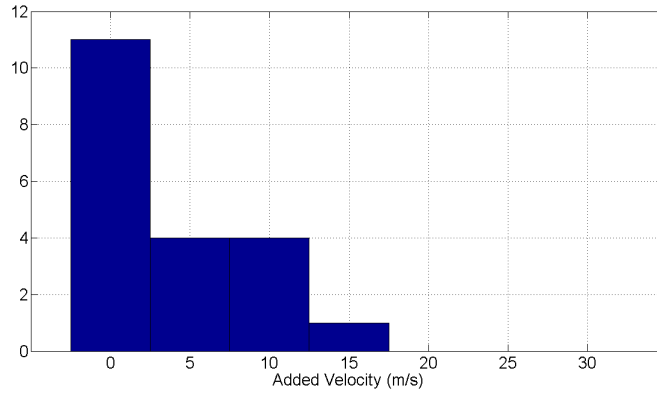
Figure 5.1　Histogram showing the distribution of the added velocity from the fragmentation to each asteroid fragment.

fragmentation velocity added, the new states of the asteroids are created and propagated along their orbital paths. Figures 5.2 and 5.3 visually show the representative scattering of the asteroid fragements from the center of mass of the original asteroid and a cross-section of the fragment cloud on a collision course with Earth on the approach trajectory of the asteroid.
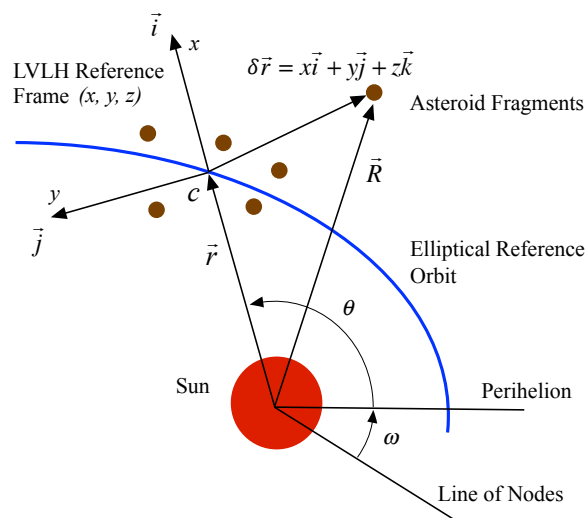
Figure 5.2 Depiction of the relative position of the asteroid fragments to the asteroid's original position/fragments' center of mass.

Before getting into the analysis of the fragments and their encounters, or lack thereof, with the Earth, there is one thing that is important to keep in mind at this point. With the simulated fragmentation of asteroid 2012 DA14, used an example to develop the computational tool being discussed in this paper, each fragment now has a different state vector (position and velocity state) than the original asteroid, therefore in the analysis conducted here each fragment is considered to be its own "new" asteroid and is treated as such. With that said, again there are assumed to be 21 equal sized pieces of the original asteroid after the fragmentation event. Each piece of the asteroid has two possible outcomes for its approach trajectory, either the fragment will cross into the Earth's SOI and have an encounter with the planet, or it will miss the SOI and continue on its path without much influence from the Earth. Given this simulation, it happens that one of the fragments doesn't encounter the Earth's SOI, meaning that the fragmentation has successfully dismissed one of the 21 asteroid pieces. That one fragment would have to be monitored to make sure that it wouldn't come back in the future, but for this analysis we assume that it doesn't have any future encounters with the planet. The remaining 20 pieces have some kind of encounter with the Earth, and Figure 5.4 shows the distributions of the asteroid fragment's orbital elements. Looking at all the distributions of orbital elements for all the encountering fragment's clouds it can be seen that the asteroid fragments will have
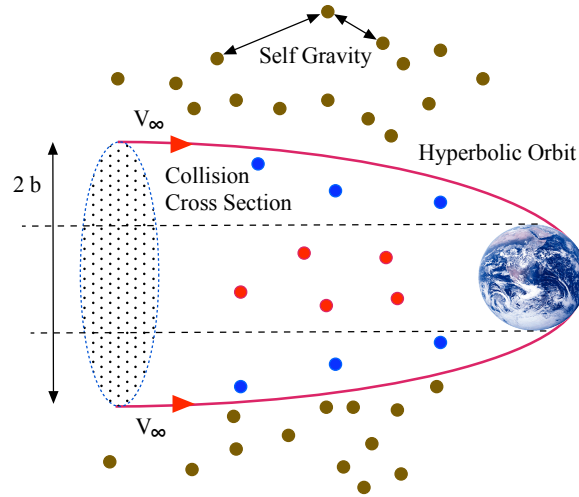
Figure 5.3   Collision cross-section of the asteroid fragment cloud.

various kinds of encounters with the Earth. Therefore, it would be expected that the fragment clouds would have crossing points spread across the B-plane, rather than centrally located like in the example of the nominal trajectory of 2012 DA14 .

5.3.1.1   Fragment Analysis

Figure 5.5 shows a composite B-plane of all the encountering asteroid fragments with Earth to show how the pieces could end up dispersing after the given fragmentation.   The green circle represents the Earth's cross-section on the B-plane, and the blue stars represent the various fragment fields of the asteroid fragments. It is easy to see how the added velocity from the fragmentation has caused some of the fragment clouds to drift away from the Earth in the B-plane.

Now looking back at Figure 4.12, the reader will recall that each encounter with a planet there are potential resonances that the body can fall into after the encounter, in addition to the potential that the asteroid can impact the planet on the current encounter. So, there are four categories that any given asteroid encounter can fall into: (1) impact and resonance potential, (2) impact and no resonance potential, (3) resonance and no impact potential, and (4) no resonance or impact potential. Even with the relatively small number of asteroid fragments simulated, there is a representative fragment for each of these four groups. Therefore, instead
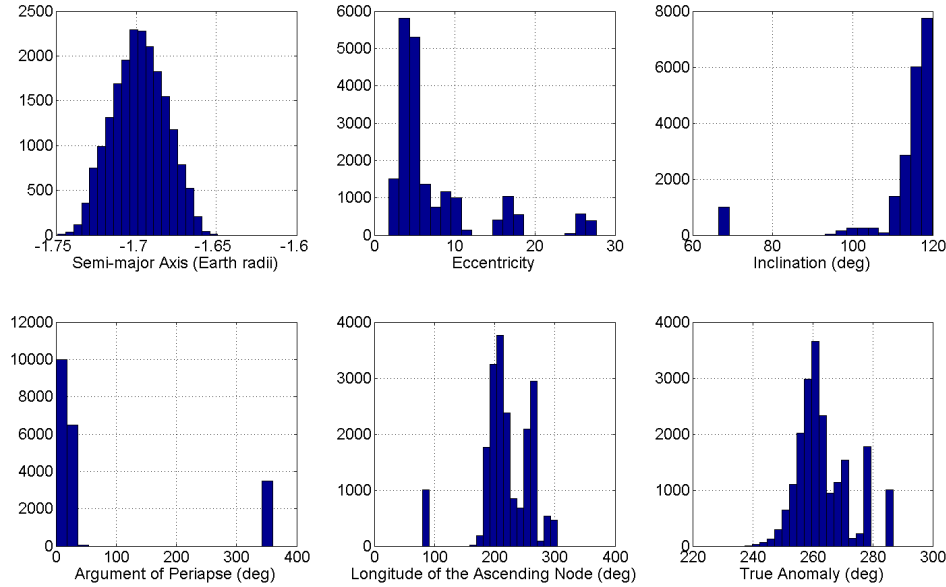
Figure 5.4 Histogram showing the distribution of the fragment clouds upon entering the Earth's sphere of influence.

of talking about the larger picture, which can get convoluted due to the number of particles and number of potential resonances for the fragmented asteroids, an analysis will be given of an asteroid fragment in each group and all other fragments can be assumed to fall into one of the four groups.

5.3.1.2 Impact and Resonance Potential

For the first case, the asteroid fragment to be looked at is one that has an impact risk on the first encounter with Earth and a potential for a resonant return impact encounter in the future. As can be seen in Figure 5.6, where the red dots show the crossing points of the fragment field and the green circle indicating the location of the Earth, this fragment turns out to have a small, but non-zero, impact probability with the Earth on its first encounter. The estimated impact probability of this fragment is about 1.15E-55, so small that it has virtually no chance of impacting the planet on this first encounter. The significance of this particular fragment field is not in its small impact potential, but in its resonance potential.   Looking closely at the figure, it can be seen that there are six potential Earth resonances based on the fragment's simulated encounter with the Earth. And, according to the analytic keyhole theory

Composite Target B-plane
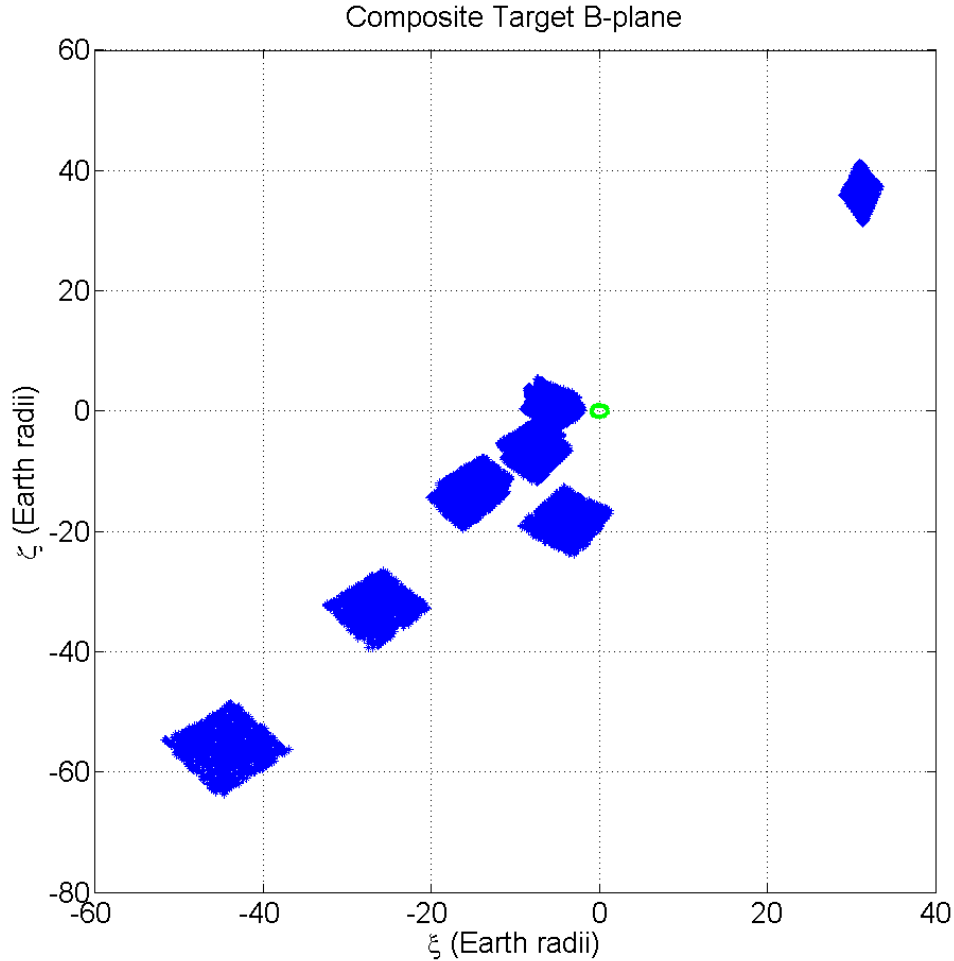
Figure 5.5   Composite B-plane of all the encountering asteroid fragment fields.

described earlier, the intersections between the vertical black line in the figure and the blue resonance circles indicate locations where keyholes may exist on this target B-plane. Given the clustering of the fragment field, the three cyan circles encompass the locations where a keyhole could exist. The other intersection points could also have keyholes associated with them, but they are not looked at based on the location of the fragment field's crossing points.

It is worth noting at this point, that the size and shape of these cyan circles do not reflect the size and shape of keyholes based on the analytic theory. The analytic theory says that the width of a given keyhole is approximately $2b_\oplus$ and has a maximum width that is dictated by the ratio of the resonance circle. The cyan circles are being used to show a region where if the asteroid fragment would pass through could result in an impact or at least very deep
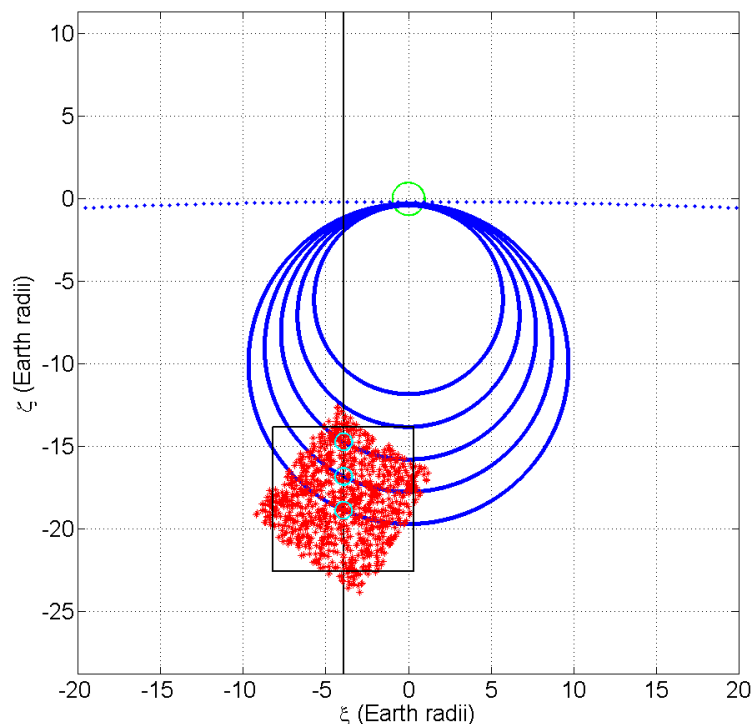
Figure 5.6   B-plane of an asteroid fragment that has potential to impact the Earth on the original encounter and has a potential for a future resonance encounter.

future orbital encounter. The probability of having the asteroid fragment pass through a given cyan circle in Figure 5.6 is calculated. Going from the top down, the probability that the fragment passes through the cyan circles on the target B-plane is 7.57E-5, 0.0045, and 0.0330, respectively. Again, these probabilities are fairly small, but are not small enough to ignore. If the probabilities are found to be large enough that they are worrisome, a more refined study can be done with larger fragment fields and/or using a long-term precision propagator to find the true potential and depth of any future encounters. However, for this study, this particular fragment field shows the capabilities of this analysis tool to find a relatively quick and robust solution to the current and future impact risk.

5.3.1.3   Impact and No Resonance Potential

Let's now look to a fragment that has a potential to impact the planet on its first encounter, but does not appear to fall into a resonance orbit with Earth within the next 10 years. In Fig-
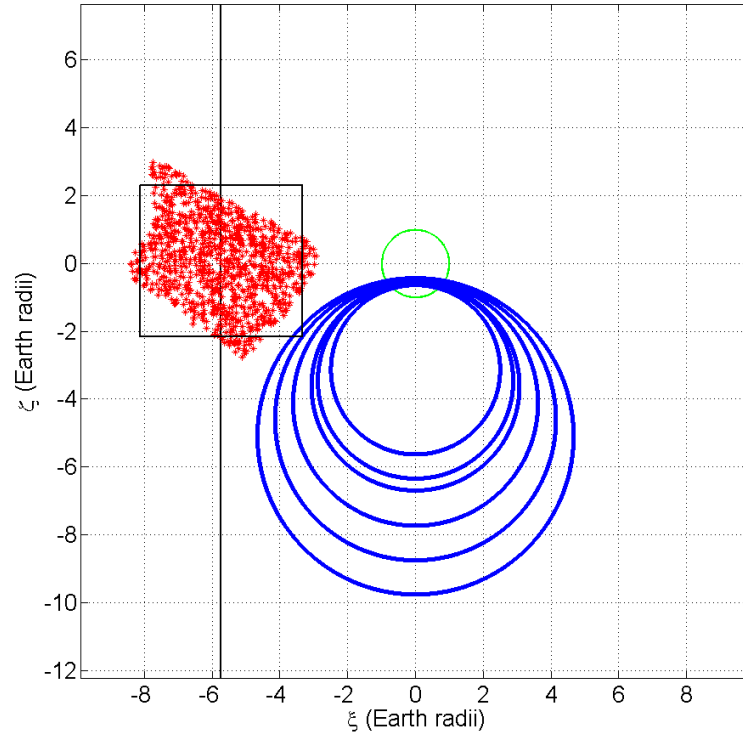
Figure 5.7   B-plane of an asteroid fragment that has potential to impact the Earth on the original encounter and has no potential for a future resonance encounter.

ure , the fragment field passes a lot closer to the planet than the field depicted in the Impact and Resonance Potential example. The impact probability of this particular field is estimated to be 0.000081%. This impact probability is much larger than in the previous example, but still fairly small and much smaller than that of the original asteroid. No resonance is said to exist between this fragment and the Earth because the multiple resonance circles shown on the target B-plane do not intersect the black, vertical line. Without that intersection, the analytic theory states that there is no existing keyhole on the plane for that kind of resonance orbit. That does not however mean that no keyhole exists on this particular B-plane, but there would be no way to find said keyhole without conducting an analysis of the fragment cloud via a high-fidelity numerical propagation scheme from the current encounter to a given point in the future. So based on the mix of analytic and numerical techniques used through this analysis this fragment is deemed to be a small threat to the Earth on its current encounter, and no threat in the near future.

5.3.1.4 Resonance and No Impact Potential

The asteroid fragment used as a representative of the group that can fall into resonance orbits while having no chance of impacting Earth on their current encounter is rather harmless. Based on the analysis, Figure 5.8 clearly reinforces the lack of a threat posed by this fragment field.   The red dots that represent the crossing points of the fragment field are about 35 Earth
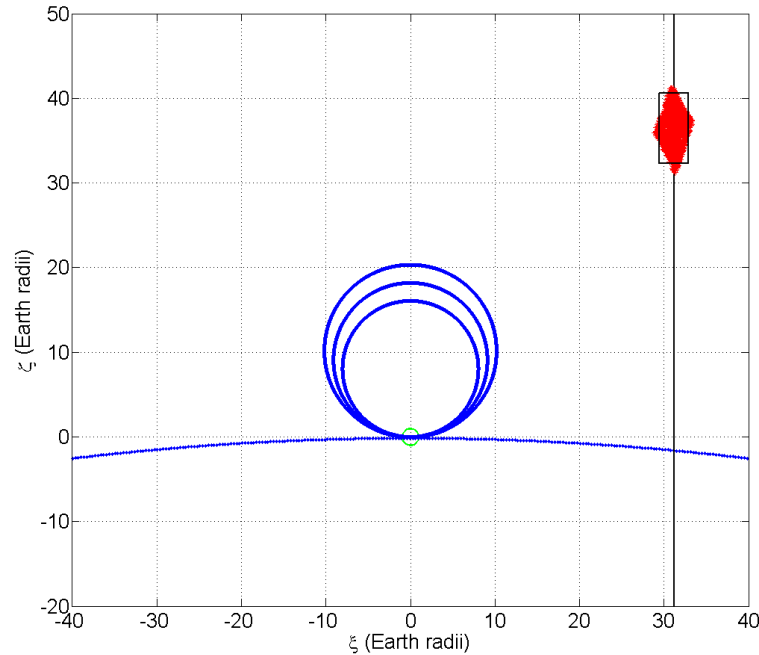
Figure 5.8   B-plane of an asteroid fragment that has a potential for a future resonance encounter and no impact potential on the current encounter.

radii from Earth, so calculating the impact probability on this encounter of this fragment field doesn't require the use of an equation but is found to be zero. In addition to the lack of impact risk on this encounter, there is no chance of the fragment to fall into a resonant return orbit after this Earth encounter. Of the four resonance circles shown in Figure 5.8, only one resonance circle intersects the black, vertical line - only one of those intersections is shown in the figure. The fragment field crosses the B-plane far from that intersection point where the keyhole would exist, so the probability of the fragment passing through that keyhole is presumed to be zero. However, if the timing of the fragment field crossing the B-plane were earlier than what it turned out to be, that fragment field would drift further down that black,

vertical line and the possibility of the fragment passing through the corresponding keyhole and making a resonant return to Earth would go up.

5.3.1.5 No Resonance or Impact Potential

The last type of encounter that an asteroid fragment could have with Earth is one where there is no threat to the Earth on the current encounter or in the near future. This would be the category where we would hope a large majority of asteroid fragments after a fragmentation event would end up, but whether that would be reality or not would depend on the effectiveness of the fragmentation and the resulting states of the fragments. The representative asteroid fragment
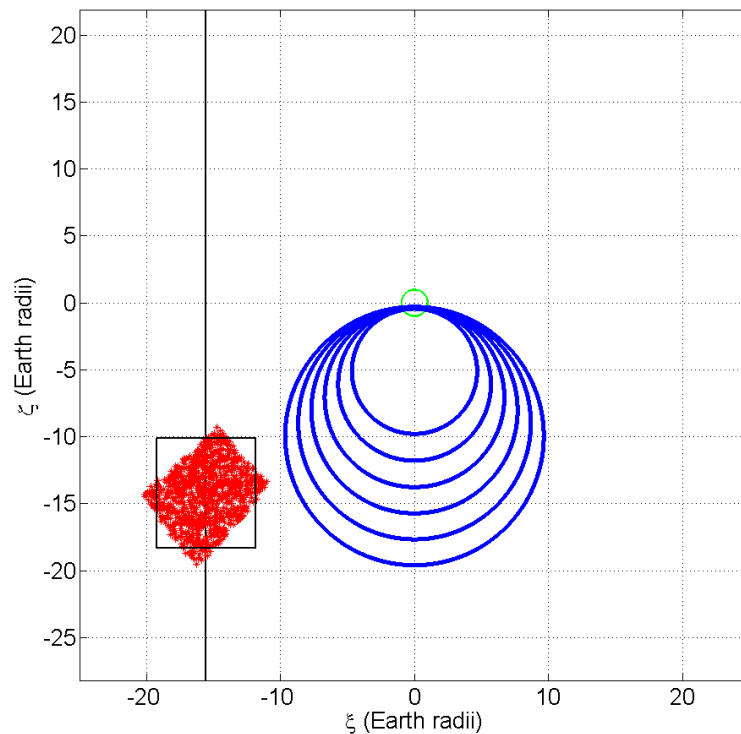
Figure 5.9   B-plane of an asteroid fragment that has no potential to impact the Earth on the original encounter or on any future resonance encounter.

of this group has its fragment field crossing the encounter B-plane on average about 21 Earth radii from the planet, so the estimated impact probability for this fragment is zero. Figure 5.9 shows that there are six resonance circles on the encounter B-plane, meaning there exist six potential resonances for the fragment after this encounter, but because none of these resonance

circles intersect the black, vertical line for this fragment there are again no analytically defined keyholes on this fragment's B-plane. Therefore, there is no chance of a resonant return for this fragment in the near future, implying no chance of a future impact during that period of time from this fragment.

5.4   Impact and Keyhole Passage Risk Assessment

To illustrate the way that the impact and keyhole passage risk assessment, a representative asteroid fragment from the fragmentation of 2012 DA14 is selected. For this example, the asteroid fragment shown with an impact and resonance risk is utilized.

Figure 5.6 shows the asteroid fragment cloud on the encounter B-plane, along with the Earth, resonance circles, and keyholes. Based on the figure, an estimate could be made on the impact potential and the keyhole passage risk posed by the asteroid fragment. As discussed previously, a quick and easy method to calculate an impact risk is to count the number of simulated virtual fragments that fall inside the outline of the Earth on the B-plane, divided by the total number of virtual fragments simulated. However, this does not really help when the asteroid or fragment cloud is not close enough to the Earth. So, in this case a histogram of the close-approach radii of the simulated virtual asteroid fragments is constructed to get an idea of the types of distances from the Earth that the cloud has, shown in Figure 5.10.   Looking at the data, it can be seen that the histogram appears nearly normal, but with a slight bias towards the higher radial distances. Two types of distributions were fit to the data, normal and gamma. The normal distribution gave a higher impact probability value than the gamma distribution due to the fact that it would over estimated the probabilities on the left end of the distribution. The gamma distribution fit the distribution a bit better overall, and gave a better probability value in the important regions. The probability values using the normal distribution and the gamma distribution, for an Earth impact by this fragment, are calculated to be 2.23E-14 and 1.15E-55 respectively. Both probabilities are very small, implying that there is virtually no risk of an Earth impact from this fragment. Given the fairly small range of radial distances and the steep slope on the left side of the histogram, it is more believable that the impact probability value provided by the gamma distribution is more correct.
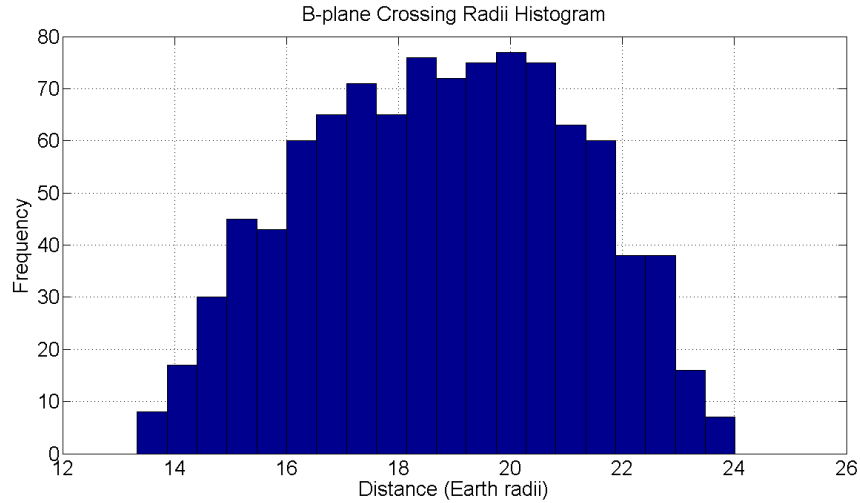
Figure 5.10   Histogram showing the radial position distribution of the virtual asteroid frag-
ments.

When looking for the possibility of passing through a keyhole on the target B-plane, looking
simply at the radial distribution of the data does not distinguish between data points that are
in the correct region of the B-plane and those that have the component combinations that
would result in the radial distance associated with a keyhole. A multitude of methods exist to
answer that question, such as long-term orbital simulations tracking the asteroids or asteroid
fragments or analytic keyhole theory to find the regions in an encounter B-plane that would
result in a resonant return with the planet. Each method has a cost associated with it, the
long-term orbital simulations can take a large amount of computation time but are fairly high-
fidelity, while the analytic theory takes a significantly smaller amount of computation time
while proving lower-fidelity results. Taking advantage of the semi-analytic protocol discussed
in this paper, as stated in the introduction, can produce reliable results while not requiring a
tremendous amount of computation time.

Looking back to Figure 4.12, it can be seen that no keyhole existed on the 2013 B-plane of
2012 DA14 that would result in a resonant return of the asteroid within the next 10 years. The
evidence for the existance of such a region in the B-plane would be indicated by the intersection
of the vertical yellow line and any one of the resonance circles. That intersection tells us that
a keyhole exists in that region of space, but not the size of that keyhole. Because a keyhole

is the projection of the Earth's future position on the current encounter B-plane, the shape of the keyhole closely follows the resonance circle, making it look like an arclet. That being said, given that each asteroid fragment is taken to be a point mass with no discernable size or shape, it would be difficult to assess the likelihood that any one fragment would actually pass through the keyhole, so instead of counting the number of fragments that would pass through that region and dividing by the number of total virtual fragments simulated, the area method for keyhole passage is constructed and employed to find the potential for a fragment to fall through that region of the encounter B-plane.

5.4.1   Area Method for Keyhole Passage Assessment

The virtual fragments constructed through the orbital uncertainty of a single asteroid fragment propagated through the encounter B-plane occupy a fraction of the B-plane's area. The keyhole on the same encounter B-plane also occupies a fraction of the B-plane area, however, not necessarily the same or even overlapping areas of the B-plane. This method claims no accuracy, only that it can be a way to quickly evaluate the risk potential of an asteroid and/or its fragments, and the method does not hold for instances where the keyhole region and the virtual fragment cloud region are too far removed from each other, where the keyhole passage probability would be assumed to be zero.

Consider the case where the keyhole region resides near the virtual fragment cloud of the asteroid fragment: how do we effectively evaluate the potential of the fragment to fall within the keyhole region? This question is answered using an area method that attempts to capture a majority of the virtual fragments within a bounding box and is proportional to the ratio of the area of the keyhole region and the bounding box. The example presented here is only to show the methodology employed, it is not intended to describe an accurate, real-life scenario.

Assume that an asteroid has a virtual asteroid cloud, comprising of 10000 virtual asteroids, passing through the Earth's encounter B-plane such as that indicated by the blue stars and the red stars showing the position of the same virtual asteroid cloud on the next encounter B-plane in Figure 5.11.   The yellow stars in each cloud indicate the virtual asteroids that pass within 1.1 Earth radii on the second encounter B-plane. It is worth mentioning that the crossing
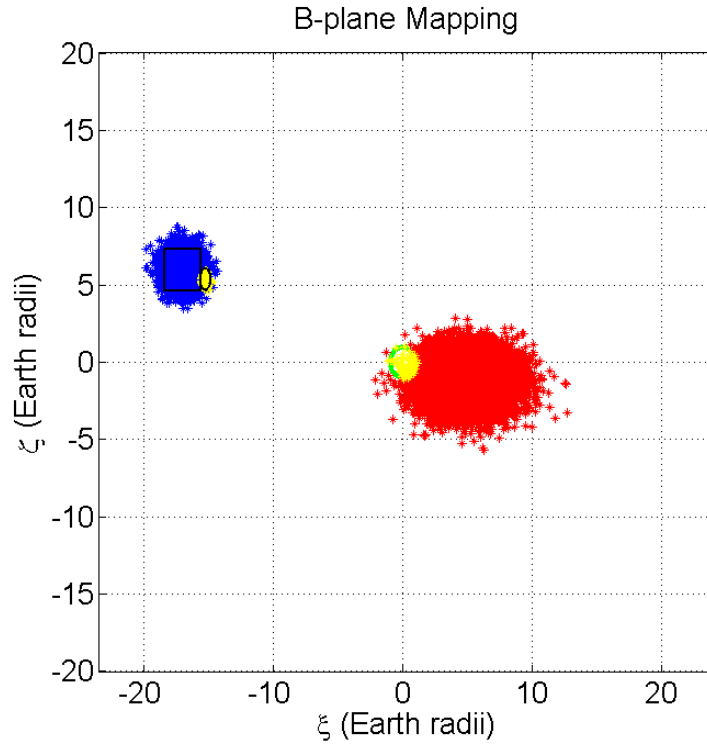
Figure 5.11   Example composite encounter B-plane for successive encounters of an asteroid with Earth.

points on the first encounter B-plane were created such that the probability of an impact with the planet on the first pass is zero. Before discussing the first encounter crossing point data, let's look at the second encounter data. Of the 10000 virtual asteroids, 66 fall within 1.1 Earth radii of Earth's surface on that particular encounter, making the impact probability for the encounter 0.66%. Calculating the impact probability using a radial position density function, the resulting impact probability is estimated to be about 0.71%, showing strong agreement between the statistical approximation and the simulated results.

Now, let's look back to the first encounter crossing data, it can be seen that there is a black box and ellipse over the crossing point data. The box is constructed to have dimensions large enough to encompass at least 90% of the data points, and the ellipse is constructed with dimensions such that 95% of the data points fall within the prescribed area. The precentage values given are simply chosen to capture a large majority of the crossing points within each region and hold no special significance. When implemented using a simulated asteroid fragment,

the dimensions of the keyhole region will be established based on the theory, so the proportion of the crossing points falling within the area will be simply the number within the region divided by the simulated fragments.

So, to construct the impact risk assessment for the asteroid based on its virtual asteroid field

$$IP = \left[\frac{A_{ellipse}}{A_{box}}\right] p_{box} \; p_{ellipse} \; (1 - p_{ellipse}) \tag{5.46}$$

where $A_{ellipse}$ and A_{box} are the areas of the ellipse and box encompassed by those shapes on the encounter B-plane, respectively, and p_{box} and $p_{ellipse}$ are the proportion of the crossing points that fall within the box and ellipse, respectively. With the resulting formula, the probability of an impact by the asteroid on its second encounter with Earth is evaluated to be about 0.5%.

Looking at the result, it is easy to see that it is not the same value as those found using either the statistical approximation or the simulated results on the second encounter B-plane crossing data. The results shouldn't be expected to be the same, or even necessarily in the same ballpark, because depending on the amount of time between encounters the field of virtual asteroids can disperse quite a bit leaving the impact probability on the second encounter plane to be essentially zero. As previously stated, this formula is not guaranteeing the accurate assessment of the impact probability of a body on future encounters, but is simply being used to find a solution so as to give an evaluation of whether or not the asteroid would need to be studied further.

So, the expression described by Equation 5.46 needs to be revised a bit to find the probability of the asteroid/fragment passing through the keyhole on the B-plane. Originally, $p_{ellipse}$ represented the proportion of the virtual cloud on the first encounter B-plane that would impact the Earth on the second encounter B-plane. Now, it represents the proportion of the cloud that falls within the keyhole region because in the case of a simulated asteroid fragment cloud, unless the cloud is simulated through to the second encounter B-plane, the number that would impact the Earth would be unknown and the size of the keyhole on the first encounter B-plane would be known (or at least established). In order to deal with the varying potential keyhole locations on the encounter B-planes, a term has to added to the expression to represent the proportion of the cloud that makes an encounter with the Earth after the fragmentation event.

108

The resulting equation used to calculate the probability of an asteroid, or asteroid fragment, passing through a keyhole now takes the form

$$KP = p_{encounter} \left[\frac{A_{ellipse}}{A_{box}} \right] p_{box} \; p_{ellipse} \; (1 - p_{ellipse}) \tag{5.47}$$

where $p_{encounter}$ is the proportion of the asteroid/fragment cloud that encounters the Earth, $A_{ellipse}$ is the area of the ellipse that represents the keyhole region of the B-plane, A_{box} is the area of the bounding box that encompasses a sizable portion of the virtual cloud, p_{box} is the proportion of the cloud that is encompassed by the bounding box, and $p_{ellipse}$ is the proportion of the virtual cloud that falls within the elliptical representation of the keyhole.

If the keyhole exists in a high density region of the virtual cloud, then the resulting keyhole passage probability from Equation 5.47 is representative based on the population. A problem arises when the keyhole falls in a low density region of the virtual cloud. In the case where a handful or so of the virtual asteroids/fragments fall into or near the keyhole region, the keyhole passage probability can drop dramatically. So something to keep in mind when looking at the resulting probability values from Equation 5.47 is the spread of the data and if the number of data points used is sufficiently large to accept the reported answer. A study could be done to find the number of sufficient bodies, which is not done within this work's scope, but every asteroid/fragment cloud used in the analyses to follow contains at least 10000 virtual bodies.

CHAPTER 6.   APPLICATIONS TO TARGET NEAR-EARTH ASTEROIDS

6.1   Asteroid 2013 PDC-E

In this section, the hypothetical asteroid 2013 PDC-E is considered for an impact scenario. The goal of the exercise was to see how different groups (media, UN, space agencies, general public, etc.) with different perspectives would respond and develop their perspective of the situation created by the potential asteroid threat. The tabletop exercise staged for the 2013 Planetary Defense Conference began with asteroid 2013 PDC-E being discovered on the last day of the conference - April 19, 2013. It was determined to be a stony Earth-threatening asteroid of 200 to 300 meter diameter, with an initial impact probability of 0.8% in 2028. If the impact velocity of the asteroid were to be about 12.4 km/s, the energy released from the impact would be equivalent to about 300 MT of TNT. Through further analysis of the asteroid orbit, it was determined that there was a 1.2 km keyhole during a 2023 Earth close-approach. If the asteroid were to pass through the keyhole on the 2023 encounter B-plane, then the asteroid would impact Earth in 2028. However, given that the impact probability is only 0.8%, the likelihood of an impact occurring is not certain. The first update to the status of the threatening asteroid comes in 2019, where the asteroid's size was known to be 300 meters and the impact probability rose to 28%. In that same update, the risk corridor for the asteroid on the Earth was known to span across the globe, with a potential impact in regions like the United Kingdom, France, Northeast Africa, and the east coast of Asia. The next update came in 2022, where based on the most recent observations the probability of impact is 100%, and the impact location has been narrowed down to a region spanning from the United Kingdom to Egypt. The final update, presented at the conclusion of the exercise (2023), where the impact

location and date was completely determined - in the Mediterranean, off the south coast of France, on November 21, 2028.

6.1.1 Pre-Keyhole Mission Designs

With asteroid 2013 PDC-E, the existence of a gravitational keyhole on the 2023 encounter B-plane allows for the unique opportunity to launch an early action mission to attempt to deflect the asteroid away from the keyhole. Despite the low probability of a keyhole passage upon discovery of the asteroid, missions launched closer to the anticipated close-approach date will not allow enough time for the deflection mission to take significant effect. So, prior to the 2023 encounter, long-dispersion missions are designed to find possible missions that can be launched not long after discovery, sparing the Earth the risk of a future Earth-impacting trajectory.

The constant contribution to the cost function used to evaluate the various mission options, depicted by Equation 3.36, comes from the total mission ΔV for the mission and the mission v_∞, illustrated by Figures 6.1 and 6.2. Looking at both the mission ΔV and v_∞, it can be
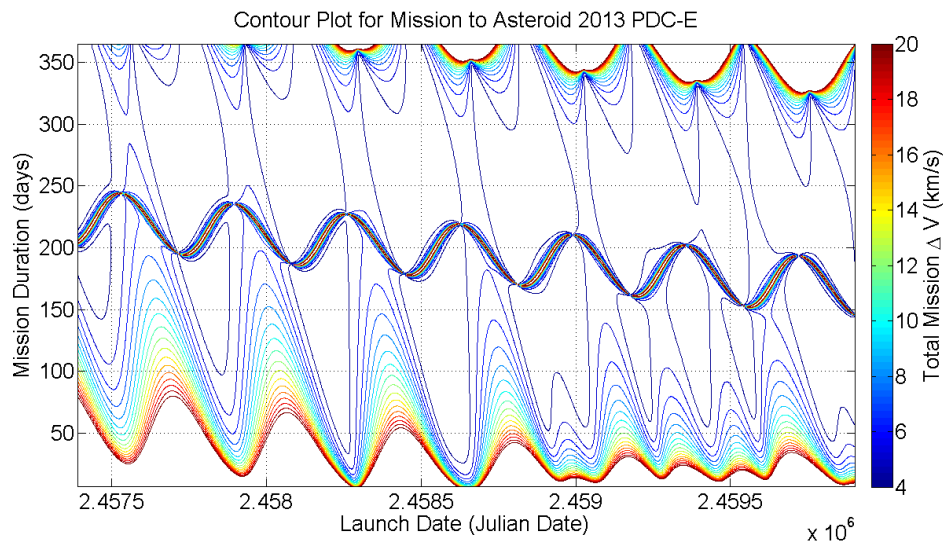
Figure 6.1   Contour plot of total mission ΔV for an intercept mission to asteroid 2013 PDC-E before its 2023 keyhole encounter.

seen that there are plenty of opportunities for missions to be launched from Earth to the target body. The date that mission would be launched on does not appear to be a limiting factor, but

depending on the launch date there are regions of mission durations that allow for a feasible trajectory to be achieved. For this pre-2023 encounter asteroid trajectory, two different
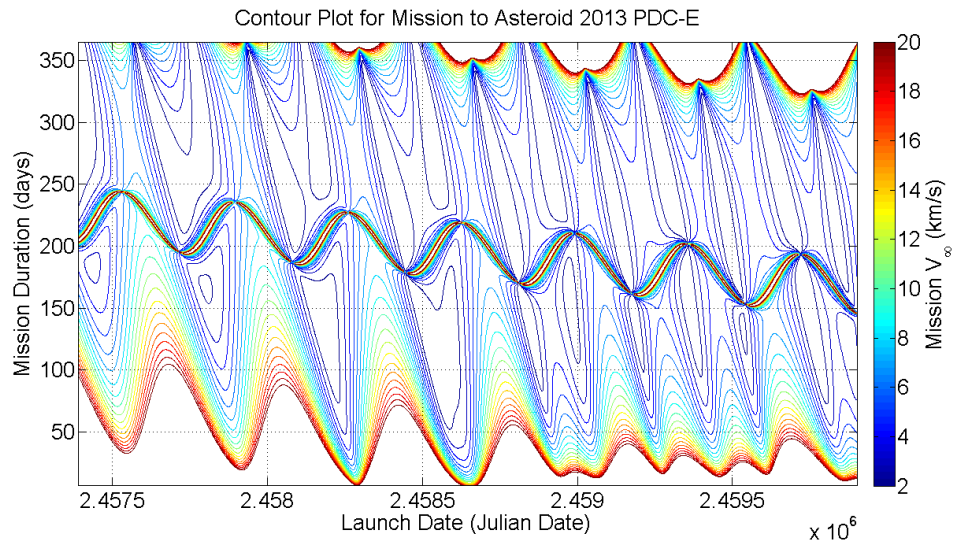
Figure 6.2   Contour plot of mission V_∞ for an intercept mission to asteroid 2013 PDC-E before its 2023 keyhole encounter.

mission designs were conducted: a long-duration, long-dispersion mission and a short-duration, long-dispersion mission. These two mission design types will optimize the spacecraft trajectory in a way that will allow for the asteroid to have as much time as possible between its impact with the spacecraft and the 2023 Earth encounter for the deflection to have an effect.

6.1.1.1   Long-duration, Long-dispersion Mission

In addition to the constant contributing components to the mission design cost function, a long-duration, long-dispersion mission optimization requires that the mission duration and dispersion time parameters are a part of the cost function evaluation. The bounds set for this long-duration, long-dispersion time mission optimization are 200 to 365 days for the mission duration and at least one year for the dispersion time. The results given are based on these parameters, and if altered can result in different optimal mission possibilities. Table 6.1 shows the top ten missions based on the prescribed mission cost function.

Table 6.1   Top 10 mission designs for a long-duration, long-dispersion mission to asteroid 2013 PDC-E before its 2023 keyhole encounter.

Rank	Launch (JD)	ΔV_{Total} (km/s)	C3 (km^2/s^2)	t_{disp} (days)	t_{dur} (days)	v_{arr} (km/s)	α_{arr} (rad)	α_{LOS} (rad)	α_{Sun} (rad)	J_{score}
1	2459646.5	3.23146	0.0755	365	259	4.7805	0.16226	0.1362	1.59769	5.14739
2	2459645.5	3.23146	0.0756	365	260	4.7788	0.16220	0.1362	1.59774	5.14758
3	2459647.5	3.23147	0.0758	365	258	4.7821	0.16232	0.1362	1.59765	5.14784
4	2459644.5	3.23148	0.0761	365	261	4.7770	0.16214	0.1362	1.59779	5.14850
5	2459648.5	3.23149	0.0763	365	257	4.7836	0.16237	0.1362	1.59761	5.14880
6	2459649.5	3.23152	0.0770	365	256	4.7850	0.16242	0.1362	1.59757	5.15015
7	2459643.5	3.23152	0.0770	365	262	4.7751	0.16208	0.1362	1.59785	5.15027
8	2459650.5	3.23156	0.0779	365	255	4.7864	0.16247	0.1362	1.59754	5.15180
9	2459642.5	3.23159	0.0785	365	263	4.7731	0.16201	0.1362	1.59790	5.15298
10	2459651.5	3.23161	0.0789	365	254	4.7876	0.16251	0.1362	1.59750	5.15361

The table shows a number of the important mission design parameters at the front and back-end of the asteroid intercept mission: launch date, total mission ΔV, mission $C3$, dispersion time, mission duration, relative arrival velocity, relative arrival angle, the line-of-sight angle, the Sun angle, and the mission cost function score, respectively. As would be expected, there is a launch window where the optimal mission resides, March 4, 2022 to March 13, 2022, and the mission ΔVs and $C3$s are all very similar over that window. The optimal mission, regardless of the launch date, pushed the dispersion time as low as possible (365 days) and had similar mission durations (254 to 263 days). Given that the optimal launch window is large enough to encompass all the top ten mission designs, the cost function evaluation for the missions are nearly the same, meaning that there is very little difference between the mission designs. Figure 6.3 shows the spacecraft mission trajectory for the first ranked mission design in Table 6.1.   The green line represents the Earth's orbital track over the time that it takes
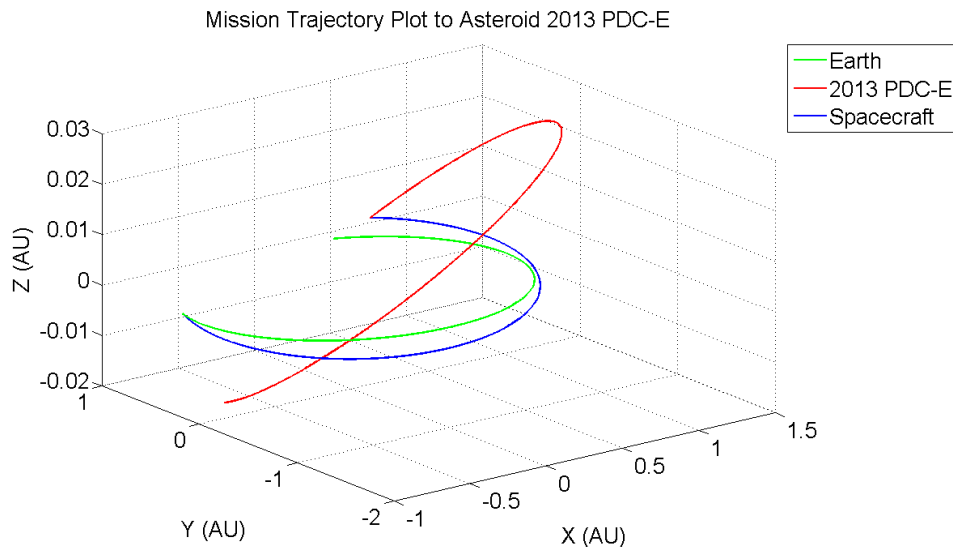
Figure 6.3   Trajectory plot for a long-duration, long-dispersion intercept mission to asteroid 2013 PDC-E.

the spacecraft (blue line) to travel from Earth to the target body, depicted by the red line. The figure shows the departure of the spacecraft from Earth, deviating slightly from the Earth's orbital plane and meeting up with asteroid 2013 PDC-E 259 days later, one year before the anticipated Earth encounter.

6.1.1.2   Short-duration, Long-dispersion Mission

The only difference between the formulation of the short-duration, long-dispersion mission design and its long-duration counterpart are the bounds placed on the acceptable mission duration. The long-duration bounds were between 200 and 365 days, for the short-duration missions the acceptable mission duration is between 7 and 90 days. With the modification to the mission cost function, Table 6.2 shows the resulting optimal mission design parameters for an intercept mission to asteroid 2013 PDC-E. In the case of this mission design, it can be seen that the launch window for the optimal trajectory is limited to a five day window. Instead of a wider launch window, more optimal missions occur on the same launch dates as other missions, but with a shorter mission duration (89 days rather than 90 days). Given the new bounds set on the mission duration, the optimal mission trajectory results show that AMiDST tried to keep the mission duration as large as possible, running into the upper bound limit set by the user. Looking closely at the mission duration and dispersion time combinations between the two pre-2023 encounter mission designs, there seems to exist a trade-off between the mission duration and the dispersion time. When a longer mission duration is favored, it appeared that the associated dispersion time ran closer to its lower bound. As opposed to when a shorter mission duration is set, a longer dispersion time resulted in a more optimal mission design. Regardless of the mission duration and dispersion time combination, for either mission type, the mission ΔV and $C3$ are fairly similar and small, implying mission feasibility. One other interesting bit of information comes from the relative arrival speed between the spacecraft and the target asteroid. Either the long-duration or short-duration mission designs resulted in relative arrival speeds that were smaller than 10 kilometers per second. The impact between the spacecraft and asteroid is still a hypervelocity impact in nature, but it is not quite as fast as what the HAIV spacecraft was designed to be able to handle, making the targeting and acquisition of the body prior to the final approach stage easier because the slower speed means more time on approach. Once again, given the similarities between the top 10 missions, the resulting cost function evaluations are close to one another, implying that there is little difference between the optimal mission options.

Table 6.2   Top 10 mission designs for a short-duration, long-dispersion mission to asteroid 2013 PDC-E before its 2023 keyhole encounter.

Rank	Launch (JD)	ΔV_{Total} (km/s)	C3 (km^2/s^2)	t_{disp} (days)	t_{dur} (days)	v_{arr} (km/s)	α_{arr} (rad)	α_{LOS} (rad)	α_{Sun} (rad)	J_{score}
1	2458549.5	3.25701	0.6396	1631	90	6.4259	0.2107	0.0526	1.5919	5.6877
2	2458550.5	3.25715	0.6426	1630	90	6.2872	0.2067	0.0538	1.5875	5.6884
3	2458548.5	3.25742	0.6486	1632	90	6.5662	0.2148	0.0512	1.5964	5.6950
4	2458551.5	3.25779	0.6569	1629	90	6.1502	0.2027	0.0550	1.5832	5.6967
5	2458550.5	3.25809	0.6634	1631	89	6.4279	0.2108	0.0526	1.5920	5.7035
6	2458551.5	3.25825	0.6670	1630	89	6.2884	0.2067	0.0538	1.5876	5.7046
7	2458549.5	3.25848	0.6721	1632	89	6.5692	0.2149	0.0512	1.5965	5.7105
8	2458547.5	3.25840	0.6704	1633	90	6.7082	0.2188	0.0496	1.6010	5.7107
9	2458552.5	3.25892	0.6818	1628	90	6.0150	0.1986	0.0561	1.5790	5.7118
10	2458552.5	3.25893	0.6821	1629	89	6.1506	0.2026	0.0550	1.5832	5.7132

So, since there are only small differences between the various mission design options, the first ranked mission is chosen to show as an example in Figure 6.4. The spacecraft mission trajectory for this short-duration, long-dispersion mission doesn't have much to show given the short arcs that the Earth (green), asteroid (red), and spacecraft (blue) travel in their respective orbits. The resulting spacecraft trajectory for this asteroid intercept mission to 2013 PDC-E
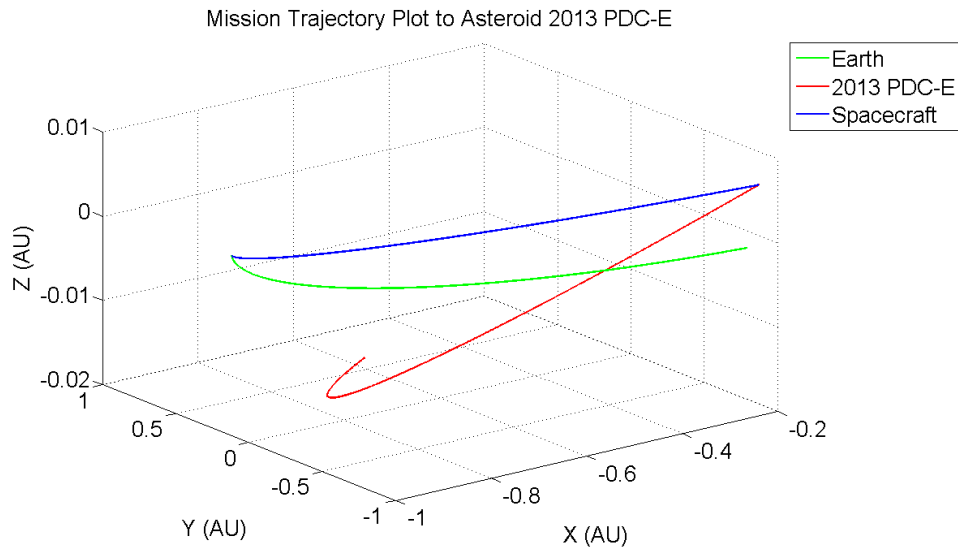
Figure 6.4 Trajectory plot for a short-duration, long-dispersion intercept mission to asteroid 2013 PDC-E.

shows a very short spacecraft orbit, that goes slightly out of the Earth's orbit plane, but does not go very far from Earth, allowing for very easy communication with the Earth throughout the terminal phase of the mission.

6.1.2 Post-Keyhole Mission Designs

After passing through a keyhole on the 2023 Earth encounter, asteroid 2013 PDC-E is said to fall into a 4:5 resonance with the Earth, where asteroid completes four complete revolutions about the Sun in the time it takes the Earth to complete five. Once those orbits are complete, the Earth and 2013 PDC-E will find each other together again for another encounter in 2028, with the result being an impact rather than a close flyby if nothing is done to perturb or disrupt the asteroid.

Looking at Figure 6.5, an understanding of the mission required ΔV to reach the target asteroid in its orbit during its post-2023 Earth encounter orbit, prior to its 2028 Earth encounter. Before any in-depth analysis is done, it can be seen that there are regions of the contour plot where an intercept mission from Earth to asteroid 2013 PDC-E would be a fairly simple endeavor, particularly the times immediately following the asteroid's 2023 encounter and as the 2028 Earth impact gets closer. It is also easy to see that there is a stretch of time where an
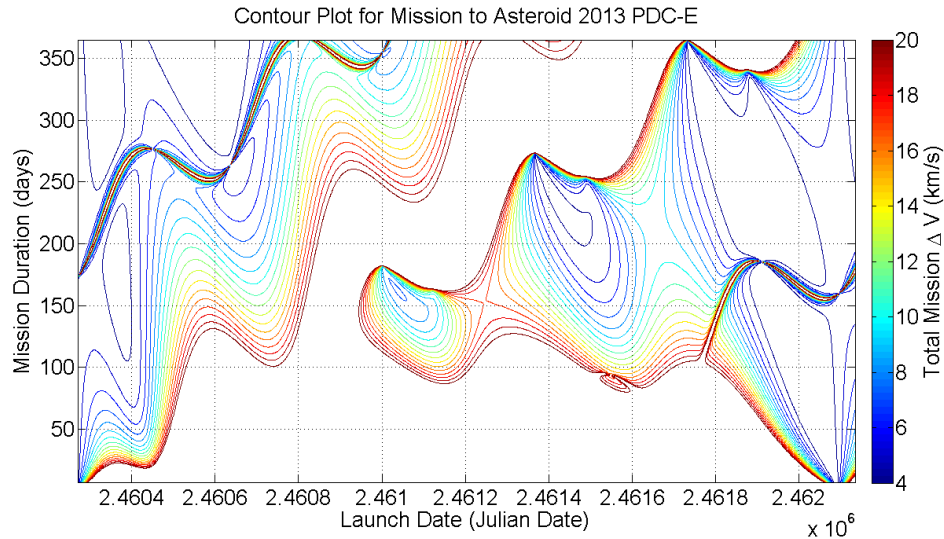
Figure 6.5   Contour plot of total mission ΔV for an intercept mission to asteroid 2013 PDC-E before its 2028 Earth encounter.

intercept mission to 2013 PDC-E would be very difficult to achieve, due to the large amount of ΔV needed to be imparted to the spacecraft in order to reach the asteroid. About one year removed from the 2023 Earth encounter, asteroid 2013 PDC-E enters a period of about two years where a very large launch vehicle and/or small spacecraft would be required to make a feasible mission to intercept the asteroid body. The total mission ΔV, which based on this mission design scenario is simply the departure ΔV required to leave LEO and enter a $C3$ orbit that would place the spacecraft in an interplanetary trajectory that would result in the interception of the target body, is around 8-10 km/s at least. The implication of such a large departure ΔV would be that the orbit v_∞ and $C3$ would large as well, and would eliminate mission possibilities due to their infeasibility. This claim is further enhanced by looking at Figure 6.6.   In that same region of the contour plot discussed previously, the v_∞ values are
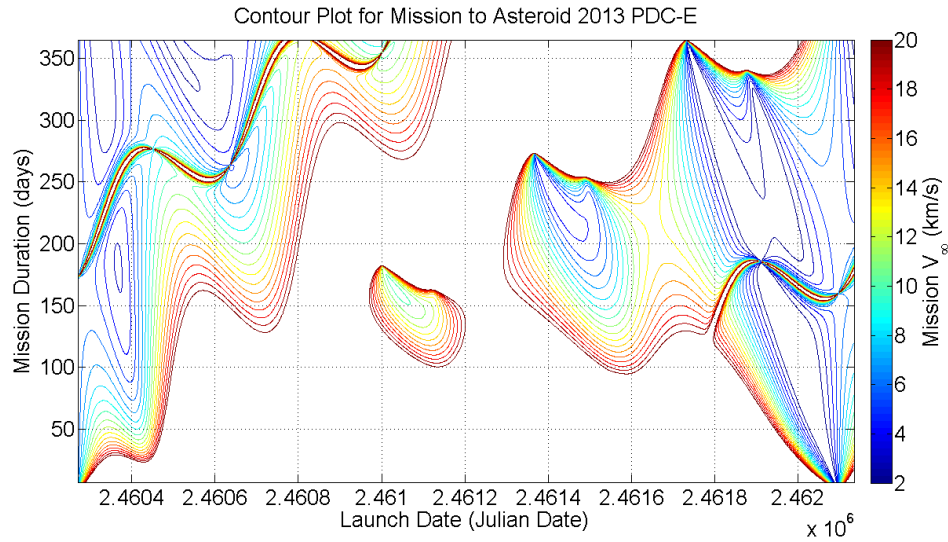
Figure 6.6   Contour plot of mission V_∞ for an intercept mission to asteroid 2013 PDC-E before its 2028 Earth encounter.

up towards 10-12 km/s, which based on the established cost function for the following mission designs ($C3 \leq 25 km^2/s^2$) would automatically rule them out as feasible, potential mission designs. Given that the asteroid is now confirmed to be on an Earth-impacting trajectory, four types of mission designs are looked at in order to safe guard the Earth from 2013 PDC-E: (1) a long-duration, long-dispersion mission, (2) a long-duration, short-dispersion mission, (3) a short-duration, long dispersion mission, and (4) a short-duration, short-dispersion mission.

6.1.2.1   Long-duration, Long-dispersion Mission

Within the makings of the cost function for a long-duration, long-dispersion mission, the allowable mission durations are between 200 and 365 days and the dispersion time has to be at least 365 days. Table 6.3 shows the missions that fit the criteria set by the cost function, and result in the smallest overall cost function evaluation. Looking at the results, a relatively small launch window exists around July 3, 2024 where a spacecraft can travel to asteroid 2013 PDC-E with a $C3$ of about 3.1 km^2/s^2. All of the top 10 mission designs resulted in mission durations near a full year in length and had dispersion times of about 3.4 years. The relative arrival speed for this mission type is over 9 km/s, the fastest closing speed between the spacecraft and asteroid of any missions looked at to this point.

Table 6.3 Top 10 mission designs for a long-duration, long-dispersion mission to asteroid 2013
PDC-E before its 2028 Earth encounter.

Rank	Launch (JD)	ΔV_{Total} (km/s)	C3 (km^2/s^2)	t_{disp} (days)	t_{dur} (days)	v_{arr} (km/s)	α_{arr} (rad)	α_{LOS} (rad)	α_{Sun} (rad)	J_{score}
1	2460494.5	3.36726	3.0884	1242	360	9.0987	0.3119	5.0401	1.6644	7.1225
2	2460496.5	3.36710	3.0848	1241	359	9.1387	0.3143	5.0387	1.6659	7.1230
3	2460495.5	3.36711	3.0851	1241	360	9.1388	0.3143	5.0387	1.6659	7.1231
4	2460493.5	3.36738	3.0910	1242	361	9.0984	0.3119	5.0401	1.6644	7.1234
5	2460495.5	3.36749	3.0934	1242	359	9.0997	0.3119	5.0401	1.6644	7.1242
6	2460492.5	3.36786	3.1017	1243	361	9.0554	0.3094	5.0415	1.6629	7.1253
7	2460497.5	3.36744	3.0924	1241	358	9.1394	0.3143	5.0387	1.6659	7.1255
8	2460494.5	3.36750	3.0936	1241	361	9.1396	0.3143	5.0387	1.6659	7.1259
9	2460497.5	3.36730	3.0892	1240	359	9.1759	0.3166	5.0371	1.6673	7.1262
10	2460493.5	3.36801	3.1050	1243	360	9.0567	0.3095	5.0415	1.6629	7.1264

Figure 6.7 shows the trajectory taken by the spacecraft (blue) with respect to the Earth
(green) and the target asteroid (red) for the first ranked mission in the table. Looking closely
at the trajectory plot, it can be seen that the spacecraft has to leave the plane of Earth's orbit
in order to intercept 2013 PDC-E a little less than a year later. This out-of-plane trajectory
is the reason for the larger $C3$ value.   Even with the required out-of-plane motion required
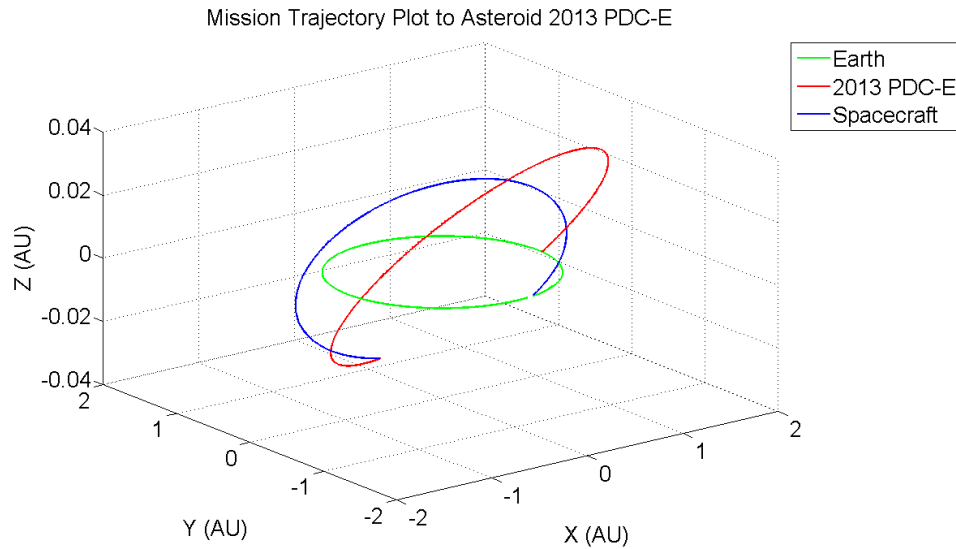
Figure 6.7   Trajectory plot for a long-duration, long-dispersion intercept mission to asteroid
2013 PDC-E.

by the spacecraft, the missions shown in Table 6.3 are still very feasible because the energy of
the Earth-centered hyperbolic orbit is not large enough that a launch vehicle and/or spacecraft
can't compensate.

6.1.2.2   Long-duration, Short-dispersion Mission

For the long-duration, short-dispersion mission the same criteria are applied for the mission
duration (between 200 and 365 days), but the allowed dispersion time for the desired missions
would be between 7 and 90 days. So, given the potential combinations of mission durations
and dispersion times, expected mission results will all be within that last year and a half to
a year before the asteroid would impact the Earth. As seen in Table 6.4, the top 10 missions
occur over a 10 day long launch window, centered around April 1, 2028.

Table 6.4   Top 10 mission designs for a long-duration, short-dispersion mission to asteroid 2013 PDC-E before its 2028 Earth encounter.

Rank	Launch (JD)	ΔV_{Total} (km/s)	C3 (km^2/s^2)	t_{disp} (days)	t_{dur} (days)	v_{arr} (km/s)	α_{arr} (rad)	α_{LOS} (rad)	α_{Sun} (rad)	J_{score}
1	2461862.5	3.23778	0.2150	7	227	5.8973	0.1833	0.0040	1.5777	5.3234
2	2461863.5	3.23779	0.2152	7	226	5.9025	0.1835	0.0040	1.5776	5.3236
3	2461861.5	3.23780	0.2154	7	228	5.8921	0.1832	0.0040	1.5779	5.3239
4	2461864.5	3.23783	0.2161	7	225	5.9078	0.1837	0.0040	1.5774	5.3245
5	2461860.5	3.23784	0.2163	7	229	5.8869	0.1830	0.0040	1.5781	5.3249
6	2461865.5	3.23789	0.2175	7	224	5.9130	0.1839	0.0040	1.5772	5.3260
7	2461859.5	3.23790	0.2176	7	230	5.8816	0.1828	0.0040	1.5782	5.3264
8	2461866.5	3.23799	0.2196	7	223	5.9183	0.1841	0.0040	1.5771	5.3283
9	2461858.5	3.23798	0.2193	7	231	5.8764	0.1826	0.0040	1.5784	5.3284
10	2461857.5	3.23807	0.2213	7	232	5.8711	0.1824	0.0040	1.5786	5.3307

Given the trajectory that the asteroid is on, prior to its anticipated impact with Earth later in the year, it is interesting to see that the best mission designs all have dispersion times that are 7 days long and mission durations between 220 and 230 days. As can be seen in Figure 6.8, the spacecraft trajectory (blue) follows that of the Earth's (green) (albeit a little out of the ecliptic) before intercepting asteroid 2013 PDC-E. The departure ΔVs for the optimal missions are
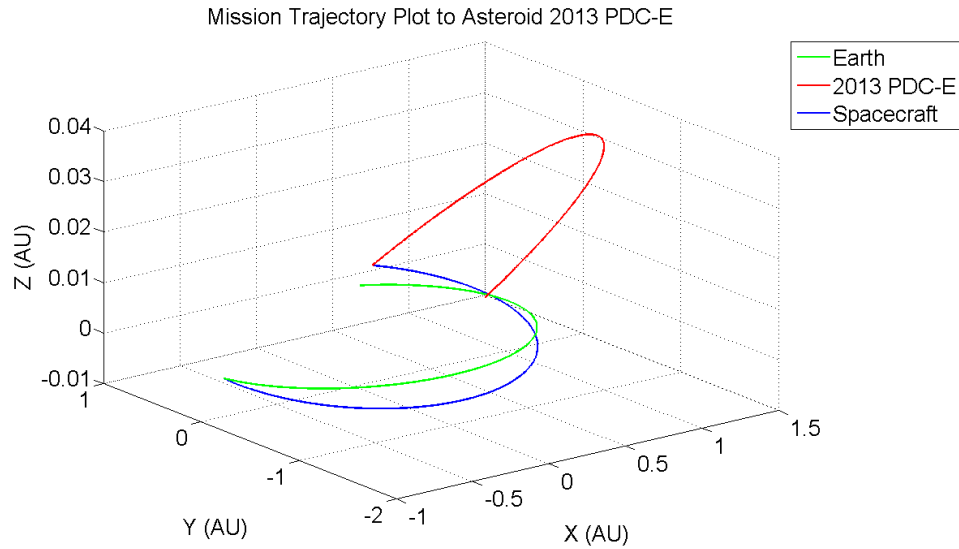
Figure 6.8   Trajectory plot for a long-duration, short-dispersion intercept mission to asteroid 2013 PDC-E.

a little under 3.24 km/s and the $C3$ values are a little less than 0.22 km^2/s^2. These missions also result in the spacecraft arriving at the target with a relative speed of about 5.9 km/s. Overall, the entire group of missions for the long-duration, short-dispersion design are very feasible missions and relatively easy to accomplish.

6.1.2.3   Short-duration, Long-dispersion Mission

A short-duration, long-dispersion mission design for the post-keyhole orbit of asteroid 2013 PDC-E has an allowable mission duration of up to 90 days and must have a dispersion time of at least 365 days. Recalling Figure 6.5, the parameter bounds on the mission duration and dispersion time, as well as the mission ΔV ($\Delta V < 7\ km/s$) and mission $C3$ ($C3 \le 25\ km^2/s^2$), the location of the optimal mission design is the bottom left corner of the contour plot.

Table 6.5   Top 10 mission designs for a short-duration, long-dispersion mission to asteroid 2013 PDC-E before its 2028 Earth encounter.

Rank	Launch (JD)	ΔV_{Total} (km/s)	C3 (km^2/s^2)	t_{disp} (days)	t_{dur} (days)	v_{arr} (km/s)	α_{arr} (rad)	α_{LOS} (rad)	α_{Sun} (rad)	J_{score}
1	2460395.5	4.26128	23.8429	1611	90	5.8582	0.1875	6.1513	1.2343	10.6692
2	2460394.5	4.26166	23.8521	1612	90	5.8914	0.1870	6.1581	1.2328	10.6693
3	2460396.5	4.26263	23.8753	1610	90	5.8237	0.1879	6.1444	1.2358	10.6751
4	2460393.5	4.26370	23.9013	1613	90	5.9234	0.1865	6.1649	1.2314	10.6753
5	2460392.5	4.26733	23.9889	1614	90	5.9541	0.1859	6.1716	1.2300	10.6867
6	2460397.5	4.26578	23.9514	1609	90	5.7879	0.1883	6.1376	1.2374	10.6872
7	2460391.5	4.27251	24.1137	1615	90	5.9835	0.1854	6.1784	1.2286	10.7035
8	2460398.5	4.27083	24.0732	1608	90	5.7510	0.1887	6.1307	1.2390	10.7060
9	2460390.5	4.27917	24.2746	1616	90	6.0115	0.1848	6.1851	1.2273	10.7254
10	2460399.5	4.27787	24.2432	1607	90	5.7129	0.1891	6.1237	1.2406	10.7316

Table 6.5 shows the optimal results for a short-duration, long-dispersion mission. The launch window for the optimal mission to intercept asteroid 2013 PDC-E is centered on March 26, 2024, only four months after the keyhole passage on the 2023 encounter B-plane. The departure mission ΔV for these missions are about 4.3 km/s, and have very large $C3$ energies ($\approx 24 km^2/s^2$). These types of missions are to be expected given that the asteroid has just had its close-approach with the Earth and is near the periapse of its orbit, implying that the asteroid is traveling rather fast, and means that the spacecraft has to "catch/keep up" with the asteroid after it has launched from Earth. The plot in Figure 6.9 doesn't really lend any new information about the spacecraft trajectory, relative to the asteroid and Earth. All of the
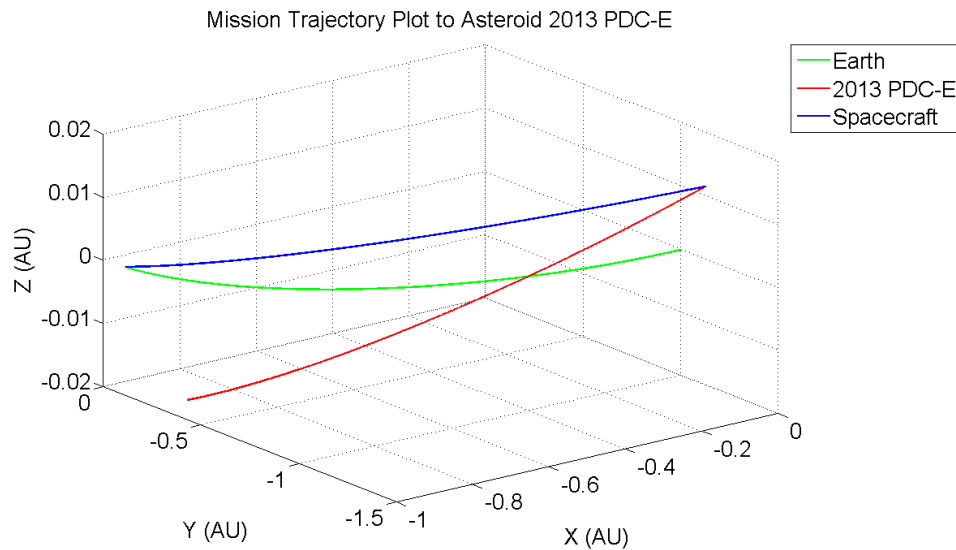
Figure 6.9   Trajectory plot for a short-duration, long-dispersion intercept mission to asteroid 2013 PDC-E.

top 10 mission designs have 90 day mission durations, and dispersion times that are dependent on the launch date of the mission. The high $C3$ energy of the mission orbit results in a relative arrival speed of near 6 km/s in all the top 10 missions. These missions can be made feasible with either a small spacecraft and/or large launch vehicle.

6.1.2.4   Short-duration, Short-dispersion Mission

A short-duration, short-dispersion mission is taken as a last attempt to deflect/disrupt the
Earth-threatening asteroid. The mission duration and dispersion time are limited to no more
than 90 days each. This means that the best scenario is the mission is launched six months prior
to the predicted impact date, and the worst case 2 weeks ahead of time. Table 6.6 shows the
optimal mission results for this last-minute deflection/disruption mission. The optimal mission
launch window is centered on August 19, 2028, about three months before the anticipated
impact date. Given that the time when the mission is launched, the spacecraft trajectory is
very short, as can be seen in Figure 6.10, and doesn't require a lot of ΔV from LEO to be
put into the necessary $C3$ orbit to intercept 2013 PDC-E.   The cost function evaluated that
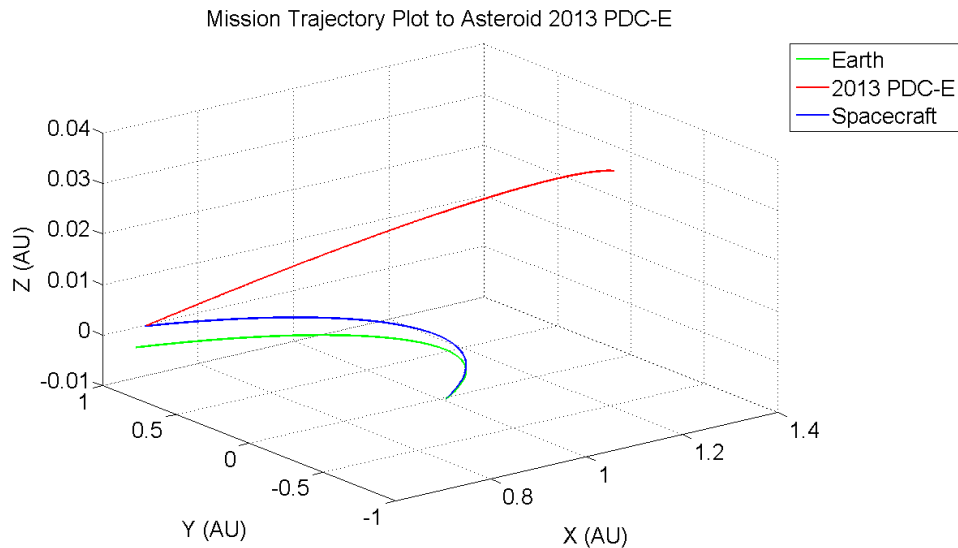
Figure 6.10   Trajectory plot for a short-duration, short-dispersion intercept mission to asteroid
              2013 PDC-E.

the most optimal mission designs had dispersion times of 7 days, and mission durations that
approach the parameter's upper bound. The relative arrival speed of the spacecraft, even for
this short-duration, short-dispersion mission design would still result in a hypervelocity impact
of approximately 6.5 km/s, requiring the use of a HAIV type spacecraft for mission success.

Table 6.6 Top 10 mission designs for a short-duration, short-dispersion mission to asteroid 2013 PDC-E before its 2028 Earth encounter.

Rank	Launch (JD)	ΔV_{Total} (km/s)	C3 (km^2/s^2)	t_{disp} (days)	t_{dur} (days)	v_{arr} (km/s)	α_{arr} (rad)	α_{LOS} (rad)	α_{Sun} (rad)	J_{score}
1	2462002.5	3.23591	0.1737	7	87	6.4263	0.2035	0.0040	1.5568	5.2680
2	2462001.5	3.23592	0.1740	7	88	6.4222	0.2033	0.0040	1.5570	5.268412
3	2462003.5	3.23593	0.1741	7	86	6.4305	0.2036	0.0040	1.5567	5.268415
4	2462000.5	3.23596	0.1749	7	89	6.4181	0.2031	0.0040	1.5571	5.2695
5	2462004.5	3.23598	0.1753	7	85	6.4347	0.2038	0.0040	1.5565	5.2699
6	2461999.5	3.23601	0.1760	7	90	6.4140	0.2030	0.0040	1.5573	5.2709
7	2462005.5	3.23608	0.1774	7	84	6.4389	0.2039	0.0040	1.5564	5.2724
8	2462006.5	3.23621	0.1804	7	83	6.4432	0.2041	0.0040	1.5562	5.2760
9	2462007.5	3.23638	0.1841	7	82	6.4475	0.2043	0.0040	1.5560	5.2805
10	2462008.5	3.23658	0.1886	7	81	6.4520	0.2044	0.0040	1.5559	5.2858

6.1.3 Fragmentation of Asteroid 2013 PDC-E

Asteroid 2013 PDC-E has two distinct portions to its trajectory between the date it was discovered and its impact with Earth - a pre-keyhole trajectory that results in a 2023 keyhole-encounter with Earth and a post-keyhole encounter that results in an Earth impact in 2028. Since it is known that the asteroid poses no immediate threat to the Earth prior to the 2023 encounter, an attempt to fragment the asteroid could prove more hazardous than simply attempting to deflect the body from its keyhole encounter. Therefore, a fragmentation analysis of asteroid 2013 PDC-E is restricted to the time period prior to its expected impact date in late November 2028.

6.1.3.1 Post-Keyhole Passage Fragmentation

Given the restriction of a fragmentation mission to asteroid 2013 PDC-E coming after its expected close approach in 2023, the analysis presented here assumes a fragmentation mission was launched and arrived to the target body one year prior to the anticipated impact date in late November 2028. So, one year before the impact date means the fragmentation of the asteroid body would occur in late November 2027, allowing only one year for the asteroid fragments to disperse from the asteroid's nominal impacting trajectory. Due to the lack of a complete, rigorous fragmentation model, the example outlined in this section assumes a fragmentation in which the fragments have applied radial velocity perturbations (maximum of 10 cm/s) and the mass of the original body is uniformly distributed to the fragment cloud. While the number of fragments born from the fragmentation event is subjective and based upon the density, porosity, and the energy input into the target body, the number of asteroid fragments simulated for the purpose of this example is 10001, where the first 10000 are newly constructed asteroid fragments and the last one is representative of the original asteroid and its impact trajectory. All 10001 asteroid fragments are propagated using the same dynamical model, and no intra-fragment gravitational forces, from the fragmentation date through their encounter with the Earth, and the resulting composite B-plane map (Figure 6.11) shows the close approach locations of the 2013 PDC-E's fragment cloud.   Simply by looking at the
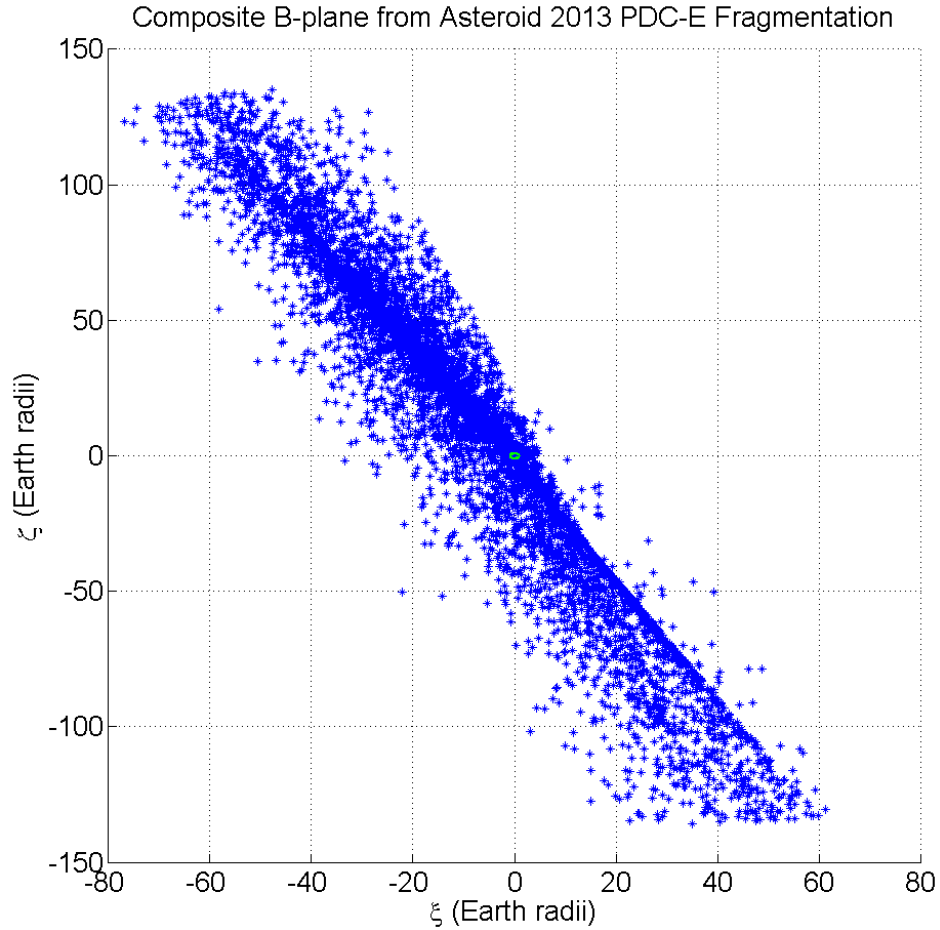
Figure 6.11   Composite encounter B-plane showing the crossing locations of asteroid 2013 PDC-E's fragments.

composite B-plane, it can be seen that the fragments, over the one year dispersion time, have scattered across the Earth's encounter B-plane. The wide range of fragment crossing locations, from the early arriving fragments in the top half the B-plane to the later arriving fragments in the bottom half of the B-plane, span such a large breadth of the B-plane that the Earth's cross-section (green circle) at the origin of the map, as reference, can only barely be seen. While the type of fragmentation used in for this example can be thought of as unrealistic, it is merely meant to exhibit one of the many possibilities arising from a fragmentation event. From the given example, asteroid fragments from this type of fragmentation can fall pretty much anywhere along the indicated corridor in Figure 6.11, including potentially impacting Earth. By observing the region of the B-plane around the origin, it can be seen that the Earth

is a fairly populated section of the fragment cloud, meaning that even after this fragmentation event the Earth is still at risk of being hit by a number of fragments.

Ignoring the asteroid fragments that run the risk of impacting the Earth on the current encounter, let's look at an asteroid fragment that does not have an immediate threat to the planet but could have one in the near future. Taking the fragment's state vector as the nominal trajectory for that fragment, and constructing a cloud of virtual fragments normally distributed about the nominal state, the fragment cloud is propagated through the Earth's encounter B–plane. The resulting asteroid fragment cloud on the B-plane is shown in Figure 6.12. The
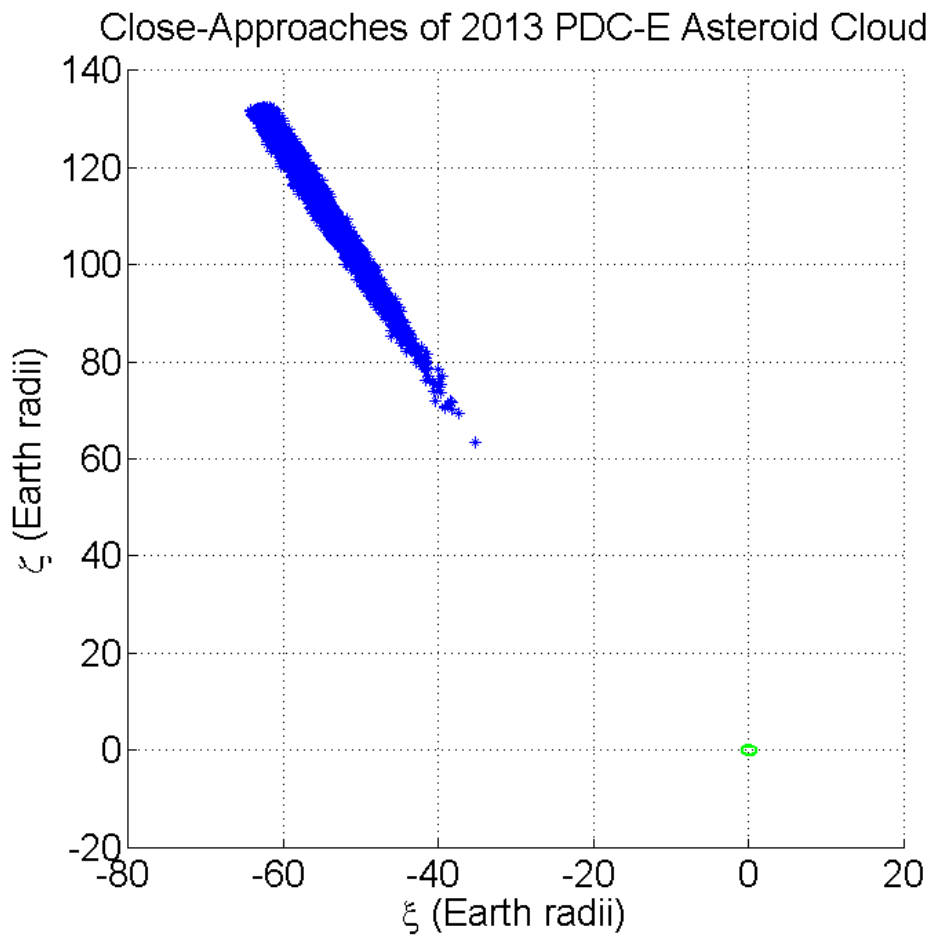
Figure 6.12   Asteroid 2013 PDC-E fragment cloud crossing locations on close-encounter B–plane.

original fragment crossing location is somewhere in the middle of this dense, linear clustering, at about (-56, 100) Earth radii. And given a small standard deviation of 10 meters and 1

meter per second in all three coordinate directions, on the fragmentation date one year prior to this close encounter, it can be seen how the cloud has dispersed and banded as it made its approach towards Earth. As previously mentioned, the fragment has virtually no chance of impacting the Earth, as is evident by plot in Figure 6.12 and the radial distribution histogram of the cloud crossing locations shown in Figure 6.13. One of the original assumptions made
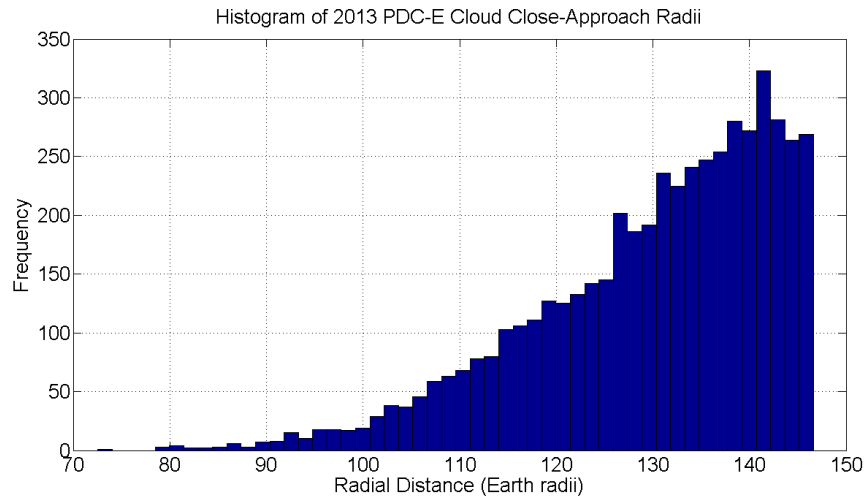
Figure 6.13   Histogram of asteroid 2013 PDC-E's fragment cloud radial crossing locations.

prior to the propagation of the asteroid/fragment propagation, is that the normal distribution of state components about the nominal states. The point is reiterated because the assumption that the B-plane crossing locations would still be normally distributed are shown to be untrue, based upon the results from the cloud distribution of this particular fragmentation event. Therefore, the use of a statistical approximation for the impact probability of the form of Equation 5.44 is irresponsible without first looking at the resulting radial (Figure 6.13) and component (Figure 6.14) distributions. It is easy to see that the distributions of the radial and B-plane components are highly skewed. In the case of this particular asteroid fragment, there is no need for the use of a statistical approach to assess the likelihood of this fragment impacting the Earth. Based on the skewness of the 10000 virtual asteroid fragment cloud, it is very safe to say that the fragment will not be impacting the Earth on this encounter. The question that needs to be asked and answered is the possibility of another future encounter between Earth and this fragment that could result in an impact.
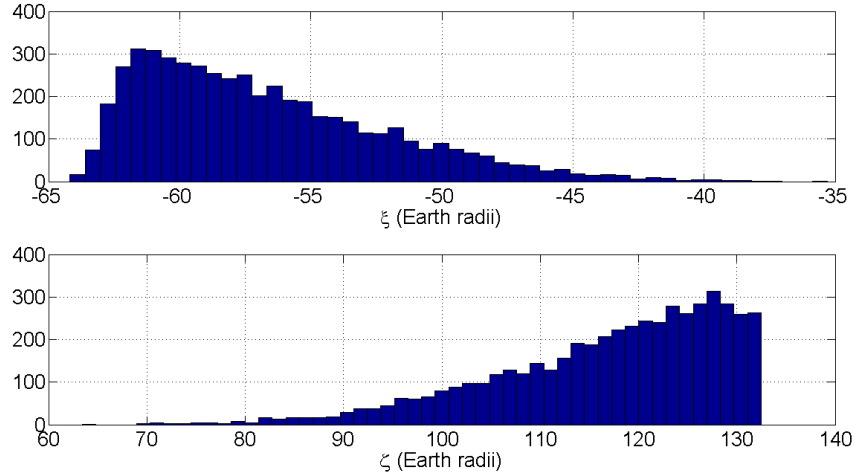
Figure 6.14 **Top:** Histogram of asteroid 2013 PDC-E's fragment cloud ξ components. **Bottom:** Histogram of asteroid 2013 PDC-E's fragment cloud ζ components.

In order to assess the risk posed by this fragment to the Earth in the future, there must be an understanding of the resonance potential of this asteroid fragment. Figure 6.15 starts to lend an understanding of the situation the Earth is in, with respect to this asteroid 2013 PDC-E fragment. The situation is as follows: based upon the possible post-Earth-encounter orbital parameters that this fragment could have there are 6 potential post-Earth-encounter orbital resonances that the fragment could fall in (4 are shown because two of those resonances result in the same size resonance circle because they are a factor larger), the estimated position of the fragment's crossing on the next encounter B-plane has four intersections with the resonance circles indicating the existence of keyholes on the B-plane, and the crossing location of the nominal fragment trajectory occurs not too far from one of those potential keyhole locations. Upon further examination, the keyhole location that the red star, indicating the B-plane crossing location of the nominal fragment trajectory, is near is for a 9:7 Earth to asteroid orbit resonance and the keyhole is a very wide arclet with a small thickness, centered between the two vertical black lines in Figure 6.15. Combining the fragment cloud crossing points with the resonance circles on the encounter B-plane, and placing a bounding box about 95% of the crossing data and a bounding circle around the significant keyhole region, the resulting B-plane plot takes the form of Figure 6.16. Unfortunately, the figure encompasses too large an area to
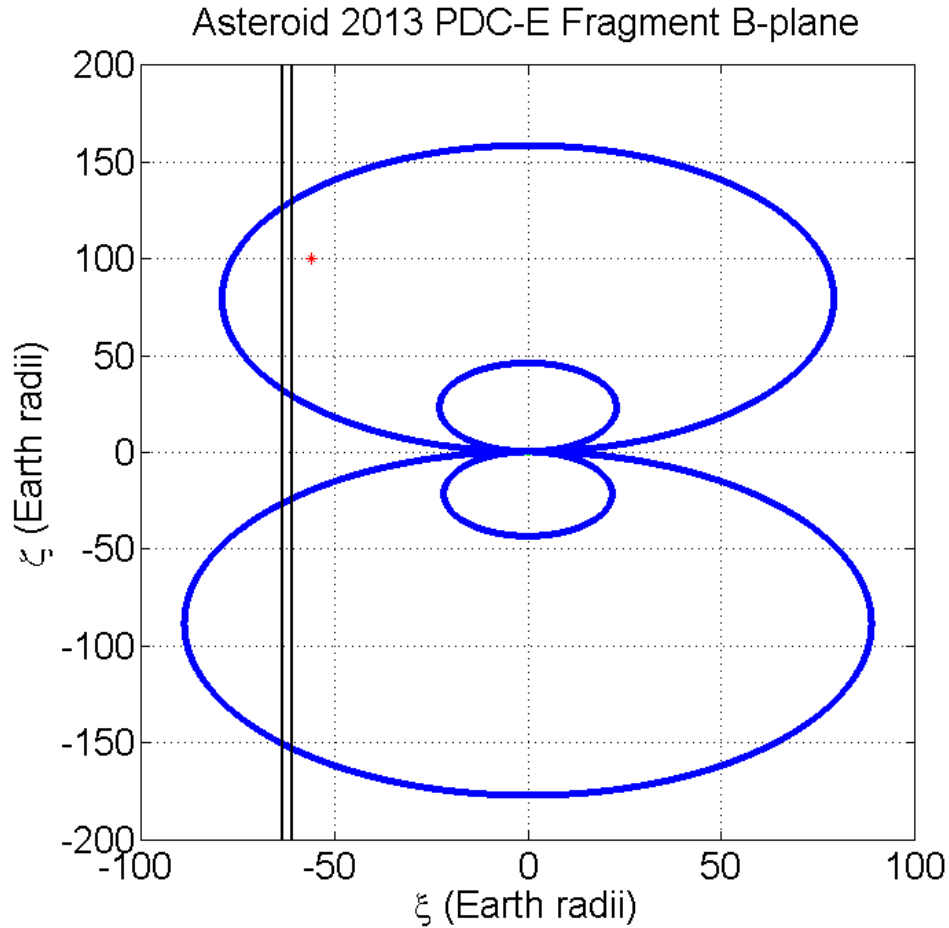
Figure 6.15   Depiction of asteroid 2013 PDC-E's fragment resonance circles. The black verti-
cal lines depict the corridor where the fragment's crossing location on the next
encounter B-plane. The red star depicts the fragment's crossing location on the
current encounter B-plane.

adequately show what is going on in the important region of the B-plane where the keyhole is

located. So, Figure 6.17 narrows in on that important region of the B-plane to show a portion

of the bounding box about the virtual fragment crossing points and the small relative size of

the established keyhole region.   What is hard to tell in this figure is the size of the keyhole

itself, in reference to the Earth for example. The keyhole width, based on the analytic the-

ory is a fraction of that of the Earth, and the keyhole itself is represented by the cyan circle

whose radius is the same as the keyhole thickness. The problem with this representation of the

keyhole on the B-plane is the misrepresentation of the entire keyhole region. It is known from
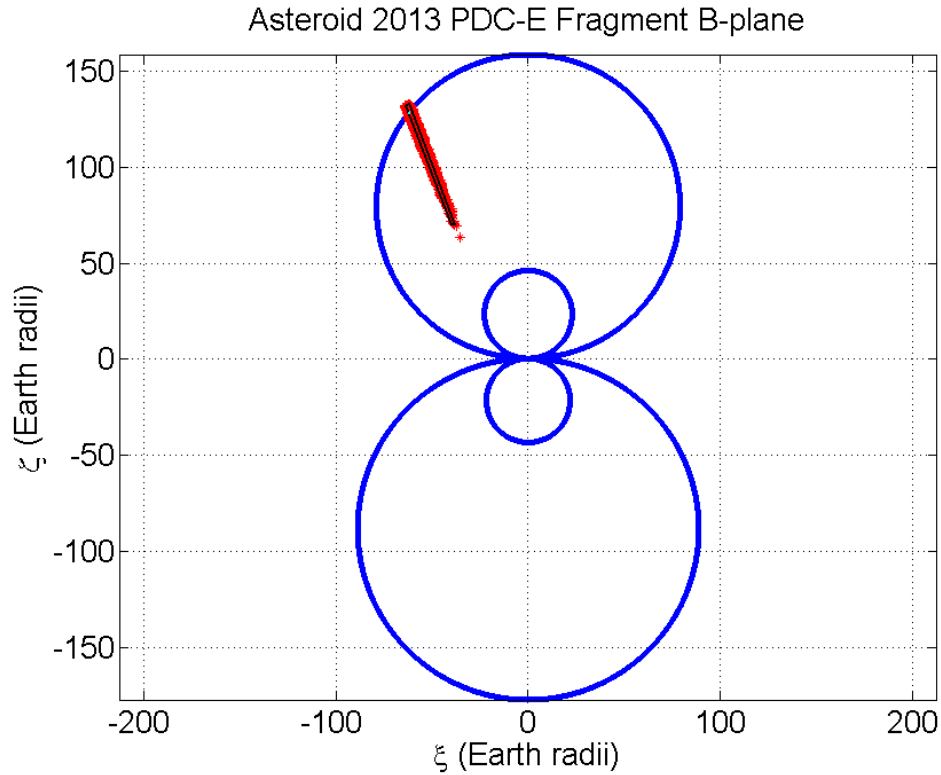
Figure 6.16   Depiction of asteroid 2013 PDC-E fragment's encounter B-plane, complete with cloud crossing locations, resonance circles, and keyhole region.

the analytic theory that a keyhole on the encounter B-plane is an arclet that follows near the resonance circle, but given the small width of the keyhole itself, the outer reaches of the arclet would not catch many more crossings than the circle representation of the keyhole. Regardless, the decision has been made to represent the keyhole region as an appropriately size circle, so the area of the keyhole circle will be used to evaluate the keyhole passage probability. So, using the area of the keyhole circle, bounding box, proportion of the crossings in the bounding box and the keyhole circle, as well as the proportion of the virtual fragments that encounter the Earth ($\approx 75\%$) in Equation 5.47, the resulting keyhole passage probability comes to be about 7.13E-06. The keyhole passage probability is highly dependent on the size of the keyhole circle, especially in this particular case where the virtual crossing locations are so linearly dense. Therefore, to a certain extent, increasing the size of the keyhole would increase the likelihood of the fragment passing through the keyhole.
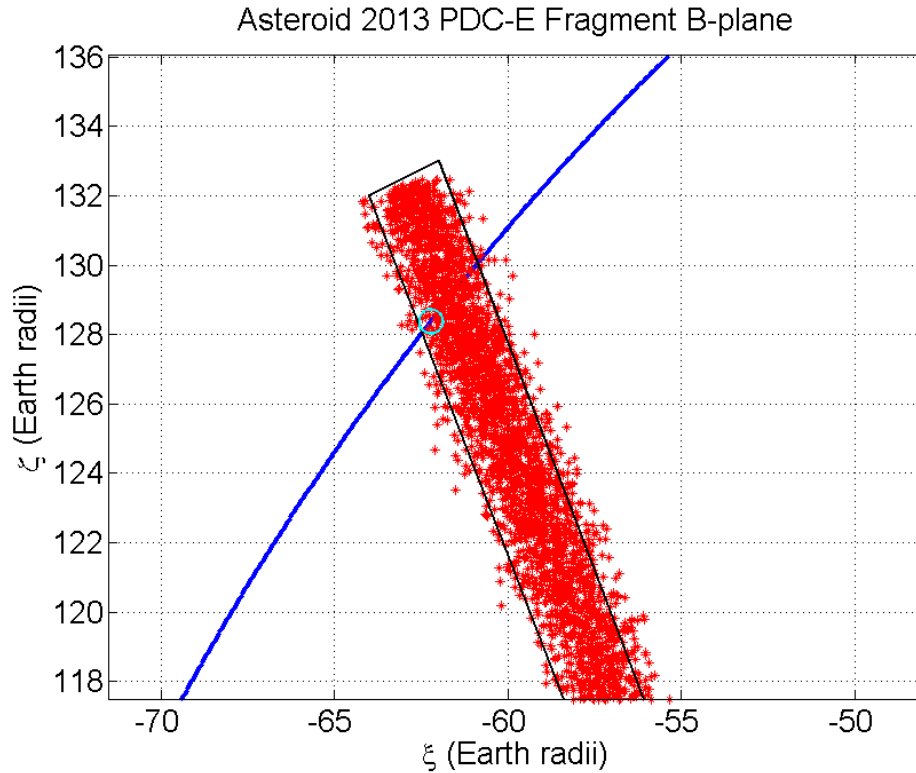
Figure 6.17   Zoomed in depiction of the keyhole region with respect to the fragment cloud crossing locations on the encounter B-plane.

At the beginning of this discussion attention was drawn to Figure 6.11 and the fact that the Earth is still at risk of being hit by a number of asteroid fragments. Common sense indicates that by simply looking at the figure, and recalling that all 10001 fragments have uniformly distributed masses, the mass impacting the Earth after the fragmentation event is substantially smaller than that of the entire asteroid mass which would have impacted the Earth had nothing been done. In fact, based on this fragmentation model of asteroid 2013 PDC-E, of the 10001 fragments simulated about 64% of the fragments had an encounter with the Earth on this close approach, and about 0.25% of those encountering fragments passed within 1.1 Earth radii of the center of the planet. So, only 0.16% of the total asteroid's mass would impact the planet. Meaning that if asteroid 2013 PDC-E had a total mass of 1.0E08 kg, the impacting asteroid mass after the fragmentation would be about 1.6E05 kg and would cause very localized damage from the potential landfall of the asteroid fragments.

6.2   Asteroid 2015 PDC

The 2015 PDC hypothetical asteroid impact scenario is considered in this section. As described in [53], the scenario begins as follows: The asteroid is discovered on April 13, 2015, the first day of the conference, at magnitude 20.9, declination -39 degrees and heading south. It is assigned the designation "2015 PDC" by the Minor Planet Center, and classified as a Potentially Hazardous Asteroid (PHA) based on its orbit. The asteroid's orbital elements are known fairly accurately even in the first few days. Its mean distance from the Sun (semi-major axis) is 1.77 AU, and the orbital eccentricity is 0.49. Its perihelion distance is 0.90 AU and aphelion distance is 2.65 AU; the orbital period is 864 days (2.37 years). The orbital inclination is fairly small: 5.35 deg. The asteroid's orbit comes very close to the Earth's orbit on its outbound leg, much like the Chelyabinsk impactor, but unlike Chelyabinsk, this asteroid impacts at its ascending node. Very little is known about the object's physical properties. Its absolute magnitude is estimated to be about H = 21.3 ± 0.4, which puts the asteroid's size at roughly 100 to 500 meters. The large size uncertainty is due to uncertainties in both albedo and H value. At discovery, the asteroid is quite distant from the Earth, about 0.34 AU (51 million kilometers or 32 million miles). It is approaching our planet and slowly brightening, but it peaks at only magnitude 20.3 on May 4. It reaches a closest approach of about 0.19 and it peaks at only magnitude 20.3 on May 4. It reaches a closest approach of about 0.19 AU (28 million km or 18 million miles) from Earth on May 12. It never gets within range of the Goldstone radar and it's too far south at close approach for the Arecibo radar. The JPL Sentry system and University of Pisa's CLOMON system both identify many potential impacts for this object at several future dates. The most likely potential impact date is September 3, 2022, but the impact probability for that date is still low in the first week after the asteroid is discovered. Nevertheless, as the object is tracked over the next few weeks, the impact probability for 2022 starts to climb, reaching 0.2% a month after discovery. Even as the asteroid fades past magnitude 22 in early June, it continues to be observed and tracked since the chance of impact just keeps rising. The first part of the scenario ends in mid-June 2015, when the probability of Earth impact in 2022 has reached 1% and will likely continue to rise as time progresses. It is

clear that the object will be observable through the rest of 2015, although it will be quite faint (22nd and 23rd magnitude) and observers will require fairly large (2-meter- class) telescopes to track it. In December 2015 and January 2016, the asteroid will fade through 24th and 25th magnitudes, requiring very large aperture telescopes such as the 4- and 8-meter class facilities of CFHT, Keck, Gemini, Subaru, VLT, etc. In the spring of 2016, the asteroid will move too close to the Sun to be observed, and it will remain unobservable for about 7 months. The asteroid's uncertainty region at the time of the potential impact is much longer than the diameter of the Earth, but its width is much less. The intersection of the uncertainty region with the Earth creates the so-called "risk corridor" across the surface of the Earth. The corridor wraps more than halfway around the globe.

6.2.1 Pre-Encounter Mission Designs

The situation with asteroid 2015 PDC is the same as that for the post-2023 encounter of asteroid 2013 PDC-E, where the asteroid is believed/known to be on an Earth-impacting trajectory and any type of mission should be looked at in order to deflect/disrupt the potentially hazardous body.
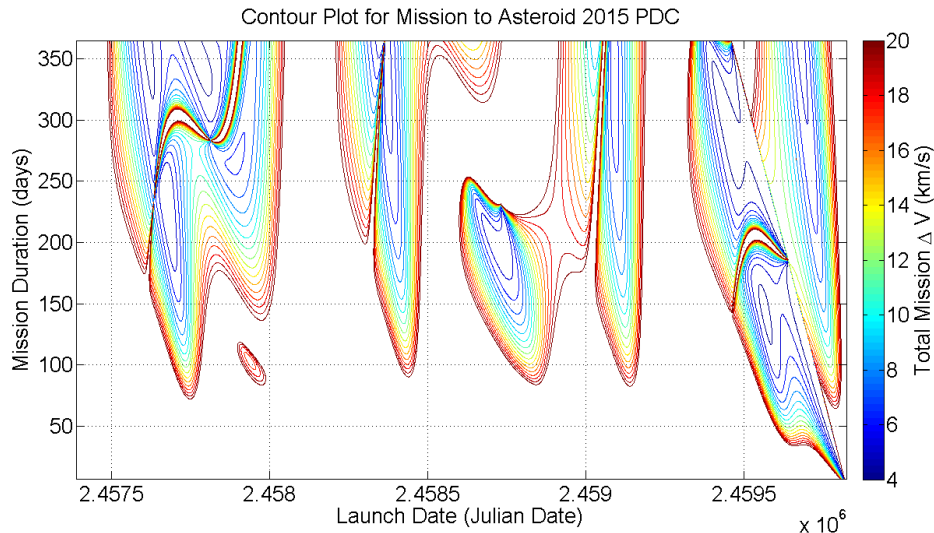
Figure 6.18 Contour plot of total mission ΔV for an intercept mission to asteroid 2015 PDC before its potential Earth impact in 2022.

Before looking at the different mission design types ((1) long-duration, long-dispersion, (2) long-duration, short-dispersion, (3) short-duration, long-dispersion, and (4) short-duration, short-dispersion), the total mission ΔV (Figure 6.18) and v_∞ (Figure 6.19) contours can be analyzed to understand how accessible asteroid 2015 PDC is from Earth between 2015 and 2022. Examining Figure 6.18, it can be seen that short-durations missions (less than 100 days) would be very difficult to be feasibly constructed for a spacecraft, before a few months before the expected impact date. When looking at mission durations of more than 100 days, it appears that there are periodic regions of the contour plot where a an intercept mission can be launched to asteroid 2015 PDC. The v_∞ contour in Figure 6.19 validates the notion that
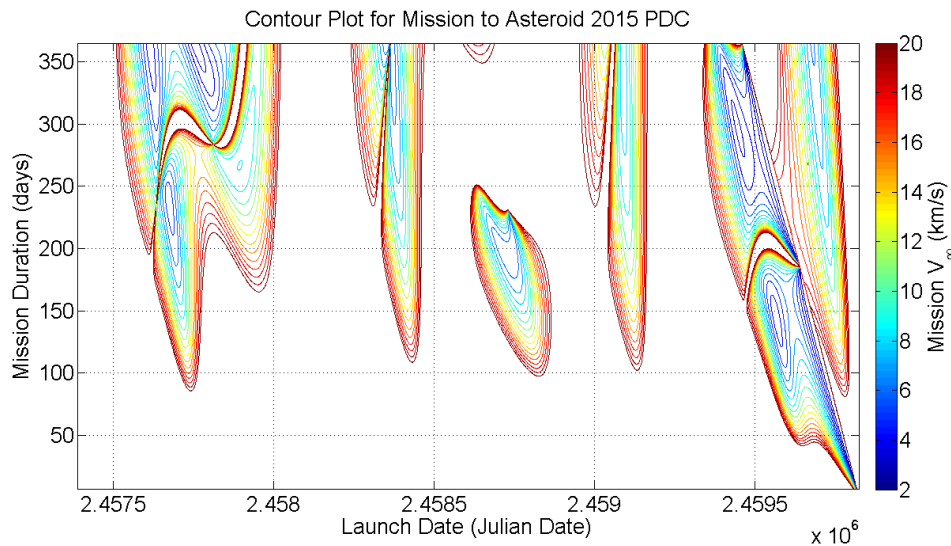
Figure 6.19   Contour plot of mission V_∞ for an intercept mission to asteroid 2015 PDC before its potential Earth impact in 2022.

short-duration missions would be hard to come by before the few months prior to the expected impact. Observing the remaining portion of Figure 6.19, it can be seen that the accessible regions of the contour plot are smaller than what they appeared to be in ΔV contour plot. Based on the v_∞ contour plot, the easiest times to launch a mission would be soon after its discovery (around the 2015/2016 time frame) and within a year of the anticipated impact date.

6.2.1.1   Long-duration, Long-dispersion Mission

Based on the assessment of the mission contours, it does not come as much of a surprise that the optimal long-duration, long-dispersion missions are soon after the asteroid's discovery. Looking at Table 6.7, it can be seen that there a small optimal launch window of about 5 days, centered around December 30, 2016, where year long missions can be launched from Earth that would easily reach asteroid 2015 PDC. Given the limited window that exists in which to launch, the majority of the last five optimal missions have the same launch date as their preferable counterparts, with a slightly smaller mission duration (364 days versus 365 days). The benefit of such an early launch would be that there is plenty of time to observe the effect of a deflection/disruption mission prior to the anticipated impact date, so if another mission needs to be launched there is time to do so. Figure 6.20 shows the trajectory that the spacecraft (blue) needs to take with respect to the Earth (green) and 2015 PDC (red) in order to accomplish the mission prescribed by the parameters in the first row of Table 6.7.

Figure 6.20   Trajectory plot for a long-duration, long-dispersion intercept mission to asteroid 2015 PDC.

Table 6.7   Top 10 mission designs for a long-duration, long-dispersion mission to asteroid 2015
PDC before its 2023 Earth encounter.

Rank	Launch (JD)	ΔV_{Total} (km/s)	C3 (km^2/s^2)	t_{disp} (days)	t_{dur} (days)	v_{arr} (km/s)	α_{arr} (rad)	α_{LOS} (rad)	α_{Sun} (rad)	J_{score}
1	2457752.5	3.49554	5.9680	1708	365	16.4705	0.5286	1.7000	1.7307	9.0174
2	2457753.5	3.49361	5.9245	1707	365	16.5462	0.5338	1.7023	1.7320	9.0219
3	2457751.5	3.49926	6.0522	1709	365	16.3904	0.5233	1.6978	1.7293	9.0244
4	2457754.5	3.49344	5.9207	1706	365	16.6177	0.5389	1.7049	1.7332	9.0376
5	2457750.5	3.50483	6.1780	1710	365	16.3060	0.5179	1.6958	1.7280	9.0428
6	2457753.5	3.50041	6.0780	1708	364	16.4760	0.5288	1.7000	1.7310	9.0448
7	2457754.5	3.49794	6.0222	1707	364	16.5501	0.5339	1.7023	1.7322	9.0462
8	2457752.5	3.50466	6.1740	1709	364	16.3975	0.5235	1.6978	1.7297	9.0546
9	2457755.5	3.49721	6.0058	1706	364	16.6199	0.5390	1.7049	1.7334	9.0588
10	2457755.5	3.49498	5.9556	1705	365	16.6848	0.5439	1.7076	1.7345	9.0644

The spacecraft has to leave the Earth's ecliptic plane, resulting in the larger $C3$ value indicated in the optimal mission designs. Due to the time that the spacecraft would be encountering the asteroid (near periapse), the relative impact speed between the two would be rather large - over 16 km/s based on the results shown in the table. The resulting mission designs would be feasible and easy to achieve, but a failure in any aspect of the mission would prove devastating because of the amount of time that would have to pass before another mission could feasibly be constructed.

6.2.1.2 Long-duration, Short-dispersion Mission

Assuming that the long-duration, long-dispersion mission failed, or did not result in a substantial deflection/disruption event, a back-up mission option would be to design a long-duration, short-dispersion mission. Trying to keep the mission duration as long as possible should reduce the necessary amount of mission ΔV needed to get into the required orbit. A short dispersion time is assumed because of the desire to gain as much knowledge of how much the previous failed missions effected the orbit of the body, if at all.

Figure 6.21   Trajectory plot for a long-duration, short-dispersion intercept mission to asteroid 2015 PDC.

Table 6.8 Top 10 mission designs for a long-duration, short-dispersion mission to asteroid
2015 PDC before its 2023 Earth encounter.

Rank	Launch (JD)	ΔV_{Total} (km/s)	C3 (km^2/s^2)	t_{disp} (days)	t_{dur} (days)	v_{arr} (km/s)	α_{arr} (rad)	α_{LOS} (rad)	α_{Sun} (rad)	J_{score}
1	2459573.5	3.27303	0.9939	7	245	10.3424	0.2558	6.2553	1.5911	5.8983
2	2459572.5	3.27304	0.9942	7	246	10.3291	0.2553	6.2553	1.5907	5.8984
3	2459571.5	3.27310	0.9955	7	247	10.3159	0.2549	6.2553	1.5903	5.898976
4	2459574.5	3.27307	0.9949	7	244	10.3556	0.2562	6.2553	1.5914	5.898980
5	2459570.5	3.27321	0.9979	7	248	10.3027	0.2544	6.2553	1.5900	5.9001
6	2459575.5	3.27318	0.9973	7	243	10.3690	0.2567	6.2553	1.5918	5.9004
7	2459569.5	3.27335	1.0010	7	249	10.2894	0.2539	6.2553	1.5896	5.9017
8	2459576.5	3.27335	1.0011	7	242	10.3823	0.2572	6.2553	1.5921	5.9026
9	2459568.5	3.27352	1.0049	7	250	10.2762	0.2535	6.2553	1.5892	5.9037
10	2459577.5	3.27359	1.0064	7	241	10.3958	0.2576	6.2553	1.5925	5.9056

Unlike the long-duration, long-dispersion mission which had to leave the plane of Earth's orbit, the top mission trajectory for a long-duration, short-dispersion mission to asteroid 2015 PDC does not have to deviate from the ecliptic as much, shown in Figure 6.21 and made evident by the results listed in Table 6.8. Again, it is interesting to note that even with the allowance for the dispersion time to be as long as 90 days and the mission duration to be as long as a full year, the optimal mission parameters include dispersion times of 7 days and mission durations around 250 days. Also, with an expected spacecraft encounter one week prior to Earth impact, the relative arrival speed between the spacecraft and the asteroid is over 10 km/s, meaning that the guidance algorithms would need to be spot on because there is no room for failure.

6.2.1.3   Short-duration, Long-dispersion Mission

As was discussed earlier, by the definition of a short-duration mission (7 - 90 days), the mission contour plots showed that other than with a short-dispersion time, no long-dispersion mission could be feasibly launched to asteroid 2015 PDC. The required mission ΔV and $C3$ orbit would be too large for any launch vehicle currently in operation to place even a small spacecraft into the necessary orbit to intercept the target body.
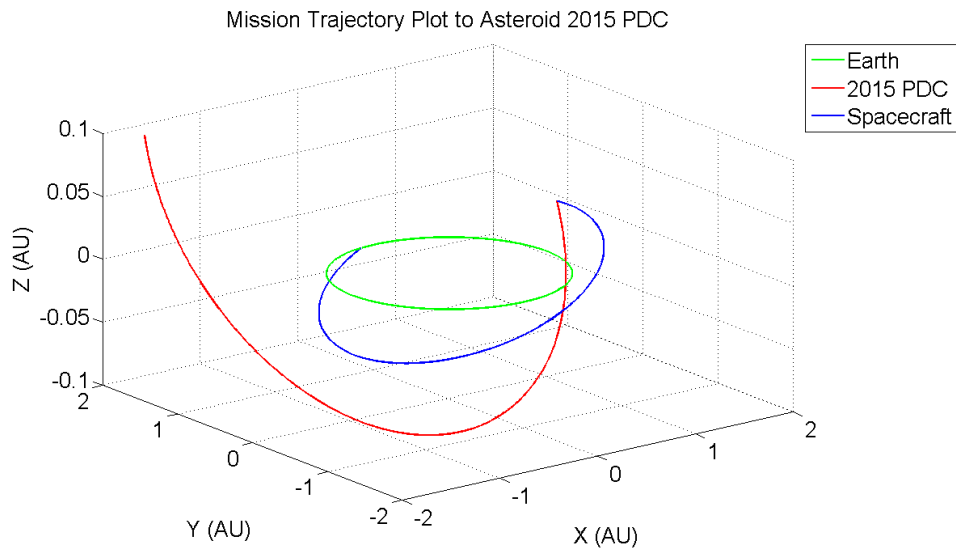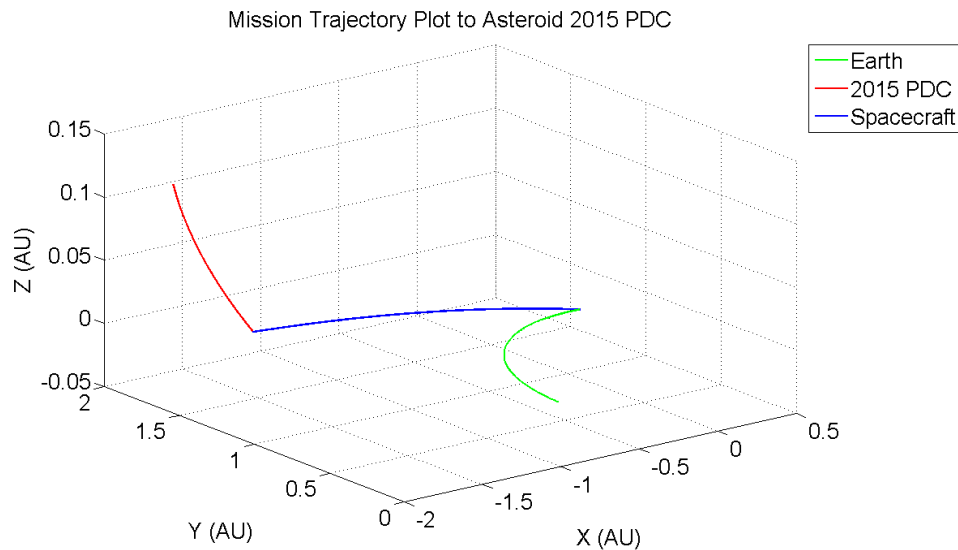

Figure 6.22   Trajectory plot for a short-duration, long-dispersion intercept mission to asteroid 2015 PDC.

Table 6.9   Top 10 mission designs for a short-duration, long-dispersion mission to asteroid 2015 PDC before its 2023 Earth encounter.

Rank	Launch (JD)	ΔV_{Total} (km/s)	C3 (km^2/s^2)	t_{disp} (days)	t_{dur} (days)	v_{arr} (km/s)	α_{arr} (rad)	α_{LOS} (rad)	α_{Sun} (rad)	J_{score}
1	2457740.5	13.8587	347.335	1995	90	34.7221	1.3926	5.8222	0.6328	33.872
2	2457739.5	13.8623	347.492	1996	90	35.0224	1.3935	5.8355	0.6305	33.877
3	2457741.5	13.8667	347.685	1994	90	34.4230	1.3918	5.8090	0.6350	33.893
4	2457738.5	13.8776	348.153	1997	90	35.3238	1.3944	5.8489	0.6283	33.908
5	2457742.5	13.8866	348.546	1993	90	34.1251	1.3909	5.7957	0.6371	33.939
6	2457737.5	13.9043	349.311	1998	90	35.6261	1.3953	5.8622	0.6260	33.962
7	2457743.5	13.9183	349.919	1992	90	33.8286	1.3901	5.7825	0.6392	34.010
8	2457736.5	13.9422	350.959	1999	90	35.9294	1.3963	5.8756	0.6236	34.042
9	2457744.5	13.9616	351.804	1991	90	33.5335	1.3894	5.7693	0.6413	34.107
10	2457735.5	13.9912	353.092	2000	90	36.2334	1.3972	5.8890	0.6212	34.145

From the results in Table 6.9, it can be seen that while AMiDST will list out the optimal mission results, none of the top 10 missions are feasible: the mission ΔV is nearly 14 km/s from LEO and the required orbit $C3$ is about 350 km^2/s^2. The trajectory depicted in Figure 6.22, gives justification for the highly energetic orbit required by the spacecraft to leave Earth and meet 2015 PDC. The optimization process tried to push the mission duration as high as possible, in an attempt to reduce the required ΔV and $C3$, but the restriction of a maximum mission duration of 90 days did not allow for more feasible missions to be considered in this analysis. Alternate definitions of short-duration could result in better mission designs, but for the sake of consistency between this example asteroid and to show the capabilities of AMiDST, the definition is unaltered.

6.2.1.4   Short-duration, Short-dispersion Mission

Assuming that it is too late for all other options, or even worse they have all failed, to diminish the threat posed by asteroid 2015 PDC, a short-duration, short-dispersion mission design is constructed to deal with the on-coming target.
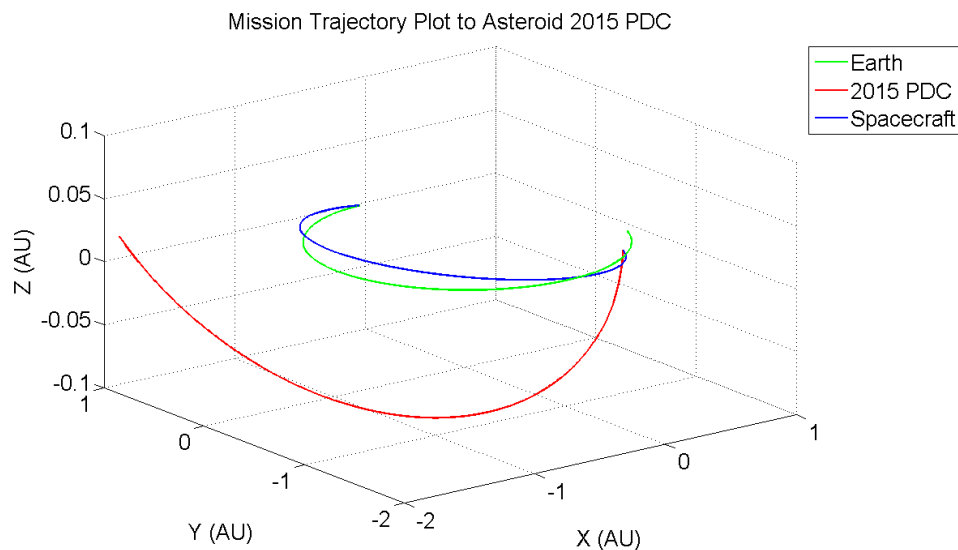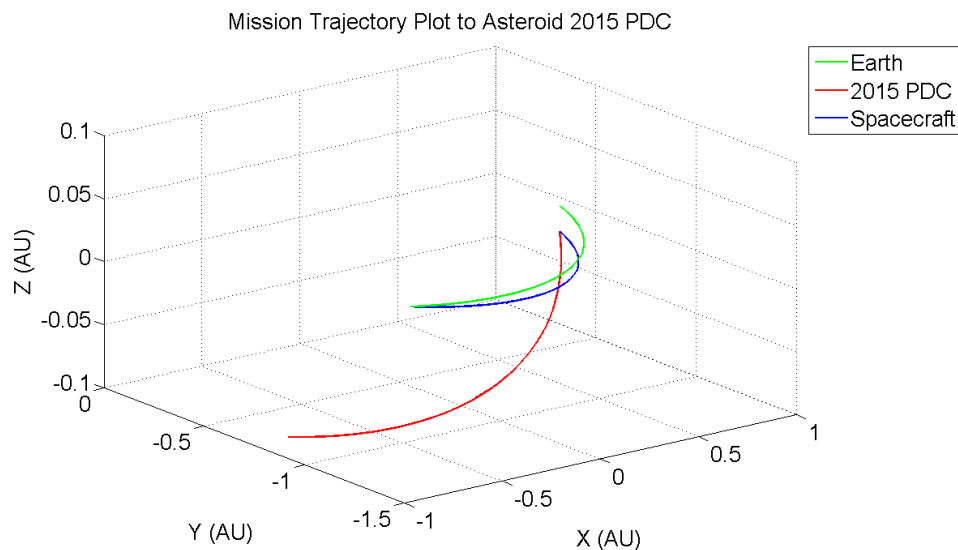

Figure 6.23   Trajectory plot for a short-duration, short-dispersion intercept mission to asteroid 2015 PDC.

Table 6.10 Top 10 mission designs for a short-duration, short-dispersion mission to asteroid
2015 PDC before its 2023 Earth encounter.

Rank	Launch (JD)	ΔV_{Total} (km/s)	C3 (km^2/s^2)	t_{disp} (days)	t_{dur} (days)	v_{arr} (km/s)	α_{arr} (rad)	α_{LOS} (rad)	α_{Sun} (rad)	J_{score}
1	2459728.5	3.2915	1.4036	7	90	11.9674	0.3036	6.2553	1.6446	6.1216
2	2459729.5	3.2922	1.4195	7	89	11.9848	0.3041	6.2553	1.6450	6.1292
3	2459730.5	3.2929	1.4350	7	88	12.0023	0.3045	6.2553	1.6454	6.1365
4	2459731.5	3.2936	1.4501	7	87	12.0200	0.3050	6.2553	1.6458	6.1436
5	2459732.5	3.2943	1.4646	7	86	12.0379	0.3055	6.2553	1.6463	6.1504
6	2459733.5	3.2949	1.4787	7	85	12.0560	0.3060	6.2553	1.6467	6.1570
7	2459734.5	3.2955	1.4921	7	84	12.0742	0.3065	6.2553	1.6471	6.1632
8	2459735.5	3.2961	1.5051	7	83	12.0926	0.3069	6.2553	1.6476	6.1693
9	2459736.5	3.2967	1.5176	7	82	12.1112	0.3074	6.2553	1.6480	6.1751
10	2459737.5	3.2972	1.5298	7	81	12.1299	0.3079	6.2553	1.6485	6.1807

The late launch window, short mission duration, and short dispersion time implies that the asteroid has now entered the terminal phase of its orbit with respect to the Earth and reaching the body from Earth should be a much simpler task. Figure 6.23 shows the simplicity of the orbit needed by the spacecraft to leave Earth and intercept the asteroid. The results from Table 6.10 show that the longer the mission duration and the longer the dispersion time for the desired intercept mission would produce a more manageable design. Low total mission ΔV and $C3$ values allow for larger spacecraft and/or smaller launch vehicles to be used, but the hypervelocity relative arrival speed between the spacecraft and the asteroid mandates the use of a spacecraft similar to the HAIV for any attempted fragmentation mission. Despite the ease of this type of mission design, it should be noted that this type of mission should be considered as a last resort when all other attempts have failed, and not considered only when there are no other options able to be taken.

6.2.2 Fragmentation of Asteroid 2015 PDC

A similar analysis is done now with asteroid 2015 PDC, as was done to asteroid 2013 PDC-E. Since the work described throughout this dissertation focuses on short warning times, the time from the disruption event to the asteroid fragments encountering the planet is set to be one year. Assuming the fragment states are normally distributed about the nominal asteroid trajectory's states, before the radial perturbation is applied, the fragments are then propagated over that year time span through to their individual encounters with the Earth. The resulting crossing points of the 10001 virtual asteroid fragments on the encounter B-plane are shown in Figure 6.24. It can be seen from the composite B-plane that the asteroid fragments are spread across a wide portion of the map. For reference, a small circular cross-section of the Earth can be seen centered at the origin with a unit radius.

The asteroid 2013 PDC-E fragment that was selected for analysis had a very shallow encounter with the Earth, crossing the B-plane over 110 Earth radii from the center of the planet. For asteroid 2015 PDC, the asteroid fragment selected crosses the B-plane a lot closer to Earth (about 9 Earth radii from the center of the planet. Using the same state standard deviations of 10 meters and 1 meter per second, normally distributed about the nominal asteroid states,
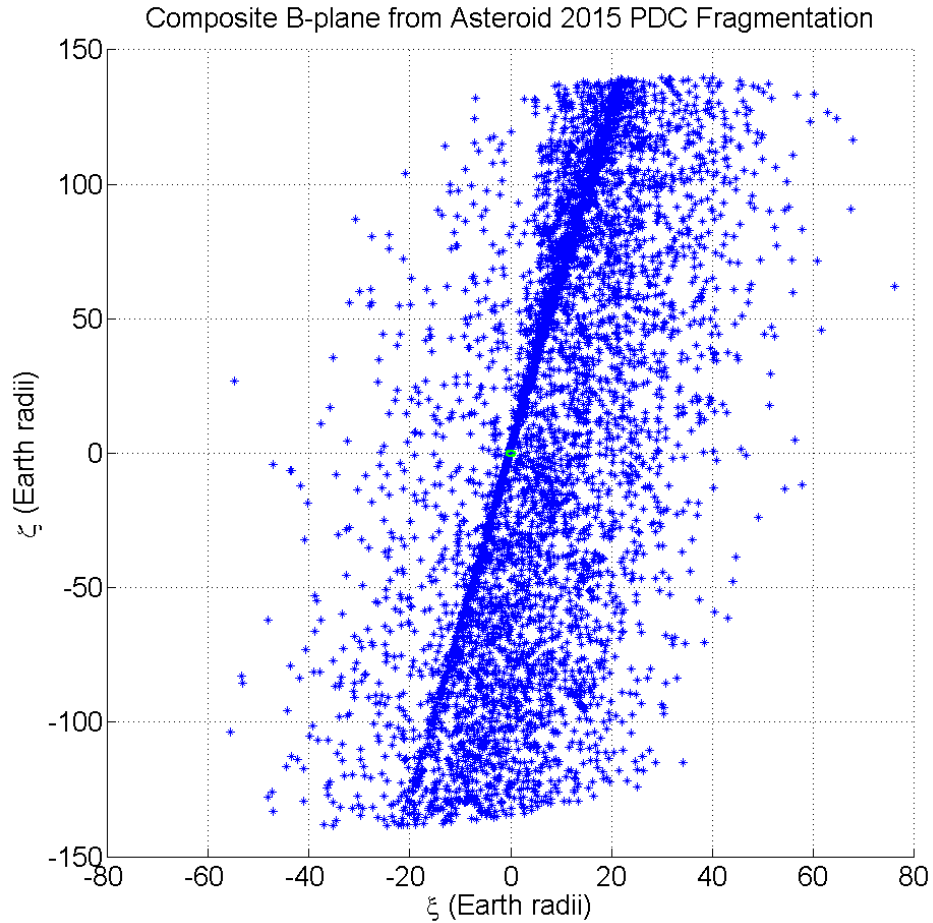
Figure 6.24   Composite encounter B-plane showing the crossing locations of asteroid 2015 PDC's fragments.

a field of 10000 virtual asteroid fragments is created and propagated through the encounter B-plane, including the nominal asteroid fragment's trajectory. Figure 6.25 shows the crossing locations of the virtual fragment field on the encounter B-plane.   Unlike the 2013 PDC-E fragment that was selected, where the fragment cloud did not reach the Earth on the B-plane, the 2015 PDC fragment cloud encompasses the Earth. In fact, about 2.9% of the 10001 simu-lated virtual fragments pass within 1.1 Earth radii of the center of the planet. Looking closely at the span of the crossing locations, it is easy to see that there are larger portion of the virtual fragments that cross the B-plane farther from the planet (in the first quadrant of the plane, implying a late encounter) as opposed to the third quadrant (earlier encounter). A histogram of the radial distances of the fragment cloud crossing positions is shown in Figure 6.26.   The
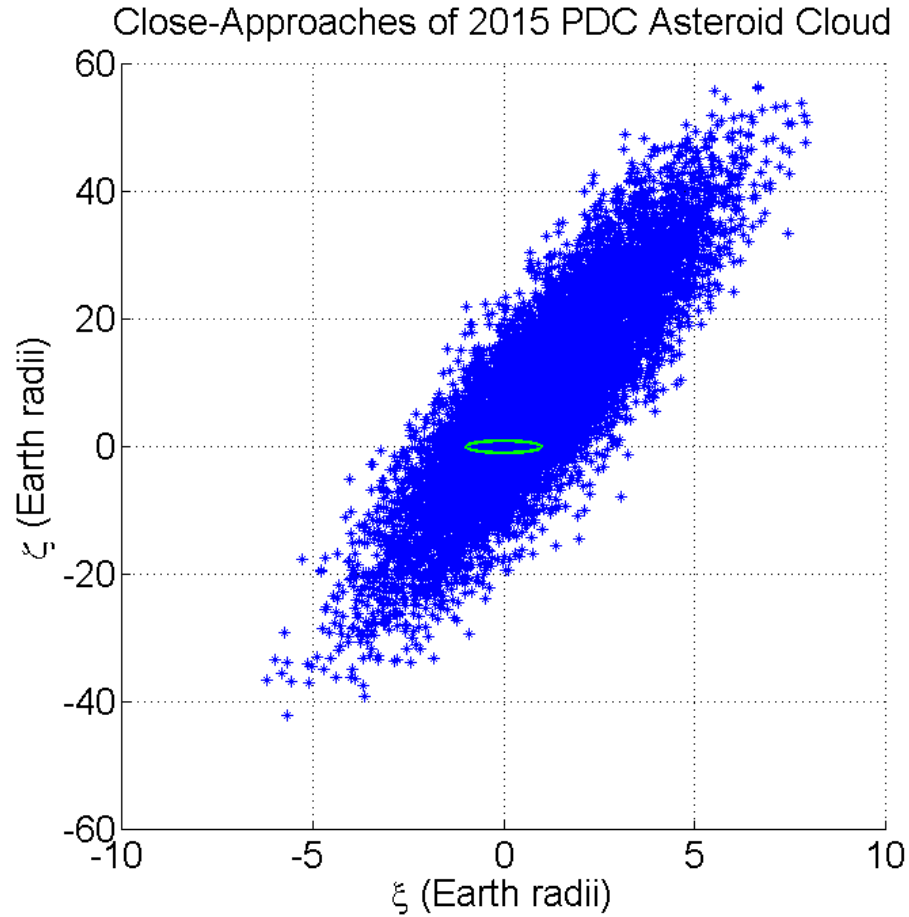
Figure 6.25   Asteroid 2015 PDC fragment cloud crossing locations on close-encounter B-plane.

radial position histogram shows a skewed distribution, with a large portion of the data being between 0 and about 12 Earth radii. Fitting a gamma distribution to the radial position data, the calculated probability that the asteroid fragment would fall within 1.1 Earth radii is approximately 2.4%.   Looking back to the representative fragment from the fragmentation of asteroid 2013 PDC-E, which also had a skewed radial histogram, the B-plane component distributions were also skewed. That is not the case however for the selected 2015 PDC asteroid fragment, as indicated by Figure 6.27. The B-plane component distributions for the 2015 PDC asteroid fragment appear to be nearly normal. But, as previously stated, it cannot be assumed that just because the initial fragment field states are normally distributed that the resulting B-plane components would be normally distributed. The histograms in Figure 6.27 show the
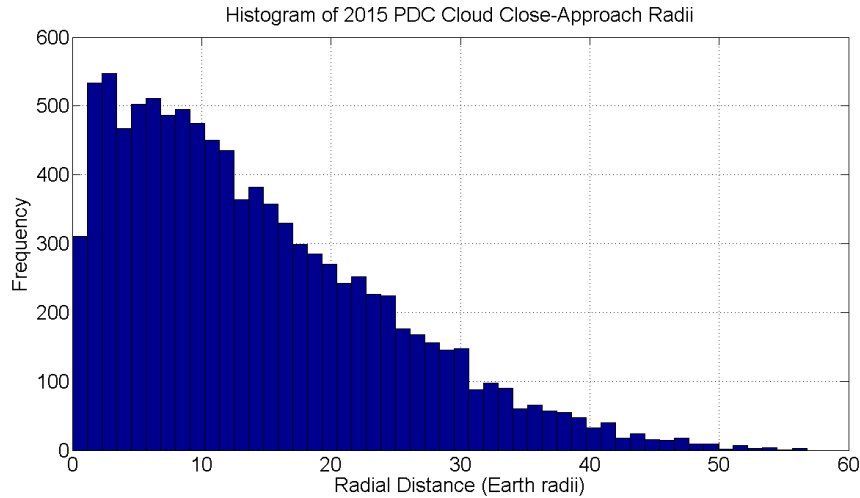
Figure 6.26   Histogram of asteroid 2015 PDC's fragment cloud radial crossing locations.

distributions of the fragment cloud's B-plane components. Looking at the ξ-component, the distribution appears to be pretty normal, with a mean a bit larger than one Earth radius. The ζ-component however, appears to be comprised of two different normal distributions (one for the left portion of the distribution and one for the right portion).

Switching focus back to the current and future risk posed by the asteroid fragment to the Earth, Figure 6.28 is used to better understand the future risk imposed by the chosen fragment. The plot shows three potential resonances that the asteroid fragment could fall into given its encounter with the Earth and the crossing location of the fragment's nominal trajectory, with respect to the cross-section of the Earth on the B-plane. However, this fragment's post-encounter trajectory does not fall into one of those resonance orbits. The calculated, expected crossing position of the asteroid fragment on the next encounter B-plane is at a ξ-value of about 120 Earth radii from the center of the Earth, nowhere near the small resonance circles. According to analytic keyhole theory, the resonances represented by the blue resonance circles have no keyholes on the depicted 2022 B-plane, due to there being no intersections between the resonance circles and the expected ξ-value line on the future encounter. Just because this fragment does not present a risk to the Earth in the near future, does not mean that the threat from this fragment is non-existent. There could be potential dangers to the Earth that go beyond the 10 year future that was looked at in this analysis, a different methodology must
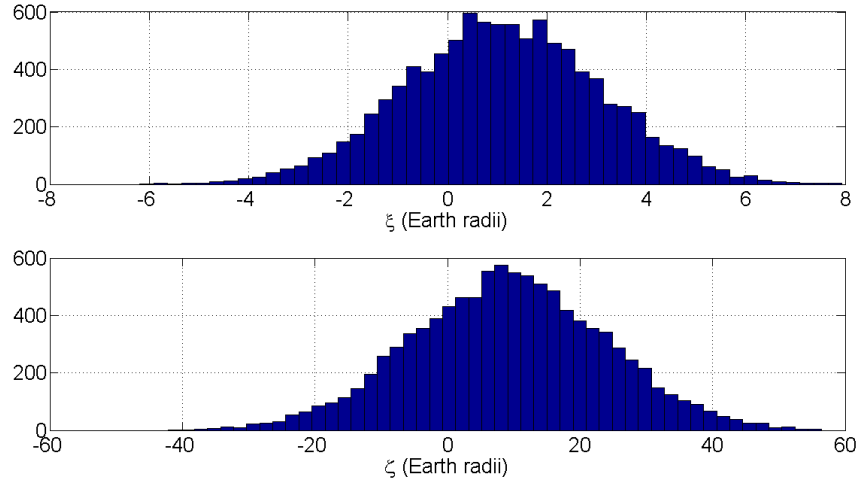
Figure 6.27 **Top:** Histogram of asteroid 2015 PDC's fragment cloud ξ components. **Bottom:** Histogram of asteroid 2015 PDC's fragment cloud ζ components.

be used to adequately evaluate those potential risks because of the length of time between the encounters and the perturbations that could sufficiently effect the orbit over that timespan.

Even though there has been an assessment of the likelihood of the fragment from asteroid 2015 PDC impacting the planet on its 2022 encounter, the keyhole passage probability equation (Equation 5.47) can be used to find another estimate for the impact probability. For this particular fragment cloud, all 10001 simulated virtual fragments had an encounter with the planet, which makes $p_{encounter}$ equal to one. Instead of putting a bounding box around the simulated crossing locations an ellipse would fit the distribution better, leaving a smaller proportion of the data outside of the bounding area while including less extraneous areas of the B-plane. Compiling the appropriate values and plugging them into the formula, the resulting impact probability comes to be about 0.011% - about two orders of magnitude smaller than the numbers listed previously. The reason for the discrepancy can attributed to a number of reasons: (1) the value obtained from Equation 5.47 is made assuming that the crossing locations on the B-plane are evenly distributed throughout the bounded areas used in the calculations, (2) the estimated impact probability calculated from the fitted distribution is dependent on how well the distribution fits the data, and (3) the calculated impact probability using the number of simulated virtual impacts and virtual asteroid fragments is dependent on the num-
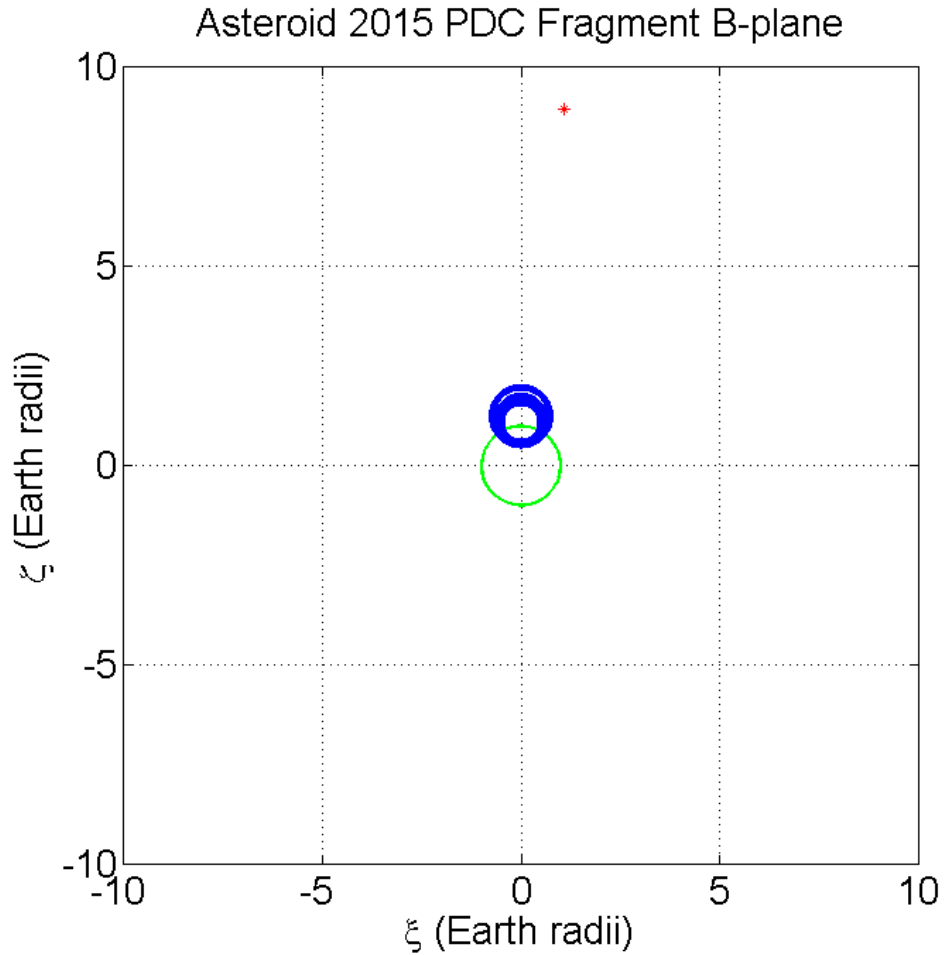
Figure 6.28   Depiction of asteroid 2015 PDC's fragment resonance circles. The red star depicts the fragment's crossing location on the current encounter B-plane.

ber of simulated asteroid fragments, where the resulting impact probability should approach the true value as the number of values increases. What can be done with the various impact probabilities from the fragment cloud is that they can be used as bounds for what the true impact probability would be for the asteroid.

Looking back at Figure 6.24, it seems that the Earth is sitting in a region of the B-plane map where there is a non-negligible chance of it getting hit by more than one asteroid fragment, given the modeled fragmentation event. If it is assumed that the fragmentation only produces the 10001 asteroid fragments simulated in this example, only about 5200 of the 10001 virtual asteroid fragments ended up having an immediate encounter with Earth, and only 15 of those

passed with 1.1 Earth radii of the planet center. What that means is that given this type fragmentation event, with a year timespan for the asteroid fragments to disperse from the original asteroid's impact trajectory, the Earth would only be impacted with about 0.15% of the total asteroid mass, rather than the full asteroid mass if nothing were done to deflect/disrupt the target body. And, if the assumption is made that the mass of the asteroid is evenly distributed among the simulated asteroid fragments, the 15 impacting virtual asteroid fragments would only cause localized damage to the parts of the Earth they impact (if they make landfall), rather than the potential regional or global damage that could be caused by the full asteroid impacting the planet.

CHAPTER 7.   CONCLUSIONS

7.1   General Summary

The work discussed in this dissertation centers around the assessment of the current and future risk posed by an asteroid or asteroid fragment with respect to the Earth. Using an in-house N-body gravitational propagator, an asteroid's trajectory is tracked over time and through planetary encounters. The interactions between the target asteroid body and the Earth are evaluated to understand the change that the orbit will undergo, in order to gain perspective on the future potential of that body to impact the planet. Given the evaluated threat of the asteroid, an in-house mission design tool (AMiDST) can be used to construct three mission scenarios (intercept, intercept at 10 km/s, and rendezvous) to help assess or deal with the threatening asteroid body.

In the past, when it comes to gauging the threat that a foreign body carries in regards to the planet there are two schools of thought: numerical simulation and analytic evaluation, with both approaches having their pros and cons. With the understanding of the limitations regarding the numerical and analytic methodologies, the purpose of this work was to develop an efficient, semi-analytic, computational tool that would be able to assess the risk imposed by those bodies before and after a deflection/disruption event. Beyond the simple assessment of the immediate impact probability, an estimate was constructed of the likelihood of the body impacting the Earth in potential future encounters. The current and future impact risk is only a small part of the problem however. If it is found that the impact risk is too large to ignore and the decision is made that something has to be done about the threat, the AMiDST component of the tool can optimize a feasible deflection, disruption, or rendezvous mission to the target.

Other computational tools look at a part of the asteroid risk assessment problem. Trajectory

design algorithms mostly attempt to optimize the interplanetary portion of the mission trajectories, neglecting the feasibility of launching a spacecraft that can enter into such trajectory or the approach of the spacecraft with respect to the target. Impact probability calculations either require large, high-fidelity simulations to be run or use analytic algorithms that make so many assumptions and deal with very short timescales. While useful to an extent, there is always something missing these algorithms are used individually.

The AMiDST program uses a fast, efficient grid-based search, along with a cost function evaluation method to find the optimal mission from launch to target acquisition that will fulfill the imposed mission requirements. The impact risk assessment tool takes advantage of the precision and high-fidelity modeling of an N-body gravitational propagator to diminish the drawbacks of incorporated analytic methods like planetary encounter geometry, B-plane targeting, and analytic keyhole theory. Drawbacks like two-body, unperturbed Keplerian orbit propagation in the analytic methodologies reduce the accuracy and overall fidelity of the computed results. When the AMiDST and impact risk assessment tools are merged, the result is an efficient, semi-analytic, computational tool that can be used to design and assess a threatening near-Earth asteroid mission from launch to post-deflection/disruption orbit propagation.

APPENDIX A.   ANALYTIC KEYHOLE THEORY: COMPUTATIONAL DETAILS

In this appendix, the full analytic theory of keyhole computation is presented.

A.1   Pre-Encounter State Vector

Using the heliocentric orbital elements $(a, e, i, \Omega, \omega, \nu)$ of the asteroid body, the pre-encounter state vector $(U, \theta, \phi, \xi, \zeta, t_0)$ is computed. In order to do this, where the encounter takes place must be considered. Let λ_P be the longitude of the encountered planet at time t_0. If at $t = t_0$ $\nu = -\omega$, then the encounter takes place at the ascending node of the asteroid's orbit, in the post-perihelion portion of the orbit if $\pi < \omega < 2\pi$, and in the pre-perihelion portion otherwise. If at $t = t_0$ $\nu = \pi - \omega$, then the encounter takes place at the descending node of the asteroid's orbit, in the post-perihelion portion of the orbit if $0 < \omega < \pi$, and in the pre-perhelion portion otherwise.

Neglecting higher order terms in the miss distance at the node of the encounter, the values of ξ and ζ at the ascending node can be calculated as follows

$$\xi = \cos\phi \left[\frac{a\left(1 - e^2\right)}{1 + e\cos\omega} - 1 \right] \tag{A.1}$$

$$\zeta = \xi\cos\theta\tan\phi - \sin\theta\left(1 + \frac{\xi}{\cos\phi}\right)\tan\left(\Omega - \lambda_P\right) \tag{A.2}$$

with $0 < \phi < \frac{\pi}{2}$ if $0 < \nu < \pi$, $\pi < \omega < 2\pi$, or $\frac{3\pi}{2} < \phi < 2\pi$ if $\pi < \nu < 2\pi$, $0 < \omega < \pi$, whereas if the encounter took place at the descending node ξ and ζ are formulated as follows

$$\xi = \cos\phi \left[\frac{a\left(1 - e^2\right)}{1 - e\cos\omega} - 1 \right] \tag{A.3}$$

$$\zeta = \xi\cos\theta\tan\phi - \sin\theta\left(1 + \frac{\xi}{\cos\phi}\right)\tan\left(\Omega - \lambda_P - \pi\right) \tag{A.4}$$

with $\frac{\pi}{2} < \phi < \pi$ if $0 < \nu < \pi$, $0 < \omega < \pi$, or $\pi < \phi < \frac{3\pi}{2}$ if $\pi < \nu < 2\pi$, $\pi < \omega < 2\pi$. The remaining components of the state vector U, θ and ϕ can be found directly from the heliocentric orbital elements

$$U = \sqrt{3 - \frac{1}{a} - 2\sqrt{a\left(1-e^2\right)}\cos i} \tag{A.5}$$

$$\cos\theta = \frac{\sqrt{a\left(1-e^2\right)}\cos i - 1}{U} \tag{A.6}$$

$$\tan\phi = \frac{\pm\sqrt{2 - 1/a - a\left(1-e^2\right)}}{\pm\sqrt{a\left(1-e^2\right)}\sin i} \tag{A.7}$$

where the quadrant of ϕ is determined based on the considerations stated above. And, the node-crossing time t_0 can be computed by standard two-body formulas. Finally, the heliocentric state vector components a, e, and i can also be calculated from U, θ, and ϕ

$$a = \frac{1}{1 - U^2 - 2U\cos\theta} \tag{A.8}$$

$$e = U\sqrt{(U + 2\cos\theta)^2 + \sin^2\theta\sin^2\phi\left(1 - U^2 - 2U\cos\theta\right)} \tag{A.9}$$

$$i = \tan^{-1}\left(\frac{U\sin\theta\cos\phi}{1 + U\cos\theta}\right) \tag{A.10}$$

The computations depicted above assume that the encounter between the planet and the asteroid body takes place at a distance $r = 1$. However, the non-zero planetocentric distance of the asteroid body affects the computation of U, θ, and ϕ from a, e, and i if $r \neq 1$. If $r = 1 + \epsilon$, then the explicit formulation of U_ϵ, θ_ϵ, and ϕ_ϵ (the corresponding values of U, θ, and ϕ in the given scenario), to first-order in ϵ are

$$U_\epsilon = U - \epsilon \cdot \frac{2U^3\cos\theta + 4U^2\cos^2\theta + U^2 + 1}{U^2 + 2U\cos\theta + 1} \tag{A.11}$$

$$\cos\theta_\epsilon = \cos\theta + \epsilon \cdot \frac{U^3\left(2\cos^2\theta + \cos\theta\right) + U^2\left(4\cos^3\theta + 2\cos^2\theta + \cos\theta + 1\right) + U\cos\theta + \cos\theta - 1}{U^3 + 2U^2\cos\theta + U} \tag{A.12}$$

$$\sin\phi_\epsilon = \sin\phi + \epsilon \cdot \frac{U^3\left(1 - \sin^2\theta\sin^2\phi\right) + 2U^2\cos\theta\left(2 - \sin^2\theta\sin^2\phi\right) + U\left(1 + 4\cos^2\theta + \sin^2\theta\sin^2\phi\right) + 2\cos\theta}{U\sin^2\theta\sin\phi\left(U^2 + 2U\cos\theta + 1\right)} \tag{A.13}$$

$$\cos\phi_\epsilon = \cos\phi\left(1 + \epsilon \cdot \frac{U^2 + 2U\cos\theta - 1}{U^2 + 2U\cos\theta + 1}\right) \tag{A.14}$$

where U, θ, and ϕ are the values calculated when $\epsilon = 0$, and

$$\epsilon = \zeta\cos\theta\sin\phi + \xi\cos\phi \tag{A.15}$$

Also, if given a generic $\vec{U}$ applied at $r = 1 + \epsilon$, a_ϵ, e_ϵ, and i_ϵ can be calculated from the components of $\vec{U}$, to first-order in ϵ,

$$\frac{1}{a_\epsilon} \approx \frac{1}{a} - 2\epsilon \tag{A.16}$$

$$a_\epsilon \approx \frac{a}{1 - 2a\epsilon} \approx a\left(1 + 2a\epsilon\right) \quad for \quad a << \frac{1}{\epsilon} \tag{A.17}$$

$$e_\epsilon = e + \epsilon \cdot U \left(2U - U \sin^2\theta \sin^2\phi + 4\cos\theta\right) \tag{A.18}$$

$$\tan i_\epsilon = \tan i \cdot \left(1 - \frac{\epsilon}{1 + U_y}\right) \tag{A.19}$$

where a, e, and i are the values calculated when $\epsilon = 0$.

A.2   Post-Encounter State Vector

The planetary encounter, within this formulation of the problem, can be seen as an operator that maps the pre-encounter state vector $(U, \theta, \phi, \xi, \zeta, t_0)$ to the post-encounter state vector $(U', \theta', \phi', \xi', \zeta', t_0')$. The components of the post-encounter state vector, given as functions of the pre-encounter state vector components and the impact parameter $(b = \sqrt{\xi^2 + \zeta^2})$, are as follows

$$U' = U \tag{A.20}$$

$$\theta' = \cos^{-1}\frac{\left(b^2 - c^2\right)\cos\theta + 2c\zeta\sin\theta}{b^2 + c^2} = \sin^{-1}\frac{\sqrt{\left[(b^2 - c^2)\sin\theta - 2c\zeta\cos\theta\right]^2 + 4c^2\xi^2}}{b^2 + c^2} \tag{A.21}$$

$$\phi' = \cos^{-1}\frac{\left[(b^2 - c^2)\sin\theta - 2c\zeta\cos\theta\right]\cos\phi + 2c\xi\sin\phi}{sqrt[(b^2 - c^2)\sin\theta - 2c\zeta\cos\theta]^2 + 4c^2\xi^2} = \sin^{-1}\frac{\left[(b^2 - c^2)\sin\theta - 2c\zeta\cos\theta\right]\sin\phi + 2c\xi\cos\phi}{\sqrt{\left[(b^2 - c^2)\sin\theta - 2c\zeta\cos\theta\right]^2 + 4c^2\xi^2}} \tag{A.22}$$

$$\xi' = \frac{\left(b^2 + c^2\right)\xi\sin\theta}{\sqrt{\left[(b^2 - c^2)\sin\theta - 2c\zeta\cos\theta\right]^2 + 4c^2\xi^2}} \tag{A.23}$$

$$\zeta' = \frac{\left(b^2 - c^2\right)\zeta\sin\theta - 2b^2c\cos\theta}{\sqrt{\left[(b^2 - c^2)\sin\theta - 2c\zeta\cos\theta\right]^2 + 4c^2\xi^2}} \tag{A.24}$$

$$t_0' = t_0 + \frac{2c\left[\xi\sin\phi\left(2\zeta\cos\theta - \xi\tan\phi\right) - \cos\phi\left(\xi^2\sin^2\theta + \zeta^2\right)\right]}{U\sin\theta\left[\left[(b^2 - c^2)\sin\theta - 2c\zeta\cos\theta\right]\cos\phi + 2c\xi\sin\phi\right]} \tag{A.25}$$

where $c = m/U^2$ and m is the mass of the encountered planet.

A.3   Propagation to the Next Encounter

Due to the analytic nature of the problem set up, the pure Keplerian propagation between the first encounter and the next encounter (the post-encounter state vector and the pre-next-encounter state vector, respectively) can also be seen as an operator mapping from one vector to the other. The transformation is as such

$$U'' = U' \tag{A.26}$$

$$\theta'' = \theta' \tag{A.27}$$

$$\phi'' = \phi' \tag{A.28}$$

$$\xi'' = \xi' \tag{A.29}$$

$$\zeta'' = \zeta' - \left[\mod \left(h \cdot 2\pi a'^{3/2} + \pi, 2\pi \right) - \pi \right] \sin \theta' \tag{A.30}$$

$$t_0'' = t_0' + h \cdot 2\pi a'^{3/2} \tag{A.31}$$

where a' is the post-encounter semi-major axis. According to classical theory, that assumes the position of the small encountering body coincides with that of the encountered planet, the post-encounter semi-major axis can be calculated from

$$a' = \frac{b^2 + c^2}{(b^2 + c^2)(1 - U^2) - 2U\left[(b^2 - c^2)\cos\theta + 2c\zeta\sin\theta\right]} \tag{A.32}$$

For finite miss distances, the first order correction to Opik's expression would be

$$\frac{1}{a'_{\epsilon'}} = \frac{1}{a'} - 2\epsilon' \tag{A.33}$$

with

$$\epsilon' = \frac{2b^2 c \sin\theta \sin\phi + \left(b^2 - c^2\right)\left(\zeta \cos\theta \sin\phi + \xi \cos\phi\right)}{b^2 + c^2} \tag{A.34}$$

A.4   Derivatives

Since the evolution of the asteroid body's orbit from before the first encounter to before the second encounter can be seen as a series of transformations from one state vector to another, assuming Keplerian propagation during the major sequences, a matrix of derivatives can be

constructed to go directly from the first pre-encounter state vector to the pre-next-encounter state vector

$$\frac{\partial(U'', \theta'', \phi'', \xi'', \zeta'', t_0'')}{\partial(U, \theta, \phi, \xi, \zeta, t_0)} = \frac{\partial(U'', \theta'', \phi'', \xi'', \zeta'', t_0'')}{\partial(U', \theta', \phi', \xi', \zeta', t_0')} \cdot \frac{\partial(U', \theta', \phi', \xi', \zeta', t_0')}{\partial(U, \theta, \phi, \xi, \zeta, t_0)} \tag{A.35}$$

where the propagation derivatives matrix is considered to be a function of the pre-first encounter state $(U, \theta, \phi, \xi, \zeta, t_0)$. For encounters computed with the extended Opik theory

$$\frac{\partial(U', \theta', \phi', \xi', \zeta', t_0')}{\partial(U, \theta, \phi, \xi, \zeta, t_0)} = \begin{bmatrix} 1 & 0 & 0 & 0 & 0 & 0 \\ \frac{\partial \theta'}{\partial U} & \frac{\partial \theta'}{\partial \theta} & 0 & \frac{\partial \theta'}{\partial \xi} & \frac{\partial \theta'}{\partial \zeta} & 0 \\ \frac{\partial \phi'}{\partial U} & \frac{\partial \phi'}{\partial \theta} & \frac{\partial \phi'}{\partial \phi} & \frac{\partial \phi'}{\partial \xi} & \frac{\partial \phi'}{\partial \zeta} & 0 \\ \frac{\partial \xi'}{\partial U} & \frac{\partial \xi'}{\partial \theta} & \frac{\partial \xi'}{\partial \phi} & \frac{\partial \xi'}{\partial \xi} & \frac{\partial \xi'}{\partial \zeta} & 0 \\ \frac{\partial \zeta'}{\partial U} & \frac{\partial \zeta'}{\partial \theta} & \frac{\partial \zeta'}{\partial \phi} & \frac{\partial \zeta'}{\partial \xi} & \frac{\partial \zeta'}{\partial \zeta} & 0 \\ \frac{\partial t_0'}{\partial U} & \frac{\partial t_0'}{\partial \theta} & \frac{\partial t_0'}{\partial \phi} & \frac{\partial t_0'}{\partial \xi} & \frac{\partial t_0'}{\partial \zeta} & 1 \end{bmatrix} \tag{A.36}$$

and, for a purely Keplerian heliocentric propagation between the two encounters

$$\frac{\partial(U'', \theta'', \phi'', \xi'', \zeta'', t_0'')}{\partial(U', \theta', \phi', \xi', \zeta', t_0')} = \begin{bmatrix} 1 & 0 & 0 & 0 & 0 & 0 \\ 0 & 1 & 0 & 0 & 0 & 0 \\ 0 & 0 & 1 & 0 & 0 & 0 \\ 0 & 0 & 0 & 1 & 0 & 0 \\ \frac{\partial \zeta''}{\partial U'} & \frac{\partial \zeta''}{\partial \theta'} & \frac{\partial \zeta''}{\partial \phi'} & \frac{\partial \zeta''}{\partial \xi'} & \frac{\partial \zeta''}{\partial \zeta'} & 0 \\ \frac{\partial t_0''}{\partial U'} & \frac{\partial t_0''}{\partial \theta'} & \frac{\partial t_0''}{\partial \phi'} & \frac{\partial t_0''}{\partial \xi'} & \frac{\partial t_0''}{\partial \zeta'} & 1 \end{bmatrix} \tag{A.37}$$

so the composite propagation matrix has the following structure

$$\frac{\partial(U'', \theta'', \phi'', \xi'', \zeta'', t_0'')}{\partial(U, \theta, \phi, \xi, \zeta, t_0)} = \begin{bmatrix} 1 & 0 & 0 & 0 & 0 & 0 \\ \frac{\partial \theta'}{\partial U} & \frac{\partial \theta'}{\partial \theta} & 0 & \frac{\partial \theta'}{\partial \xi} & \frac{\partial \theta'}{\partial \zeta} & 0 \\ \frac{\partial \phi'}{\partial U} & \frac{\partial \phi'}{\partial \theta} & \frac{\partial \phi'}{\partial \phi} & \frac{\partial \phi'}{\partial \xi} & \frac{\partial \phi'}{\partial \zeta} & 0 \\ \frac{\partial \xi'}{\partial U} & \frac{\partial \xi'}{\partial \theta} & \frac{\partial \xi'}{\partial \phi} & \frac{\partial \xi'}{\partial \xi} & \frac{\partial \xi'}{\partial \zeta} & 0 \\ \frac{\partial \zeta''}{\partial U} & \frac{\partial \zeta''}{\partial \theta} & \frac{\partial \zeta''}{\partial \phi} & \frac{\partial \zeta''}{\partial \xi} & \frac{\partial \zeta''}{\partial \zeta} & 0 \\ \frac{\partial t_0''}{\partial U} & \frac{\partial t_0''}{\partial \theta} & \frac{\partial t_0''}{\partial \phi} & \frac{\partial t_0''}{\partial \xi} & \frac{\partial t_0''}{\partial \zeta} & 1 \end{bmatrix}. \tag{A.38}$$

The computation of the propagation matrix can give a lot of information about the evolution of the orbit in terms of the encounter variables, however the $\partial(\xi'', \zeta'')/\partial(\xi, \zeta)$ submatrix is of

particular interest. The Keplerian heliocentric propagation does not affect the MOID ($\xi'' = \xi'$), so the first row of the submatrix comes out to be

$$\frac{\partial \xi''}{\partial \xi} = \frac{\partial \xi'}{\partial \xi} = \frac{\partial X_0'}{\partial \xi} \cos \phi' + X_0' \frac{\partial \cos \phi'}{\partial \xi} \tag{A.39}$$

$$\frac{\partial \xi''}{\partial \zeta} = \frac{\partial \xi'}{\partial \zeta} = \frac{\partial X_0'}{\partial \zeta} \cos \phi' + X_0' \frac{\partial \cos \phi'}{\partial \zeta} \tag{A.40}$$

Unlike ξ, ζ is affected by the Keplerian heliocentric propagation through a', and U is invariant through that motion. So, the structure of the derivatives of ζ'' with respect to ξ and ζ have the following structure

$$
\begin{aligned}
\frac{\partial \zeta''}{\partial \xi} =\ & \frac{\partial \zeta''}{\partial \theta'}\frac{\partial \theta'}{\partial \xi} + \frac{\partial \zeta'}{\partial \xi} \\
=\ & h \cdot \frac{2\pi a'^{5/2}\left[U' \cos^2 \theta' + \cos \theta'\left(1 - U'^2\right) - 3U'\right]}{\sin \theta'} \cdot \frac{\partial \cos \theta'}{\partial \xi} \\
& + h \cdot \frac{10\pi a'^{7/2}\left[U' \cos^2 \theta' + \cos \theta'\left(1 - U'^2\right) - 3U'\right]\left(\zeta' \cos \theta' \sin \phi' + \xi' \cos \phi'\right)}{\sin \theta'} \cdot \frac{\partial \cos \theta'}{\partial \xi} \\
& - h \cdot \frac{2\pi a'^{5/2}\left[2\xi' \cos \theta' \cos \phi' + \zeta' \sin \phi'\left(2 \cos^2 \theta' + 3 \sin^3 \theta'\right)\right]}{\sin \theta'} \cdot \frac{\partial \cos \theta'}{\partial \xi} + \frac{\partial \zeta'}{\partial \xi}
\end{aligned}
\tag{A.41}
$$

$$
\begin{aligned}
\frac{\partial \zeta''}{\partial \zeta} =\ & \frac{\partial \zeta''}{\partial \theta'}\frac{\partial \theta'}{\partial \zeta} + \frac{\partial \zeta'}{\partial \zeta} \\
=\ & h \cdot \frac{2\pi a'^{5/2}\left[U' \cos^2 \theta' + \cos \theta'\left(1 - U'^2\right) - 3U'\right]}{\sin \theta'} \cdot \frac{\partial \cos \theta'}{\partial \zeta} \\
& + h \cdot \frac{10\pi a'^{7/2}\left[U' \cos^2 \theta' + \cos \theta'\left(1 - U'^2\right) - 3U'\right]\left(\zeta' \cos \theta' \sin \phi' + \xi' \cos \phi'\right)}{\sin \theta'} \cdot \frac{\partial \cos \theta'}{\partial \zeta} \\
& - h \cdot \frac{2\pi a'^{5/2}\left[2\xi' \cos \theta' \cos \phi' + \zeta' \sin \phi'\left(2 \cos^2 \theta' + 3 \sin^3 \theta'\right)\right]}{\sin \theta'} \cdot \frac{\partial \cos \theta'}{\partial \zeta} + \frac{\partial \zeta'}{\partial \zeta}
\end{aligned}
\tag{A.42}
$$

where the derivatives of ζ' with respect to ξ and ζ are

$$\frac{\partial \zeta'}{\partial \xi} = \frac{\partial X_0'}{\partial \xi} \cos \theta' \sin \phi' + X_0' \frac{\partial \cos \theta'}{\partial \xi} \sin \phi' + X_0' \cos \theta' \frac{\partial \sin \phi'}{\partial \xi} + \frac{\partial Y_0'}{\partial \xi} \sin \theta' + Y_0' \frac{\partial \sin \theta'}{\partial \xi} \tag{A.43}$$

$$\frac{\partial \zeta'}{\partial \zeta} = \frac{\partial X_0'}{\partial \zeta} \cos \theta' \sin \phi' + X_0' \frac{\partial \cos \theta'}{\partial \zeta} \sin \phi' + X_0' \cos \theta' \frac{\partial \sin \phi'}{\partial \zeta} + \frac{\partial Y_0'}{\partial \zeta} \sin \theta' + Y_0' \frac{\partial \sin \theta'}{\partial \zeta} \tag{A.44}$$

The second and third terms in the derivatives of the Keplerian propagation are first order in ξ' and ζ', so they are much smaller than the first term and can be ignored for many practical situations of interest.

The derivatives that appear in the previous expressions are

$$\frac{\partial X_0'}{\partial \xi} = \frac{\partial X'(t_b)}{\partial \xi} - \frac{Z'(t_b)}{U_z'}\frac{\partial U_x'}{\partial \xi} - U_x'\left(\frac{1}{U_z'}\frac{\partial Z'(t_b)}{\partial \xi} - \frac{Z'(t_b)}{U_z'^2}\frac{\partial U_z'}{\partial \xi}\right) \tag{A.45}$$

$$\frac{\partial X_0'}{\partial \zeta} = \frac{\partial X'(t_b)}{\partial \zeta} - \frac{Z'(t_b)}{U_z'}\frac{\partial U_x'}{\partial \zeta} - U_x'\left(\frac{1}{U_z'}\frac{\partial Z'(t_b)}{\partial \zeta} - \frac{Z'(t_b)}{U_z'^2}\frac{\partial U_z'}{\partial \zeta}\right) \tag{A.46}$$

$$\frac{\partial Y_0'}{\partial \xi} = \frac{\partial Y'(t_b)}{\partial \xi} - \frac{Z'(t_b)}{U_z'} \frac{\partial U_x'}{\partial \xi} - U_y' \left(\frac{1}{U_z'} \frac{\partial Z'(t_b)}{\partial \xi} - \frac{Z'(t_b)}{U_z'^2} \frac{\partial U_z'}{\partial \xi} \right) \tag{A.47}$$

$$\frac{\partial Y_0'}{\partial \zeta} = \frac{\partial Y'(t_b)}{\partial \zeta} - \frac{Z'(t_b)}{U_z'} \frac{\partial U_x'}{\partial \zeta} - U_y' \left(\frac{1}{U_z'} \frac{\partial Z'(t_b)}{\partial \zeta} - \frac{Z'(t_b)}{U_z'^2} \frac{\partial U_z'}{\partial \zeta} \right) \tag{A.48}$$

$$\frac{\partial U_x'}{\partial \xi} = U \left(\frac{\partial \sin \theta'}{\partial \xi} \sin \phi' + \sin \theta' \frac{\partial \sin \phi'}{\partial \xi} \right) \tag{A.49}$$

$$\frac{\partial U_x'}{\partial \zeta} = U \left(\frac{\partial \sin \theta'}{\partial \zeta} \sin \phi' + \sin \theta' \frac{\partial \sin \phi'}{\partial \zeta} \right) \tag{A.50}$$

$$\frac{\partial U_y'}{\partial \xi} = U \frac{\partial \cos \theta'}{\partial \xi} \tag{A.51}$$

$$\frac{\partial U_y'}{\partial \zeta} = U \frac{\partial \cos \theta'}{\partial \zeta} \tag{A.52}$$

$$\frac{\partial U_z'}{\partial \xi} = U \left(\frac{\partial \sin \theta'}{\partial \xi} \cos \phi' + \sin \theta' \frac{\partial \cos \phi'}{\partial \xi} \right) \tag{A.53}$$

$$\frac{\partial U_z'}{\partial \zeta} = U \left(\frac{\partial \sin \theta'}{\partial \zeta} \cos \phi' + \sin \theta' \frac{\partial \cos \phi'}{\partial \zeta} \right) \tag{A.54}$$

$$\frac{\partial X'(t_b)}{\partial \xi} = \frac{4c^2 \xi \sin \phi \left(\zeta \cos \theta + c \sin \theta \right) + \left(b^4 - c^4 \right) \cos \phi}{\left(b^2 + c^2 \right)^2} \tag{A.55}$$

$$\frac{\partial X'(t_b)}{\partial \zeta} = \frac{4c^2 \zeta \left(c \sin \theta \sin \phi + \xi \cos \phi \right) + \left(b^4 - c^4 + 4c^2 \zeta^2 \right) \cos \theta \sin \phi}{\left(b^2 + c^2 \right)^2} \tag{A.56}$$

$$\frac{\partial Y'(t_b)}{\partial \xi} = \frac{4c^2 \xi \left(c \cos \theta - \zeta \sin \theta \right)}{\left(b^2 + c^2 \right)^2} \tag{A.57}$$

$$\frac{\partial Y'(t_b)}{\partial \zeta} = \frac{4c^2 \zeta \left(c \cos \theta - \zeta \sin \theta \right) + \left(c^4 - b^4 \right) \sin \theta}{\left(b^2 + c^2 \right)^2} \tag{A.58}$$

$$\frac{\partial Z'(t_b)}{\partial \xi} = \frac{4c^2 \xi \cos \phi \left(c \sin \theta + \zeta \cos \theta \right) - \left(b^4 - c^4 + 2c^2 \xi^2 \right) \sin \phi}{\left(b^2 + c^2 \right)^2} \tag{A.59}$$

$$\frac{\partial Z'(t_b)}{\partial \zeta} = \frac{4c^2 \zeta \left(c \sin \theta \cos \phi - \xi \sin \phi \right) - \left(b^4 - c^4 + 4c^2 \xi^2 \right) \cos \theta \cos \phi}{\left(b^2 + c^2 \right)^2} \tag{A.60}$$

$$\frac{\partial t_b}{\partial \xi} = -\frac{\tan \phi}{U \sin \theta} \tag{A.61}$$

$$\frac{\partial t_b}{\partial \zeta} = \frac{1}{U \tan \theta} \tag{A.62}$$

$$\frac{\partial t_0'}{\partial \xi} = \frac{\partial t_b}{\partial \xi} - \frac{1}{U_z'} \frac{\partial Z'(t_b)}{\partial \xi} + \frac{Z'(t_b)}{U_z'^2} \frac{\partial U_z'}{\partial \xi} \tag{A.63}$$

$$\frac{\partial t_0'}{\partial \zeta} = \frac{\partial t_b}{\partial \zeta} - \frac{1}{U_z'} \frac{\partial Z'(t_b)}{\partial \zeta} + \frac{Z'(t_b)}{U_z'^2} \frac{\partial U_z'}{\partial \zeta} \tag{A.64}$$

$$\frac{\partial a'}{\partial \xi} = \frac{8Uc\xi \left(c \cos \theta - \zeta \sin \theta \right)}{\left[\left(b^2 + c^2 \right) \left(1 - U^2 \right) - 2U \left[\left(b^2 - c^2 \right) \cos \theta + 2c\zeta \sin \theta \right] \right]^2} \tag{A.65}$$

$$\frac{\partial a'}{\partial \zeta} = \frac{8Uc\zeta\left(c\cos\theta - \zeta\sin\theta\right) + 4U\left(b^2 + c^2\right)c\sin\theta}{\left[\left(b^2 + c^2\right)\left(1 - U^2\right) - 2U\left[\left(b^2 - c^2\right)\cos\theta + 2c\zeta\sin\theta\right]\right]^2} \tag{A.66}$$

$$\frac{\partial \epsilon}{\partial \xi} = \cos\phi \tag{A.67}$$

$$\frac{\partial \epsilon}{\partial \zeta} = \cos\theta\sin\phi \tag{A.68}$$

$$\frac{\partial \epsilon'}{\partial \xi} = \frac{4c^2\xi\left(c\sin\theta\sin\phi + \epsilon\right) + \left(b^4 - c^4\right)\cos\phi}{\left(b^2 + c^2\right)^2} \tag{A.69}$$

$$\frac{\partial \epsilon'}{\partial \zeta} = \frac{4c^2\xi\left(c\sin\theta\sin\phi + \epsilon\right) + \left(b^4 - c^4\right)\cos\theta\sin\phi}{\left(b^2 + c^2\right)^2} \tag{A.70}$$

$$\frac{\partial a'_{\epsilon'}}{\partial \xi} = \frac{\partial a'}{\partial \xi} + 2a'^2 \cdot \frac{\partial \epsilon'}{\partial \xi} + 4\epsilon'a' \cdot \frac{\partial a'}{\partial \xi} \tag{A.71}$$

$$\frac{\partial a'_{\epsilon'}}{\partial \zeta} = \frac{\partial a'}{\partial \zeta} + 2a'^2 \cdot \frac{\partial \epsilon'}{\partial \zeta} + 4\epsilon'a' \cdot \frac{\partial a'}{\partial \zeta} \tag{A.72}$$

$$\frac{\partial t''_0}{\partial \xi} = \frac{\partial t'_0}{\partial \xi} + 3h\pi\sqrt{a'_{\epsilon'}}\frac{\partial a'_{\epsilon'}}{\partial \xi} \tag{A.73}$$

$$\frac{\partial t''_0}{\partial \zeta} = \frac{\partial t'_0}{\partial \zeta} + 3h\pi\sqrt{a'_{\epsilon'}}\frac{\partial a'_{\epsilon'}}{\partial \zeta} \tag{A.74}$$

$$\frac{\partial \cos\theta'}{\partial \xi} = \frac{4c\xi\left(c\cos\theta - \zeta\sin\theta\right)}{\left(b^2 + c^2\right)^2} \tag{A.75}$$

$$\frac{\partial \cos\theta'}{\partial \zeta} = \frac{2c\left[\left(b^2 + c^2\right)\sin\theta + 2\zeta\left(c\cos\theta - \zeta\sin\theta\right)\right]}{\left(b^2 + c^2\right)^2} \tag{A.76}$$

$$\frac{\partial \sin\theta'}{\partial \xi} = -\frac{\left(b^2 - c^2\right)\cos\theta + 2c\zeta\sin\theta}{\sqrt{\left[\left(b^2 - c^2\right)\sin\theta - 2c\zeta\cos\theta\right]^2 + 4c^2\xi^2}} \cdot \frac{\partial \cos\theta'}{\partial \xi} \tag{A.77}$$

$$\frac{\partial \sin\theta'}{\partial \zeta} = -\frac{\left(b^2 - c^2\right)\cos\theta + 2c\zeta\sin\theta}{\sqrt{\left[\left(b^2 - c^2\right)\sin\theta - 2c\zeta\cos\theta\right]^2 + 4c^2\xi^2}} \cdot \frac{\partial \cos\theta'}{\partial \zeta} \tag{A.78}$$

$$\frac{\partial \cos\phi'}{\partial \xi} = \frac{2\left(\xi\sin\theta\cos\phi + c\sin\phi\right)}{\sqrt{\left[\left(b^2 - c^2\right)\sin\theta - 2c\zeta\cos\theta\right]^2 + 4c^2\xi^2}} - \frac{2\xi\left[\left(b^2 - c^2\right)\sin^2\theta - 2c\left(\zeta\sin\theta\cos\theta - c\right)\right]\left[\left[\left(b^2 - c^2\right)\sin\theta - 2c\zeta\cos\theta\right]\cos\phi + 2c\xi\sin\phi\right]}{\sqrt{\left[\left[\left(b^2 - c^2\right)\sin\theta - 2c\zeta\cos\theta\right]^2 + 4c^2\xi^2\right]^3}} \tag{A.79}$$

$$\frac{\partial \cos\phi'}{\partial \zeta} = \frac{2\cos\phi\left(\zeta\sin\theta - c\cos\theta\right)}{\sqrt{\left[\left(b^2 - c^2\right)\sin\theta - 2c\zeta\cos\theta\right]^2 + 4c^2\xi^2}} - \frac{2\left[\left[\left(b^2 - c^2\right)\sin\theta - 2c\zeta\cos\theta\right]\left(\zeta\sin\theta - c\cos\theta\right)\right]\left[\left[\left(b^2 - c^2\right)\sin\theta - 2c\zeta\cos\theta\right]\cos\phi + 2c\xi\sin\phi\right]}{\sqrt{\left[\left[\left(b^2 - c^2\right)\sin\theta - 2c\zeta\cos\theta\right]^2 + 4c^2\xi^2\right]^3}} \tag{A.80}$$

$$\frac{\partial \sin\phi'}{\partial \xi} = \frac{2\left(\xi\sin\theta\sin\phi + c\cos\phi\right)}{\sqrt{\left[\left(b^2 - c^2\right)\sin\theta - 2c\zeta\cos\theta\right]^2 + 4c^2\xi^2}} - \frac{2\xi\left[\left(b^2 - c^2\right)\sin^2\theta - 2c\left(\zeta\sin\theta\cos\theta - c\right)\right]\left[\left[\left(b^2 - c^2\right)\sin\theta - 2c\zeta\cos\theta\right]\sin\phi + 2c\xi\cos\phi\right]}{\sqrt{\left[\left[\left(b^2 - c^2\right)\sin\theta - 2c\zeta\cos\theta\right]^2 + 4c^2\xi^2\right]^3}} \tag{A.81}$$

$$\frac{\partial \sin\phi'}{\partial \zeta} = \frac{2\sin\phi(\zeta\sin\theta - c\cos\theta)}{\sqrt{[(b^2-c^2)\sin\theta - 2c\zeta\cos\theta]^2 + 4c^2\xi^2}}$$
$$- \frac{2\big[\big[(b^2-c^2)\sin\theta - 2c\zeta\cos\theta\big](\zeta\sin\theta - c\cos\theta)\big]\big[\big[(b^2-c^2)\sin\theta - 2c\zeta\cos\theta\big]\sin\phi + 2c\xi\cos\phi\big]}{\sqrt{\big[[(b^2-c^2)\sin\theta - 2c\zeta\cos\theta]^2 + 4c^2\xi^2\big]^3}} \qquad \text{(A.82)}$$

There also exist approximations for all the previously mentioned equations and derivatives for both small and large deflections. A discussion of those equations and scenarios is not included in this work in order to avoid redundancy. For a full discussion of those equations and more details related to analytic keyhole theory I would direct readers to the works of Valsecchi, Milani, Chesley, Gronchi, and Chodas [39, 42].

APPENDIX B.   ALGORITHM FOR ANALYTIC KEYHOLE THEORY

This appendix contains the code used to validate the algorithms necessary for analytic keyhole theory. The provided code comes with no guarantees. If any of the codes in this appendix are used in another project, the author simply asks that this thesis be referenced in any published works.

All the included subroutines and programs have been tested to work with the gfortran compiler.

```fortran
PROGRAM test_analytic_keyhole_theory
IMPLICIT NONE
REAL(KIND=8) :: U,theta,phi,a,ecc,incl,lomega,bOMEGA,ksi,eta,tol
INTEGER :: h,k,ntrials
REAL(KIND=8) :: deg,rad,pi,AU,DU,mass_E,mass_S,m_ratio,factor
REAL(KIND=8) :: zeta1,zeta2,zeta_a,ksi_dprime_a,zeta_dprime_a
REAL(KIND=8) :: dzetadp_dksi_a,dzetadp_dzeta_a
REAL(KIND=8) :: dksip_dksi_a,dksidp_dksi_a,dksidp_dzeta_a,R_a,D_a,ksi_a
REAL(KIND=8) :: t0,zeta,ksi_dprime,zeta_dprime,dzetadp_dksi,dzetadp_dzeta
REAL(KIND=8) :: dksip_dksi,dksidp_dksi,dksidp_dzeta,R,D
REAL(KIND=8) :: submatrix_falsi(2,2),submatrix_key(2,2)
REAL(KIND=8) :: b,c,r_Earth,b_Earth,width,max_thickness
REAL(KIND=8) :: input1,input2,input3,input4,input5,input6,input7
REAL(KIND=8) :: output1,output2,output3,output4,output5,output6,output7

pi = 4.0d0*datan(1.0d0)
deg = pi/180.0d0  ! converts deg to rad
rad = 180.0d0/pi  ! converts rad to deg

! Asteroid: 1999 AN10
U = 0.884
theta = 105.3*pi/180  ! rad
phi = 41.3*pi/180  ! rad
!a = 0
!ecc = 0
!incl = 0
ksi = 0.000246
```

```fortran
eta = 0
h = 7  ! asteroid orbits
k = 13  ! Earth orbits
ntrials = 10000

! Constants
AU = 149597870.700d0  ! km
DU = 6378.145d0  ! km
mass_E = 5.972D24  ! kg
mass_S = 1.9891D30;  ! kg
m_ratio = mass_E/mass_S
factor = AU/DU


zeta1 = -0.03d0
zeta2 = 0.03d0
input1 = U
input2 = theta
input3 = phi
input4 = a
input5 = ecc
input6 = incl
input7 = ksi
CALL regula_falsi(input1,input2,input3,input4,input5,input6,lomega,bOMEGA, &
      zeta1,zeta2,input7,eta,t0,k,h,tol,ntrials, &
                        zeta_a,ksi_dprime_a,zeta_dprime_a,dzetadp_dksi_a, &
      dzetadp_dzeta_a,dksip_dksi_a,dksidp_dksi_a, &
                        dksidp_dzeta_a,R_a,D_a,output1,output2,output3,output4, &
                        output5,output6,output7)
U = output1
theta = output2
phi = output3
a = output4
ecc = output5
incl = output6
ksi = output7
CALL analytic_keyhole_development(input1,input2,input3,input4,input5,input6,lomega, &
      bOMEGA,zeta_a,input7,eta,k,h, &
                                    tol,t0,ksi_dprime,zeta_dprime,dzetadp_dksi, &
                                  dzetadp_dzeta,dksidp_dksi,dksidp_dzeta,R,D, &

WRITE(*,*) 'OUTPUT VARIABLES FROM ANALYTIC KEYHOLE DEVELOPMENT'
WRITE(*,*) 'AFTER REGULA FALSI METHOD CALL'
WRITE(*,*) 'zeta_a:',zeta_a
WRITE(*,*) 'ksi_dprime:',ksi_dprime
WRITE(*,*) 'zeta_dprime:',zeta_dprime
WRITE(*,*) 'dzetadp_dksi:',dzetadp_dksi
WRITE(*,*) 'dzetadp_dzeta:',dzetadp_dzeta
```

```fortran
WRITE(*,*) 'dksidp_dksi:',dksidp_dksi
WRITE(*,*) 'dksidp_dzeta:',dksidp_dzeta
WRITE(*,*) 'R:',R
WRITE(*,*) 'D:',D
WRITE(*,*) ' '

! Double prime submatrix
submatrix_falsi(1,1) = dksidp_dksi_a
submatrix_falsi(1,2) = dksidp_dzeta_a
submatrix_falsi(2,1) = dzetadp_dksi_a
submatrix_falsi(2,2) = dzetadp_dzeta_a
submatrix_key(1,1) = dksidp_dksi
submatrix_key(1,2) = dksidp_dzeta
submatrix_key(2,1) = dzetadp_dksi
submatrix_key(2,2) = dzetadp_dzeta

! Parameters
WRITE(*,*) 'PARAMETERS OF EARTH PRE-IMAGE ON TARGET B-PLANE'
b = dsqrt(ksi*ksi + zeta_a*zeta_a)
WRITE(*,*) 'b:',b
c = m_ratio/(U*U)
WRITE(*,*) 'c:',c
r_Earth = 1.0d0  ! Earth radii
b_Earth = r_Earth*dsqrt(1.0d0 + (2.0d0*c)/r_Earth)
WRITE(*,*) 'b_Earth:',b_Earth
width = 2.0d0*b_Earth  ! ksi axis, in Earth radii
WRITE(*,*) 'width:',width
max_thickness = (2.0d0*b_Earth)/submatrix_falsi(2,2)  ! 2*b_Earth/dzetadp_dzeta, R_E
WRITE(*,*) 'max_thickness:',max_thickness

END PROGRAM test_analytic_keyhole_theory

SUBROUTINE regula_falsi(input1,input2,input3,input4,input5,input6,lomega,bOMEGA, &
zeta1,zeta2,input7,eta,t0,k,h,tol,ntrials,zeta, &
ksi_dprime,zeta_dprime,dzetadp_dksi,dzetadp_dzeta, &
dksip_dksi,dksidp_dksi,dksidp_dzeta,R,D, &
output1,output2,output3,output4,output5,output6,output7)
IMPLICIT NONE
REAL(KIND=8),INTENT(IN) :: input1,input2,input3,input4,input5,input6,input7
REAL(KIND=8),INTENT(IN) :: lomega,bOMEGA,zeta1,zeta2,eta,t0,tol
INTEGER,INTENT(IN) :: k,h,ntrials
REAL(KIND=8),INTENT(OUT) :: zeta,ksi_dprime,zeta_dprime,dzetadp_dksi
REAL(KIND=8),INTENT(OUT) :: dzetadp_dzeta,dksip_dksi,dksidp_dksi,dksidp_dzeta,R,D
REAL(KIND=8),INTENT(OUT) :: output1,output2,output3,output4,output5,output6,output7
INTEGER :: j
REAL(KIND=8) :: val_a_old,val_b_old,f_a_old,f_b_old,c_old,f_c_old,num1,num2,num3
REAL(KIND=8) :: val_a_new,val_b_new,f_a_new,f_b_new,c_new,f_c_new,s
REAL(KIND=8) :: U,theta,phi,a,ecc,incl,ksi
```

```fortran
j = 1
val_a_old = zeta1
val_b_old = zeta2
U = input1
theta = input2
phi = input3
a = input4
ecc = input5
incl = input6
ksi = input7

CALL analytic_keyhole_development(U,theta,phi,a,ecc,incl,lomega,bOMEGA,zeta1,ksi,eta, &
     k,h,tol,t0,ksi_dprime,zeta_dprime,dzetadp_dksi, &
     dzetadp_dzeta,dksidp_dksi,dksidp_dzeta,R,D, &
     output1,output2,output3,output4,output5, &
     output6,output7)


f_a_old = zeta_dprime
CALL analytic_keyhole_development(U,theta,phi,a,ecc,incl,lomega,bOMEGA,zeta2,ksi,eta, &
      k,h,tol,t0,ksi_dprime,zeta_dprime,dzetadp_dksi, &
      dzetadp_dzeta,dksidp_dksi,dksidp_dzeta,R,D, &
      output1,output2,output3,output4,output5, &
      output6,output7)
f_b_old = zeta_dprime
c_old = val_a_old - ((val_b_old - val_a_old)*f_a_old)/(f_b_old - f_a_old)
zeta = c_old
CALL analytic_keyhole_development(U,theta,phi,a,ecc,incl,lomega,bOMEGA,zeta,ksi,eta, &
      k,h,tol,t0,ksi_dprime,zeta_dprime,dzetadp_dksi, &
      dzetadp_dzeta,dksidp_dksi,dksidp_dzeta,R,D, &
      output1,output2,output3,output4,output5, &
      output6,output7)
f_c_old = zeta_dprime

num1 = 1.0d0
num2 = 1.0d0
num3 = 1.0d0

DO WHILE (j < ntrials)

    IF (f_a_old .GE. 0.0d0) THEN
        s = 1.0d0
        num1 = dabs(f_a_old/f_a_old)*s
    ELSE
        s = -1.0d0
        num1 = dabs(f_a_old/f_a_old)*s
    END IF
```

```fortran
IF (f_b_old .GE. 0.0d0) THEN
    s = 1.0d0
    num2 = dabs(f_b_old/f_b_old)*s
ELSE
    s = -1.0d0
    num2 = dabs(f_b_old/f_b_old)*s
END IF
IF (f_c_old .GE. 0.0d0) THEN
    s = 1.0d0
    num3 = dabs(f_c_old/f_c_old)*s
ELSE
    s = -1.0d0
    num3 = dabs(f_c_old/f_c_old)*s
END IF


IF (num2 == num3) THEN
    val_b_new = c_old
    val_a_new = val_a_old
ELSEIF (num1 == num3) THEN
    val_a_new = c_old
    val_b_new = val_b_old
END IF
CALL analytic_keyhole_development(U,theta,phi,a,ecc,incl,lomega,bOMEGA,val_a_new, &
 ksi,eta,k,h,tol,t0,ksi_dprime,zeta_dprime,dzetadp_dksi, &
 dzetadp_dzeta,dksidp_dksi,dksidp_dzeta,R,D, &
 output1,output2,output3,output4,output5, &
 output6,output7)
f_a_new = zeta_dprime

!PAUSE

CALL analytic_keyhole_development(U,theta,phi,a,ecc,incl,lomega,bOMEGA,val_b_new, &
 ksi,eta,k,h,tol,t0,ksi_dprime,zeta_dprime,dzetadp_dksi, &
 dzetadp_dzeta,dksidp_dksi,dksidp_dzeta,R,D, &
 output1,output2,output3,output4,output5, &
 output6,output7)
f_b_new = zeta_dprime
c_new = val_a_new - ((val_b_new - val_a_new)*f_a_new)/(f_b_new - f_a_new)
zeta = c_new
CALL analytic_keyhole_development(U,theta,phi,a,ecc,incl,lomega,bOMEGA,zeta, &
 ksi,eta,k,h,tol,t0,ksi_dprime,zeta_dprime,dzetadp_dksi, &
 dzetadp_dzeta,dksidp_dksi,dksidp_dzeta,R,D, &
 output1,output2,output3,output4,output5, &
 output6,output7)
f_c_new = zeta_dprime

IF (dabs(zeta_dprime) < tol .and. j < ntrials) THEN
```

```fortran
         !index = j + 1
         EXIT
      END IF
      j = j + 1
      val_a_old = val_a_new
      val_b_old = val_b_new
      f_a_old = f_a_new
      f_b_old = f_b_new
      f_c_old = f_c_new
      c_old = c_new
END DO


zeta = c_new


END SUBROUTINE regula_falsi

SUBROUTINE analytic_keyhole_development(input1,input2,input3,input4,input5,input6, &
lomega,bOMEGA,zeta,input7,eta,k,h, &
                                       tol,t0,ksi_dprime,zeta_dprime,dzetadp_dksi, &
                                       dzetadp_dzeta,dksidp_dksi,dksidp_dzeta,R,D, &
                                       output1,output2,output3,output4,output5, &
                                       output6,output7)
IMPLICIT NONE
REAL(KIND=8),INTENT(IN) :: input1,input2,input3,input4,input5,input6,input7
REAL(KIND=8),INTENT(IN) :: lomega,bOMEGA,zeta,eta,tol,t0
INTEGER,INTENT(IN) :: k,h
REAL(KIND=8),INTENT(OUT) :: ksi_dprime,zeta_dprime,dzetadp_dksi,dzetadp_dzeta
REAL(KIND=8),INTENT(OUT) :: dksidp_dksi,dksidp_dzeta,R,D
REAL(KIND=8),INTENT(OUT) :: output1,output2,output3,output4,output5,output6,output7
REAL(KIND=8) :: ksi,U,theta,phi,a,ecc,incl,pi,mass_E,mass_S,m_ratio,AU,r_Earth
REAL(KIND=8) :: R_SOI_km,R_SOI_rE,DU,factor
REAL(KIND=8) :: epsilon,a_eps,ecc_eps,incl_eps,U_eps,num_costheta_eps
REAL(KIND=8) :: den_costheta_eps,theta_eps,phi_eps,b,c,Ux,Uy,Uz,X0,Y0
REAL(KIND=8) :: X,Y,Z,gamma,U_prime,t_b,theta_prime,phi_prime,ap,eccp,inclp
REAL(KIND=8) :: Ux_prime,Uy_prime,Uz_prime,ksi_prime,zeta_prime,bprime_vec(3)
REAL(KIND=8) :: b_prime,numerator,denominator,t0_prime,a0_prime,a_prime
REAL(KIND=8) :: cos_theta0p,theta0p,X0_prime,Y0_prime,Z0_prime
REAL(KIND=8) :: Xprime_tb,Yprime_tb,Zprime_tb,t0_dprime,mod_time,dY0
REAL(KIND=8) :: D_t0_dprime,Ux_dprime,Uy_dprime,Uz_dprime
REAL(KIND=8) :: U_dprime,theta_dprime,phi_dprime,X0_dprime,Y0_dprime,tb_dprime
REAL(KIND=8) :: dcosthetap_dksi,dcosthetap_dzeta,dsinthetap_dksi,dsinthetap_dzeta
REAL(KIND=8) :: dcosphip_dksi,dcosphip_dzeta,dsinphip_dksi,dsinphip_dzeta,dXptb_dksi
REAL(KIND=8) :: dXptb_dzeta,dYptb_dksi,dYptb_dzeta,dZptb_dksi,dZptb_dzeta
REAL(KIND=8) :: dUxp_dksi,dUxp_dzeta,dUyp_dksi,dUyp_dzeta,dUzp_dksi,dUzp_dzeta
REAL(KIND=8) :: dX0p_dksi,dX0p_dzeta,dY0p_dksi
REAL(KIND=8) :: dY0p_dzeta,dzetap_dksi,dzetap_dzeta,dksip_dksi,dksip_dzeta


! Analytic Keyhole Theory
```

```
! Inputs: {a, e, i} or {r_rel, v_rel}, m (mass of planet)
! distance from planet to the Sun = 1
! circular orbit, period of planet = 2*pi
! m_sun = 1, mu_sun = 1, v_planet = 1
! planetocentric velocity vector U: [Ux; Uy; Uz]

pi = 4.0d0*datan(1.0d0)
mass_E = 5.972D24   ! kg
mass_S = 1.9891D30   ! kg
m_ratio = mass_E/mass_S
AU = 149597870.70d0   ! km
r_Earth = 6378.145d0   ! km
R_SOI_km = AU*(m_ratio**(2.0d0/5.0d0))   ! km
R_SOI_rE = R_SOI_km/r_Earth   ! r_Earth
DU = 6378.145d0   ! km
factor = AU/DU

U = input1
theta = input2
phi = input3
a = input4
ecc = input5
incl = input6
ksi = input7

!! Pre-encounter state vector
epsilon = 0.0d0   ! Should be set as an input
IF (a /= 0.0d0 .and. ecc /= 0.0d0 .and. incl /= 0.0d0) THEN
    U = dsqrt(3.0d0 - 1.0d0/a - 2.0d0*(dsqrt(a*(1.0d0 - ecc*ecc)))*dcos(incl))
    theta = dacos((dsqrt(a*(1.0d0 - ecc*ecc))*dcos(incl) - 1.0d0)/U)
    phi = datan2(dsqrt(2.0d0 - 1.0d0/a - a*(1.0d0 - ecc*ecc)), &
        dsqrt(a*(1.0d0 - ecc*ecc))*dsin(incl))
    IF (epsilon /= 0.0d0) THEN
        a_eps = a/(1.0d0 - 2.0d0*a*epsilon)
        IF (a*epsilon < tol) THEN
            a_eps = a*(1.0d0 + 2.0d0*a*epsilon)
        END IF
        ecc_eps = ecc + epsilon*U*(2.0d0*U - U*((dsin(theta))*(dsin(theta)))* &
            ((dsin(phi))*(dsin(phi))) + 4.0d0*dcos(theta))
        incl_eps = datan(dtan(incl)*(1.0d0 - epsilon/(1.0d0 + Uy)))
        U_eps = U - epsilon*((2.0d0*U*U*U*dcos(theta) + &
         4.0d0*U*U*dcos(theta)*dcos(theta) + U*U + 1.0d0)/ &
                (U*U + 2.0d0*U*dcos(theta) + 1.0d0))
        num_costheta_eps = (U*U*U)*(2.0d0*dcos(theta)*dcos(theta) + dcos(theta)) + &
                            (U*U)*(4.0d0*dcos(theta)*dcos(theta)*dcos(theta) + &
                            2.0d0*dcos(theta)*dcos(theta) + &
                            dcos(theta) + 1.0d0) + U*dcos(theta) + dcos(theta) - 1.0d0
```

```fortran
            den_costheta_eps = U*U*U + 2.0d0*U*U*dcos(theta) + U
            theta_eps = dacos(dcos(theta) + epsilon*(num_costheta_eps/den_costheta_eps))
            phi_eps = dacos(dcos(phi)*(1.0d0 + epsilon* &
              ((U*U + 2.0d0*U*dcos(theta) - 1.0d0)/(U*U + &
                2.0d0*U*dcos(theta) + 1.0d0))))
        END IF
        ksi = dcos(phi)*((a*(1 - ecc*ecc))/(1.0d0 - ecc*dcos(lomega)) - 1.0d0)
    ELSEIF (U /= 0.0d0 .and. theta /= 0.0d0 .and. phi /= 0.0d0) THEN
        a = 1.0d0/(1.0d0 - U*U - 2.0d0*U*dcos(theta))
        ecc = U*dsqrt((U + 2.0d0*dcos(theta))*(U + 2.0d0*dcos(theta)) + &
            dsin(theta)*dsin(theta)*dsin(phi)*dsin(phi)*(1.0d0 - U*U - 2.0d0*U*dcos(theta)))
        incl = datan((U*dsin(theta)*dcos(theta))/(1.0d0 + U*dcos(theta)))
        IF (epsilon /= 0.0d0) THEN
            a_eps = a/(1.0d0 - 2.0d0*a*epsilon)
            IF (a*epsilon < tol) THEN
                a_eps = a*(1.0d0 + 2.0d0*a*epsilon)
            END IF
            ecc_eps = ecc + epsilon*U*(2.0d0*U - U*dsin(theta)*dsin(theta)* &
             dsin(phi)*dsin(phi) + 4.0d0*dcos(theta))
            incl_eps = datan(dtan(incl)*(1.0d0 - epsilon/(1.0d0 + Uy)))
            U_eps = U - epsilon*((2.0d0*U*U*U*dcos(theta) + &
             4.0d0*U*U*dcos(theta)*dcos(theta) + U*U + 1.0d0)/ &
                    (U*U + 2.0d0*U*dcos(theta) + 1.0d0))
            num_costheta_eps = (U*U*U)*(2.0d0*dcos(theta)*dcos(theta) + dcos(theta)) + &
                               (U*U)*(4.0d0*dcos(theta)*dcos(theta)*dcos(theta) + &
                               2.0d0*dcos(theta)*dcos(theta) + &
                               dcos(theta) + 1.0d0) + U*dcos(theta) + dcos(theta) - 1.0d0
            den_costheta_eps = U*U*U + 2.0d0*U*U*dcos(theta) + U
            theta_eps = dacos(dcos(theta) + epsilon*(num_costheta_eps/den_costheta_eps))
            phi_eps = dacos(dcos(phi)*(1.0d0 + epsilon*((U*U + 2.0d0*U*dcos(theta) - 1.0d0)/ &
                    (U*U + 2.0d0*U*dcos(theta) + 1.0d0))))
        END IF
    END IF
END IF

b = dsqrt(ksi*ksi + zeta*zeta)
c = m_ratio/(U*U)

IF (epsilon /= 0.0d0) THEN
    a = a_eps
    ecc = ecc_eps
    incl = incl_eps
    U = U_eps
    theta = theta_eps
    phi = phi_eps
END IF

Ux = U*dsin(theta)*dsin(phi)
```

```
        Uy = U*dcos(theta)
        Uz = U*dsin(theta)*dcos(phi)


        X0 = ksi/dcos(phi)
        Y0 = (ksi*dcos(theta)*dtan(phi) - zeta)/dsin(theta)


        X = X0 - (X0*dsin(theta)*dsin(phi) + Y0*dcos(theta))*dsin(theta)*dsin(phi)
        Y = -(X0*dcos(theta)*dsin(phi) - Y0*dsin(theta))*dsin(theta)
        Z = -(X0*dsin(theta)*dsin(phi) + Y0*dcos(theta))*dsin(theta)*dcos(phi)


        D = X*X + Y*Y + Z*Z
        gamma = 2.0d0*datan(c/b)


        U_prime = U
        t_b = t0 - (X0*dsin(theta)*dsin(phi) + Y0*dcos(theta))/U


        theta_prime = dacos(((b*b - c*c)*dcos(theta) + 2.0d0*c*zeta*dsin(theta))/(b*b + c*c))
        phi_prime = dacos((((b*b - c*c)*dsin(theta) - 2.0d0*c*zeta*dcos(theta))*dcos(phi) + &
        2.0d0*c*ksi*dsin(phi))/dsqrt((((b*b - c*c)*dsin(theta) - &
        2.0d0*c*zeta*dcos(theta))*((b*b - c*c)*dsin(theta) - &
                     2.0d0*c*zeta*dcos(theta)) + 4.0d0*c*c*ksi*ksi)))


        ap = 1.0d0/(1.0d0 - U_prime*U_prime - 2.0d0*U_prime*dcos(theta_prime))
        eccp = U_prime*dsqrt((U_prime + 2.0d0*dcos(theta_prime))*(U_prime + &
        2.0d0*dcos(theta_prime)) + dsin(theta_prime)*dsin(theta_prime) &
        *dsin(phi_prime)*dsin(phi_prime)*(1.0d0 - U_prime*U_prime - &
        2.0d0*U_prime*dcos(theta_prime)))
        inclp = datan((U_prime*dsin(theta_prime)*dcos(phi_prime))/ &
        (1.0d0 + U_prime*dcos(theta_prime)))


        Ux_prime = U*dsin(theta_prime)*dsin(phi_prime)
        Uy_prime = U*dcos(theta_prime)
        Uz_prime = U*dsin(theta_prime)*dcos(phi_prime)


        ksi_prime = ((b*b + c*c)*ksi*dsin(theta))/ &
                     dsqrt(((b*b - c*c)*dsin(theta) - 2.0d0*c*zeta*dcos(theta))* &
                     ((b*b - c*c)*dsin(theta) - 2.0d0*c*zeta*dcos(theta)) + 4.0d0*c*c*ksi*ksi)
        zeta_prime = ((b*b - c*c)*zeta*dsin(theta) - 2.0d0*b*b*c*dcos(theta))/ &
                      dsqrt(((b*b - c*c)*dsin(theta) - 2.0d0*c*zeta*dcos(theta))* &
                      ((b*b - c*c)*dsin(theta) - 2.0d0*c*zeta*dcos(theta)) + 4.0d0*c*c*ksi*ksi)


        bprime_vec(1) = ksi_prime
        bprime_vec(2) = 0.0d0
        bprime_vec(3) = zeta_prime
        b_prime = dsqrt(ksi_prime*ksi_prime + zeta_prime*zeta_prime)


        numerator = 2.0d0*c*(ksi*dsin(phi)*(2.0d0*zeta*dcos(theta) - ksi*dtan(phi)) - &
```

```fortran
dcos(phi)*(ksi*ksi*dsin(theta)*dsin(theta) + zeta*zeta))
denominator = U*dsin(theta)*(((b*b - c*c)*dsin(theta) - &
2.0d0*c*zeta*dcos(theta))*dcos(phi) + 2.0d0*c*ksi*dsin(phi))
t0_prime = t0 + numerator/denominator

a0_prime = (real(k*k)/real(h*h))**(1.0d0/3.0d0)
a_prime = a0_prime
cos_theta0p = (1.0d0 - U*U - 1.0d0/a0_prime)/(2.0d0*U)

theta0p = dacos(cos_theta0p)
theta_prime = theta0p
R = dabs((c*dsin(theta0p))/(cos_theta0p - dcos(theta)))
D = (c*dsin(theta))/(cos_theta0p - cos(theta))

! Xprime_t0prime = X0_prime
X0_prime = Ux_prime*(t0_prime - t0) + X0
! Yprime_t0prime = Y0_prime
Y0_prime = Uy_prime*(t0_prime - t0) + Y0
! Zprime_t0prime = Z0_prime
Z0_prime = Uz_prime*(t0_prime - t0)

Xprime_tb = Ux_prime*(t_b - t0_prime) + X0_prime
Yprime_tb = Uy_prime*(t_b - t0_prime) + Y0_prime
Zprime_tb = Uz_prime*(t_b - t0_prime)

t0_dprime = t0_prime + h*2.0d0*pi*a_prime**(3.0d0/2.0d0)
mod_time = (t0_dprime - t0_prime + pi) - INT((t0_dprime - t0_prime + pi)/ &
(2.0d0*pi))*(2.0d0*pi)
dY0 = -(mod_time - pi)

D_t0_dprime = dsqrt(X0_prime*X0_prime + (Y0_prime + dY0)*(Y0_prime + dY0))
Ux_dprime = Ux_prime
Uy_dprime = Uy_prime
Uz_dprime = Uz_prime
U_dprime = U_prime
theta_dprime = theta_prime
phi_dprime = phi_prime

X0_dprime = X0_prime
Y0_dprime = Y0_prime + dY0
tb_dprime = t0_dprime - (X0_dprime*dsin(theta_prime)*dsin(phi_prime) + &
Y0_dprime*dcos(theta_prime))/U
ksi_dprime = X0_dprime*dcos(phi_prime)
zeta_dprime = X0_dprime*dcos(theta_prime)*dsin(phi_prime) - Y0_dprime*dsin(theta_prime)

! Derivatives of cos(thetap) and sin(thetap)
denominator = (b*b + c*c)*(b*b + c*c)
```

```fortran
dcosthetap_dksi = (4.0d0*c*ksi*(c*dcos(theta) - zeta*dsin(theta)))/denominator
dcosthetap_dzeta = (2.0d0*c*((b*b + c*c)*dsin(theta) + 2.0d0*zeta*(c*dcos(theta) - &
zeta*dsin(theta))))/denominator
numerator = -((b*b - c*c)*dcos(theta) + 2.0d0*c*zeta*dsin(theta))
denominator = dsqrt(((b*b - c*c)*dsin(theta) - 2.0d0*c*zeta*dcos(theta))* &
((b*b - c*c)*dsin(theta) - 2.0d0*c*zeta*dcos(theta)) + 4.0d0*c*c*ksi*ksi)
dsinthetap_dksi = (numerator/denominator)*dcosthetap_dksi
dsinthetap_dzeta = (numerator/denominator)*dcosthetap_dzeta


! Derivatives of cos(phip) and sin(phip)
dcosphip_dksi = (2.0d0*(ksi*dsin(theta)*dcos(phi) + c*dsin(phi)))/ &
                (dsqrt(((b*b - c*c)*dsin(theta) - 2.0d0*c*zeta*dcos(theta))* &
                ((b*b - c*c)*dsin(theta) - 2.0d0*c*zeta*dcos(theta)) + &
                4.0d0*c*c*ksi*ksi)) - (2.0d0*ksi*((b*b - c*c)*dsin(theta)*dsin(theta) - &
                2.0d0*c*(zeta*dsin(theta)*dcos(theta) - c))* &
                (((b*b - c*c)*dsin(theta) - 2.0d0*c*zeta*dcos(theta))*dcos(phi) + &
                2.0d0*c*ksi*dsin(phi)))/(dsqrt((((b*b - c*c)*dsin(theta) - &
                2.0d0*c*zeta*dcos(theta))*((b*b - c*c)*dsin(theta) - &
                2.0d0*c*zeta*dcos(theta)) + 4.0d0*c*c*ksi*ksi)**3))
dcosphip_dzeta = (2.0d0*dcos(phi)*(zeta*dsin(theta) - c*dcos(theta)))/ &
                 dsqrt(((b*b - c*c)*dsin(theta) - 2.0d0*c*zeta*dcos(theta))* &
                 ((b*b - c*c)*dsin(theta) - 2.0d0*c*zeta*dcos(theta)) + &
                 4.0d0*c*c*ksi*ksi) - (2.0d0*(((b*b - c*c)*dsin(theta) - &
                 2.0d0*c*zeta*dcos(theta))*(zeta*sin(theta) - c*cos(theta)))* &
                 (((b*b - c*c)*dsin(theta) - 2.0d0*c*zeta*dcos(theta))*dcos(phi) + &
                 2.0d0*c*ksi*dsin(phi)))/dsqrt((((b*b - c*c)*dsin(theta) - &
                 2.0d0*c*zeta*dcos(theta))*((b*b - c*c)*dsin(theta) - &
                 2.0d0*c*zeta*dcos(theta)) + 4.0d0*c*c*ksi*ksi)**3)
dsinphip_dksi = (2.0d0*(ksi*dsin(theta)*dsin(phi) - c*dcos(phi)))/ &
                dsqrt(((b*b - c*c)*dsin(theta) - 2.0d0*c*zeta*dcos(theta))* &
                ((b*b - c*c)*dsin(theta) - 2.0d0*c*zeta*dcos(theta)) + &
                4.0d0*c*c*ksi*ksi) - (2.0d0*ksi*((b*b - c*c)*dsin(theta)*dsin(theta) - &
                2.0d0*c*(zeta*dsin(theta)*dcos(theta) - c))* &
                (((b*b - c*c)*dsin(theta) - 2.0d0*c*zeta*dcos(theta))*dsin(phi) - &
                2.0d0*c*ksi*dcos(phi)))/dsqrt((((b*b - c*c)*dsin(theta) - &
                2.0d0*c*zeta*dcos(theta))*((b*b - c*c)*dsin(theta) - &
                2.0d0*c*zeta*dcos(theta)) + 4.0d0*c*c*ksi*ksi)**3)
dsinphip_dzeta = (2.0d0*dsin(phi)*(zeta*dsin(theta) - c*dcos(theta)))/ &
                 dsqrt(((b*b - c*c)*dsin(theta) - 2.0d0*c*zeta*dcos(theta))* &
                 ((b*b - c*c)*dsin(theta) - 2.0d0*c*zeta*dcos(theta)) + &
                 4.0d0*c*c*ksi*ksi) - (2.0d0*(((b*b - c*c)*dsin(theta) - &
                 2.0d0*c*zeta*dcos(theta))*(zeta*dsin(theta) - c*dcos(theta)))* &
                 (((b*b - c*c)*dsin(theta) - 2.0d0*c*zeta*dcos(theta))*dsin(phi) - &
                 2.0d0*c*ksi*dcos(phi)))/dsqrt((((b*b - c*c)*dsin(theta) - &
                 2.0d0*c*zeta*dcos(theta))*((b*b - c*c)*dsin(theta) - &
                 2.0d0*c*zeta*dcos(theta)) + 4.0d0*c*c*ksi*ksi)**3)
```

```fortran
! Derivatives of Xp_tb, Yp_tb, and Zp_tb
denominator = (b*b + c*c)*(b*b + c*c)
dXptb_dksi = (4.0d0*c*c*ksi*dsin(phi)*(zeta*dcos(theta) + c*dsin(theta)) + &
(b*b*b*b - c*c*c*c)*dcos(theta))/denominator
dXptb_dzeta = (4.0d0*c*c*zeta*(c*dsin(theta)*dsin(phi) + ksi*dcos(phi)) + &
(b*b*b*b - c*c*c*c + 4.0d0*c*c*zeta*zeta)* &
                dcos(theta)*dsin(phi))/denominator
dYptb_dksi = (4.0d0*c*c*ksi*(c*dcos(theta) - zeta*dsin(theta)))/denominator
dYptb_dzeta = (4.0d0*c*c*zeta*(c*dcos(theta) - zeta*dsin(theta)) + &
(c*c*c*c - b*b*b*b)*dsin(theta))/denominator
dZptb_dksi = (4.0d0*c*c*ksi*dcos(phi)*(c*dsin(theta) + zeta*dcos(theta)) - &
(b*b*b*b - c*c*c*c + 2.0d0*c*c*ksi*ksi)*dsin(phi))/denominator
dZptb_dzeta = (4.0d0*c*c*zeta*(c*dsin(theta)*dcos(phi) - ksi*dsin(phi)) + &
(b*b*b*b - c*c*c*c + 4.0d0*c*c*zeta*zeta)*dcos(theta)*dcos(phi))/ &
denominator

! Derivatives of Ux_prime, Uy_prime, and Uz_prime
dUxp_dksi = U*(dsinthetap_dksi*dsin(phi_prime) + dsin(theta_prime)*dsinphip_dksi)
dUxp_dzeta = U*(dsinthetap_dzeta*dsin(phi_prime) + dsin(theta_prime)*dsinphip_dzeta)
dUyp_dksi = U*dcosthetap_dksi
dUyp_dzeta = U*dcosthetap_dzeta
dUzp_dksi = U*(dsinthetap_dksi*dcos(phi_prime) + dsin(theta_prime)*dcosphip_dksi)
dUzp_dzeta = U*(dsinthetap_dzeta*dcos(phi_prime) + dsin(theta_prime)*dcosphip_dzeta)

! Derivatives of Xp_0 and Yp_0
dX0p_dksi = dXptb_dksi - (Zprime_tb/Uz_prime)*dUxp_dksi - &
Ux_prime*((1.0d0/Uz_prime)*dZptb_dksi - &
              (Zprime_tb/(Uz_prime*Uz_prime))*dUzp_dksi)
dX0p_dzeta = dXptb_dzeta - (Zprime_tb/Uz_prime)*dUxp_dzeta - &
Ux_prime*((1.0d0/Uz_prime)*dZptb_dzeta - &
               (Zprime_tb/(Uz_prime*Uz_prime))*dUzp_dzeta)
dY0p_dksi = dYptb_dksi - (Zprime_tb/Uz_prime)*dUyp_dksi - &
Uy_prime*((1.0d0/Uz_prime)*dZptb_dksi - &
             (Zprime_tb/(Uz_prime*Uz_prime))*dUzp_dksi)
dY0p_dzeta = dYptb_dzeta - (Zprime_tb/Uz_prime)*dUyp_dzeta - &
Uy_prime*((1.0d0/Uz_prime)*dZptb_dzeta - &
               (Zprime_tb/(Uz_prime*Uz_prime))*dUzp_dzeta)

! Derivatives of zeta_prime
dzetap_dksi = dX0p_dksi*dcos(theta_prime)*dsin(theta_prime) + &
X0_prime*dcosthetap_dksi*dsin(phi_prime) + &
                X0_prime*dcos(theta_prime)*dsinphip_dksi + &
                dY0p_dksi*dsin(theta_prime) + Y0_prime*dsinthetap_dksi
dzetap_dzeta = dX0p_dzeta*dcos(theta_prime)*dsin(phi_prime) + &
X0_prime*dcosthetap_dzeta*dsin(phi_prime) + &
                 X0_prime*dcos(theta_prime)*dsinphip_dzeta + &
                 dY0p_dzeta*dsin(theta_prime) + Y0_prime*dsinthetap_dzeta
```

```fortran
! Derivatives of ksi_prime
dksip_dksi = dX0p_dksi*dcos(phi_prime) + X0_prime*dcosphip_dksi
dksip_dzeta = dX0p_dzeta*dcos(phi_prime) + X0_prime*dcosphip_dzeta

! Derivatives of zeta_dprime
dzetadp_dksi = h*((2.0d0*pi*a_prime**(5.0d0/2.0d0)* &
(U_prime*dcos(theta_prime)*dcos(theta_prime) + &
                dcos(theta_prime)*(1.0d0 - U_prime*U_prime) - 3.0d0*U_prime))/ &
                dsin(theta_prime))*dcosthetap_dksi + &
                h*((10.0d0*pi*a_prime**(7.0d0/2.0d0)* &
                (U_prime*dcos(theta_prime)*dcos(theta_prime) + &
                dcos(theta_prime)*(1.0d0 - U_prime*U_prime) - 3.0d0*U_prime)* &
                (zeta_prime*dcos(theta_prime)*dsin(phi_prime) + &
                ksi_prime*dcos(phi_prime)))/dsin(theta_prime))*dcosthetap_dksi - &
                h*((2.0d0*pi*a_prime**(5.0d0/2.0d0)*(2.0d0*ksi_prime* &
                dcos(theta_prime)*dcos(phi_prime) + zeta_prime*dsin(phi_prime)* &
                (2.0d0*dcos(theta_prime)*dcos(theta_prime) + &
                3.0d0*dsin(theta_prime)*dsin(theta_prime)* &
               dsin(theta_prime))))/dsin(theta_prime))*dcosthetap_dksi + dzetap_dksi
dzetadp_dzeta = h*((2.0d0*pi*a_prime**(5.0d0/2.0d0)* &
(U_prime*dcos(theta_prime)*dcos(theta_prime) + &
                dcos(theta_prime)*(1.0d0 - U_prime*U_prime) - &
                3.0d0*U_prime))/dsin(theta_prime))*dcosthetap_dzeta + &
                h*((10.0d0*pi*a_prime**(7.0d0/2.0d0)*(U_prime* &
                dcos(theta_prime)*dcos(theta_prime) + dcos(theta_prime)* &
                (1.0d0 - U_prime*U_prime) - 3.0d0*U_prime)* &
                (zeta_prime*dcos(theta_prime)*dsin(phi_prime) + &
                ksi_prime*dcos(phi_prime)))/dsin(theta_prime))*dcosthetap_dzeta - &
                h*((2.0d0*pi*a_prime**(5.0d0/2.0d0)*(2.0d0*ksi_prime* &
                dcos(theta_prime)*dcos(phi_prime) + zeta_prime*dsin(phi_prime)* &
                (2.0d0*dcos(theta_prime)*dcos(theta_prime) + &
                3.0d0*dsin(theta_prime)*dsin(theta_prime)* &
                dsin(theta_prime))))/dsin(theta_prime))*dcosthetap_dzeta + dzetap_dzeta
! Derivatives of ksi_dprime
dksidp_dksi = dksip_dksi
dksidp_dzeta = dksip_dzeta
! Necessary output variables
output1 = U
output2 = theta
output3 = phi
output4 = a
output5 = ecc
output6 = incl
output7 = ksi

END SUBROUTINE analytic_keyhole_development
```

BIBLIOGRAPHY

[1] Giorgini, J. D., Benner, L. A. M., Ostro, S. J., Nolan, M. C., and Busch, M. W. Predicting Apophis' Earth Encounters in 2029 and 2036. *Icarus*, 193:1–19, 2008.

[2] United Launch Alliance. Delta II Payload Planner's Guide. 2006.

[3] United Launch Alliance. Delta IV Payload Planner's Guide. 2007.

[4] Commercial Launch Services. Lockheed Martin Atlas Launch System Mission Planner's Guide. 2004.

[5] Pitz, A., Kaplinger, B., Vardaxis, G., Winkler, T., and Wie, B. Conceptual Design of a Hypervelocity Asteroid Intercept Vehicle (HAIV) and Its Flight Validation Mission. *Acta Astronautica*, Vol.101, pp.1-15 2014.

[6] Wie, B. and Barbee, B. An Innovative Solution to NASA's NEO Impact Threat Mitigation Grand Challenge and Flight Validation Mission Architecture Development. Technical Report NNX12AQ60G, NASA Innovative Advanced Concepts, 2012-2014.

[7] Samuel A. Wagner. *Automated trajectory design for impulsive and low thrust interplanetary mission analysis*. PhD thesis, Iowa State University, 2014.

[8] Hazards Due to Comets and Asteroids. *The University of Arizona Press*, 1994.

[9] Dearborn, D. 21st Century Steam for Asteroid Mitigation. *2004 Planetary Defense Conference: Protecting Earth from Asteroids*, AIAA-2004-1413, Feb. 23-26 2004.

[10] Adams, R., et al. Survey of Technologies Relevant to Defense from Near-Earth Objects. *NASA MSFC*, NASA-TP-2004-213089, July 2004.

[11] Mitigation of Hazardous Comets and Asteroids. *Cambridge University Press*, 2005.

[12] Lu, E. and Love, S. Gravitational Tractor for Towing Asteroids. *Nature*, 438.

[13] Near-Earth Object Survey and Deflection Study. *Final Report, NASA HQ, PA&E*, Dec. 28 2006.

[14] Barbee, B. W. and Fowler, W. T. Spacecraft Mission Design for the Optimal Impulsive Deflection of Hazardous Near-Earth Objects (NEOs) Using Nuclear Explosive Technology. *Planetary Defense Conference*, March 5-8 2007.

[15] Wie, B. *Space Vehicle Dynamics and Control.* American Institute of Aeronatics and Astronautics, Inc., Reston, VA 20191, 2nd edition, 2008.

[16] Kaplinger, B., Wie, B., and Basart, J. A Preliminary Study on Nuclear Standoff Explosions for Deflecting Near-Earth Objects. *Proceedings of the 1st IAA Planetary Defense Conference*, April 27-30 2009.

[17] *Effects of Nuclear Earth-Penetrators and Other Weapons.* National Research Council, The National Academies Press, 2005.

[18] Bate, R. B., Mueller, D. D., and White, J. E. *Fundamentals of Astrodynamics.* Dover Publications Inc., 1971.

[19] Vallado, D. A. *Fundamentals of Astrodynamics and Applications.* The Space Technology Library, 2007.

[20] Chodas, P. W. and Yeomans, D. K. Orbit Determination and Estimation of Impact Probability for Near Earth Objects. *AAS/AIAA Space Flight Mechanics Meeting*, AAS 09-002 2009.

[21] Yeomans, D. K., Chodas, P. W., Sitarski, G., Szutowicz, S., and Krolikowska, M. *Cometary Orbit Determination and Nongravitational Forces.* The Lunar and Planetary Institute, 2004.

[22] Sharaf, M. A. and Selim, H. H. Final State Predictions for J2 Gravity Perturbed Motion of the Earth's Artificial Satellites Using Bispherical Coordinates. *NRIAG Journal of Astronomy and Geophysics*, 2:134–138, 2013.

[23] Burden, R. L. and Faires, J. D. *Numerical Analysis, Ninth Edition.* Brooks/Cole, Cengage Learning, 2005.

[24] Mathematics source library, c & asm, 2004.

[25] Pitz, A., Vardaxis, G., and Wie, B. A Hypervelocity Nuclear interceptor System (HNIS) for Optimal Disruptions of Near-Earth Objects. *22nd AAS/AIAA Space Flight Mechanics Meeting*, AAS-12-125, Jan. 2012.

[26] Melamed, N. Development of a handbook and an on-line tool on defending Earth against Potentially Hazardous Objects. *Acta Astronautica*, 2012.

[27] Lttt suite optimization tools. 2012.

[28] General mission analysis tool (gmat). 2012.

[29] Winkler, T., Wagner, S., and Wie, B. Optimal Target Selection for a Planetary Defense Technology Demonstration Mission. *22nd AAS/AIAA Space Flight Mechanics Meeting*, AAS-12-226, Jan. 2012.

[30] Vardaxis, G. and Wie, B. Asteroid Mission Design Software Tool for Planetary Defense Applications. *AIAA/AAS Astrodynamics Specialist Conference*, AIAA 2012-4872 2012.

[31] Vardaxis, G. and Wie, B. Development of an Asteroid Mission Design Software Tool for Planetary Defense. *The 3rd IAA Planetary Defense Conferense*, IAA-PDC13-04-019, April 2013.

[32] NASA JSC Cost Estimating and Models. Advanced Missions Cost Model. 2007.

[33] Curtis, H. *Orbital Mechanics for Engineering Students.* Ch. 5: Preliminary Orbit Determination, Elsevier Butterworth-Heinemann, Linacre House, Jordan Hill, Oxford, 1st edition, 2005.

[34] Battin, R. *An Introduction to the Mathematics and Methods of Astrodynamics, Revised Edition.* Ch. 7: Solving Lambert's Problem, AIAA Education Series, 1801 Alexadner Bell Drive, Reston, VA, Revised Edition edition, 1999.

[35] Wagner, S. and Wie, B. Target Selection for a HAIV Flight Demo Mission. *AIAA Guidance, Navigation, and Control Conference*, AIAA 2013-4545, Aug. 2013.

[36] Vardaxis, G. and Wie, B. Near-Earth Object Intercept Trajectory Design for Planetary Defense. *Acta Astronautica*, 2013.

[37] Carusi, A., Valsecchi, G. B., and Greenberg, R. Planetary Close Encounters: Geometry of Approach and Post-Encounter Orbital Parameters. *Celestial Mechanics and Dynamical Astronomy*, 49:111–131, 1990.

[38] Eagle, D. C. Gravity Assist Interplanetary Trajectories. Welcome to the Orbital and Celestial Mechanics Website, Dec. 2013.

[39] Valsecchi, G. B., Milani, A., Chodas, P. W., and Chesley, S. R. *Asteroid Close Approaches: Analysis and Potential Impact Detection.* Asteroids III, The Lunar and Planetary Institute, 2002.

[40] Born, G. H. Design of the Approach Trajectory: B-plane Targeting. University of Colorado Boulder: ASEN 5519-Interplanetary Mission Design, 2005.

[41] B-Plane Targeting. Astrogator: Technical Notes.

[42] Valsecchi, G. B., Milani, A., Chodas, P. W., and Chesley, S. R. Resonant Returns to Close Approaches: Analytic Theory. *Astronomy & Astrophysics*, 2001.

[43] Foster, J. L. and Estes, H. S. A Parametric Analysis of Orbital Debris Collision Probability and Maneuver Rate for Space Vehicles. *NASA/JSC-25898*, August 1992.

[44] Chan, K. Collision Probability Analyses for Earth-Orbiting Satellites. In *Proceedings of the 7th International Space Conference of Pacific Basin Societies*. Nagasaki, Japan, July 1997.

[45] Patera, R. P. General Method for Calculating Satellite Collision Probability. *Journal of Guidance, Control, and Dynamics*, 24(4):716–722, July-Aug. 2001.

[46] Alfano, S. A Numerical Implementation of Spherical Object Collision Probability. *Journal of Astronautical Sciences*, 53(1):103–109, Jan.-March 2005.

[47] Kessler, D. J. Derivation of the Collision Probability between Orbiting Objects: The Lifetimes of Jupiter's Outer Moons. *Icarus*, 48:39–48, 1981.

[48] Milani, A. The Dynamics of Planet-Crossing Asteroids. 522:95–126, 1999.

[49] Alfano, S. Review of Conjunction Probability Methods for Short-term Encounters. *AAS/AIAA Space Flight Mechanics Meeting*, Feb. 2007.

[50] Bombardelli, C., Ayuso, J. H., and Pelayo, R. G. Collision Avoidance Maneuver Optimization. *24th AAS/AIAA Space Flight Mechanics Meeting*, AAS 14-335, Jan. 2014.

[51] Pitz, A., Teubert, C., and Wie, B. Earth-Impact Probability Computation of Disrupted Asteroid Fragments Using GMAT/STK/CODES. *AIAA/AAS Astrodynamics Specialist Conference*, AAS 11-408, Aug. 2011.

[52] Vardaxis, G., and Wie, B. Impact Risk Assessment for a Fragmented Asteroid in Earth Resonant Orbits. *AIAA/AAS Astrodynamics Specialist Conference*, AIAA-2014-4300, Aug. 2014.

[53] Near Earth Object Program. The 2015 pdc hypothetical asteroid impact scenario, 2015.

[54] Myatt, D. R., Becerra, V. M., Nasuto, S. J. and Bishop, J. M. Advanced Global Optimisation for Mission Analysis and Design. Technical Report 03-4101a, ESA Ariadna, 2004.

[55] Davis, K. and Parker, J. . Constructing Resonant Orbits. University of Colorado Boulder:ASEN 5519-Interplanetary Mission Design, 2012.

[56] Conway, B. An Improved Method Due to Laguerre for the Solution of Keplers Equation. *Celestial Mechanics*, 39:199–211, 1986.

[57] Prussing, J.E. and Conway, B.A. . *Orbital Mechanics*. Oxford University Press, 1993.

[58] Crocco, G.A. One-Year Exploration-Trip Earth-Mars-Venus-Earth. *VII International Astronautical Congress*, Sept. 1956.

[59] Lawden, D.F. Interplanetary Rocket Trajectories. *Advances in Space Science*, 1, 1959.

[60] Ruppe, H.O. Minimum Energy Requirements for Space Travel. *X International Astronautical Congress*, 1959.

[61] Battin, R. Determination of Round-Trip Planetary Reconnaissance Trajectories. *Journal of the Aero/Space Sciences*, 26(9):545–567, Sept. 1959.

[62] M.A. Minovitch. The invention that opened the solar system to exploration. *Planetary and Space Science*, 58(6):885 – 892, 2010.

[63] Breakwell, J.V. and Gillespie, R.W. and Ross, S. Researches in Interplanetary Transfer. *American Rocket Society Journal*, 31(2):201–208, 1959.

[64] Smith. A Manned Flyby Mission to [433] Eros . *Northrup Space Laboratory*, Feb. 1966.

[65] Orloff, R. Apollos by the Numbers. *U.S. Government Printing Office*, pages 256–257, 2001.

[66] Landis, R. and Korsmeyer, D. and Abell, P. and Adamo, P. A Piloted Orion Flight to a Near-Earth Object: A Feasibility Study. *NASA*, 2001.

[67] Landis, R.n Abell, P.n Korsmeyer, D., Jone, T., and Adamo, D. . Piloted Operations at a Near-Earth Object (NEO). *Acta Astronautica*, 2009(65):1689–1967, June 2009.

[68] Korsmeyer, D., Landis, R., and Abell, P. Into the Beyond: A Crewed Mission to a near-Earth object. *Acta Astronautica*, 2008(63):213–220, April 2008.

[69] Creech, S., Sumrall, P., and Cockrell, C. Ares V Overview and Status. *60th Internation Astronautical Congress*, (IAC-09-D2.8.1), Oct. 2009.

[70] Wagner, S. and Wie, B. A Crewed 180-Day Mission to Asteroid Apophis in 2028-2029. *60th International Astronautical Congress* , IAC-09-D2.8.7, Oct. 2009.

[71] Wagner, S., Pitz, A., Zimmerman, D., and Wie, B. Interplanetary Ballistic Missile (IPBM) System Architecture Design for Near-Earth Object Threat Mitigation. *60th International Astronautical Congress* , IAC-09-D1.1.1, Oct. 2009.

[72] Wagner, S. and Wie, B. Minimum ΔV Launch Windows for a Fictive Post-2029 Apophis Deflection/Disruption Mission. *20th AAS/AIAA Space Flight Mechanics Meeting*, AAS-10-245, Feb. 2010.

[73] Wagner, S. and Wie, B. Design of Fictive Post-2029 Apophis Intercept Mission for Nuclear Disruption. *AIAA/AAS Astrodynamics Specialist Conference*, AIAA-2010-8375, Aug. 2010.

[74] Wagner, S. and Wie, B. Target Asteroid Selection for Human Exploration of Near Earth Objects. *20th AAS/AIAA Space Flight Mechanics Meeting*, AAS-10-249, Feb. 2010.

[75] Wagner, S., Winkler, T., and Wie, B. Analysis and Selection of Optimal Targets for a Planetary Defense Technology Demonstration Mission. *AIAA/AAS Guidance Navigation and Control Conference*, AIAA 2012-4874, Aug. 2012.

[76] Pitz, A., Kaplinger, B., and Wie, B. Preliminary Design of a Hypervelocity Nuclear Interceptor Spacecraft for Optimal Disruption/Fragmentation of NEOs. *22nd AAS/AIAA Space Flight Mechanics Meeting*, AAS-12-225, Jan. 2012.

[77] Vardaxis, G., Pitz, A., and Wie, B. Conceptual Design of Planetary Defense Technology Demonstration Mission. *22nd AAS/AIAA Space Flight Mechanics Meeting*, AAS-12-128, Jan. 2012.

[78] Wagner, S. and Wie, B. Preliminary Design of a Crewed Mission to Asteroid Apophis in 2029-2039. *AIAA/AAS Astrodynamics Specialist Conference*, AIAA-2010-8374, Aug. 2010.

[79] Kaplinger, B., Wie, B., and Dearborn, D. Preliminary Design of a Crewed Mission to Asteroid Apophis in 2029-2039. *AIAA/AAS Astrodynamics Specialist Conference*, AIAA-2010-79824, Aug. 2010.

[80] Kaplinger, B. and Wie, B. NEO Fragmentation and Disperion Modeling and Simulation. *Proceedings of 2nd IAA Planetary Defense Conference*, May 2011.

[81] Wie, B. Hypervolocity Nuclear Interceptors for Asteroid Deflection or Disruption. *Proceedings of 2nd IAA Planetary Defense Conference*, May 2011.

[82] NASA. 99942 Apophis (2004 MN4). *JPL Small-Body Database Browser* , 2010.

[83] Giorgini, J., Benner, L., Ostro, S., Nolan, M., and Busch, M. Predicting the Earth encounters of 99942 Apophis. *ScienceDirect* , Icarus(193), 2008.

[84] Wie, B. Dynamics and Control of Gravity Tractor Spacecraft for Asteroid Deflection. *Journal of Guidance, Control, and Dynamics*, 31(5):1413–1423, Nov. 2008.

[85] Gooding, R.H. On the Solution of Lambert's Orbital Boundary-Value Problem. *Royal Aerospace Establishment*, Apr. 1988.

[86] Gooding, R.H. A Procedure for the Solution of Lambert's Orbital Boundary-Value Problem. *Kluwer Academic Publishers*, Jan. 1990.

[87] Press, W.H., Flannery, B.P., Teukolsky, S.A., and Vetterling, W.T. *Numerical Recipes in Fortran: The art of Scientific Computing*. Cambridge University Press, 2 edition, September 1992.

[88] Battin, R. *An Introduction to the Mathematics and Methods of Astrodynamics, Revised Edition*. AIAA Education Series, 1801 Alexadner Bell Drive, Reston, VA, Revised Edition edition, 1999.

[89] Meeus, J. *Astronomical Algorithms*. Willmann-Bell, Inc., Richmond, VA, 1991.

[90] Kahaner, D., Moler, C., and Nash, S. *Numerical Methods and Software*. Prentice Hall Series in Computational Mathematics, Englewood Cliffs, New Jersey 07632, 2nd edition, 1989.

[91] Chobotov, V.A. . *Orbital Mechanics Third Edition.* Ch. 4: Positin and Velocity as a Function of Time, AIAA Education Series, 1801 Alexander Bell Drive, Reston, Virginia, 2002.

[92] Curtis, H. *Orbital Mechanics for Engineering Students.* Elsevier Butterworth-Heinemann, Linacre House, Jordan Hill, Oxford, 1st edition, 2005.

[93] Weiland, C. *Computational Space Flight Mechanics.* Springer-Verlag Berlin Heidelberg, 2010.

[94] Gurfil, P., editor. *Modern Astrodynamics.* Elsevier Astrodynamics Series, 1st edition, 2006.

[95] Tapley, B. D., Schutz, B. E., and Born, G. H. *Statistical Orbit Determination.* Elsevier Inc., 2004.

[96] Arnaud Bourdoux. *Characterisation and hazard mitigation of resonant returning Near Earth Objects: the case of 2004 MN4.* PhD thesis, Universite de Liege, 2005.

[97] Gronchi, G. F. and Milani, A. Proper elements for Earth crossing asteroids. Sept. 2000.

[98] Gronchi, G. F. and Michel, P. Secular Orbital Evolution, Proper Elements, and Proper Frequencies for Near-Earth Asteroids: A Comparison between Semianalytic Theory and Numerical Integrations. *Icarus*, 152:48–57, Jan. 2001.

[99] Gronchi, G. F. and Milani, A. Averaging on Earth-crossing Orbits. *Celestial Mechanics and Dynamical Astronomy*, 71:109–136, Sept. 1998.

[100] Alfano, S. Orbital Covariance Interpolation. *14th AAS/AIAA Space Flight Mechanics Conference*, AAS 04-223, Feb. 2004.

[101] Davis, J., Singla, P., and Junkins, J. Identifying Near-term Missions and Impact Keyholes for Asteroid 99942 Apophis. 2005.